University of Alberta

Effects of yttrium on high temperature wear behavior of cobalt based alloys

by

Iulian Radu

A thesis submitted to the Faculty of Graduate Studies and Research
in partial fulfillment of the requirements for the degree of

Doctor of Philosophy

in

Materials Engineering

Chemical and Materials Engineering

Edmonton, Alberta
Spring 2008

Library and Archives Canada

Published Heritage Branch

395 Wellington Street
Ottawa ON K1A 0N4
Canada

Bibliothèque et Archives Canada

Direction du Patrimoine de l'édition

395, rue Wellington
Ottawa ON K1A 0N4
Canada

Your file Votre référence
ISBN: 978-0-494-45584-5
Our file Notre référence
ISBN: 978-0-494-45584-5

NOTICE:
The author has granted a non-exclusive license allowing Library and Archives Canada to reproduce, publish, archive, preserve, conserve, communicate to the public by telecommunication or on the Internet, loan, distribute and sell theses worldwide, for commercial or non-commercial purposes, in microform, paper, electronic and/or any other formats.

The author retains copyright ownership and moral rights in this thesis. Neither the thesis nor substantial extracts from it may be printed or otherwise reproduced without the author's permission.

AVIS:
L'auteur a accordé une licence non exclusive permettant à la Bibliothèque et Archives Canada de reproduire, publier, archiver, sauvegarder, conserver, transmettre au public par télécommunication ou par l'Internet, prêter, distribuer et vendre des thèses partout dans le monde, à des fins commerciales ou autres, sur support microforme, papier, électronique et/ou autres formats.

L'auteur conserve la propriété du droit d'auteur et des droits moraux qui protège cette thèse. Ni la thèse ni des extraits substantiels de celle-ci ne doivent être imprimés ou autrement reproduits sans son autorisation.

In compliance with the Canadian Privacy Act some supporting forms may have been removed from this thesis.

While these forms may be included in the document page count, their removal does not represent any loss of content from the thesis.

Conformément à la loi canadienne sur la protection de la vie privée, quelques formulaires secondaires ont été enlevés de cette thèse.

Bien que ces formulaires aient inclus dans la pagination, il n'y aura aucun contenu manquant.

Canada

ABSTRACT

Wear damage at elevated temperatures caused by sliding contact between metallic components during service is a common problem in many mechanical systems. Wear is a complex surface failure process affected by many factors, including material properties, loading condition, and environment. Among various factors, temperature is an important environmental factor that largely influences the wear behavior of a material through changing its mechanical strength, adhesion, and oxidation kinetics.

Cobalt-base alloys most commonly known as Stellite® alloys, have been used extensively as bearing materials for applications that require high resistance to wear, particularly at elevated temperatures and/or in corrosive environments . Considerable efforts have been made to reduce wear at elevated temperatures.

The improvement can be achieved through the development of Stellite alloys with improved high temperature wear and corrosion performance without compromising other engineering properties. One approach is to add reactive elements such as yttrium, in order to beneficially affect the oxidation behavior of these alloys.

Various techniques were used to investigate the effects of yttrium addition to Stellite 21 and 712, including optical microscopy, X-ray diffraction, SEM (scanning electron microscopy), EDS (energy dispersive spectroscopy), micro- and nano-mechanical probes, micro-scratch tests, AFM (atomic force microscopy), SIMS (secondary ion mass spectroscopy), and pin-on-disc wear tests.

The research demonstrated that alloying a small amount of yttrium (e.g., less than 1%Y) rendered the oxide scale on Stellite alloys stronger with higher adherence to the substrate, which was largely beneficial to the wear performance of the alloys at elevated temperatures.

TABLE OF CONTENTS

List of Tables

List of Figures

1.0 Introduction **Page 1**

2.0 Literature review **Page 8**

2.1 General wear concepts and wear modes 8

2.1.1 Adhesive wear 9

2.1.2 Abrasive wear 11

2.1.3 Fatigue wear 13

2.1.4 Corrosive wear 14

2.2 General wear mechanisms/theories and factors that influence wear in different modes. 15

2.2.1 Archard's wear equation 16

2.2.2 Factors that influence wear in different modes 19

2.2.3 Delamination wear theory 21

2.2.4 Oxidational wear theory 25

2.3 Wear at elevated temperatures 30

2.3.1 Mechanism of high-temperature wear and glaze formation 35

2.3.2 Factors that affect high-temperature wear 38

2.3.3 Approaches to reduce high-temperature wear 44

2.4 Effects of reactive elements on oxidation and oxidative wear 45

2.4.1 Enhanced scale plasticity 51

2.4.2 Graded seal mechanism 53
2.4.3 Enhancement of scale nucleation process 53
2.4.4 Modification of the oxide growth mechanism 55
2.4.5 Oxide pegging to the alloy 56
2.4.6 Vacancy sink model 57
2.4.7 Reduction of compressive stresses within the oxide 58
2.4.8 Improved chemical bonding to the alloy 59
2.4.9 Sulfur getter mechanism 60
2.4.10 Dynamic segregation model 61
2.4.11 Poisoned interface model 63
2.4.12 Effects of reactive elements on oxidative wear 66
2.5 Possibilities of reactive elements to resist high temperature wear 68

3.0 Microstructure Page 72
3.1 General properties of Stellite alloys 72
3.2 Alloy preparation and heat treatment 75
3.3 Results of microstructure examination 78
3.4 Crystal structure of phases developed in the samples 86

4.0 Evaluation of the mechanical properties 91
4.1 Hardness 91
4.2 Stress induced $\gamma \rightarrow \varepsilon$ transformation in Stellite 21 samples with and without yttrium addition 96

5.0 Evaluation of oxide's scale mechanical properties Page 102
5.1 The mechanical behavior of the oxide scale 102
5.2 Evaluation of the interfacial strength of the oxide/matrix interface 106
5.3 Crystal structure of phases developed in the oxide scale 110

6.0 Wear behavior **Page 115**

6.1 Wear performance of yttrium-free and yttrium-containing samples from room temperature up to 600^0C. 115

6.1.1 Stellite 21 115

6.1.2 Stellite 712 122

6.2 The role of oxide scale in resisting wear at elevated temperature 125

7.0 Oxidation behavior of yttrium-free and yttrium-containing Stellite 21 and 712 **Page 135**

7.1 The oxidation behavior of yttrium-free and yttrium-containing Stellite 21 and 712 samples at 600^0C. 135

7.2 Oxidation of yttrium-Free and yttrium-containing Stellite 21 samples at 1000^0C. 160

8.0 Conclusions and possible further research topics **Page 180**

8.1 Conclusions 180

8.2 Further research topics 184

9.0 Bibliography **Page 188**

LIST OF TABLES

Table 1.1: Chemical composition of the widely most used valve alloys in the automotive industry. **Page 4**

Table 1.2: Chemical composition of the most common valve hardfacing alloys. **Page 5**

Table 3.1: Nominal composition of Stellite 21 and 712 alloys. **Page 73**

Table 3.2: Experimental Conditions for Re-melting of Stellite 21. **Page 77**

Table 3.3: XRD phases on Stellite 712 corresponding to the peak numbers. **Page 90**

Table 5.1: Mechanical properties of the oxide scale obtained from nano-indentation test. **Page 104**

Table 5.2: Mechanical properties of the oxide scale obtained from nano-indentation test. **Page 105**

Table 7.1: Surface roughness of oxide scales developed on yttrium-free and yttrium-containing Stellite712 samples after oxidation at 600^0C for 25 hours. **Page 158**

Table 7.2: Chemical composition of the scale developed on 5% yttrium-containing sample as revealed by EDS analysis. **Page 167**

Table 7.3: The overall chemical composition of the top surface of the oxide scales. **Page 168**

LIST OF FIGURES

Figure 1.1: Sealing mechanism of a high-temperature nuclear valve - The interface between the valve's disc and body seat ring is protected by hardfacing with Stellite alloy. **Page 4**

Figure 2.1: Adhesive wear. **Page 10**

Figure 2.2: Abrasive wear: a) two body abrasion; b) three body abrasion. **Page 11**

Figure 2.3: Modes of deformation during abrasive wear: a) cutting; b) wedge formation; c) ploughing. **Page 12**

Figure 2.4: Archard's equation - Idealized model of abrasion. **Page 17**

Figure 2.5: Delamination wear theory - Cross-section of a worn surface. **Page 23**

Figure 2.6: Idealized model of a contact at a dominant plateau on the surface. **Page 27**

Figure 2.7: Interfacial defects at a semi-coherent oxide/matrix interface: (I) misfit dislocation, (II) misorientation dislocation, (III) disconnection, and (IV) ledge. **Page 64**

Figure 2.8: Growing of an oxide scale by major anion diffusion at oxide/matrix interface - the translation of the disconnections and the need of removing an extra atom from the interface: a) first step; b) a subsequent step. **Page 65**

Figure 2.9: Schematic representation of reactive ions pining misfit dislocations at the oxide/matrix interface. **Page 66**

Figure 3.1: a) SEM images of yttrium powder that was alloyed to Stellite 21 and 712 alloys and b) the corresponding EDS analysis. **Page 76**

Figure 3.2: Optical microstructures of Stellite 21 alloy modified with: a) 0%Y; b) 0.5%Y; c) 1%Y; d) 2%Y; e) 5%Y. **Page 79**

Figure 3.3: Optical microstructures of Stellite 712 alloy samples with a) 0%Y, b) 0.5%Y, and c) 5%Y. The light and dark domains are dendritic and interdendritic regions, respectively. **Page 80**

Figure 3.4: EDS compositional dot maps of Stellite 21 alloy modified with: a) Yttrium free; b) 0.5%Y; c) 5%Y. **Page 82**

Figure 3.5: SEM images of Stellite 712 alloy samples with a) 0%Y - untreated; b) 5%Y - untreated; c) 0%Y - heat treated; d) 5%Y - heat treated; e) 0%Y - heat treated, a closer view. **Page 84**

Figure 3.6: EDS compositional dot maps of Stellite 712 alloy containing 5%Y; a) Y, b) Cr, c) Mo, d) Co, e) Ni, f) corresponding SEM image. **Page 85**

Figure 3.7: X-ray diffraction patterns of Y-free, 1%, and 5% yttrium-containing samples, respectively. **Page 87**

Figure 3.8: X-ray diffraction patterns of Y-free, 0.5%, and 5% yttrium-containing Stellite 712 samples, respectively. **Page 89**

Figure 4.1: Macro-hardness (HRC) values of yttrium-free and yttrium-containing Stellite 21 samples. **Page 92**

Figure 4.2: A load-depth curve from micro-hardness test. **Page 93**

Figure 4.3: Curves of η ratio and indentation depth versus indentation load: Dendritic regions. **Page 93**

Figure 4.4: Curves of η ratio and indentation depth versus indentation load: Interdendritic regions. **Page 94**

Figure 4.5: Curves of η value and indentation depth versus indentation load: a) Interdendritic regions; b) Dendritic regions. **Page 95**

Figure 4.6: X-ray diffraction patterns of unstrained and strained Yttrium-free samples. **Page 97**

Figure 4.7: X-ray diffraction patterns of unstrained and strained 0.5% Yttrium-containing samples. **Page 98**

Figure 4.8: X-ray diffraction patterns of unstrained and strained 5% Yttrium-containing samples. **Page 99**

Figure 5.1: Nano-indentation curves of the oxide scales on Yttrium-free and Yttrium-containing samples of Stellite 21. **Page 103**

Figure 5.2: Nano-indentation curves of the oxide scales on yttrium-free, 0.5% and 5% yttrium-containing Stellite 712 samples, respectively. **Page 103**

Figure 5.3: Micro-scratch test with *in situ* monitoring changes in electric contact resistance on Stellite 21 specimens: a) Yttrium free; b) 0.5%Y; c) 5%Y. **Page 108**

Figure 5.4: Micro-scratch test with *in situ* monitoring changes in electric contact resistance on Stellite 712 specimens: a)Yttrium-free; b) 0.5%Y; c) 5%Y. **Page 109**

Figure 5.5: Low angle X-ray diffraction patterns of the oxide scales developed on: I) yttrium free; II) 0.5%Y; III) 5% yttrium-containing samples, respectively **Page 111**

Figure 5.6: Low angle X-ray diffraction patterns of the oxide scales developed on: a) yttrium free; b) 0.5%Y; c) 5% yttrium Stellite 712 containing samples, respectively. **Page 113**

Figure 6.1: Wear loss with respect to temperature of Stellite 21 samples with and without yttrium. **Page 116**

Figure 6.2: Micrographs of wear tracks at 600^0C – 4000 laps: a) Yttrium-free; b) 0.5%Y; c) 1%Y; d) 5%Y – containing Stellite 21 samples. **Page 117**

Figure 6.3: Figure 6.3: Morphology of wear track on sample after sliding for 2000 laps at: a) 150^0C – 0.5%Y; b) 600^0C – 2%Y; c) 600^0C – 2%Y a closer view. **Page 119**

Figure 6.4: Morphology of wear track after sliding wear at room temperature: a) 2%Y, b) detailed view showing wide spread cracking of the debris layer. **Page 121**

Figure 6.5: Wear losses of yttrium-free and yttrium-containing Stellite 712 samples at 600^0C. **Page 123**

Figure 6.6: Micrographs of wear tracks (wear at 600^0C) on Stellite 712 specimens: a) yttrium-free; b) 0.5%Y; c) yttrium-free – a closer view. **Page 125**

Figure 6.7: Wear loss at 200^0C under a load of 2N after sliding for 2000 laps in air and in argon, respectively. **Page 126**

Figure 6.8: Morphology of wear track on samples after sliding for 2000 laps at 200^0C: a) 0.5%Y in air; b) 0.5%Y in argon; c) Yttrium free in argon (SEM); d) 0.5%Y in argon (SEM). **Page 128**

Figure 6.9: Wear loss at 600^0C under a load of 2N after sliding for 10000 laps in air and in argon, respectively. **Page 129**

Figure 6.10: Wear loss at 600^0C under a load of 5N after sliding for 10000 laps in air and in argon, respectively. **Page 131**

Figure 6.11: Wear loss at 600^0C under a load of 10N after sliding for 3000 laps in air and in argon, respectively. **Page 132**

Figure 7.1: Mechanical properties of the oxide scales resulting from oxidation at 600^{0}C for 1 min: a) Depth of indentation, b) Elastic behavior - η value. **Page 136**

Figure 7.2: SEM image of the polished cross-section of the scale formed on yttrium- free sample. **Page 138**

Figure 7.3: AFM three-dimensional topographic profiles (2x2μm) of the oxide scales developed on samples of Stellite 21 after oxidation at 600^{0}C for 1 min: a) Yttrium-free; b) 0.5%Y; and c) 5%Y. **Page 140**

Figure 7.4: Roughness of the oxide scales formed at 600^{0}C for 1 min on Stellite 21 with and without yttrium. **Page 141**

Figure 7.5: AFM images of the oxide scales developed after oxidation of Stellite 21 samples at 600^{0}C for 1 min a) Yttrium-free; b) 0.5%Y; c) 5%Y. **Page 142**

Figure 7.6: Mean grain sizes (diameter) of oxide scales developed on Stellite 21 samples with and without yttrium after 1min-exposure in air at 600^{0}C. **Page 143**

Figure 7.7: SIMS composition-depth profiles of the oxide developed on Y-free Stellite 21 sample after oxidation at 600^{0}C for 125 hours. **Page 146**

Figure 7.8: SIMS composition-depth profiles of the oxide developed on 0.5% Y-containing Stellite 21 sample after oxidation at 600^0C for 125 hours. **Page 147**

Figure 7.9: SIMS composition-depth profiles of the oxide developed on 5% Y-containing Stellite 21 sample after oxidation at 600^0C for 125 hours. **Page 148**

Figure 7.10: Negative SIMS profiles of oxide scales formed at 600^0C in $^{16}O_2$ for 8 hours followed by 24-hours oxidation in $^{18}O_2$ on a) yttrium-free, b) 0.5% yttrium-containing, and c) 5% yttrium-containing Stellite 21 samples. **Page 150**

Figure 7.11: Changes in grain size, roughness, and hardness or indentation depth of oxides formed on different samples with respect to the oxidation time: a) grain size, b) roughness, c) depth of indentation. **Page 153**

Figure 7.12: Nano-indentation curves of oxide scales developed on pure Cr and Mn samples after oxidation at 600^0C for 8 hours. **Page 154**

Figure 7.13: AFM three-dimensional topographic pictures (10x10μm) and roughness profiles of the oxide scales developed at 600^0C for 25 hours on a) Yttrium-free; b) 0.5%Y; c) 5%Y – containing Stellite 712 samples. **Page 157**

Figure 7.14: AFM images of oxide scales developed at 600^{0}C for 25 hours on different Stellite 712 samples: a) Yttrium-free; b) 0.5%Y; c) 5%Y. **Page 159**

Figure 7.15: SEM images of the oxide surface morphology: a) Y-free, b) 0.5%Y, c) 5%Y. **Page 162**

Figure 7.16: Detailed view of the oxide surface morphology: a) Y-free, b) 0.5%Y, c) 5%Y. **Page 163**

Figure 7.17: Details of an area where spallation occurred; a) 5%Y, b) 0.5%Y. **Page 165**

Figure 7.18: SEM image of the oxide scale developed on 5% yttrium-containing sample showing the locations of the EDS point analysis. **Page 166**

Figure 7.19: Hardness of the oxide scale developed at 1000^{0}C for 125 hours. **Page 168**

Figure 7.20: η ratio of the oxide scale developed at 1000^{0}C for 125 hours. **Page 169**

Figure 7.21: SEM images of the cross-section of the scale formed on a) yttrium- free, b) 0.5%Y, and c) 1%Y-containing Stellite 21 samples. **Page 170**

Figure 7.22: SEM images of the cross-section of the oxide scale formed on a) 5%Y, and b) the substrate in cross-section after exposure at 1000^{0}C for 125 hours. **Page 171**

Figure 7.23: SEM images of the oxide/substrate interface; a) yttrium-free; b) 0.5%Y; c) 5%Y-containing Stellite 21 samples. **Page 174**

Figure 7.24: Depth of indentation and η ratio of the substrate and peg-like structure near the oxide/matrix interface. **Page 176**

Figure 7.25: Depth of indentation versus distance from oxide/substrate interface a) Y-free; b) 0.5%Y; c) 5%Y - containing Stellite 21. **Page 177**

Figure 7.26: Chromium EDS profiles across the oxide/substrate interface: a) Y-free; b) 0.5%Y; c) 5%Y – containing Stellite 21. **Page 179**

1.0 INTRODUCTION

Wear damage caused by sliding contact between metallic components during service is a common problem in many industries. It results in material loss, failure of mechanical systems, and additional energy consumption. Among various processes that cause material losses and failure, wear is one of the most destructive. It is estimated that the capitalized loss due to wear costs one to five percent of the Gross National Product of industrialized countries [1]. More than five billions dollars per year represent losses in Canada due to friction and wear [2]. Because of the economic and engineering significance, wear and friction have been for a long time a major subject of study, named "tribology". The name of tribology comes from the Greek word "τριβοζ"(tribos) which mean rubbing. Tribology is defined as "the science and technology of interacting surfaces in relative motion and of practices related there to" [3].

Wear is a complex surface failure process affected by many factors, including material properties, loading condition, and environment. Among various factors, temperature is an important environmental factor that markedly influences the wear behavior of a material through changing its mechanical strength, adhesion, and oxidation kinetics [4]. Aggressive environments and high temperatures make traditional methods of reducing friction and wear ineffective.

Considerable efforts have been made to reduce wear at elevated temperatures using different approaches such as applications of coatings [5], preoxidation [6], cladding [7-9], different processing techniques [10,11], alloying treatment [11,13]

etc. However, material selection is severely limited by the requirements of high temperature applications such as oxidation resistance, high temperature strength, and creep resistance. Cobalt-based alloys represent one choice of selection for applications where high resistance to both corrosion and wear is required, especially at elevated temperatures. Nickel-based alloys are the most widely used materials for high temperature applications (e.g., aerospace, nuclear etc.) due to their enhanced hardening mechanisms but cobalt-based alloys provide several advantages over them, including higher melting points, superior hot corrosion resistance especially to contaminated gas-turbine atmospheres, enhanced fatigue resistance, better weldability, and galling wear resistance [14,15].

Due to the above properties, the cobalt-based alloys are used for two main applications [15]. First, as a surgical implant material such as hip and knee orthopedic implant prostheses, and dental components [16-22]. The worldwide cobalt consumption for the biomedical applications was estimated to be 2000 t/year [15]. Second, cobalt based alloys have been used extensively for applications that require high resistance to wear, particularly at elevated temperatures and/or in corrosive environments [14, 23-27] such as valves and valves seats for automobile's engines and nuclear power plants [28-31], hardfacing material for turbines and pumps [32], sleeve and bush materials in continuous hot-dip galvanizing processes [33] etc. Three basic alloy types are used for the above applications: (1) carbide type such as Stellite 1 or 6, (2) intermetallic type such as Tribaloy T800 or T400, and (3) solid-solution type such as Stellite 21 [15]. The worldwide cobalt consumption for the applications involving wear resistance is estimated at 4000 t/year [15].

One of the standard Co-base alloys, Stellite 21, is used predominantly to resist the synergistic effects of corrosion and mechanical damage, especially at elevated temperatures; e.g., wear of valve seats in nuclear power plants and in automobile engines and other high temperature applications [7,8,23,34]. Recently, significant efforts have been made to develop an improved type of engine, which operates at higher efficiency than conventional gasoline and diesel engines. However, the development is hindered by the corrosion and wear of the engine's valves especially of the exhaust valves due to high temperatures (i.e., 600^0C) and contact pressures up to 100 MPa [29,30]. High temperature wear of the valves may lead to the formation of pits that can join together forming channels, which reduce the valve's sealing ability to hot gases. As a result, the gases can escape from the combustion chamber, reducing efficiency [29,30,35]. Valves for conventional engines are made either from ferritic-martensitic stainless steel, austenitic stainless steel or nickel-based alloys [29-31]. For heavy fuel operation engines, nickel-based alloys such as Nimonic 80A or 81 have become the industry standard materials [31,35]. The valve's seat contact surface is further protected against wear and corrosion by hardfacing (figure 1.1). The standard hardfacing alloys used by automotive industry are cobalt-based alloys named Stellite, but nickel-based alloys became also common (e.g. Deloro Alloy 60).

Tables 1.1 and 1.2 presents the chemical composition of common existing valve materials and hardfacing alloys, respectively, used in the automotive industry.

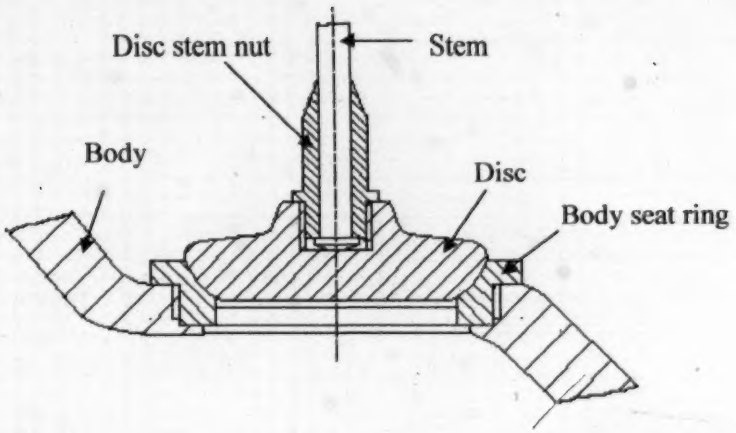

Figure 1.1: Sealing mechanism of a high-temperature nuclear valve - The interface between the valve's disc and body seat ring is protected by hardfacing with Stellite alloy.

Table 1.1: Chemical composition of the most widely used valve alloys in the automotive industry [30,31,35].

	Chemical Composition [%]						
Material	**C**	**Fe**	**Ni**	**Cr**	**Mn**	**Si**	**Others**
Nimonic 80A	0.06	-	Bal	19.5	-	-	Zr 0.04, Ti 2.3, Al 1.4
Nimonic 81	0.05	-	Bal	30	-	-	Zr 0.06, Ti 1.8, Al 0.9
En 52	0.45	Bal	0.5	9	0.5	3.5	-
X45CrNiW18 9	0.45	Bal	9	18	1.2	2.5	-
21-4N	0.5	Bal	3.8	21	9	0.25	N 0.42
X45CrSi9 3	0.45	Bal	-	9	0.45	3.1	-
HNV6	0.8	Bal	1.5	20	0.4	2.25	-

Table 1.2: Chemical composition of the most common valve hardfacing alloys [24,26,29,35].

	Chemical Composition [%]									
Material	**C**	**Co**	**Ni**	**Cr**	**W**	**Mo**	**Si**	**Fe**	**Mn**	**B**
Stellite 1	2.5	Bal	3	32	13	1	2	3	1	-
Stellite 6	1.2	Bal	3	28	5	1	2	3	1	-
Stellite 12	1.4	Bal	3	30	9	1	2	3	1	-
Stellite 20	2.5	Bal	3	33	18	1	2	3	1	-
Stellite 21	0.25	Bal	2.5	28	-	5.5	2	2	1	-
Alloy 60	0.75	-	Bal	15	-	-	4.4	3.5	-	3.2
Colmonoy 8	2	-	Bal	26	-	-	4	1	-	-
Tristelle TS	2	12	10	35	-	-	5	Bal	0.2	-

In contrast with the wide use of metallic alloys for valve hardfacing, fewer ceramics materials have been tested. For example, valve hardfacing systems based on yttria-stabilized zirconia have been tried for exhaust valves but the results were unsatisfactory [36, 37]. Ceramic hardfacing based on a continuously graded coating of Cr_3C_2/NiCr seems promising [38], but are not comparable to Stellite hardfaced surfaces. In spite of extensive efforts made to substitute Stellite alloys for valve hardfacing applications in the automotive industry, success is limited. In fact, the development of high efficiency engines used in harsher environments is leading to increased use of cobalt-based alloys [15].

Recently, attempts have been made to replace Stellite 21 alloy for nuclear applications because of radioactivity concerns [39,40]. This alloy is hardfaced on the seat contact surfaces (figure 1.1), made from a 300 series of stainless steel alloy (usually 304) [39,41,42]. The source of radiation was found to be cobalt-based alloy valve wear debris, which may reach the Zircaloy fuel rod in the reactor core. The debris are activated by the neutron flux, leading to the formation of radioactive Co^{60} isotope deposits [39,40]. The radioactive isotope deposits are released by dissolution and/or erosion then transported through the flow out system of the nuclear core, contaminating all out-of-core internal surfaces in the primary circuit such as pipe walls [28,39,40]. It has been estimated that valve wear debris is responsible for 10% of total out of core radioactivity. Attempts at alloy replacement failed to duplicate all the required tribological properties as those provided by Stellite 21 alloy, especially the properties that depend on the fcc-hcp cobalt transformation (i.e., galling wear resistance) [27,28,32,43-46]. Consequently, efforts have been continuously made to improve Stellite 21 and other Stellite alloys not only for nuclear application, but also for other tribological uses [12, 47-51].

The improvement can be achieved through the development of Stellite alloys with improved high temperature wear and corrosion performance without compromising other engineering properties, which represents the main goal of the research presented in the following chapters of this thesis.

This thesis has the following structure:

Chapter one consists of a short introduction to wear, its economical effects, the materials that are usually selected for high temperature wear service, and the

objectives of this research.

Chapter two provides a review of the most pertinent literature regarding wear phenomena and the effects of reactive elements on oxidation and oxidative wear. Chapter three presents the results of the study on the main effects of yttrium on the microstructure of Stellite alloys 21 and 712, while chapter four illustrates the changes to the mechanical properties when alloying yttrium to Stellite 21 and 712 alloys. Chapter five reports the results of studies on the mechanical properties of the oxide scales developed on yttrium-free and yttrium containing Stellite 21 and 712 alloys after oxidation at elevated temperatures. Chapter six is focused on the evaluation of the wear performance of Stellite alloys, with and without yttrium, from room temperature up to 600^0C. Chapter seven presents the results of the study on the effect of yttrium on the oxidation behavior of Stellite alloys 21 and 712, respectively, at elevated temperatures for up to 125 hours. The final chapter summarizes the effects of yttrium on Stellite 21 and 712 microstructure, mechanical properties of the alloy and its oxide scale, oxidation behavior, and high-temperature wear performance. In addition, further research topics are suggested.

2.0 LITERATURE REVIEW

This chapter provides a critical review of the literature regarding wear phenomena, factors that influence it, and the effects of reactive elements on oxidation and oxidative wear. The purpose is to provide a comprehensive view of the research conducted worldwide in the field of high temperature wear and a framework to facilitate interpretation of the results presented in this thesis. Chapter two comprises five main sections: the first section presents general wear concepts; the second section describes the general wear mechanisms/theories and factors that influence the wear behavior; the third section deals with wear phenomena at high temperatures; the fourth section is focused on the effects of reactive elements on oxidation and the current models explaining this effect. The last section summarizes possibilities of applying reactive elements to improve high temperature wear, and the objective of this research.

2.1 General wear concepts and wear modes

Wear is defined as the damage to a surface by progressive loss of material due to the mechanical contact and relative motion between two surfaces [4, 52]. This is a complex process involving different wear modes and failure mechanisms. A given material may exhibit a high resistance to wear in a specific wear mode but may perform unsatisfactorily in another wear mode. The solution to a specific wear problem depends on many factors, including material properties and the wear

condition. System analysis is generally used to identify the factors affecting wear in a particular industrial application, by isolating the elements of the tribological contact of interest from the whole system [53]. The result is a simplified tribosystem consisting usually of four main components [4, 52]:

- Main body (must be solid) – represents the component that is worn and plays an important role in the system,
- Counter-body (solid, liquid, gaseous, or a mixture of them), represents an object in relative motion to the main body and in direct or indirect contact so that the forces can be transmitted to the main body.
- Interfacial component (solid, liquid, gaseous, a mixture of them, or may be absent), e.g. lubricants, wear debris or oxide films.
- Environment (liquid, gaseous, a mixture of them, or vacuum).

Depending on the tribosystem parameters and variables, four basic wear modes or any combination of them are involved in wear processes [54-57]:

- Adhesive wear,
- Abrasive wear,
- Fatigue wear,
- Corrosive wear.

2.1.1 Adhesive wear

Adhesive wear occurs when two surfaces slides against each other in the absence of an interfacial element. Engineering surfaces do not have an ideally planar

surface; therefore, the contact between two surfaces takes place at the asperities tip [58]. As a result, the real area of contact is smaller than the apparent contact area [4,58]; thus, the stress at the asperities tip is very high causing plastic deformation and strong bonding between the asperities tips. Breaking the bond junctions is required to maintain motion between surfaces. When a junction is broken, wear debris usually is generated, mostly from the weaker material. In general, the worn debris transfers to the harder surface [59]. Adhesive wear occurs when the shear strength of the softer material is less than the junction bonding strength (figure 2.1).

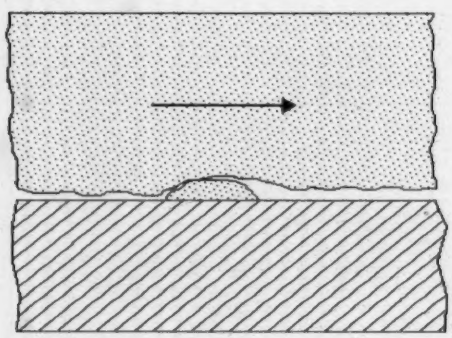

Figure 2.1: Adhesive wear

There are several applications where adhesion is the major wear failure mode, such as: satellite components (no interfacial contamination thus higher adhesion), wear under vacuum conditions [60,61], computer disc drives, computer storage data devices [62], CD players, nano-machines, biomedical implants (acetabular components [63]), gear seats, cams [59] etc.

2.1.2 Abrasive wear

Abrasive wear occurs due to material loss by scratching when relatively hard asperities or particles move along a solid surface under a contact force. Abrasion does not involve material transfer between contacting surfaces as adhesive wear does [59]. There are two types of abrasive wear (figure 2.2): (1) two body abrasion, where small asperities of the harder surface scratch the counter-face and (2) three body abrasion, when abrasive particles are caught between the two surfaces in contact and abrade the surfaces (rotation of abrasive is involved). However, the wear loss in three body abrasion is two orders of magnitude lower than that in two body abrasion [4].

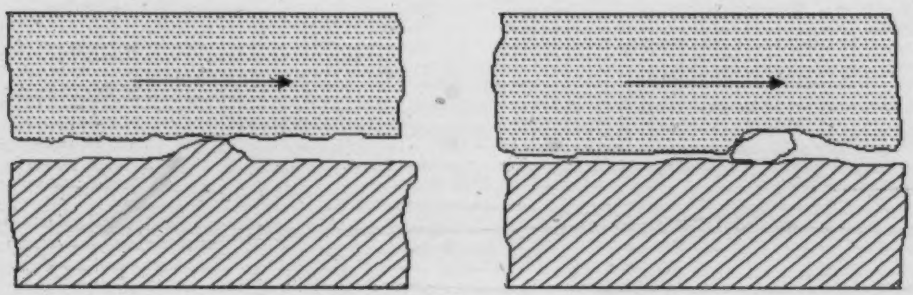

Figure 2.2: Abrasive wear: a) two body abrasion; b) three body abrasion.

Also, abrasive wear can be categorized as low stress abrasion when the abrasive remain intact or as high stress abrasion when the abrasive is broken up during the wear process [59]. Gouging abrasion is a variant of high stress abrasion

when relatively large abrasive particles are cutting the material removing large fragments from the worn surface [64].

The mechanism of abrasive wear involves both plastic deformation and fracture. Three different modes of deformation are often observed during abrasive wear: cutting, wedge formation, and ploughing [65] (figure 2.3).

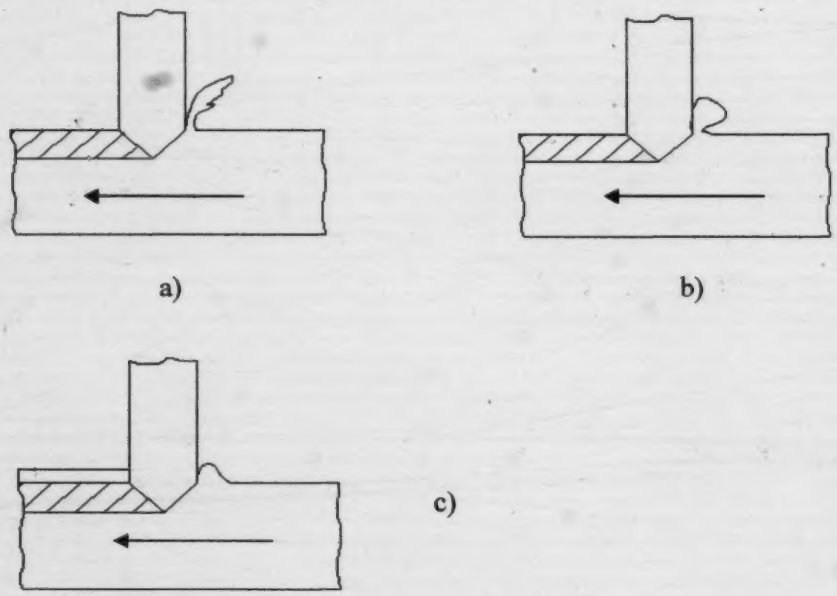

Figure 2.3: Modes of deformation during abrasive wear: a) cutting; b) wedge formation; c) ploughing.

Cutting is characterized by formation of a chip at the front of the abrasive and represents the most severe form of abrasive wear. Wedge formation consists of the formation of a wedge in the front of the abrasive tip. When the adhesion between the wedge and abrasive tip is strong, sliding occurs between the wedge bottom and the

flat surface. Otherwise, removal of material takes place by shear of the raised prow along its bottom. Ploughing occurs when the material is displaced from a groove to the sides; therefore, no material is removed from the surface. The material is displaced from the surface when subsequent furrows intersect due to continued passage of abrasive particles [59].

There are several industrial areas where abrasive wear is commonly encountered such as drilling heads, digger teeth [66], truck tires, biomedical implants, ore transport, crushing, screening etc. [59].

2.1.3 Fatigue wear

Fatigue wear takes place when the surface is attacked under cyclic loading that exceeds the fatigue limit of the material. The stress induced during fatigue wear in the surface layer leads to elastic deformation followed by plastic deformation, work hardening, crack nucleation and propagation, which results in surface damage [54,55].

There are two types of fatigue wear: (1) stress fatigue, when crack nucleation is the main failure process (i.e., ceramic materials) and (2) strain fatigue, when crack propagation is the main failure process (i.e., ductile materials) [54,55].

There are several industrial applications where fatigue wear is the predominant mode of failure such as railroad tracks, ball and roller bearings, parts that connects the wind and the body of an airplane, rollers for cold or hot rolling, mechanical printing devices etc [1,4].

2.1.4 Corrosive wear

When surfaces are in contact with gaseous or liquid aggressive environments, corrosion products form a film that affects the underlying material in subsequent corrosion damage. This film could be removed partially of totally during wear processes, leaving fresh metal to the environment, which allows further corrosion. Both the lost of material due to continual removal and formation of reaction layers on the contacting surfaces are involved in corrosive wear [54,55]. The synergy of wear and corrosion results usually in a greater material loss than those caused by wear and corrosion, separately. Corrosion wear occurs prevalently on pumps components and pipes in the chemical industry. However, one beneficial application of corrosive wear is chemical mechanical planarization of metals and dielectrics in building multilevel microelectronic circuits in the semiconductor industry [67-69].

Wear can be further classified according to the motion type of the tribosystem components, i.e., sliding (e.g., sliding wear, galling wear, fretting wear etc.), rolling, and impacting (e.g., erosion, impact wear, cavitation wear etc.) [1,4]. Galling wear is often associated with sliding wear but refers to damage resulting from sliding at low speeds, characterized by localized bonding between contacting surfaces leading to transfer between surfaces or displacement of large fragments of material that results in a severely roughened surface [64,70,71]. Also, fretting wear is associated with sliding wear but refers to damage resulted from small amplitude oscillatory movements between contacting surfaces [72].

2.2 General wear mechanisms/theories and factors that influence wear in different modes

In practice, a wear process may involve more than one wear mode but only one of the wear modes will be the dominant wear mechanism. For example, in impact/erosion wear the prevailing mechanism is abrasive wear. In turn, for sliding wear the prevailing mechanism is influenced by many factors including type of contact, loading condition, interfacial element etc.

These factors can be divided in two main groups: (1) external factors, including operating conditions (e.g. speed, load, temperature, and geometry), environment (e.g. air, lubricant, vacuum, surface contamination), material combinations (e.g. hard on hard) and (2) internal factors, including materials properties such as hardness, microstructure, mutual solubility, crystal structure, etc. [73]. Each wear mode could be affected differently by a given factor.

Many wear theories have been proposed to explain the wear behavior under a combination of wear modes and factors. However, since a wear process depends on many factors and variables, there is no equation or analytical model able to precisely predict wear loss [73].

2.2.1 Archard's wear equation

One of the earliest wear theories is the Archard's wear equation, which was developed first as a model for adhesive wear mode. The model considers a single asperity-to-asperity contact, which is assumed to be circular (having a radius "a") in plane view [74]. The normal load, (∂W), supported by the contact is given by the following expression:

$$\partial W = P\pi a^2 \qquad \{2.1\}$$

where P represents the yield pressure for the plastically deforming asperity. During the sliding process, wear take place by formation and destruction of individually asperity contacts. Detachments of fragments of material from asperities results in wear loss. The volume of each fragment depends on the asperity junction size from which it originated: $\partial V = \frac{2\pi a^3}{3}$. However, only a proportion, k, of all asperities contact gives rise of wear particles [74]. The average volume of material, ∂Q worn per sliding distance (2a) of one pair of asperity contact is given by:

$$\delta Q = k\frac{\delta V}{2a} = k\frac{2\pi a^2}{3}$$

The overall rate, Q, of all asperities contacts is given by:

$$Q = \Sigma \delta Q = \frac{k}{3}\Sigma \pi a^2 \qquad \{2.2\}$$

Combining equations {2.1} and {2.2}: $Q = \frac{k}{3}\frac{W}{P}$. Considering K=k/3 and P≅H (indentation hardness), the wear volume loss expression became:

$$Q = K\frac{W}{H} \qquad \{2.3\}$$

where K is a constant named wear coefficient and have values lower than unity, W is the normal load and H, represents the hardness of the softer surface. Equation {2.3} is known as the Archard's wear equation [74].

Archard's wear equation can be used also to describe the abrasive wear mode for ductile materials. The model considers an abrasive particle idealized as a cone of semi-angle α (figure2.4).

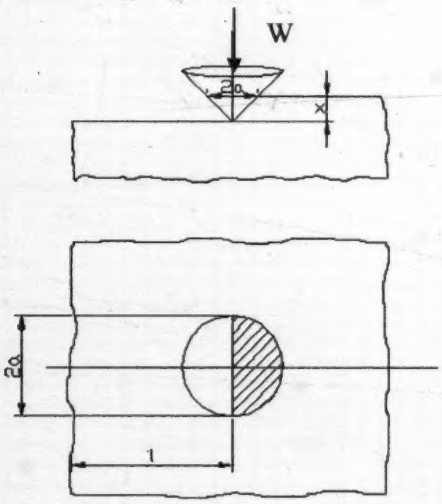

Figure 2.4: Archard's equation - Idealized model of abrasion [64,74].

The abrasive particle moves across the surface of a ductile material, which flows under an indentation pressure, P, forming a groove in the material [64]. Since

it is moving, the applied pressure acts only over its front surface:

$$W = P\frac{\pi a^2}{2} = \frac{1}{2}P\pi x^2 \tan^2\alpha \qquad \{2.4\}$$

The following relation gives the volume of material displaced from the groove per length: $q = l\frac{1}{2}2ax = lx^2 \tan\alpha$. However, only a proportion, k, of the material is actually removed as wear debris therefore the wear volume produced by one asperity per unit length is: $q = kx^2 \tan\alpha$ {2.5}

Combining equation {2.4} and {2.5}, the expressions of the overall wear rate, Q, of all asperities in contact become: $Q = k\sum\frac{2W}{P\pi\tan\alpha}$. Considering $K_a = \frac{k}{\pi\tan\alpha}$ and P≅H then

$$Q = K_a\frac{W}{H} \qquad \{2.6\}$$

The above equation is similar to Archard's wear equation, only the wear coefficient is different [64].

Archard's wear equation often agrees with experimental observations [75-77] but ignores physical metallurgy of metals, influence of modulus of elasticity, and cannot be used to compare wear of metals under different sliding conditions [78]. Also, Archard's wear equation cannot predict the wear of pseudoelastic TiNi alloys [79,80]. The wear coefficient, K_a, is not constant and can change by orders of magnitude when transitions occur in response to changes in experimental variables (e.g. load, speed) [81]. The complexity of the wear process hindered the

development of more sophisticated wear equations. Attempts to improve the Archard's wear equation led to the following expression:

$$Q = \left(\frac{K_1}{H} + \frac{K_2}{E} \right) W \qquad \{2.7\}$$

where E stands for Young's modulus.

Equation {2.7} is known as the modified Archard's wear equation [82]. However, other attempts have been made to modify Archard's equation in order to apply it to a pseudoelastic TiNi material [80].

2.2.2 Factors that influence wear in different modes

According to equation {2.7}, the abrasive wear mode is affected by material properties such as hardness, modulus of elasticity, roughness/abrasive shape ($1/\tan\alpha$), and load (W). Wear volume loss is decreased when hardness, and modulus of elasticity are increased or when load, and angularity of the abrasive are decreased. Others factors affect abrasive wear, including microstructure (e.g., volume fraction of the reinforcing phase), abrasive size, ratio of hardness of the abrasive to that of the surface being worn, strain hardening coefficient, fracture toughness, etc. [4,59]. For example, increasing the abrasive size increases the wear loss. However, after reaching a critical abrasive size, the wear loss became stable due to clogging of the abrasive, which hinders further abrasion. When the abrasive size is much higher than the grain size, wear is affected by the entire microstructure while in the reverse case, the wear rates depend strongly on the properties of individual phases.

As shown by Archard's wear equation, adhesive wear is influenced by hardness and load. Adhesive wear is also influenced by mutual solubility of material couple, crystal structure, microstructure, strain hardening coefficient, surface films etc. For example, wear loss decreases when mutual solubility is low, therefore the highest wear occurs between identical pairs of materials in contact [83,84]. Chemical elements that are closer in the periodic table exhibit usually larger adhesive forces during wear processes. A high hardening coefficient increases the resistance to seizure. The best performance occurs for a homogeneous distribution of hard particles (i.e., carbides) in a matrix with a high hardening coefficient [57]. Hexagonal closed packed (hcp) metals exhibit lower adhesion and wear than face-centered cubic (fcc) and body-centered cubic metals (bcc) due to the differences in the operation of slip systems [85, 86]. Since wear is associated with plastic deformation, metals that have fewer slip systems give higher wear resistance. Among hcp metals, as c/a ratio decrease, slip can occur along planes other than the basal plane (0001), therefore friction and wear may increase [85,87]. At room temperature, surface films may form in the presence of oxygen, which reduces the metal-metal contact and could reduce adhesion, friction, and finally wear [61,88-91].

In contrast with adhesive and abrasive wear, fatigue wear is strongly influenced by the presence of defects such as inclusions, pores, and voids. These defects might play an important role in nucleation of cracks that could lead to fatigue spallation. The effects of inclusions on wear loss depend on their volume fraction and the matrix properties. However, fatigue cracks could originate at inclusions but crack propagation depends actually on matrix properties. For example, a lower grain

size will increase the critical shear stresses for crack nucleation reducing wear. Also, residual austenite is beneficial to wear resistance by increasing the strain hardening capability and by introducing compressive stresses when transforming under applied stress to martensite [92]. As proved before, hardness is considered one of the most important material properties that help reducing wear loss [93,94]. Fatigue wear could be also influenced by increased roughness or amplitude of oscillation.

Corrosive wear is mainly influenced by microstructure, properties of passive film and pH level of the corrosive medium. An adherent, dense, and strong passive film could provide more protection against corrosion and mechanical damage [95-97]. Microstructural heterogeneities (e.g., presence of a second phase) could increase corrosion which, in turn, could increase wear loss, but the presence of a second phase may also increase the strength and, therefore, the resistance to mechanical wear. However, it is recommended to use solid solution strengthened materials rather than those strengthened by second phases [97], if the contact stress is not too high.

2.2.3 Delamination wear theory

It was observed that plate-like debris was generated during sliding wear at low speeds. [4,64]. Delamination wear model was proposed to explain the above behavior [78,98-101]. The model is based on plastic deformation, dislocation, and fracture theories. All events occur within a small surface layer at the rubbing surfaces [100]. During sliding of two surfaces, normal and tangential loads are transmitted through the asperities. The asperities of the softer surface are more easily

deformed under the applied load. As a result, the softer surface smoothes and the contact between the two rubbing surfaces became asperity-to-plane contact, therefore, the softer surface experiences cyclic loading as the asperities of the harder surface plow it [99-101]. Plastic shear deformation is induced in the softer surface, which accumulates under repeated loading. It is assumed that material near the surface is strain hardened less than that of the sub-surface layer. The former does not attain a high dislocation density due to the action of the image forces on those dislocations that are parallel to the surface, eliminating them [100]. Dislocations pile up at a given distance from the surface leading to voids formation that is enhanced by the presence of second hard phases [78]. Crack nucleation take place at the interface of second phases and matrix. Cracks extend and propagate parallel to the surface at a depth that depends on material properties (e.g., hardness), friction coefficient, and load [102], producing long and thin delaminated wear sheets [99-101]. The overall wear rate is determined by the slowest process among subsurface deformation, crack nucleation, and propagation processes [102]. For example, when cracks cannot propagate, crack nucleation became the wear rate-controlling factor [99-101].

Later developments of delamination wear theory suggest the formation of a cellular structure in the highly deformed region near the contact surface during a sliding process [103,104]. The cellular region has a different microstructure than the bulk material; it contains regions less than 1μm that are relatively free of dislocations, separated by much smaller regions having high dislocation density. The latter serve as cell boundaries or walls [103] (figure 2.5). Cell size depends on

material property and applied stress, being approximated as $\frac{Gb}{\sigma}$ [105] where G represents shear modulus, b is he Burger's vector, and σ is the applied stress.

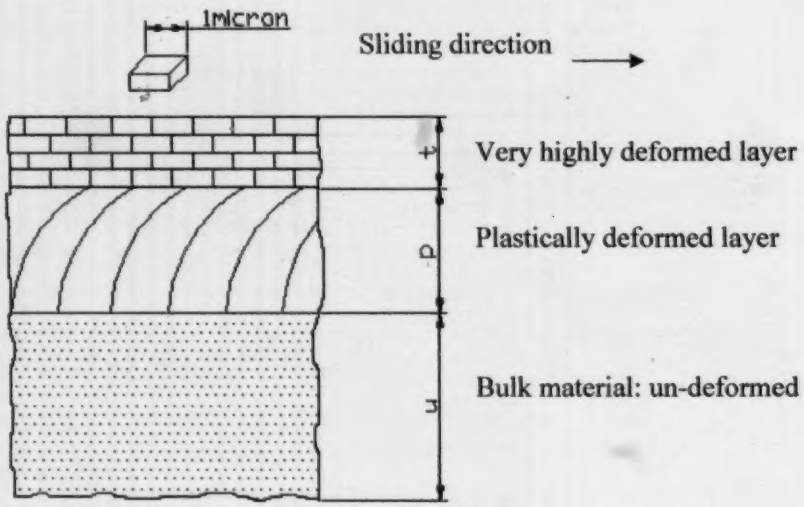

Figure 2.5: Delamination wear theory - Cross-section of a worn surface (adapted after [103, 104]).

As the applied stress increases, the cell dimensions decrease. The cell wall serves as sources and sinks of dislocations. Dislocations movements from one side of the cell to the other do not change the cellular arrangement [106]. The cells are elongated in the sliding direction having their thickness much smaller than the other dimensions. The cell structure is produced on the surface during early stages of sliding [104] and is capable of accommodating large strains in the sliding direction [103]. Cracks nucleate at the cell boundaries and propagate parallel to the cell boundaries leading to the formation of plate-like wear debris. The depth of the

cellular structure depends on the parameters of the sliding wear test (i.e., applied load), and material properties (e.g. crystal structure, grain size, and staking fault energy). However, the thickness of the cellular layer and the average cell dimension are constant during the wear process [104].

The latest development of the theory assumes a monotonically or a step-wise varying structure [107]. For each material there is a minimum cell size that can be attained as a function of applied stress [108]. When the minimum cell size is attained, the maximum level of work hardening is also reached [109] which, in turn, results in enhanced wear losses [108,110].

However, it is difficult to distinguish between the substrate's cellular structure and transferred layer from the counterface as some material transferred from the counterface may contribute to the cellular layer [4].

Delamination theory cannot be applied when surface temperature is increased during wear (frictional or supplied) due to difficulties of crack nucleation (e.g. extensive cross slip, dynamic recovery and recrystallization that consume stored energy) [102].

Both Archard's and delamination models do not consider the environmental effects on wear process. In practice, most of the tribosystems are performing in an environment where oxygen is present. Even at ambient temperature oxygen gas molecules have a strong chemisorption on the metal surfaces; therefore, they could exert a larger influence on friction and wear behavior [111,112].

2.2.4 Oxidational wear theory

Wear rates may decrease substantially at a critical applied load or speed. [113-115]. This behavior was denoted as "severe" wear before the critical value and "mild" wear after it [115]. However, in particular conditions, after reaching a minimum, the wear rate could increase again when speed or load is largely increased from the critical value [81,116-118].

Mild wear is characterized by smooth oxidized worn surfaces, less deformed surface layers, small wear debris (approximately 10^{-4} mm diameter) that are partially or completely oxidized. It occurs under three distinct sets of conditions [119]: (1) under relatively low applied load and sliding speeds when a thin and stronger oxide layer prevent metal-to-metal contact; (2) under relatively low applied loads but at higher sliding speeds when a thicker but brittle oxide layer is continuously generated due to high flash temperatures at the asperities contacts; and (3) under high loads and sliding speeds when micro-structural transformations takes place (usually on carbon steels) strengthening the underlying substrate which corroborated with enhanced oxidation due to large flash temperatures that prevent metal-to-metal contact, lead to low wear rates.

As a conclusion, mild wear is associated with the development of stable oxide films on the worn surfaces.

Severe wear is characterized by very rough worn surfaces, generation of relatively large wear particles (approximately 10^{-2} mm diameter) that are mostly metallic in nature [115,120-122]. It occurs also under three different conditions

[119]: (1) under relatively low applied loads and sliding speeds when contact pressures are high enough to disrupt the oxide film so that metal-to-metal contact happen; (2) under relatively low applied loads but at higher sliding speeds when the load is able to penetrate the brittle oxide leading to metal-to-metal contact; and (3) when sliding conditions are so severe that the flash temperature exceeds the melting point of the substrate so that a liquid film forms at the contact asperities.

Oxidational wear theory is used to explain the mild wear regime [120-130] under the second set of conditions. The oxidational wear mechanism/model involves oxidation of metal asperities. In the initial stages (severe wear) contact occurs at asperities tips. Under highly local stresses the asperities in contact are deformed; therefore, the real area of contact is increased. As a result, the real contact consists of several relatively large areas that bear most of the load. These contact areas could expand to form a plateau of contact that remains a region of contact between the rubbing surfaces until removed by wear.

When sliding speed or load is too low so that frictional heating is negligible, the expansion of the contacting plateau is not sufficiently large to become the preferred contact region. The contact between surfaces became mainly metallic in nature owning to low temperature and oxidation rate [131,132]. As a result the junction can grow significantly resulting in high friction and wear rates [121,124,127].

Increasing sliding speed increases contact temperatures [81]; therefore, a large frictional heat is created. Under these conditions, the contacting plateau is oxidized preferentially to the remainder of the surface [121]. On the plateau there are

at any time, N instantaneous asperity contacts (figure 2.6). The oxidation occurs by inward diffusion of oxygen ions and outward diffusion of metal ions. The plateau builds up its height uniformly because the N contact spots are randomly distributed across the plateau at any given time.

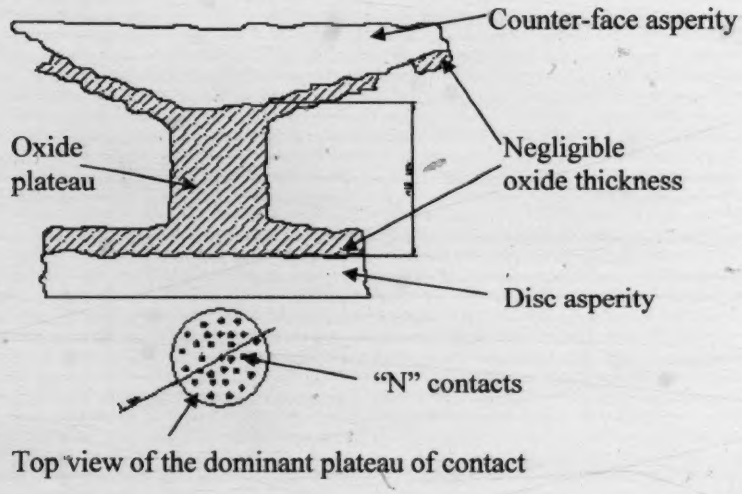

Figure 2.6: Idealized model of a contact at a dominant plateau on the surface [121].

It is assumed that "tribological" oxidation follows a parabolic rate [126]. The oxide plateau grows and reaches a critical thickness (approximately 10μm for mild steel) at which oxide spalling occurs at the oxide/matrix interface forming oxidized wear debris [121, 133]. When the contacting plateau breaks completely, another plateau became operative elsewhere on the contacting surfaces and the cycle is repeated. Wear loss depend on the contact temperature and the mechanical characteristics of the oxide layer [121,122,131,134,135].

However, even when the sliding speed is high enough to generate a large increase in flash temperature, during the initial wear period the severe wear regime still occurs. At the initial wear stages the oxide layer is too thin to withstand the frictional forces and is removed easily from the surface. Mild wear regime is established when thick oxide layers are formed. As a result, the wear rate is related to the rate of oxidation.

The oxidational wear model led to the following quantitative expression for the wear rate under mild wear conditions [128]:

$$W = \frac{d * A_p e^{-\left(Q_p / RT_0\right)}}{\xi^2 \rho^2 v f^2} A \qquad \{2.8\}$$

where: d – sliding distance; A_p – Arrhenius constant for parabolic oxidation during wear; Q_p – activation energy for oxidation; R – universal gas constant; T_0 – flash temperature; ξ - critical oxide film thickness; ρ- average density of oxide; f – fraction of oxygen in the oxide film; v – sliding speed; A – real area of contact.

Parameters as ξ, T_0, and A_p are extremely difficult to determine [134, 136] which hinder the relation usage for practical applications. The assumptions that tribo-oxidation follows a parabolic rate, and tribo-activation energy and Arrhenius constant are similar to static oxidation are questionable [127,128,132,134]. According to reference [130] the activation energy, Q_p, is not really influenced by the way that the oxide grew, but A_p is. Furthermore, it might be possible that the oxide film is spalling off due to growth of fatigue cracks and not because of reaching a critical thickness [123].

Mild wear under the third set of conditions is based on a slightly different mechanism. Increasing sliding speed could increase the strain rate which, in turn increases hardness or flow strength, reducing the true contact area thus diminishing friction and wear [116]. Furthermore, increase[illegible]ntact temperature due to frictional heat might soften the substrate, leading to an increase in wear rate. This is the possible mechanism that explains why wear rate reaches a minimum then increases with increasing speed and/or load. It follows that the strain hardening mechanism is predominant over the softening effect, up to a critical load/speed [116].

However, none of these theories take in account the oxygen pressure and/or the chemical species present in the environment. There were identified three categories of wear behaviors in terms of the chemisorption strength of atmospheric gas molecules on the metal surface, and atmospheric pressure [111,112]:

(1) Type I: strong chemisorption of gases on the metal surface (e.g., oxygen or hydrogen on iron, cobalt and nickel). A maximum amount of wear exists at an arbitrary atmospheric pressure of the gas. The wear rate is reduced when the pressure is higher than the critical pressure at which a large number of gas molecules are chemisorbed onto the surface, preventing the metal-to-metal contact. For example, when the partial pressure of oxygen is higher than 10^{-5}Pa over a Fe-5%Cr alloy ($P_{O2}>10^{-5}$Pa) islands of partially oxidized debris develop on the contact surfaces leading to low friction coefficients and mild wear regime [137].

(2) Type II: weak chemisorption of gases on the metal surface (e.g., oxygen on zinc). A gradual increase in wear rate occurs with the increase of gas molecules chemisorbed onto the metal.

(3) Type III: no chemisorption of gases on the metal surface (e.g., nickel or zinc in nitrogen, gold in any king of gas). The wear rate does not show any dependence with gas pressure but the wear is lower than that in type I or II for a given metal.

2.3 Wear at elevated temperatures

As shown in the previous chapters, wear is a very complex process, affected by many factors. Increasing temperature further complicates the wear process. Prediction of the high-temperature wear is difficult since the temperature, stress, material properties, and oxidation behavior interact in a complex way and significantly affect wear [138]. Temperature causes significant changes in the overall wear rates [139].

It is well known that alloys react with the environment to form protective layers, which act as barriers to further oxidation damage. When a compact oxide layer is formed, further oxidation proceeds by diffusion of reactants through the film [140]. The oxidation rate increase exponentially with increasing temperature following an Arrhenius type equation:

$$K = K_0 \exp^{-Q_p/RT} \qquad \{2.9\}$$

where Q_p stands for activation energy; R – universal gas constant; T – absolute temperature; K – oxidation rate constant; K_0 – constant.

The surfaces of contacting materials during high-temperature wear processes are subjected not only to contact stresses as in ambient temperature wear, but also to oxidation, loss of mechanical strength, and change in adhesion, which causes material degradation and consequently reduces the material resistance to wear [141]. If a dense and strong oxide barrier layer forms on the surface (e.g. Cr_2O_3, SiO_2 or Al_2O_3), it may reduce the oxidation rate by giving effective protection against further oxidation [142]. If a defective oxide is formed on the surfaces (e.g. FeO at temperatures higher than 570^0C), the oxidation rate is increased leading to larger loss of the material. As a result, for application at higher temperatures, the alloys must contain significant amounts of alloying elements such as chromium, cobalt, molybdenum, nickel, tungsten or aluminum in order to provide hot strength and/or to form protective oxide films that inhibit surface damage by oxidation [142,143].

It has been observed that wear rates significantly decrease above a certain temperature, named the transition temperature [144-157]. The value of the transition temperature depends on load and/or sliding speed. In certain circumstances, at temperatures higher than the transition temperature, the wear rates may increase rapidly [158]. Transition from the severe wear to mild wear regime at the transition temperature is related to the development on the rubbing surfaces of oxide films and/or oxidized compacted wear debris layers that reduce adhesion and are able to withstand some of the applied load [9,137,144,145,147-157,159-162].

When sliding wear occurs under vacuum conditions at elevated temperatures, the amount of wear became more extensive as the temperature was increased [85,163]. For example, when vacuum is present, seizure may occur for a Fe-4.9%Cr alloy [164]. However, when oxygen is leaked into the system, development of oxides on the contacting surfaces could prevent seizure and reduce metal-to-metal contact, leading to low friction and wear rates [61,164-166].

The oxide film and/or the compacted oxide debris layer might prevent direct metal-to-metal contact. When the interaction between asperities is metallic in nature, significantly junction growth occurs, leading to high wear rates and friction coefficients [160] (see also chapter 2.1.1). When an oxide film is present at the asperities contact, the junctions may not be generated before the oxide film is broken. When junction is generated and grows, small cracks may nucleate and propagate in the oxide leading to a reduction in the shear strength of the oxide film and to brittle failure of the junction [160,167]. Due to lower tendency for adhesion and junction growth, friction coefficient is lower than that under the metal-to-metal contact [168]. Also, wear rates decrease because breaking of junctions occurs at or near the oxide film producing relatively fine oxide or partially oxidized debris [160,167], which might play an important role in reducing the frictional force.

Besides the oxidation and debris generation, the high-temperature wear transition to mild wear may be influenced by material transfer from the bearing surface of the sample material to that of the counterface. The transfer process influences the wear loss by changing the contact area between the sliding couple and/or by changing the relative hardness, ductility, and composition of the materials

at the sliding interface [169]. Under particular conditions, the transferred material can be re-transferred back to the original surface or can be mechanically mixed with the material of the other surface.

As a conclusion, the oxide film may benefit the resistance of an alloy to high temperature wear by reducing metal-to-metal contact between rubbing surfaces, reducing the direct wearing force and reducing friction or generating a porous oxide as a solid lubricant. Although, the oxide layer developed on contacting surfaces could provide resistance to wear damage by itself, the oxide and/or partially oxidized particles generated during sliding may significantly influence the subsequent wear behavior either positively by generating a glaze layer that may further diminish wear damage or negatively by acting as hard abrasives.

Considerable efforts were made to model and understand high temperature wear. There were identified three mechanisms for the generation of oxides during sliding wear:

(1) Oxide-scrape-reoxidation mechanism when oxide is formed by oxidation of metallic asperities and by general oxidation of all the apparent contact areas [150,160,170,171]. The above process occurs between two subsequent sliding passes. The subsequent sliding pass may remove the oxide formed leaving clean metal exposed to the environment which results in re-oxidation until the subsequent sliding pass when the process is repeated.

(2) Total oxide mechanism when the oxide developed during sliding may be removed only partially or not at all during subsequent sliding passes [150,160,170,171]. The remaining oxide film thickens slowly as sliding proceeds. If the oxide/metal interface is strong, the oxide film can withstand the sliding stresses for a given time period, reducing wear loss.

(3) Metal debris mechanism when the metallic debris, formed usually in the early stages of sliding, is broken and reduced in size by the sliding action [150,160,170,171]. As a result, fresh metal is exposed at the surface of the broken debris and oxidized by the environment.

The oxidized debris generated by any of the above mechanisms might develop into a glaze layer. The oxide debris produced during sliding wear may be removed immediately from the rubbing surfaces and will not influence the subsequent wear process or may be retained between the sliding surfaces and influence further the wear process [169]. The debris could be retained: (1) as non-moving particles on one of the contacting surfaces leading to the glaze formation, (2) as moving particles causing third body abrasion damage on both contacting surfaces, or (3) by being embedded in one of the contacting surfaces causing two body abrasion damage [139].

The overall protective effect of oxidized wear debris that were retained between the rubbing surfaces was demonstrated by several studies in which air was blown between contacting surfaces [172]. At temperatures ranging from ambient temperature to 400^0C, an increase in wear rate occurred due to the removal of

oxidized wear debris from contacting surfaces that led to higher adhesion. When temperature was increased to 500^0C, the effect on increasing wear rate could be only marginal because some coverage of the sliding surfaces by oxidized debris still occurred [172]. This behavior was attributed to the sintering effect of the oxidized debris particles at elevated temperatures.

2.3.1 Mechanism of high-temperature wear and glaze formation

Based on experimental observations, a mechanism was developed to account for the wear behavior at elevated temperatures when glaze layers are formed.

During initial stages of sliding, the oxide formed on the rubbing surfaces may be removed as wear debris and metal-to-metal contact occurs leading to severe adhesive wear (called "running-in") [163,167,173]. The average size of particles generated during running-in is large due to large contact pressures and metal-to-metal contact [174,175]. Some of the wear particles are removed from the rubbing surfaces, causing direct material loss, but most of the particles are retained within the sliding interface and became involved in the development of glaze [139,142,167]. However, no build-up of glaze layers occurs during running-in period, therefore wear rates are large.

During subsequent sliding, the debris particles entrapped between the sliding surfaces are subjected to compressive stresses, undergoing further deformation, fragmentation and comminution [176]. This process is repeated until a stable debris size is reached, typically 50 nm to 5 μm in diameter [145,160]. Most of the debris

particles are agglomerated at certain locations on the wear track, particularly in the previous grooves formed during metal-to-metal contact [177]. By filling up the depressions in the contact surfaces, development of relatively smooth surfaces is facilitated.

As sliding continues, the agglomerated clusters of debris particles are further compressed and sintered to form more solid layers. When the size of the oxidized debris became smaller than a critical size for compaction, the glaze coverage increases rapidly, resulting in a significant decrease in wear rate and friction [145,174]. Depending upon temperature, a very smooth and shiny layer (glaze) develops on the top of the compacted particles layer [144,167,177-179]. TEM studies have shown that the wear affected region consists of three successive layers: (1) on top, the glaze layer formed with a uniform nano-grain structure having a low dislocation density, (2) the intermediate layer consisting of oxidized particles having larger dimensions than those in the glaze layer and showing a higher dislocation density and (3) the sub-surface layer showing elongated grains in the direction of sliding [180,181]. EDS analysis has proved that the amount of elements in glaze are approximately the same as those in alloy except containing oxygen [160,162,171,178,180]. This suggests intermixing of debris generated during the wear process.

During subsequent sliding, the contact surroundings are worn down and the sintered oxide layer came in contact with the counterface and became a load-bearing area. The glaze layer that is in contact with the counterface is subjected to repeated contact stresses, which may initiate and propagate cracks through the glaze layer,

leading to breakdown of the glaze layer. Two competitive processes take place as sliding continues: (1) the breakdown of glaze bearing layer areas that results in the formation of debris particles, and (2) the consolidation of the glaze layer due to further sintering of the worn debris [139,142]. If the glaze layer is well compacted before becoming load bearing, the wear is relatively low. When the oxidized particles in the glaze layer are not well compacted and sintered, loose particles having large dimensions are removed from the layer causing third body abrasion that enhances wear loss [176].

A mathematical model was proposed to model the formation of glaze layers and to estimate the wear volume loss based on determining the criteria for removal or retention of worn debris on systems where severe to mild wear occurs due to the presence of a compact worn oxidized-debris particles layer [177]. The model assumes that the wear rate of glaze layers is negligible compared to the area without protective debris layers and the wear debris is generated only from the area unprotected by glaze [174]. A number of possible mechanisms were proposed to describe the possible movement of wear debris within the rubbing interface: (1) the retained mechanism, when a particle is entrapped in front of a fixed particle and is not able to move in the direction of sliding but able to rotate around its own centre, (2) the skidding mechanism, when a worn debris particle skids against a fixed particle in the opposite surface, (3) the rolling mechanism, when the particles are able to move/roll free in the direction of sliding for a given distance, and (4) the entrapped mechanism, when high adhesion occurs between adjacent particles and

debris cannot move. It is believed that rolling and skidding mechanisms causes loss of wear debris from the rubbing interfaces resulting in wear loss.

Based on the above assumptions, the model is estimating the volume and total area of compacted debris layers that cover the rubbing surfaces at a given time and temperature. However, the model does not really agree with experimental results: wear losses versus temperature show the same trend as the experimental ones but the amount of wear volume loss is in all cases from 30 to 60% lower than the real one. Nevertheless, the model represents a step for understanding high temperature wear processes when protective oxidized layers are formed on the rubbing surfaces.

2.3.2 Factors that affect high-temperature wear

At elevated temperatures glaze layers could form after sliding for a certain period [163]. The time required for the development of glaze layers is related to the extend of oxidation [160]. When large amounts of oxides are present on the rubbing surfaces prior to sliding or when temperature is increased above a critical value, glaze layers are formed as soon as the sliding starts. In general, no glaze layers develop under 200^0C [163]. High temperatures enhance sintering and oxidation of particles leading to much lower wear rates, in some cases even than that at ambient temperature [174].

The average size of oxide particles that are agglomerated and compacted to form the glaze layer is increased with increasing temperature [167,175,182]. However, further increase of temperature may lead to softening of the underlying

matrix that supports the glaze layer. The softer matrix could exhibit larger plastic deformation than the glaze layer leading to delamination fracture of the glaze so glaze is easily removed by the sliding action [158,163].

It seems that at elevated temperatures the wear rates are controlled by the consolidation and detachment of glaze layers. The development of such protective layers is mainly influenced by the tribological parameters including load, speed, geometry of the contacting surfaces, and temperature. When load and/or speed are increased above a critical value the wear debris cannot agglomerate between the rubbing surfaces to form glaze [183]. Higher loads promote generation of larger wear debris that cannot be accommodated inside the previous formed groove so the time until these particles are fragmented to the critical compaction size is increased, delaying glaze formation. Higher speeds increase the probability that the debris particles are removed from between the rubbing interfaces, leaving fewer particles to form glaze [175]. Besides that, the glaze might not be able to withstand the larger wearing force.

Substrate hardness plays a role in the glaze formation. Rubbing surfaces become closer as hardness is increased; grooves are shallower during the running-in period thereby worn particles could be removed more easily from the interface [175]. Also, strength of material determines the wear volume loss during the running-in period [163]. A "softer" substrate may generate a large number of wear debris during the running-in period that are easily accommodated into the grooves that are deeper on a "softer" material, thereby glaze layers are easily formed. However, a "softer" substrate does not offer adequate support to glaze layers as temperature is increased

above a certain limit. An adequate balance between a softer and a harder substrate is required for the best performance.

The amount of oxide debris developed during the running-in period has an important role in the glaze formation; as the amount of oxidized debris is increased formation of glaze is easier. Oxidation rates influence the amount of oxide present on the rubbing surfaces. It was observed that a peak in wear rate occurs with respect to the partial pressure of oxygen; the wear rate increased as oxygen partial pressure was decreased [164,165]. However, no study explains the effect of the oxide's mechanical properties on glaze formation and on wear behavior.

The glaze does not form under all wear modes (e.g., sliding-abrasion wear). Under sliding-abrasion wear conditions, a transition from severe to mild wear could occur at a given temperature [184,185]. The transition is not related to the glaze formation but rather to the hard constituents (flint particles) that are embedded in the worn surface forming a protecting layer against abrasion. These embedded protective layers are lost with increasing temperature due to further softening of the matrix.

As a conclusion, the film that forms on the contacting surfaces during a high temperature wear process affects the wear rate. The high temperature wear is influenced by the factors that influence the ambient wear (as presented previously) but the role of temperature, hot strength, environment (oxidation), and third body films become important.

2.3.3 Approaches to reduce high-temperature wear

Considerable efforts have been made to reduce wear at elevated temperature using different approaches such as applications of coatings [186-188], preoxidation [6,189], cladding [7,8,9,190-192], different processing techniques [10], and alloying treatment [191].

Preoxidation of materials at elevated temperatures prior to sliding could supply enough oxide debris particles during the initial stages of sliding that could help the development of glaze thus reducing the running-in wear. When samples were pre-oxidized at 800^0C to form a protective Cr_2O_3 rich oxide scale followed by sliding, the running-in period is almost eliminated. However, the preoxidation treatment does not always function [160]. When samples were cooled to room temperature after pre-oxidation treatment then subjected to sliding wear, the wear rates were relatively high due to the loss of oxide scale [160]. In other cases, (9% chromium steel) the pre-oxidation treatment does not have any effect on wear rates [181]. In this particular case, the pre-oxidation time was relatively long (e.g., 750 hours at 390^0C); thereby, a thick oxide develops on the contacting surfaces. As an oxide thickens, it is subjected to internal stresses due to the formation of new oxide; thus, the oxide could easily fail under external applied stresses.

Coating, cladding or modifying the surfaces of standard steels are attractive options to protect mechanical components against wear damage [194]. Surface treatments as electroplating, nitriding, case carburizing and induction hardening could also be used to enhance the wear resistance of industrial components but their

application is limited by the residual stress induced in the near surface material that could lead to premature wear damage. Another option is to use ion implantation, which could strengthen the near surface region of an industrial component through pinning the defects and/or formation of hard second phases by reaction with interstitial species such as nitrogen or carbon [194]. Ion beam assisted deposition (IBAD) offers the advantage of low substrate temperatures that reduce the residual stresses at the coating/substrate interface, improved adhesion, and low toxic residues [194]. IBAD of diamond-like carbon coatings using hydrocarbon precursors (e.g., polyphenyl ether) are usually employed for combustion engine components (e.g., rocker shafts, roller pins). However, proper adhesion of coating to substrate is a major problem therefore, an intermediate binding silicon layer coating is generally used [194]. The above approach showed good performance up to 160^0C against lubricated wear [194].

Another coating technique proven to be successful to provide corresponding resistance to fretting wear of a gas turbine engine's components at temperatures up to 500^0C is high velocity oxy fuel (HVOF) technique [195].

The choice of material used for coating is an important issue for the overall wear performance at elevated temperatures. For example, coatings based on TiN, TiAlN, Cr_3C_2, Ti_2AlC are limited in use to 500^0C due to inadequate oxidation resistance [196-198]. As a result, coating materials having high resistance to oxidation as well as to wear are usually used for service temperatures larger than 500^0C, such as cobalt based coatings (e.g. CoMoCrSi – Triballoys) or Cr_3C_2+25%NiCr [195].

However, coatings are not effective against harsh wear conditions such as high-stress sliding wear or galling at elevated temperatures due to their low thickness (up to several hundred microns) and interfacial debonding problem under large contact stresses. In some cases, cladding (arc, laser or plasma) is used to deposit a hard resistant layer having a relatively good adherence to the substrate and a larger thickness (up to several millimeters) depending on the application. Laser or plasma coating technique offers the advantage of *in situ* mixing of different components due to the high temperatures attained in the arc/laser column that lead to claddings, which may be obtained by other techniques. For example, Fe-Al-Ti-C powder could be used during laser cladding treatment to form a composite coating of FeAl intermetallic reinforced with TiC hard phases [196]. The cladding of the above material offers enhanced high temperature (up to 600^0C) sliding wear resistance than the classical FeAl intermetallic alloy cladding.

Plasma cladding of a self lubricated composite layer (PS304 – NASA designation) consisting of a high chrome-nickel alloy matrix (80%Ni+20%Cr) and three solid lubricants that act as lubricants at different temperatures, was proven to offer good galling resistance to steam turbine lift roads [199]. The high nickel alloy matrix provides excellent corrosion/oxidation resistance and high temperature mechanical properties. The high-temperature strength is enhanced by Cr_2O_3 oxide particles that form during the cladding process. The Cr_2O_3 particles could function as a solid lubricant. The other two solid lubricants are silver (up to 450^0C) and BaF_2/CaF_2 eutectic compound (above 400^0C), which are known for their strong lubrication effect [200]. BaF_2/CaF_2 worn debris could act as a binder to hold the

other type of debris formed during the wear process in order to form glaze that could further reduce the wear loss [199].

For wear protection at elevated temperatures where abrasion is the main wear mode (e.g., parts in crushing, sieving, and compacting of hot sinter and dust in the steel industry [201]), conventional materials are used, such as cast irons or metal matrix composites (MMC). MMC consist of coarse hard particles such as Cr_3C_2, CrB_2, WC/W_2C dispersed in a soft and tough metal matrix (e.g., nickel base alloys, high-speed steel etc.). However, at higher temperatures, the oxidation resistance of reinforcement particles is diminished which may lead to less overall wear resistance [201].

Alloying treatment is used to enhance wear resistant properties of the existing alloys by adding certain chemical elements. For example, carbon and silicon were added to a Fe-Cr alloy [43], which enhanced the strain-induced martensitic transformation, leading to lower wear losses than Stellite 6 up to 250^0C. Several attempts were made to add alloying elements to conventional cobalt-based alloys, such as molybdenum [49], silicon [51,202] or iron [13,48]. However, not all additions proved to be beneficial to high temperature wear resistance, e.g., silicon additions to Stellite 6 decreased the wear resistance [202] or iron additions to Triballoy 400 reduced the amount of Laves phases and oxidation resistance [13].

2.4 Effects of reactive elements on oxidation and oxidative wear

All metallic components that are exposed to the environment at elevated temperatures react with oxygen to form an oxide layer on their surfaces. There are two essential requirements for the alloys that are designed to operate at high temperatures: (1) they must form a coherent crack-free oxide scale that thickens at low rates and isolates the metal from environmental attack, and (2) the oxide scale must be adherent to the alloy matrix [203-209]. The most common oxides scales used in practice are based on chromia (Cr_2O_3) or alumina (Al_2O_3) that forms on iron, nickel or cobalt based alloys [207,209-216]. Chromium or aluminum have a relatively high oxygen affinity; therefore they are preferentially oxidized when added as alloying elements to iron, nickel or cobalt based materials [212]. Chromia scale forming alloys contain more than 15%Cr but also could contain up to 2%Al (e.g. Co-25%Cr-1%Al), while alumina scale forming alloys contain at least 5%Al plus substantial chromium additions [206]. Chromia and alumina are stoichometric oxides having less defects such as interstitial ions or vacancies that could help ions diffuse; therefore, oxidation rate is low and their scales thickens very slowly [211,216,217]. Also, these oxides are thermodynamically very stable, have high melting points, and result in a very dense and adhesive scale [211,215,218]. However, at temperatures higher than 900^0C, chromia may react further with the environment to form a volatile species, CrO_3, which reduce scale protection [211,215]. As a result, chromia scale forming alloys are used up to 900^0C [211,215,219,220]. Alumina scale forming alloys could be used at temperatures up to 1200^0C because they do not form volatile

species [211, 219, 210] but are more prone to failure than chromia scale forming alloys.

Under thermal cycling, cooling to room temperature or during oxide growth, cracks and spallation of oxide could occur, diminishing the protective effect [140,207,218,221]. The mechanical properties of oxide scale become important because they determine whether mechanical failure of the oxide scale will occur during service [193]. The failure rate depends on the severity of any crack that opens on the oxide scale surface allowing attack of the underlying metal by the environment. Healing of less severe cracks could occur during oxide growth [222-225].

Properties of chromia and alumina scales could be improved by minor additions of rare earth elements such as cerium [226]. It was also found that addition of reactive elements such as yttrium, zirconium, titanium, or hafnium had the same effect on oxidation behavior of chromia or alumina scales forming alloys [206,213,214,220,227-229]. Almost all elements that have a higher affinity for oxygen than the base alloy could be effective in improving the oxidation resistance of chromia and alumina scales [203,209]. Elements that have higher affinity for oxygen than the other alloying elements are termed "reactive elements" and their effect on oxidation behavior is termed "the reactive element effect" [206,230].

The main effects of reactive elements on the oxidation behavior of chromia/alumina forming alloys are:

(1) Reducing the growth rate of chromia scales particularly at temperatures up to 1000^0C, leading to thinner scales [209,217,231-239]. However, the reduced growth rates on alumina scale forming alloys are less evident [213,240].

(2) Improving markedly the scale adherence to the substrate by increasing the resistance to scale spallation, both on thermal cycling and mechanical straining [209,217,219,231,234-239,241-245].

(3) Changing the oxidation mechanism through the oxide scale from predominant outward metal ion transport to predominant inward oxygen ion transport [209,217,219,231,234-239,241,243,246-248]. As a result, the scale grows at the metal/scale interface instead of at the scale/gas interface.

(4) Promoting a fine grained microstructure of the oxide [207,209,217,231,234-239,243,244,247-249].

(5) Promoting the selective oxidation of chromium either by lowering the amount needed to form a continuous protective chromia layer or by reducing the formation of un-protective base metal oxides in the external scale [209,232,240,250].

(6) Reducing the internal oxide layer stresses [235].

The most obvious effect of the reactive elements on alumina-forming alloys is the significant improvement in scale adherence [238,248]. Some of the above effects are interrelated: a reduction of the growth rate may be a result of a change in oxidation mechanism; or thinner scales generate lower thermal mismatch stresses on cooling which, may lead to improved scale adherence [206].

The reactive elements could be introduced by: (1) alloying additions to the bulk material either as metallic particles or oxide dispersions [206,251-254]; (2) ion implantation [205,208,255,256-261]; or (3) superficial application as a thin coating using the following techniques: metal organic chemical vapor deposition (MOCVD) [262,263-268], sol-gel [264,269-271], electrophoresis [264,272], dipping [272], electrochemical deposition [264,273], and hot spraying [274].

In general, the reactive element effect is relatively similar whether the reactive element is implanted, alloyed or coated [213,274-276] but the efficiency of the reactive element in improving high temperature oxidation differs, depending on the type of reactive element, its amount, its form (elemental or oxide), and method of introduction into the alloy [277,278]. It was shown that alumina scale's adherence increased when yttrium was introduced into a coating or by ion implantation compared with alloying to the bulk of the material [279]. In another study [240], the reactive element was more effective on chromia forming scales as an oxide dispersion addition rather than as metal addition to the bulk material at short oxidation times. However, when oxidation time was increased, no clear difference was present in reducing the growth rate of chromia forming scales whether the reactive element was implanted, coated or alloyed [240].

Some reactive elements are more effective than others. Cerium, yttrium, and lanthanum are the most effective reactive elements [280], while scandium and titanium do not appear to be effective on chromia forming scales alloys but had some minor effects on alumina forming scales alloys [247]. Some studies suggest yttrium

to be the most effective element on high temperature oxidation, followed by lanthanum, cerium, praseodymium, neodymium, and samarium [280-282].

It is assumed that the reactive effect depends on the position of the reactive element inside the lanthanide series: yttrium and "light" lanthanides (La, Ce, Pr, Nd, Pm, and Sm) are more effective to improve high temperature oxidation behavior of chromia forming alloys than "heavy" lanthanides (Gd, Tb, Ho, Er, Yb, and Lu), at least under relatively short oxidation times (100 hours) [282-284]. At larger oxidation times (1000 hours) no difference in spallation behavior occurred among yttrium, neodymium, and ytterbium containing samples [263] but at shorter oxidation times there was a large difference [285]. The reason behind the different effectiveness of reactive elements on high temperature oxidation behavior is supposed to be the ionic size; reactive elements with small ionic radius oxidize faster from Lu to Dy while the "light" lanthanides such as Ce and Pr do so slowly [283]. Large ions could have a large driving force (i.e., relaxation of misfit energy) for segregation to grain boundaries [237], blocking efficiently the diffusion short-paths and slowing the diffusion. Actually, there is no correlation between the reactive element's ionic radius and the reactive element effect on oxidation behavior [285] e.g. yttrium and Yb have similar ionic radius (see table 2.1) but yttrium is the most effective element while Yb exhibits the least effect among rare earths. It is also assumed that the effectiveness of reactive elements depends on how readily the perovskite compounds of the form $(RE)CrO_3$ are formed [280,282]. Yttrium to Sm form the perovskite type compounds relatively easily while Eu to Lo do not. The perovskite compounds are insoluble in chromia and could form along chromia grain

boundaries or at the metal/oxide interface where they could act as sources for reactive element ions, inhibiting outward diffusion of chromium ions and favoring the inward transport of oxygen ions [217,282,286-290]. Y_2O_3, La_2O_3, and CeO_2 are assumed to have the same effect as perovskite compounds [140]. When perovskite compounds cannot be formed, the reactive element is distributed through the oxide (e.g., Sc has solid solubility for chromia) and cannot block the grain boundaries in an efficient manner [280].

Temperature has a major influence on effectiveness of the reactive element [247]; the benefits are increased with increasing temperature [203,291]. The maximum benefits are attained at a temperature range of 0.4 to 0.6 of the absolute melting temperature of the oxide scale [203].

The beneficial effects are usually observed at low concentrations of reactive elements, usually less than 1% (e.g. 0.1 to 0.2% for Ni-Cr-Al alloys [292]). Amounts over 1% seem to be detrimental [203,210,293,294] usually to the scale adhesion [292] or increases internal oxidation [295]. The amount required to produce the same reactive element effect may differ from one reactive element to another [213].

It is generally accepted that reactive elements must be uniformly and relatively finely distributed through the surface to be highly effective in improving oxidation resistance [160,203,280,140].

Different theories have been proposed to explain the reactive element effect [206, 296,297] but the exact mechanism is not clear [227]; thereby, the debate over the main mechanism continues.

The most known models that have been proposed are [206,250]:

(I) Enhanced scale plasticity [298-300],

(II) Graded seal mechanism [206],

(III) Enhancement of scale nucleation process [254,258,301-304]

(IV) Modification of the oxide growth mechanism [56,217,247,260,266, 280,291,297,305-312],

(V) Oxide pegging to the alloy [213, 299,313-318],

(VI) Vacancy sink model [229,294,319],

(VII) Reduction of compressive stresses within the oxide [299,313],

(VIII) Improved chemical bonding to the alloy [320]

(IX) Sulfur (i.e., tramp elements) getter mechanism [210,321-327],

(X) Dynamic segregation model [247],

(XI) Poisoned interface model [238,328].

2.4.1 Enhanced Scale Plasticity

It has been proposed that reactive elements may improve the resistance to spallation and thereby the adherence of the oxide scale to the substrate by relieving the induced stresses. Stresses can be introduced into the oxide scale either during isothermal oxidation or during cooling [299,329]. Under isothermal oxidation, stresses could be generated due to epitaxial growth of the oxide, ion or vacancy gradients in the oxide or alloy, oxide structural transformations, and porosity along the oxide/matrix interface [299]. Stresses generated during cooling come from the differences between matrix and oxide thermal expansion coefficient [329]. The

stresses at the oxide/matrix interface have higher values than these at the oxide/gas interface; thereby, the oxide scale adherence is related to the amount of stresses developed at the oxide/metal interface [330]. However, the stress amplitude depends on several factors including coherency of the interface, oxide microstructure, relevant diffusivities, growth mechanism, etc. [331]. For example, columnar oxide grains are likely to induce larger oxidation stresses than equiaxed grains [331].

The stress generated into the oxide scale can be relieved in several ways, including creep, cracking, and spalling [207]. The creep rate is related to the grain size according to Herring-Nabbaro or Coble models; as the grain size decreases the creep rate increases [140,217]. It has been shown that one effect of adding reactive elements to alloys is to reduce the oxide grain size. According to the above models, scale plasticity could be improved by a small grain size. However, it is not very clear if the reactive element additions promote the finer grain size throughout the scale thickness or just at the scale/gas interface [217]. In some cases, the oxide grain size can decrease throughout the scale when the concentration of reactive element is high enough [217] while in other cases the reactive elements do not result in a finer oxide grain size [311,332].

Another explanation for the enhanced scale plasticity assumes that the reactive elements increase the chemical potential gradients for atom transport, resulting in increases in the amount and mobility of vacancy defects.

However, the enhanced plasticity model could be correct only for relaxing of the isothermally induced stresses; during cooling it is unlikely that thermally activated plastic deformation processes are able to keep up with the highly developed

stresses [217,237]. As a result, enhanced scale plasticity plays only a minor beneficial role.

2.4.2 Graded seal mechanism

The graded seal mechanism is based on the assumption that the reactive elements form an interlayer of oxide between the outer oxide layer and the matrix. This graded layer has a thermal expansion coefficient intermediate between that of the outer scale and the substrate and/or provides a graded transition of lattice constant [206,220]. As an example, an intermediate titanium oxide layer could form between alumina outer layer and the substrate of a ferritic Fe-Al-Ti alloy [220]. SIMS (secondary ion mass spectroscopy) investigations on oxide scales developed on specimens that were implanted with reactive elements showed that the reactive element oxides were found near the oxide/gas interface [217,300,319]. The graded seal mechanism may not fully account for the beneficial effects of reactive elements on oxidation.

2.4.3 Enhancement of scale nucleation process

Transient oxidation is defined as the rapid oxidation that takes place on the metal surface immediately after being exposed to environment and before steady state oxidation occurs [148,206,215]. The oxidation rate is high and all the elements present in the alloy form oxides proportional with their concentration [215]. Some

oxides (CoO, NiO) grow faster than others (Cr_2O_3), leading to the formation of a continuous layer of NiO or CoO [258,301,302,333]. These oxides are not very protective; thereby oxygen may diffuse relatively easily through them to react with chromium to form highly protective chromia. Eventually, a complete chromia-healing layer develops under the NiO or CoO oxide layer [333]. The healing layer forms first at the intersections of grain boundaries with the surface then penetrates across the grains in a step-like manner, as chromium diffuses laterally from these locations [333]. After formation of the healing chromia layer, further oxidation proceeds by the transport of reactants throughout it, which is a relatively slow process.

When reactive elements are present on the alloy surface, they oxidize first. Base metal oxides are undercutting the slow growing transient oxides and the reactive element oxides. However, the reactive element oxides act as heterogeneous nucleation sites for chromia oxides thereby decreasing the distance between adjacent chromia nuclei and reducing the time required for those to grow laterally and to form a continuous chromia layer [203,206,304]. As a result the transient oxidation is shortened. Decreasing the inter-nuclei spacing is also thought to promote a finer grain size. As a result, finer distribution and small spacing between reactive element sources promotes the formation of the healing chromia layer [254]. However, improved selective chromia oxidation and reducing oxide grain size do not occur only with the reactive elements. Any process or addition that reduces alloy grain size could increase chromium diffusion (due to large number of grain boundaries) and promote its selective oxidation [247]. Reactive element additions could pin alloy

grain boundaries and refine structure [12] thereby increasing chromium diffusion and finally promoting selective chromium oxidation.

However, the above model cannot explain why finer grains are present on the top surface of the oxide layer.

2.4.4 Modification of the oxide growth mechanism

It is well known that Cr_2O_3 and NiO grow as a result of predominant outward cation diffusion through oxide grain boundaries [140,218,260,261,291,309,310,332, 334-336]. It was proved that reactive elements segregate at chromia grain boundaries in the form of small particles of RE_2O_3 or perovskite compounds $(RE)CrO_3$ [258]. The segregation may inhibit chromium ions outward diffusion such that the inward diffusion of oxygen ions could exceed that of the cations, causing a change in the oxide growth mechanism [280].

There are several ways by which reactive elements are supposed to decrease the grain boundary chromium ions diffusion flux: (1) blocking effect, (2) trapping effect, (3) decreasing in grain boundary concentration of chromium or a doping effect at the grain boundary [217,291]. It is assumed that reactive element ions that have larger sizes are able to block diffusion efficiently at oxide grain boundaries and to change the oxidation mechanism [337]. Also, segregation of the alloy addition should be easier than the oxide dispersion [213]. It is suggested that reactive elements with higher solubility in Cr_2O_3 are less effective in modifying the growth behavior due to less segregation [338]. The change in oxidation growth mechanism

may influence the condensation of vacancies at the oxide/matrix interface thus affecting the oxide scale adherence [208] and the oxidation behavior [217]. For example, a reduction in cation outward diffusion can cause a reduction in growth rate of the oxide scale; thereby, the growth stresses become smaller [220].

2.4.5 Oxide pegging to the alloy

The improved oxidation behavior is often accompanied with the development of pegs in many alumina-forming alloys [213], but for chromia forming alloys the pegs are seldom observed. It is believed that oxide pegs could improve the scale adherence due to their potential to arrest crack propagation at the oxide/matrix interface therefore reducing the loss by spallation [339]. The adherence benefited by interfacial bonds strengthening with intrusion of pegs into the substrate [322]. The pegs are assumed to form due to selective oxidation of the reactive element at the oxide/matrix interface [315,316]. When reactive element is added as an oxide dispersion, the oxide particles intersecting the oxide/matrix interface are regarded as pegs. The oxidation process continues until all reactive element precipitates are oxidized; then alumina or chromia could form around the complex reactive element oxide core [315]. Further reaction may occur between the reactive element rich oxide-core and crust, to form intermediate oxide. The pegs are usually located at the substrate grain boundaries intersection with the oxide/matrix interface [313], and their number and depth increase with increasing reactive element addition.

However, when reactive elements were implanted or added as oxides, no pegs were observed but oxide scales were adherent to the substrate [319,332,340-342]. Other research suggested that oxide pegs might act as stress concentrators and/or thermal mismatch between the alloy and the scale leading to increase in spallation [229].

As a conclusion, it is basically agreed that the oxide pegs could contribute, to some degree, to the improvement in scale resistance to spallation but this mechanism may not be the primary one that could fully explain the improved adherence of oxide developed on reactive metal containing alloys.

2.4.6 Vacancy sink model

The interface between the oxide and the matrix is weakened by the vacancies created by the oxidation process, vacancies that condense at the interface and have a detrimental effect on scale adhesion [213]. The vacancy sink model assumes that reactive elements prevent vacancy condensation at the oxide/matrix interface by providing alternative sites for vacancy sinks [318,343]. These sites could be the internal oxide particles of the reactive element, the reactive atoms or stable oxide dispersions [206,319]. It is suggested that vacancies arise from outward diffusion of cations to the scale especially during transient oxidation when base metal oxides are growing faster [206,319]. Also, the unequal substrate flux of alloy elements can lead to a net flow of vacancies to the interface [206]. However, it was proposed later that the supply of vacancies does not arise from the interface as a result of metal atoms

transfer into the scale but rather from vacancy sources within the metal that are activated by the growth stresses [213].

After oxidation of a reactive element implanted alloy there is no evidence for the presence of reactive element's precipitates inside the alloy and the concentration of the reactive element in solid solution is very low so that reactive element sites for vacancy sinks do not exist [217]. As a result, the vacancy sink mechanism may not account for the beneficial effect of reactive elements addition on oxide adherence.

2.4.7 Reduction of compressive stresses within the oxide

Compressive stresses develop when new oxide forms within the oxide layer due to a predominant outward flux of cations; thereby, higher growth stresses may result at the outer layer of the oxide scale [330]. No relevant stresses develop when oxide forms on the surface. However, stresses may be introduced due to transition of metal atoms to the oxide lattice at the oxide/matrix interface [331]. All of the stresses are high enough to plastically distort the oxide scale and the substrate [313].

Reactive elements prevent the formation of oxide within the oxide scale, shifting the reaction to the oxide/matrix interface [278,313]. It was proposed that the oxide/matrix interface was a better place for oxide formation [313,319]. Reduction of oxide formation within the scale leads to lower intrinsic compressive stresses [344]. As a result, the stresses introduced during the growth of oxide could increase to a large extent before failure occurs [344]. In addition, the stresses introduced

isothermally and/or during cooling are lower for thinner scales which are promoted by reactive elements [278].

2.4.8 Improved chemical bonding to the alloy

The scale adhesion to the substrate depends on the nature of the atomic bonding across the oxide/matrix interface [206]. Reactive element additions are believed to improve directly the chemical bonding or indirectly by enhancing the epitaxial matching at oxide/matrix interface [228].

Two theoretical models were proposed to account for the improved adherence:

(1) The work of adherence depends on the standard free energy of oxide formation: the more negative is the standard free energy, the higher is the work of adherence [278]. The work of adherence is increased when reactive elements are present because their energy of formation is more negative than the matrix oxides.

(2) A mathematical model based on molecular orbital quantum theory. However, the model does not apply to other systems than Ni-Al-Y-O [228].

It was suggested that increasing bond strength could facilitate the substrate deformation instead of more destructive cracking and spalling [278]. However, the explanation for the chemical bonding model seems to be unsatisfactory [228] in explaining the enhanced adherence of reactive element-containing scales.

2.4.9 Sulfur getter mechanism

It was demonstrated that sulfur had a detrimental effect to the scale adhesion of both chromia and alumina forming alloys [228,322-324,326,327,345,346] even when sulfur was present at very low levels (e.g. 10 ppm). Reducing the sulfur content leads to better scale adhesion [324,327,347]. Sulfur segregation can lower the oxide scale adherence to the substrate by lowering the free energy at the interface or reducing the activation energy for void formation and growth at the oxide/matrix interface [446].

It was observed that reactive element additions prevented sulfur segregation, leading to increased adherence of oxide scales [210,321-327,348]. There have been several hypotheses proposed by which reactive elements could prevent sulfur segregation:

(1) Reactive elements are known to have a deoxidizing and desulfurizing action when added to a molten alloy [228]; thereby, reactive elements are able to react with sulfur to form stable sulfides [213] or oxysulfides of the reactive element [210].

(2) Sulfur is tied up by segregation to internal reactive element oxides [210,213,228].

(3) Reactive element segregates at the interface, increasing the interfacial energy and thus decreasing the driving force for sulfur segregation [210].

However, hypothesis (1) cannot apply when reactive elements are added to alloys as oxide dispersions; reactive element oxides (yttria) are more stable than its

sulfides or oxisulfides [247]; therefore, the latter cannot be formed. In addition, when reactive elements are implanted in alloys, there is not enough supply of reactive element to form bulk sulfides [247] and sulfur cannot segregate at internal reactive element oxides (hypothesis 2). The third hypothesis seems more reasonable.

2.4.10 Dynamic segregation model

The dynamic segregation model is based on segregation of reactive ions at the oxide/matrix interface and oxide's grain boundaries. During transient oxidation, base metal oxides are dominant. It is assumed [247] that reactive elements effects on transient oxidation are minimal. After the transient oxidation is over and a continuous layer of protective oxides (chromia or alumina) is formed, the reactive elements strongly affect the scale growth mechanism and scale adherence. As oxidation proceeds, reactive elements diffuse toward the scale/gas interface following the fastest paths for diffusion in both metal and oxide scale [247]. Grain boundaries are the fastest paths for diffusion because they have a more open structure than the lattice allowing faster diffusion of species [140,349]. The oxygen potential gradient across the metal-scale-gas system represents the driving force for reactive element diffusion [140,247]. Reactive elements ions that diffuse towards the gas interface will segregate first at the matrix/scale interface [247]. When a critical amount of reactive element ions segregated at the matrix/scale interface is reached, two effects occur. First, larger reactive element ions diffuse slower than chromium or aluminum cations inhibiting the outward short circuit transport of cations along grain

boundaries; thereby oxygen inward diffusion along scale's grain boundaries become predominant leading to a reduction in oxidation rate especially for chromia forming alloys [247]. Second, the oxide scale grain growth is reduced both in chromia and alumina forming alloys due to a solute drag effect of reactive ions on the scale's grain boundaries. The presence of reactive ions at the matrix/oxide interface improves in scale adherence by raising the free energy at the interface, which diminishes the driving force for sulfur segregation, and by preventing growing of voids.

As oxidation continues, scale grows primarily by inward oxygen diffusion along scale's grain boundaries while reactive ions continue to diffuse toward the oxide/gas interface and eventually, after hundreds of hours of oxidation, could enrich the scale in reactive elements near the gas interface [247].

However, for a coating, the reactive elements are mainly concentrated in the external part of the scale [236,243,282,285] but the reactive element is able to diffuse back from the outer to the inner part of the scale due to the reactive element chemical potential across the scale [218]. In this case, it was suggested [218] that the dynamic segregation model could be applied in the opposite way: the reactive element diffuses back to the alloy and blocks scale grain boundaries to inhibit the outward chromium transport.

2.4.11 Poisoned interface model

The interface poisoning model is focused on the importance of interfacial reactions steps, discounting any role of reactive element doping in the scale [238,247]. Interfacial reactions provide the means for point defect creation and annihilation as well as facilitating the incorporation of cations and anions into the newly formed lattice sites [238]. Segregation of reactive elements at the oxide/matrix interface could pin the interfacial dislocations and stop cation vacancy annihilation by blocking cation transport across the scale; thereby, anion transport becomes predominant [238,328].

The model suggests that a semi-coherent interface is needed to maintain the adherence of the scale to the matrix. There are several kinds of defects that could be present at the matrix/oxide interface (figure 2.7): (I) misfit dislocations in the alloy, that occur due to inherent difference between the lattice parameters of alloy and oxide scale, (II) misorientation dislocations that appear in both metal and oxide scale due to interactions of glide planes with the interface, (III) disconnections, that is formed by the attractive bonding of a two misorientation dislocations of opposite signs, one from the alloy, the other form the scale, and (IV) ledge defects that provide a step corresponding to a rational number of misfit dislocations in order to maintain semi-coherency [238,350-352].

The metal/scale interface cation vacancies can be annihilated or interstitial cations created both by climb of misfit dislocations into the matrix and into the interface of misorientation dislocation [350].

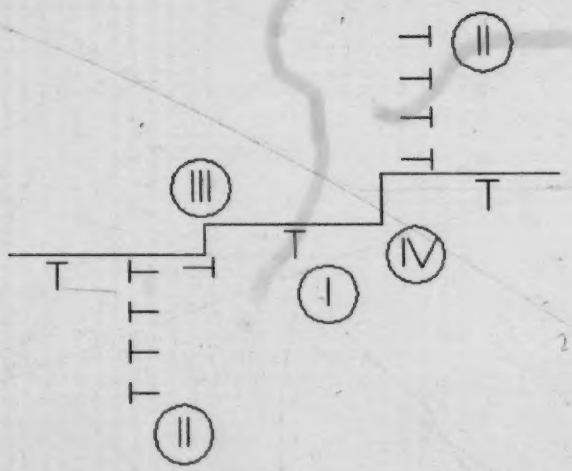

Figure 2.7: Interfacial defects at a semi-coherent oxide/matrix interface: (I) misfit dislocation, (II) misorientation dislocation, (III) disconnection, and (IV) ledge [351].

It is assumed that climb of misfit dislocations is favored due to their inherent presence and close spacing [238]. For cation diffusion scales, the new lattice grows at the ledge sites. For anion diffusion scales, the new lattice forms at metal/scale interface (figure 2.8). The attachment of the diffusion anions occurs either by climb of misorientation dislocations of the scale or by the translation of the disconnections in the metal/scale interface. The latter process must involve minor cation diffusion in order to repeat the misfit between the two lattices (figure 2.8) [238,351].

If the misfit dislocations are not maintained at the interface, tensile stress is induced in the metal and compressive stress is introduced in the scale, which could result in spallation [352].

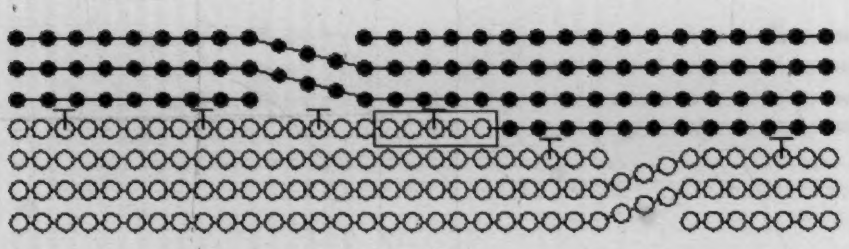

a)

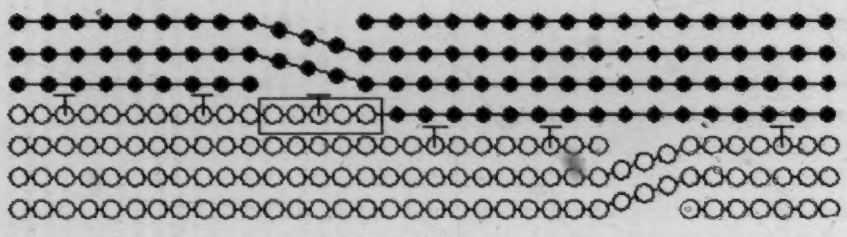

b)

Figure 2.8: Growing of an oxide scale by major anion diffusion at oxide/matrix interface - the translation of the disconnections and the need of removing an extra atom from the interface: a) first step; b) a subsequent step [351].

As reactive elements segregate at the oxide/matrix interface during oxidation, they could pin the interfacial misfit dislocations in the metal, preventing their movement (figure 2.9). By doing so, reactive elements block the creation of interstitial cations and/or annihilation of cations vacancies required to support cation transport in the scale [238]. If the anionic interfacial step is not similarly blocked then anionic scale growth becomes predominant. However, disconnections do not represent sites for strong absorption of reactive elements and could function as sites for creation/annihilation of defects [238].

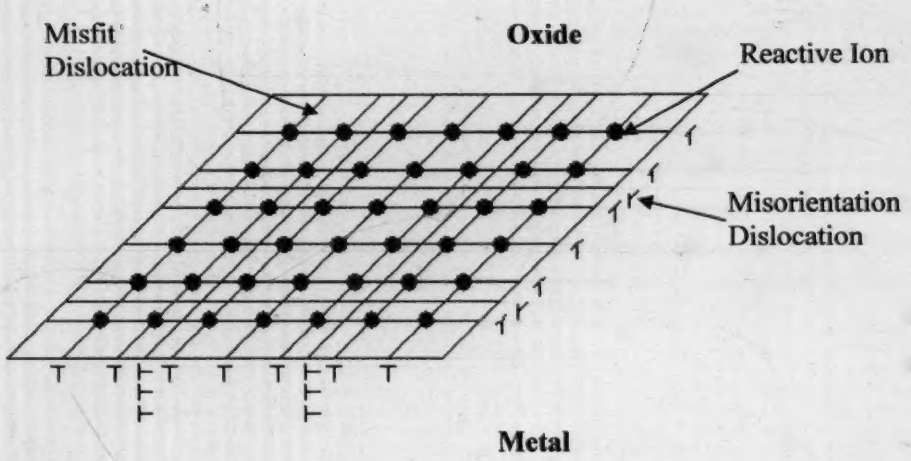

Figure 2.9: Schematic representation of reactive ions pining misfit dislocations at the oxide/matrix interface [351].

2.4.12 Effects of reactive elements on oxidative wear

Studies on the effect of reactive elements on the tribological behavior are rare. Most of the studies refer to the effects of yttrium or cerium on reducing synergistic action of wear and corrosion on different alloys at ambient temperatures. It was proved that yttrium or cerium addition, either in metallic form or as oxides, are beneficial in reducing corrosive wear when added to lubricants [353,354-356], to bulk alloys [357-359], as a constituent in protective coatings [275,279,360-365] or as a constituent gas during a nitriding process [366, 367]. Enhancing the surface passive film properties is the main factor that leads to the beneficial effects of yttrium and cerium additions on the wear resistance in aggressive environments. The main properties of the passive film that are improved by the reactive element additions are:

chemical stability, mechanical properties such as hardness, and adherence to the substrate.

However, the enhanced passive film does not always function. For example, yttrium markedly increased the resistance of 304 stainless steel to corrosion-erosion in a slurry of 0.1M H_2SO_4 containing 30% silica sand particles when tested at slurry velocities up to 4 m/s. However, when the velocity exceeded 4 m/s, no beneficial effect was observed [368]. The above behavior implies that at larger slurry velocities the passive film is not able to withstand the mechanical action and/or there is not enough time for the passive film to reform on the surface.

When yttrium was added to aluminide coatings, an increase in the hardness of the aluminide coating resulted; thereby, improved wear behavior was achieved [358,362-364]. It was suggested that the resistance to corrosion-erosion of a 27Cr white cast iron containing 1%Y in different slurries was enhanced mainly due to the improvements of the passive film rather than the mechanical properties of the bulk material [369].

When yttrium was implanted to a wrought heat resistant alloy (ASTM A286) the abrasive wear resistance was improved. This improvement was related to the better mechanical properties (hardness, elastic recovery) of the surface layer [370,371]. Implanting erbium to 20Cr2Ni4 alloy led to a hardening effect on the surface layer which led to improved wear behavior under lubricated conditions [372]. Moreover, cerium implantation of GCr5 alloy improved the fretting wear behavior up to 50^0C that was attributed to increase in the cohesive strength of the oxide film [373].

Presence of reactive elements in alloys could lead to improvement in wear resistance at ambient temperatures due to beneficial effects of reactive elements on bulk mechanical properties of the alloys. For example, additions of reactive elements compounds such as ceria or lanthana to the composition of laser or flame sprayed clad layers markedly improved the wear behavior at room temperature under sliding conditions because reactive elements increased the hardness of the surface layer, refined its microstructure, reduced the number of inclusions, and formed hard phases [374-377]. Cerium additions to Al-Si alloys improved the wear behavior through solid solution strengthening and precipitation hardening effects [378]. However, in some cases reactive element additions do not improve the mechanical properties of the surface layer but wear rates are decreased at room temperature [379]. This behavior is attributed to the effects of reactive elements on the oxidative wear process; for example, Ce additions retarded the oxidation of MoS_2 in the surface film on a Fe-Mo-S alloy [379].

Thermo-chemical treatments using reactive elements are proven to improve the erosion-corrosion wear behavior due to high hardness of the surface layer, better toughness, finer nitrides and improved passive film [366,367].

2.5 Possibilities of reactive elements to resist high temperature wear

There are only three studies that refer to the applications of reactive elements to enhance high temperature wear resistance. The first one, in chronological order, studied the effects of yttrium implantation to a precipitation-hardened stainless steel

(ASTM A286) [371]. Wear tests were carried out at 400^{0}C in a reciprocating ball on disc apparatus under a low load of 0.57 N. The ball was made of alumina. The wear test showed that yttrium implanted samples had a lower wear rate than the un-implanted material. However, the wear behavior benefited from the higher surface hardness of the implanted region. The authors believed that the improvement was due to the beneficial effects of yttrium to oxidation but no proof was provided.

The second study, considered the effects of yttrium (0.02%) on the wear resistance of a PVD-deposited TiAlN coating [186]. Wear tests were performed in a reciprocating ball on disc configuration at temperatures up to 900^{0}C. Yttrium resulted in a significantly finer grained structure of the coating but did not show any beneficial effects on wear rates up to 800^{0}C, when compared with the conventional TiAlN coating. At 900^{0}C the wear behavior of the yttrium containing coating was improved over the conventional TiAlN coating. The authors refer to a "curing" behavior of the yttrium containing coating as temperature was increased. However, no explanation was provided regarding the above behavior and how yttrium affected the wear behavior.

The most recent study demonstrated that a yttrium addition as an alloying element could make Stellite 6 considerably more resistant to high temperature wear [12]. Such improvement was attributed to the enhanced bulk hardness of the yttrium-containing alloy but also to the enhancement of the mechanical properties of its oxide scale, especially hardness and adherence to the substrate. However, it was not clear which one provided the major contribution to the improvement of wear resistance. It was shown that 2% yttrium additions to Stellite 6 resulted in the

greatest improvement in the alloy wear performance. The 2% yttrium-containing sample showed the highest bulk hardness and the highest improvement of the oxide mechanical properties. This is in disagreement with the oxidation studies found in literature, which demonstrated that the highest improvement in oxidation behavior occurred at a reactive element concentration below 1%. It seems that the benefits to the wear behavior come in large fraction from the enhanced hardness of the bulk material.

The objective of this work is to explore the mechanism responsible for the beneficial effect of yttrium on high-temperature wear resistance of cobalt based alloys and relevant issues through studying the effects of yttrium additions as an alloying element on the wear behavior of Stellite 21, from room temperature up to 600^0C, as related to microstructure, mechanical properties of both the alloy and its oxide scale, and oxidation behavior. A similar approach was applied to Stellite 712 for comparison purposes.

As presented in this chapter, there is no doubt that the oxide scale is beneficial to the high-temperature wear resistance at low stress conditions. However, how much an oxide scale contributes to the high-temperature wear resistance and whether or not there is a critical wearing force beyond which the oxide scale does not function need to be investigated in order to properly take advantage of an oxide scale to minimize wear at elevated temperatures.

Various techniques were used to investigate the effects of yttrium addition to Stellite 21 and 712, including optical microscopy, X-ray diffraction, SEM (scanning

electron microscopy), EDS (energy dispersive microscopy), micro- and nano-mechanical probes, micro-scratch tests, AFM (atomic force microscopy), SIMS (secondary ion mass spectroscopy), and pin-on-disc wear tests.

3.0 MICROSTRUCTURE

This chapter presents results of the study on the main effects of yttrium on microstructure when alloyed to Stellite 21 and 712 alloys. The purpose is to provide a comprehensive view of yttrium effects on Stellite 21 and 712 alloy's microstructure and a base for interpreting corresponding wear behavior. This chapter comprises four main sections. The first one is related to the role of the alloying elements in modification of microstructure, phase formation, and general properties of cobalt based alloys; the second section describes alloy preparation and heat treatment; the third section illustrates the results of the microstructure examination while the last section presents the crystal structure of phases developed in the samples.

3.1 General properties of Stellite alloys

The nominal composition of Stellite 21 and 712 are given in table 3.1. Pure cobalt exhibits an allotropic phase transformation on cooling at 390^0C (M_s) from a high-temperature stable γ phase (FCC) to a low-temperature stable ε phase (HCP). The transformation is reversible on heating, occurring at 430^0C (A_s) [14]. When alloying elements are present, the transformation temperatures are affected, e.g., A_s is increased to 970^0C for a Co-27Cr-5Mo-0.05C alloy [16]. However, under most cooling conditions, the transformation tends to be sluggish in a cobalt-based alloy; therefore, the cobalt matrix is a mixture of ε and metastable γ at room temperature

[26,380-382]. The volume fractions of the two cobalt allotropes determine the mechanical behavior of the alloy, e.g., the ductility is increased with increasing γ phase [231,380,383]. As a result, alloying elements are carefully balanced to avoid lower ductility.

Table 3.1: Nominal composition of Stellite 21 and 712 alloys as provided by Delloro Stellite Inc.

Element	Co	Cr	Mo	Ni	Fe	Si	Mn	C
Stellite 21 - composition[wt%]	Bal	27	5.5	2	3	1	1	0.25
Stellite 712 – composition[wt%]	Bal	29	8.5	2.5	2.5	1.5	1	1.8

The γ→ε transformation may be induced by:

(1) plastic deformation (strain-induced transformation - SIT) [380,384,385],

(2) quenching from γ phase field when casting [19,386],

(3) aging at temperatures near 800^0C [16,387,388].

The transformation is affected by several factors including the grain size of the parent phase [380,384], cooling rate [19,386,389], temperature and the duration of solution heat treatment prior to aging [16,22], and cooling procedure (e.g. quenching from the solution temperature directly to the aging temperature) [16]. The SIT can be linked to the absorption of energy in various wear situations, which explains the excellent galling resistance of cobalt base alloys [27,390]. Furthermore, the residual γ phase has relatively low stacking fault energy (SFE) [380], which increases the work

hardening capability by hindering dislocation movement. For lower SFE (15 mJ/m^2) the SIT mechanism prevails, while twinning is the predominant deformation mode at 20 mJ/m^2 [380].

Chromium improves the resistance to corrosion and oxidation and is the main carbide former (e.g. $Cr_{23}C_6$). The amount of carbon present affects the formation of carbides and thus influences hardness, ductility and wear resistance of the alloy. Molybdenum is utilized as a solid-solution strengthener and to provide additional strength to the matrix by forming an intermetallic compound Co_3Mo. Molybdenum also benefits the corrosion resistance of the alloy [14]. Molybdenum and chromium decrease the SFE [380,391] and can stabilize the ε phase, while iron, nickel and manganese increase the SFE and stabilize the γ phase [13,14,392,393].

Silicon and manganese are used for the casting procedure to enhance castability in terms of deoxidation, sulfur control and fluidity [14].

Both solid solution strengthening and carbide precipitation are used to confer Stellite 21 and 712 alloys adequate high-temperature mechanical properties. Carbides impede grain boundary growth, dislocation movement, and grain boundary sliding (creep resistance). Above temperatures of 1000^0C the benefit of carbides is reduced (due to agglomeration and size increase of carbides); thereby solid solution strengthening becomes more important for the alloy high temperature strength [14].

Stellite 712 (table 3.1) contains high amounts of molybdenum for solid solution hardening and has relatively high carbon content (1.8%) that is necessary for increasing the amount of carbides, which will confer higher abilities to withstand the effect of wear at high temperature.

3.2 Alloy preparation and heat treatment

There are several ways to introduce reactive elements to an alloy, including ion implantation, coatings or alloying. However, the reactive element effect is similar and independent of the method chosen to introduce the active elements to the alloy [240].

Ion implantation offers some advantages such as controlling the concentration of the reactive element into a thin surface layer, providing a homogeneous distribution of the reactive element, and not altering the substrate's microstructure. Coatings also offer some advantages, including relative ease of application and low cost in terms of reactive element quantity used. However, both methods have the major disadvantage of not providing an adequate supply of reactive element to reestablish protection when the oxide fails by spallation or mechanical contact.

Alloying may have a negative impact on Stellite alloy's properties by reducing the high-temperature ductility due to internal oxidation of the reactive element compounds [281] or making it difficult to control the composition during casting procedures. However, hardening due to dispersed reactive elements and their oxides or intermetallic compounds could benefit the wear resistance. In addition, the segregation of reactive element at oxide grain boundaries, an important step for the reactive element effect to happen, should be favored for alloy additions rather than oxide dispersion additions. Alloying with the addition of a reactive element is an effective method of incorporation into bulk Stellite alloys in order to improve their

wear resistance under the harsh wear conditions (e.g., galling wear) encountered in practice.

Stellite 21 and 712 alloys provided by Deloro Stellite Inc. were re-melted with added yttrium powder (-40 mesh) in an arc-melting furnace (MRF INC. SA338-V&G). Figure 3.1 presents the SEM images of the yttrium powder and the corresponding EDS analysis that confirmed that no other impurity elements were present.

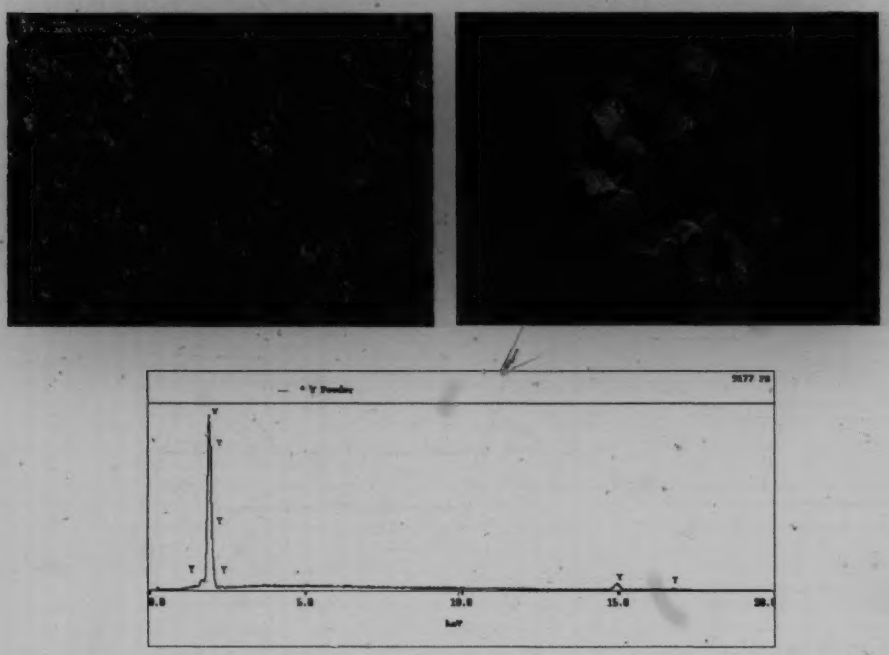

Figure 3.1: a) SEM images of yttrium powder that was alloyed to Stellite 21 and 712 alloys and b) the corresponding EDS analysis.

Several groups of alloy samples were made containing 0, 0.5, 1, 2, and 5-wt% yttrium, respectively. The cast samples had the following dimensions:

10x10x30 mm. Special care was taken in order to limit yttrium exposure to oxygen. The melting and solidification conditions are given in Table 3.2. In order to increase the degree of homogenization, all samples were turned over and re-melted consecutively five times.

Table 3.2: Experimental Conditions for Re-melting of Stellite 21

Parameters	**Melting conditions**
Vacuum pressure before filling with Ar gas	-90 to -95 kPa (27-28" Hg)
Ratio of vacuum/back-fill with Ar gas	3 times
Protection gas	Argon
Gas flow during melting and cooling	2 l/min
Pressure during melting and cooling	10 kPa (1.5 psi)
Electrode type	Thoriated tungsten
Electrode diameter	4.8 mm
Arc current	160/240A
No. of turning over and re-melting	5 times

Some difficulties were encountered during arc melting regarding arc stability, which were attributed to the presence of yttrium. The presences of rare earths (e.g., less than 0.02wt% cerium that is used for desulphurization and to modify sulphide shape during rolling procedures) in the composition of steels that are welded create arc instabilities, leading to "flaring" behavior. The flares originate at rare earth oxysulphide inclusions that float around the weld pool when the electrode polarity is

positive. The oxides of rare earths have a low work function and thereby emit electrons very easily [394-396].

Due to Lorentz forces within the weld pool, these oxides move around from one area to another, causing multi-directional forces on the arc column. Under the present conditions, the electrode was on negative polarity, so the flaring was minimized as electron emission takes place at the electrode tip and not at the sample. However, the arc was unstable with reduced penetration.

The reactive element was likely still able to emit electrons due to plasma impingement on the sample surface, which could create a back-reaction force in the arc column. As a result, the maximum arc time was reduced to 8 s in order to protect the electrode.

The samples were homogenization annealed at 815°C for three hours followed by air cooling. After the homogenization treatment, samples were cut using an abrasive disc cutter machine (Buehler, NY, USA).

3.3 Results of microstructure examination

Standard techniques were used to prepare specimens for optical metallography. Final polishing was performed using a 0.05 μm alumina slurry. A solution of HCl and 30% H_2O_2 (volume fraction 6:1) was used to etch the samples. Microstructures of the samples were observed using an optical microscope (Olympus PME3-ADL). Figure 3.2 and 3.3 illustrate microstructures of Stellite 21 and 712 samples with and without yttrium additions, respectively.

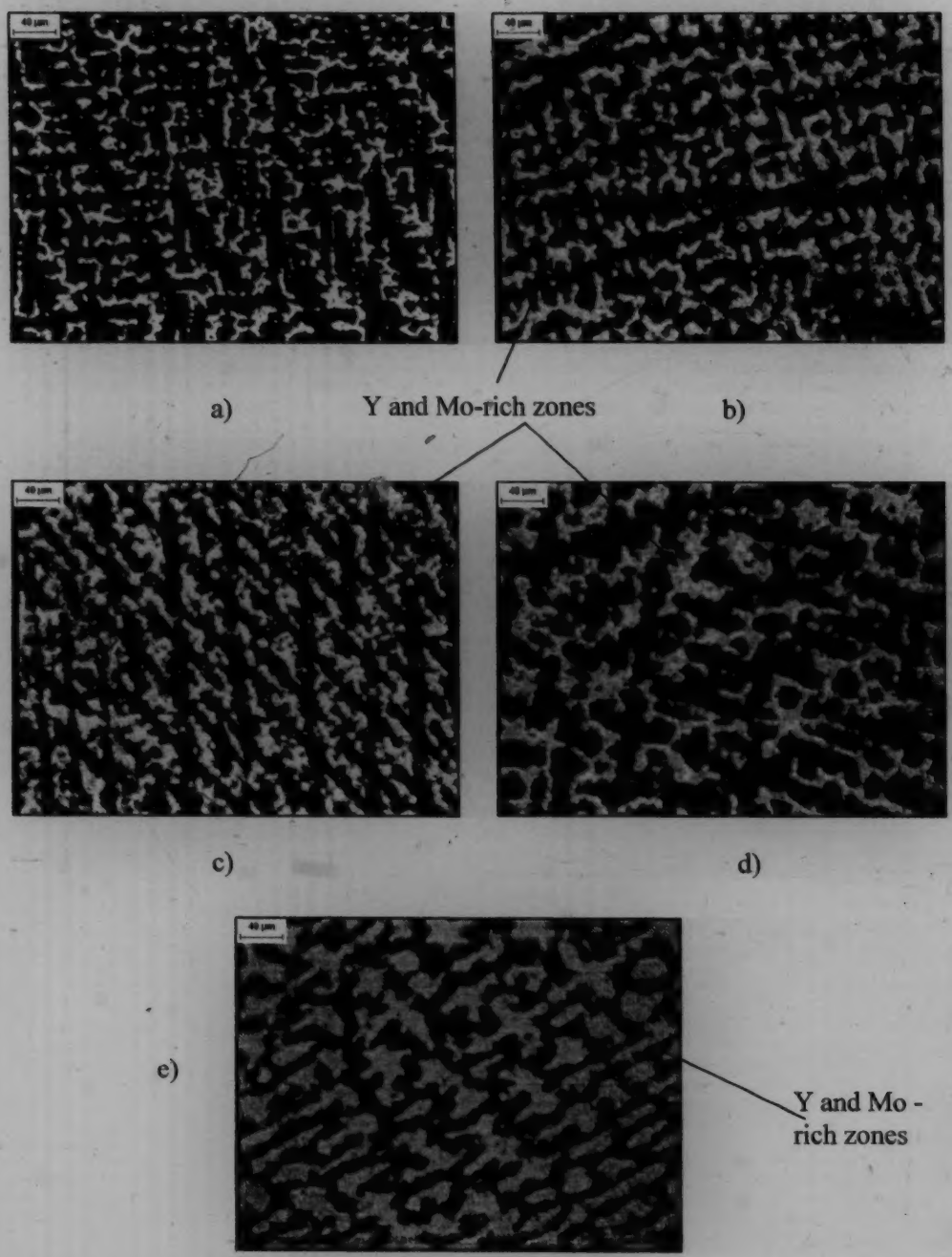

Figure 3.2: Optical microstructures of Stellite 21 alloy modified with: a) 0%Y; b) 0.5%Y; c) 1%Y; d) 2%Y; e) 5%Y.

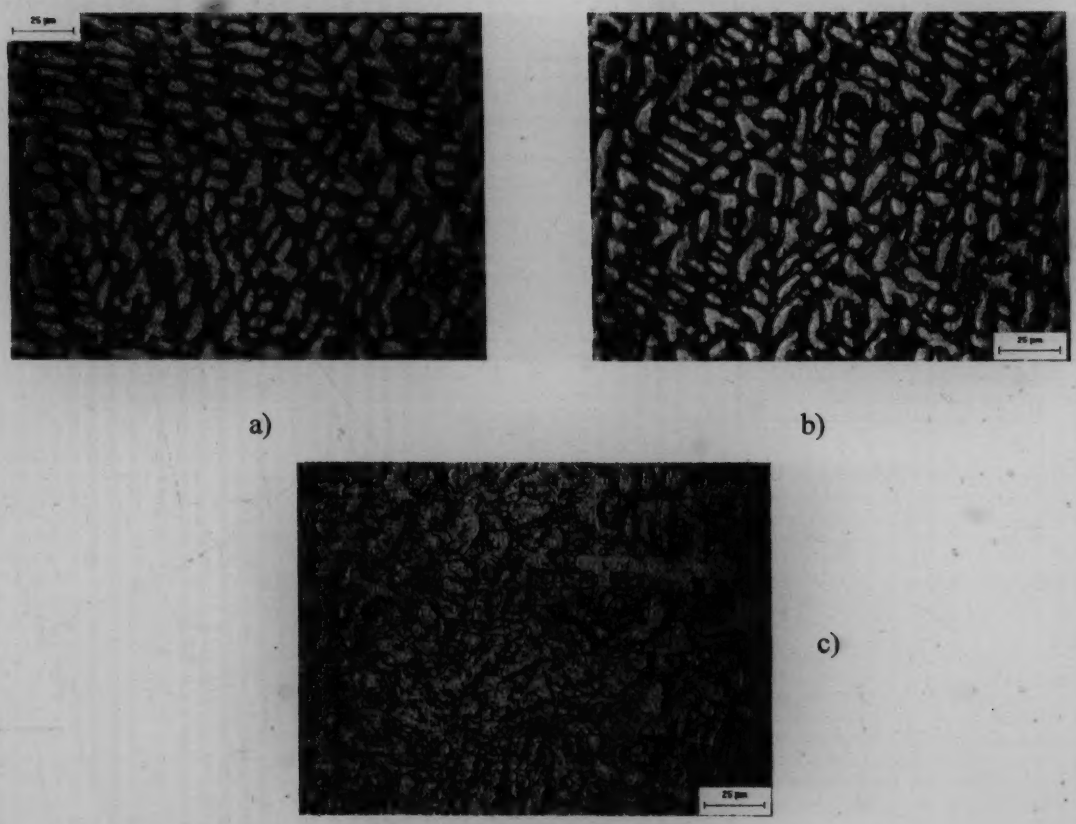

Figure 3.3: Optical microstructures of Stellite 712 alloy samples with a) 0%Y, b) 0.5%Y, and c) 5%Y. The light and dark domains are dendritic and interdendritic regions, respectively.

All the samples showed a typical dendritic microstructure. The unmodified Stellite 21 sample had a finer form than the yttrium-modified ones. No marked differences in microstructure were observed among the specimens. However the inerdendritic regions of the 5% yttrium-containing specimens showed a slightly different response to etching. The changes in the shades of grey for the diffe.ent

domains resulted from changes in composition and the formation of a new phase, Co_2YSi_2 (see chapter 3.4), which could influence the etching effect.

Figure 3.4 presents EDS maps of molybdenum and yttrium in Stellite 21 samples containing 0, 0.5, and 5-wt% yttrium, respectively. Corresponding SEM back-scattered electron images are also presented in figure 3.4.

Molybdenum is concentrated in the interdendritic regions. The 1% and 2% yttrium-containing samples have similar molybdenum and yttrium distributions as the samples presented in figure 3.4. Yttrium was not homogeneously distributed but appeared to be concentrated in some small regions in the interdendritic regions especially where the molybdenum was rich.

SEM images of heat-treated (homogenization) and untreated Y-free and 5%Y- containing Stellite 712 specimens are presented in figure 3.5.

Figure 3.6 presents EDS maps of molybdenum, chromium, cobalt, nickel and yttrium in Stellite 712 sample containing 5-wt% yttrium after heat treatment. It was demonstrated that rich molybdenum eutectics and chromium eutectics, respectively, were formed in the interdendritic regions. The 0.5%, 1% and 2% Y-containing samples had similar molybdenum and chromium distributions but as the amount of yttrium increased it seems that the chromium-rich eutectic became slightly coarser due to enhanced atomic diffusion at the high homogenization temperature. No silicon was detected in the chromium-rich phase in all specimens.

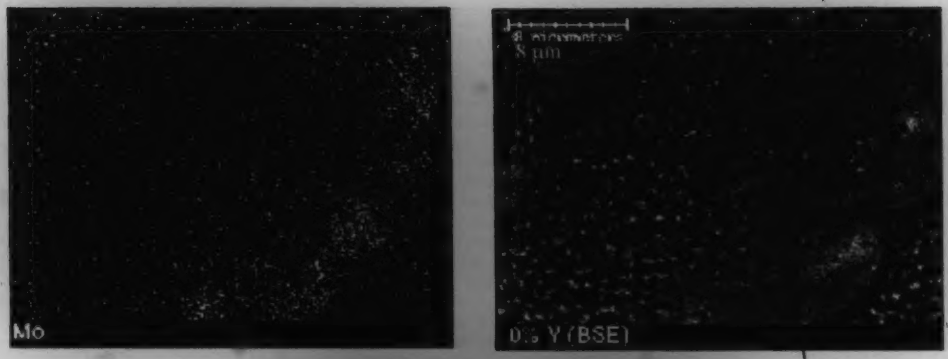

EDS (Mo)

SEM

SEM

Interdendritic region

a)

EDS (Mo)

EDS (Y)

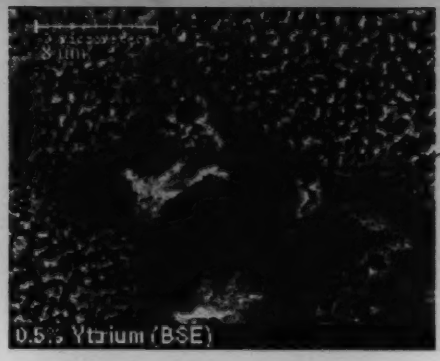

Interdendritic region

SEM

b)

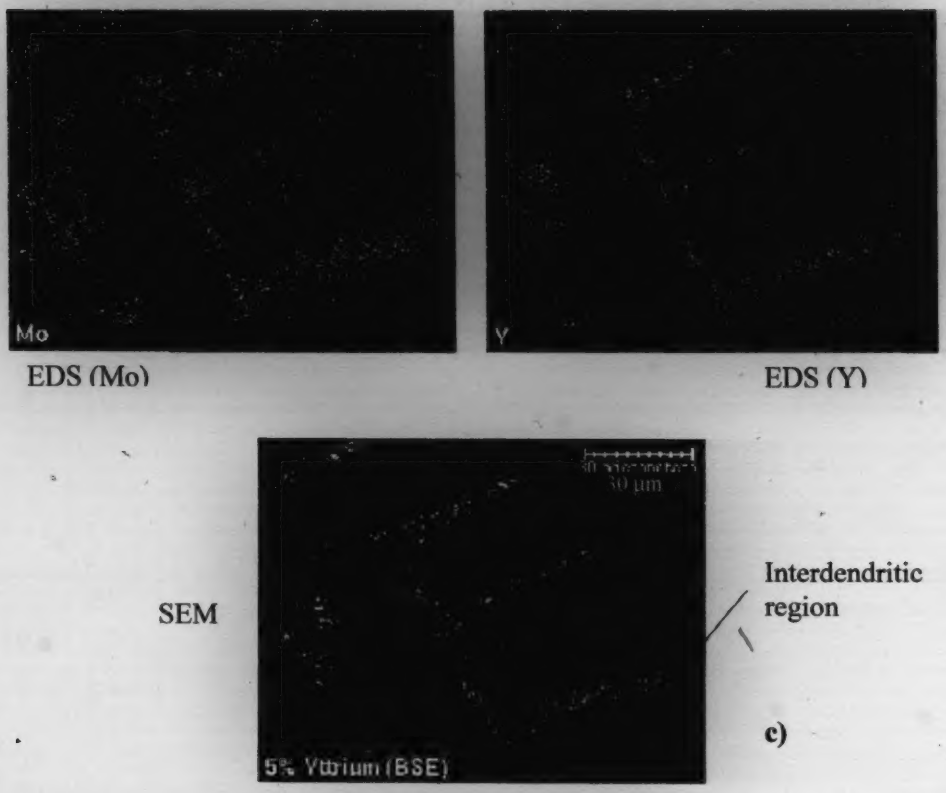

Figure 3.4: SEM and EDS compositional dot maps of Stellite 21 alloy modified with: a) Yttrium free; b) 0.5%Y; c) 5%Y.

Similar to Stellite 21, yttrium was distributed where molybdenum was rich. Before the homogenization treatment, yttrium was not homogeneously distributed in the 5%Y-containing sample and appeared to be concentrated in some interdendritic regions. According to binary phase diagrams (e.g. Co-Y, Ni-Y), yttrium has very limited solid solubility in the elements present in Stellite 21 and 712 at room temperature; therefore, yttrium could segregate in the interdendritic regions.

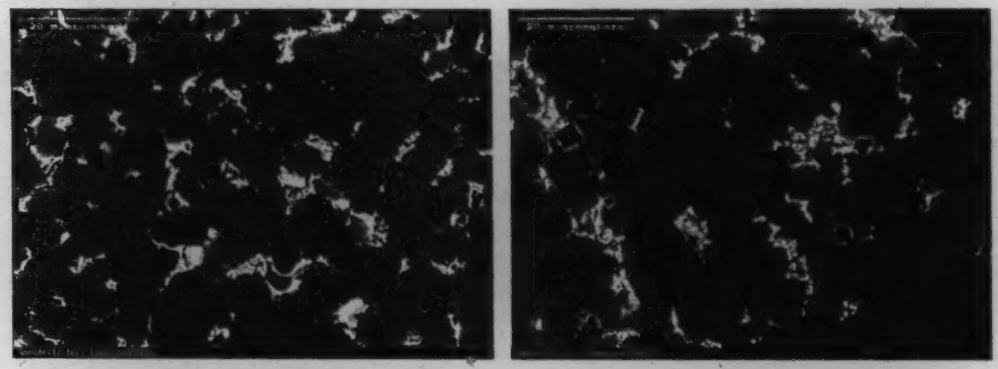

a) b)

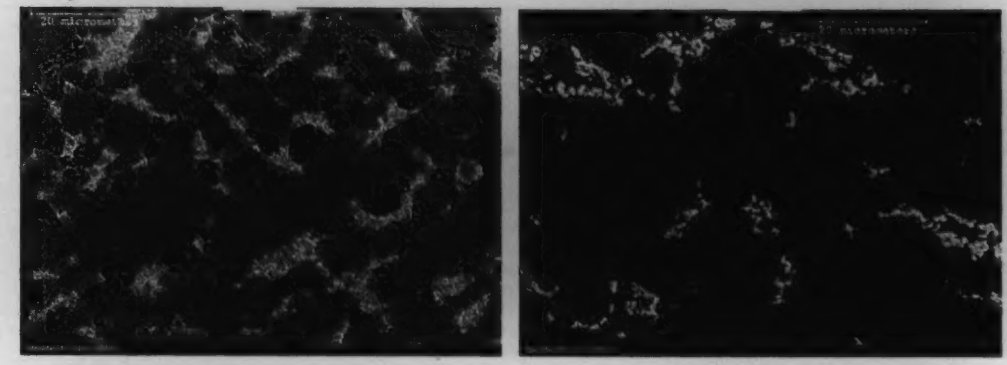

c) d)

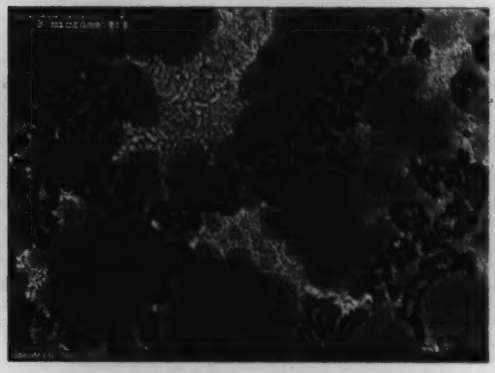

e)

Figure 3.5: SEM images of Stellite 712 alloy samples with a) 0%Y - untreated; b) 5%Y - untreated; c) 0%Y - heat treated; d) 5%Y - heat treated; e) 0%Y - heat treated, at higher magnification

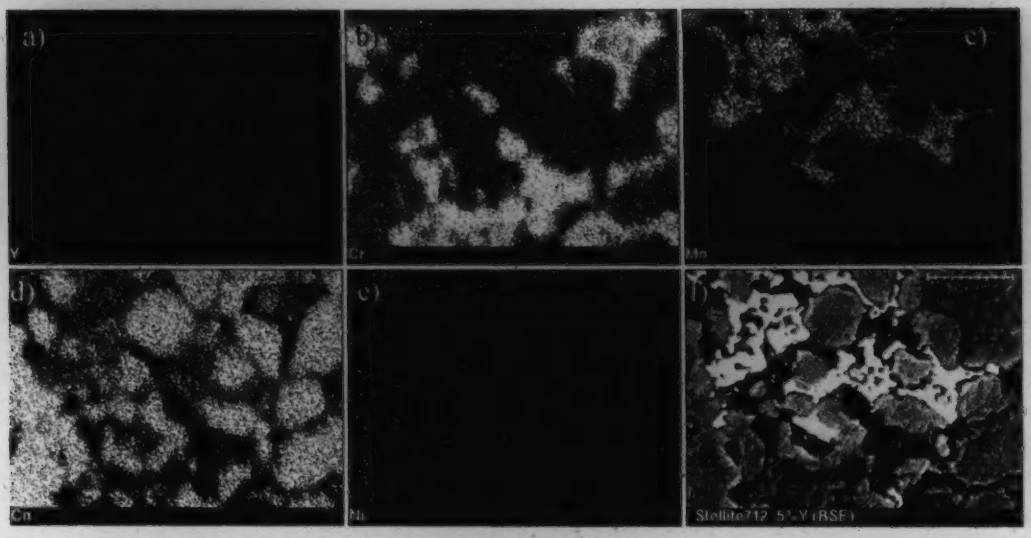

Figure 3.6: EDS compositional dot maps of Stellite 712 alloy containing 5%Y; a) Y, b) Cr, c) Mo, d) Co, e) Ni, f) corresponding SEM image.

According to a binary Mo-Y diagram, molybdenum and yttrium are insoluble in each other at room temperature.

It is known that molybdenum solutes diffuse preferentially to stacking faults [389] which might provide more space to accommodate yttrium atoms that have a larger radius (0.181 nm), compared to other elements in the alloy (e.g. Co, Ni, Fe, Cr, and Mo). This might be a reason why yttrium was more concentrated in the molybdenum-rich regions.

Exposure at 815^0C for three hours (homogenization treatment) promoted the diffusion of molybdenum to the interdendritic regions. Segregation of molybdenum, a HCP stabilizer, could play a strong role on the generation of preferential nucleation sites for isothermal cobalt martensite. However, the homogenization temperature and

duration were too low and short, respectively, to promote carbide dissolution or coarsening.

3.4 Crystal structure of phases developed in the samples

A Rikagu X-ray diffractometer using Cu K_α radiation (λ = 0.154056 nm) was used to determine the crystal structures of phases developed in the samples. The samples for X-ray examination had a dimension of 10x10x1 mm. Prior to X-ray analysis, the specimens were polished using a 0.05μm alumina slurry then etched to remove the deformed surface layer caused by polishing.

Figure 3.7 presents X-ray diffraction patterns of Y-free, 1% and 5% yttrium-containing Stellite 21 samples, respectively. X-ray patterns of 0.5, and 2% yttrium-containing Stellite 21 samples were similar to that of the sample containing 1% yttrium.

Identified major phases were:

- Co_3Mo (HCP),
- γ-Co (FCC),
- ε-Co (HCP).

As shown in figure 3.7, some minor phases such as $M_{23}C_6$ (where M was Cr, Co, Mo, or Fe - e.g., $Cr_{17}Co_4Mo_2C$ [14,26]), or NiCrCoMo may be present but cannot not be positively identified due to peak superposition. Reference [14] indicates that $M_{23}C_6$ usually forms in cobalt based alloys and NiCrCoMo may also be present.

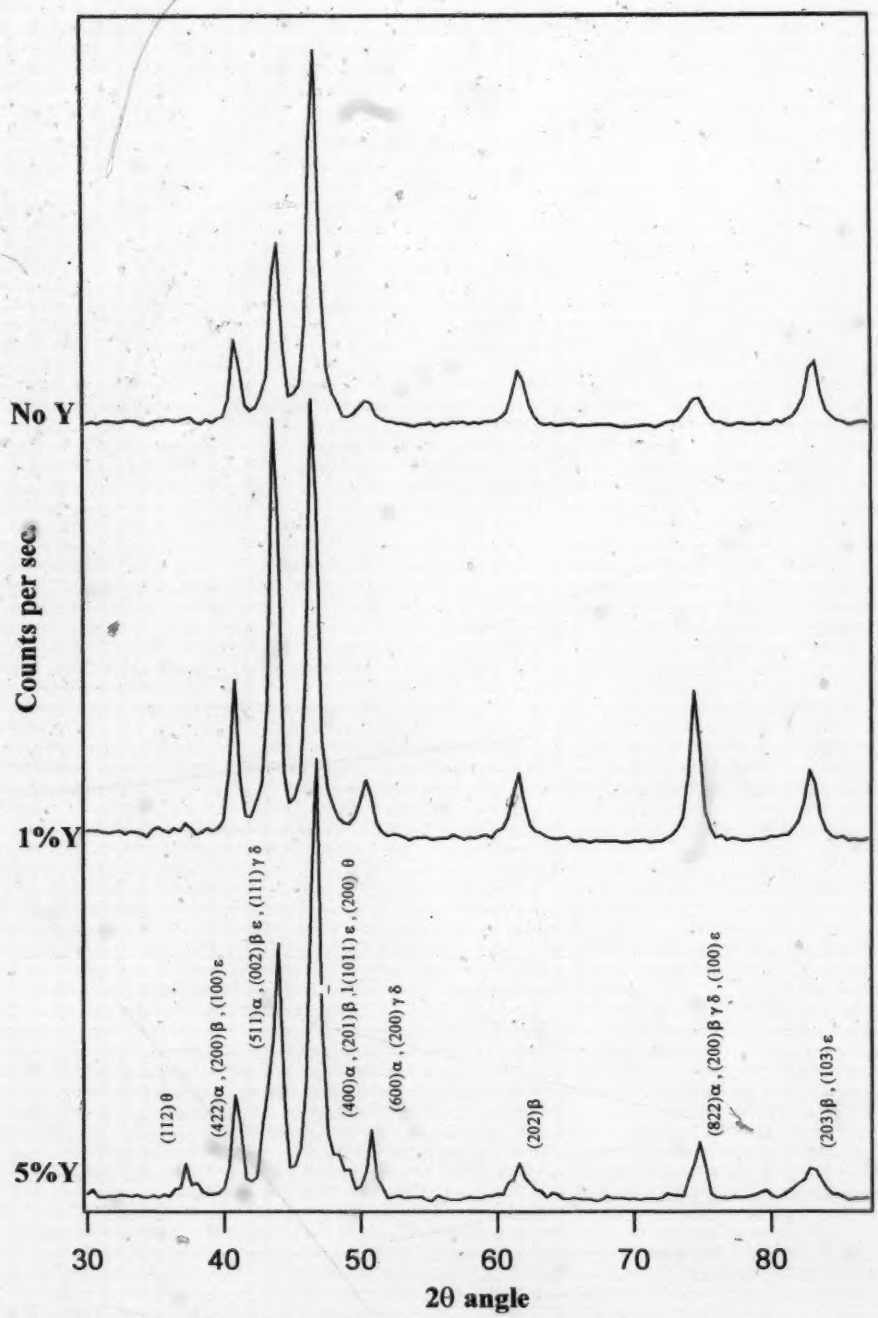

Figure 3.7: X-ray diffraction patterns of Y-free, 1%, and 5% yttrium-containing samples, respectively, in Stellite 21. α - $M_{23}C_6$ β - Co_3Mo ε- ε Co γ - γ Co δ - NiCrCoMo θ - Co_2YSi_2

Figure 3.8 illustrate X-ray diffraction patterns of Y-free, 0.5% and 5% Y-containing Stellite 712 samples, respectively. X-ray patterns of 1 and 2% Y-containing Stellite 712 specimens are similar to that of the specimen containing 0.5% yttrium. Identified phases were:

- Co_3Mo (HCP),
- γ-Co (FCC),
- ε-Co (HCP)
- $Cr_{23}C_6$ (FCC).

which were similar to these found in Stellite 21. An additional minor phase was identified: Fe_2Mo_3 (Table 3.3). NiCrCoMo phase may be present but cannot be positively identified due to the peak superposition.

The X-ray result was consistent with these reported in literature [14,24,26,49]. Addition of a small amount of yttrium did not result in the formation of any new phase. All specimens contained both γ and ε cobalt allotropes at room temperature. This happened because the ε phase was hard to generate under normal cooling conditions such as air cooling [389]. The metastable γ phase could fully transform to ε phase if the γ phase is aged at 815^0C prior to cooling.

For 0.5, 1, and 2 wt% yttrium-containing samples, no extra x-ray diffraction peaks were detected, probably because the amount of yttrium was not sufficient for the formation of new phases or more probably because any phases formed were too small to be detected. However, a new phase (Co_2YSi_2) was formed at higher yttrium contents, e.g. at 5%.

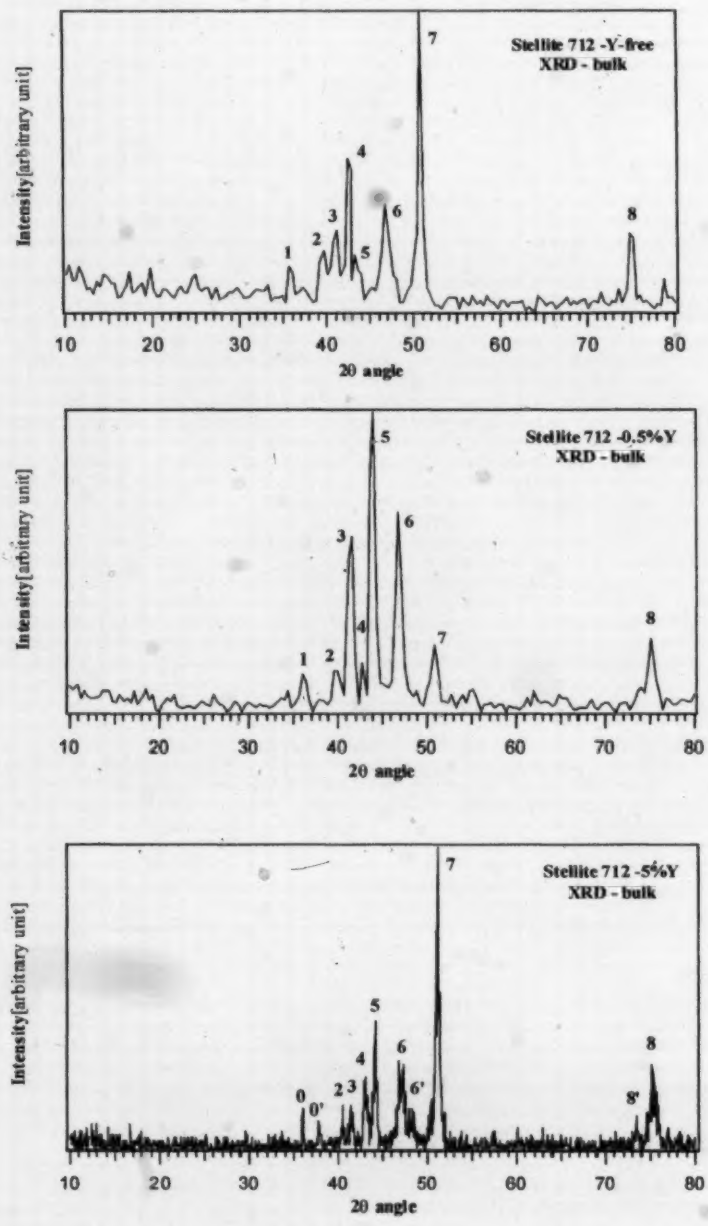

Figure 3.8: X-ray diffraction patterns of Y-free, 0.5%, and 5% yttrium-containing Stellite 712 samples, respectively.

Table 3.3: XRD of phases in Stellite 712 corresponding to the peak numbers in figure 3.9.

Phase	Peak number											
	0'	0	1	2	3	4	5	6	6'	7	8'	8
ε-Co	-	-	-	-	(100)	-	(002)	(101)	-	-	-	(110)
γ-Co	-	-	-	-	-	-	(111)	-	-	(200)	-	(220)
Ni-Cr-Co-Mo	-	-	-	-	-	-	(111)	-	-	(200)	-	(220)
Co_3Mo	-	-	-	(200)	-	-	(002)	(201)	-	-	(220)	-
$Cr_{23}C_6$	-	(420)	-	-	(422)	-	(511)	-	(440)	(600)	-	(822)
Fe_2Mo_3	-	-	X	X	-	X	-	X	-	-	-	X
Co_2YSi_2	(103)	(112)	-	-	-	-	-	(200)	-	-	-	-

Note: "x" indicates that the h k l are not indexed.

As described in the next section, the mechanical behavior of Stellite 21 was improved by the γ→ε transformation as well as by the formation of the Co_3Mo intermetallic and by $M_{23}C_6$ carbides. It appears that yttrium did not affect the existence/extent of these phases but produced a slightly coarser microstructure.

4.0 EVALUATION OF THE MECHANICAL PROPERTIES

This chapter presents results of the studies on changes of mechanical properties of Stellite 21 and 712 when alloying different amounts of yttrium to the alloys. The purpose of this investigation is to provide a framework for interpreting their wear behavior. This chapter comprises two main sections: the first one describes the changes of hardness at both macro and micro levels while the second section estimates the amount of cobalt allotropes present in the samples after heat treatment and strain hardening, respectively.

4.1 Hardness

Macro-hardness was measured using a conventional Rockwell hardness tester under a load of 1471 N. The HRC value reported is an average of five measurements. Results of the macro-hardness measurement (HRC) on Stellite 21 are given in figure 4.1. It was demonstrated that yttrium did not markedly influence the hardness of the alloy.

Similar to Stellite 21, the macro-hardness of Stellite 712 samples was not affected by the yttrium addition; both show a value around 52 HRC.

Local mechanical properties of different phases in the samples were determined using a micro-mechanical probe (Fisher Technology Ltd., Windsor, CT, USA) under different maximum loads (from 20 to 1000 mN). Each reported value is an average of ten measurements.

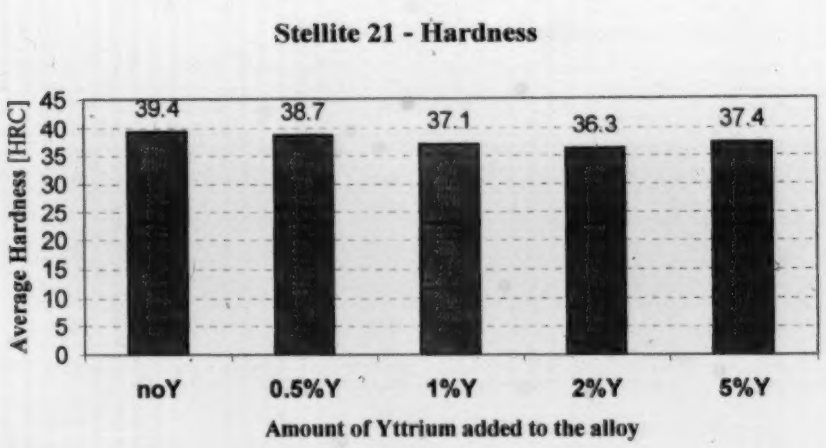

Figure 4.1: Macro-hardness (HRC) values of yttrium-free and yttrium-containing Stellite 21 samples. Error range: ±0.3 HRC.

The technique is based on Vickers indentation, which provides information on local hardness and elastic behavior [397]. The η value, a measure of elastic behavior, and indentation depth were determined. The elastic behavior was established using the ratio of elastic deformation energy (W_e) to the total deformation energy (W_{tot}) [398]:

$$\eta = \frac{W_e}{W_{tot}} \qquad \{4.1\}$$

The area enclosed by the loading curve and the maximum depth of penetration (area ABC) represents W_{tot}, and W_e is represented by the area DBC (figure 4.2).

Figures 4.3 and 4.4 present plots of η ratio and depth versus indentation load for dendritic and slightly harder interdendritic areas of Stellite 21 samples as shown in figure 3.2.

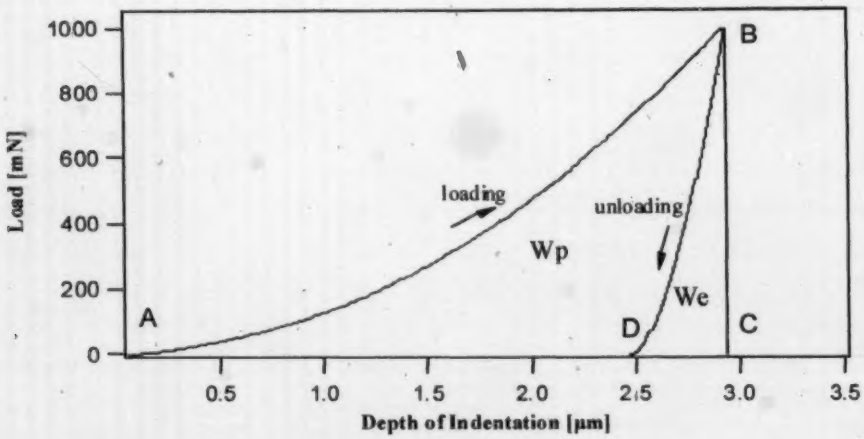

Figure 4.2: A load-depth curve from micro-hardness test.

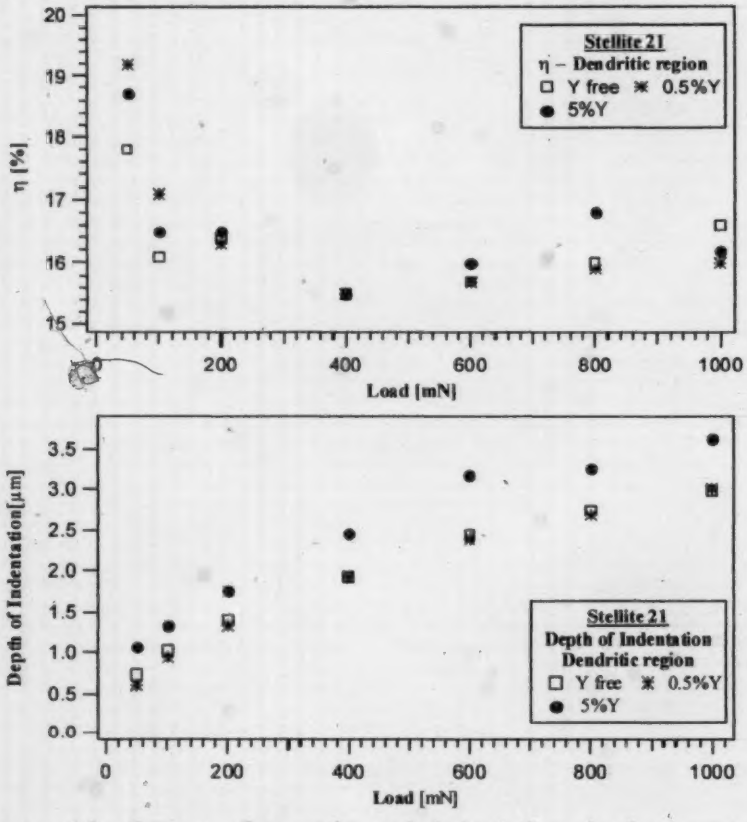

Figure 4.3: Curves of η ratio and indentation depth versus indentation load: Dendritic regions. Error range: ±5%.

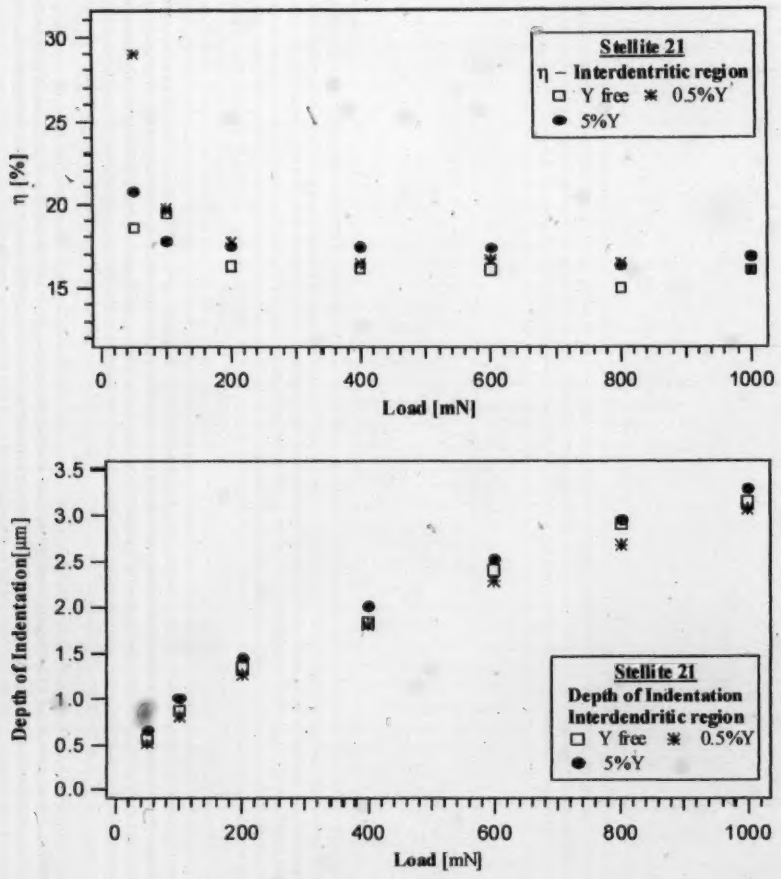

Figure 4.4: Curves of η ratio and indentation depth versus indentation load: Interdendritic regions. Error range: ±5%.

The local mechanical properties of various phases or domains in Stellite 712 samples were also evaluated using the micromechanical probe. Similar to Stellite 21, yttrium additions did not significantly modify the mechanical properties of these regions in the Stellite 712 samples as illustrated in figure 4.5.

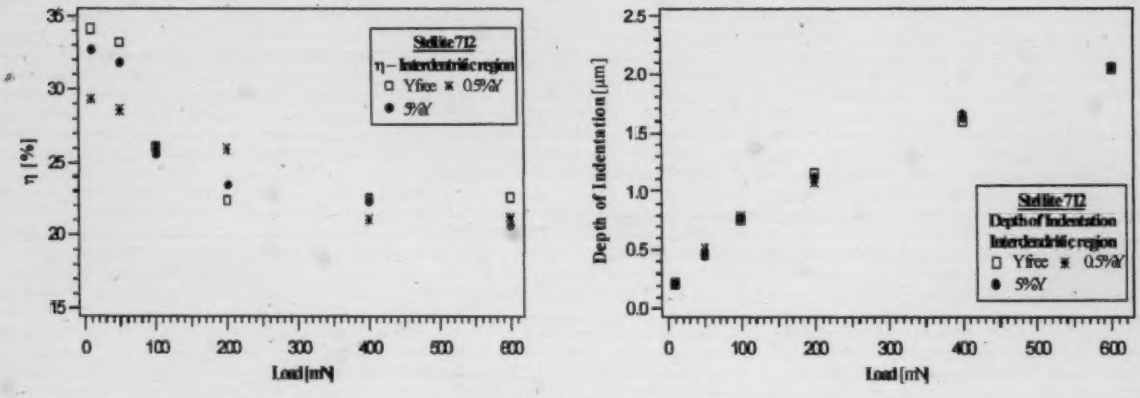

a)

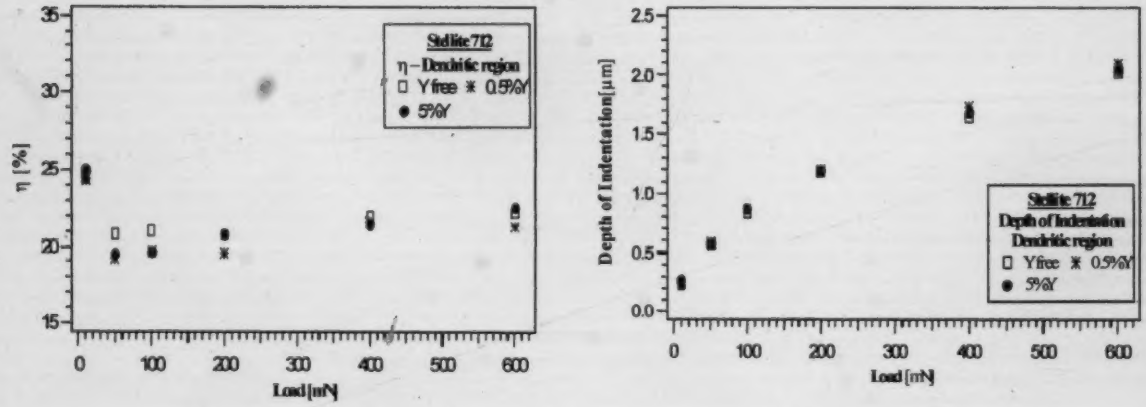

b)

Figure 4.5: Curves of η value and indentation depth versus indentation load: a) Interdendritic regions; b) Dendritic regions; Error range: ±5%.

4.2 Stress induced γ → ε transformation in Stellite 21 samples with and without yttrium addition

Deformed and un-deformed specimens were examined using the X-ray diffraction technique in order to check if the γ→ε transformation was induced by stress. Un-deformed specimens were polished using a 0.05 μm alumina slurry then etched in order to remove additional strain caused by polishing. The deformation was achieved by hammering, which was performed in the same manner to all samples. Statistically, the hammering effect should be the same to all samples. Macro-hardness (HRC) of the deformed specimens was also measured in order to determine the degree of strain hardening for all samples.

Figures 4.6, 4.7, and 4.8 respectively present X-ray diffraction patterns of deformed and un-deformed yttrium-free and yttrium-containing samples. Relative fractions of metastable γ phase (x), and ε phase (1-x) were estimated from integrated intensities, I, of $(10\bar{1}1)$ ε, and (200)γ peaks using the following equation [399]:

$$\frac{x}{1-x} = 1.5\frac{I^{fcc}_{200}}{I^{hcp}_{10\bar{1}1}} \qquad \{4.2\}$$

The quantitative analysis (Equation {4.2}) indicated that the fraction of ε phase in the stress-free specimens was 0.2 for the yttrium-free sample, 0.25 for the 0.5% yttrium-containing sample, and 0.3 for the 5% yttrium-containing sample, respectively. Those amounts are considerably less than the saturation level of 0.9 [384].

It is clear that athermal martensite was hard to generate under the present solidification conditions.

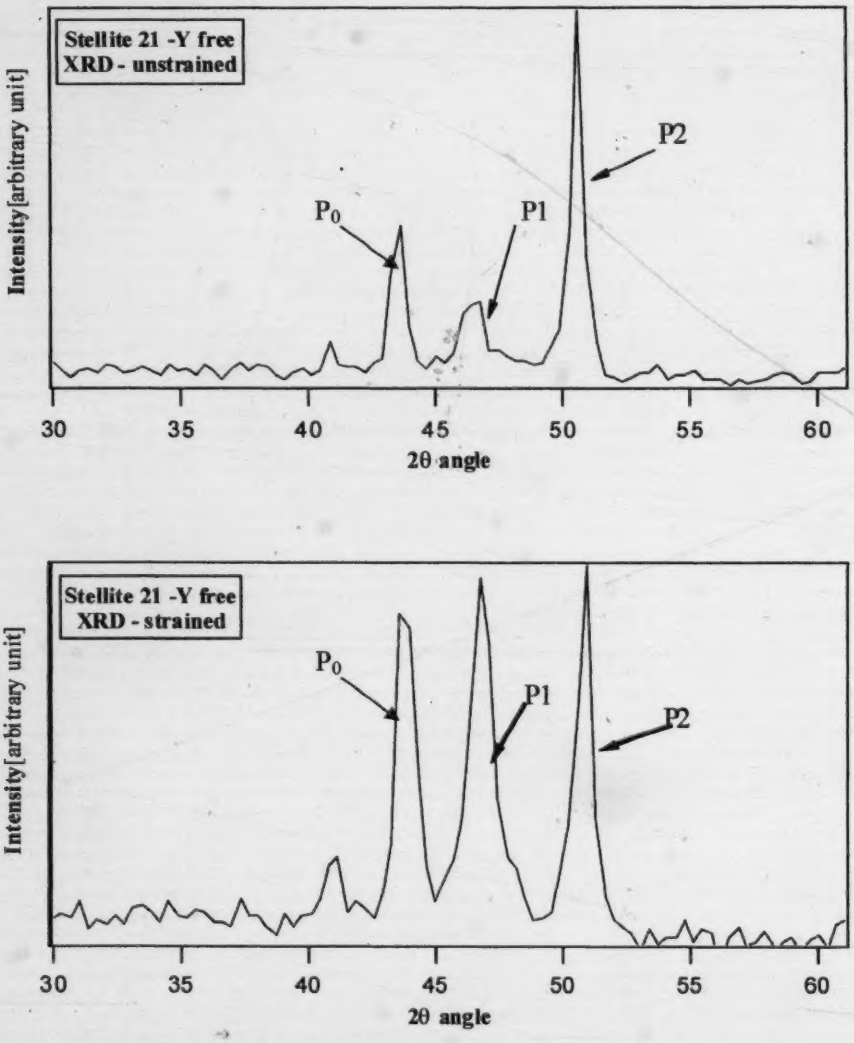

Figure 4.6: X-ray diffraction patterns of unstrained and strained Yttrium-free samples

P_0 – (002) ε, (511)$M_{23}C_6$, (002)Co_3Mo,

P_1 - (1011) ε, (400)$M_{23}C_6$, (201)Co_3Mo P_2 – (200)γ, (600)$M_{23}C_6$, (200)NiCrMo

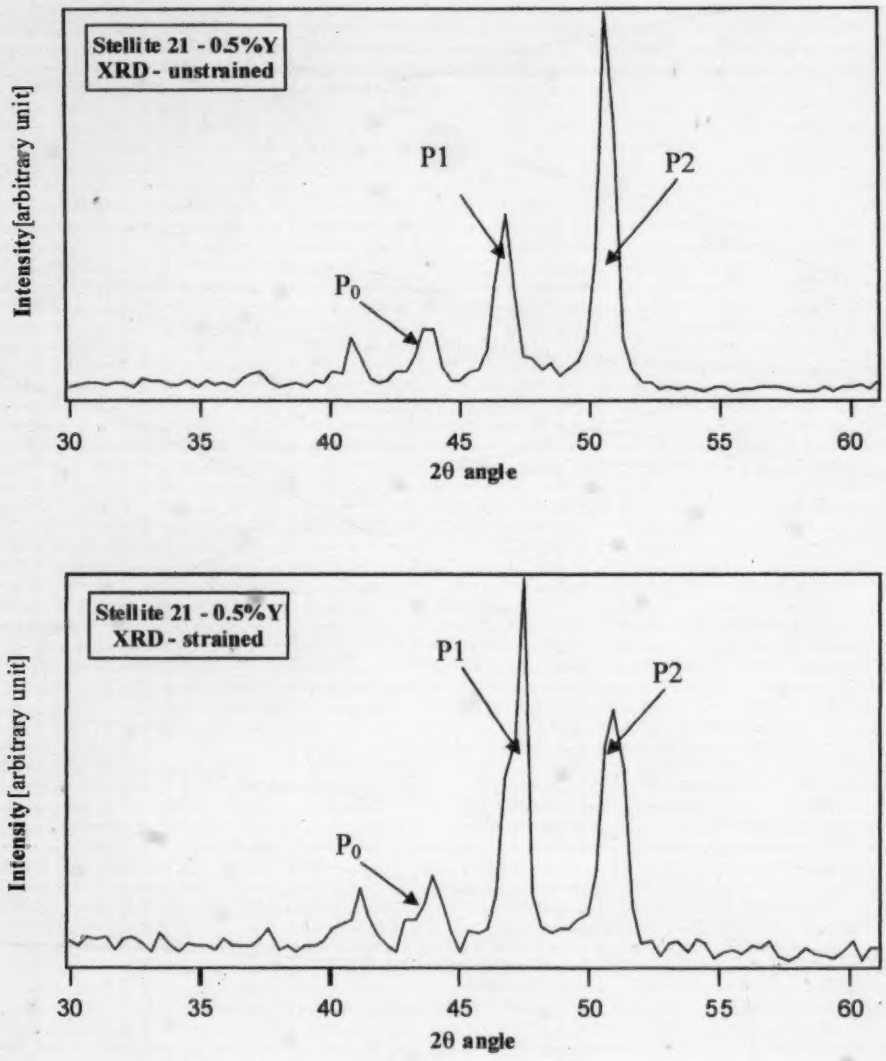

Figure 4.7: X-ray diffraction patterns of unstrained and strained 0.5% Yttrium-containing samples

P_0 – (002) ε, (511)$M_{23}C_6$, (002)Co_3Mo, (111)γ

P_1 - (10$\bar{1}$1) ε, (400)$M_{23}C_6$, (201)Co_3Mo P_2 – (200)γ, (600)$M_{23}C_6$, (200)NiCrMo

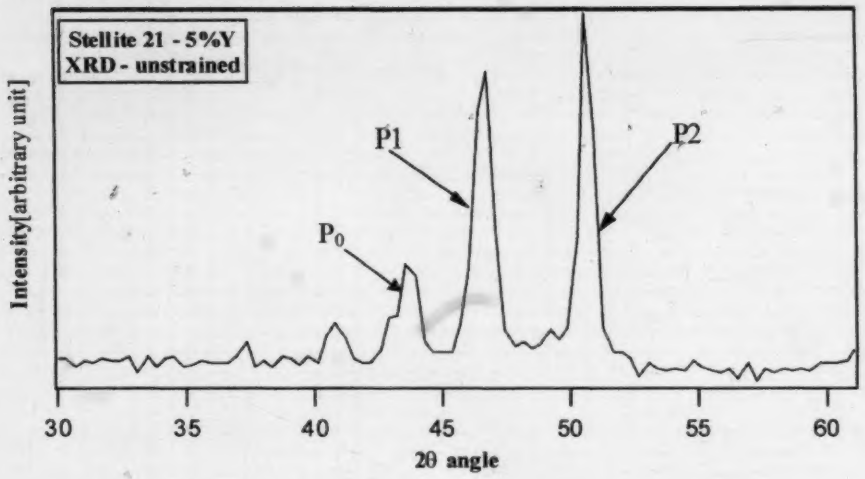

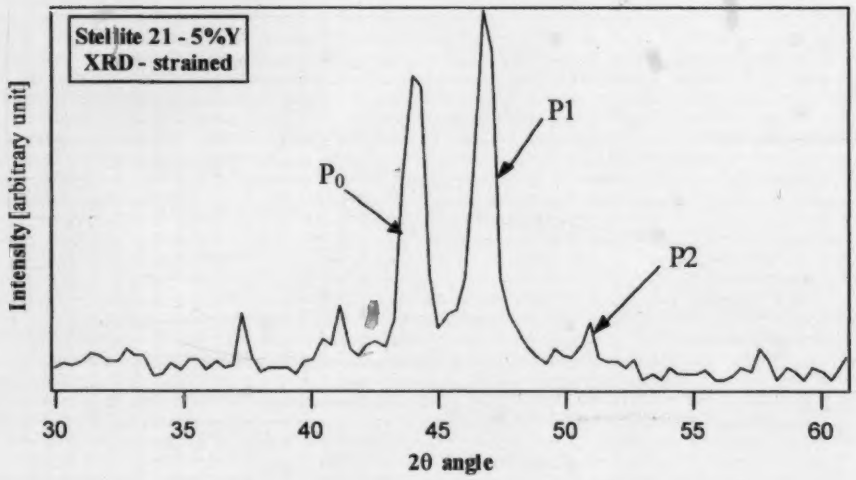

Figure 4.8: X-ray diffraction patterns of unstrained and strained 5% Yttrium-containing samples

P_0 – (002) ε, (511)$M_{23}C_6$, (002)Co_3Mo, (111)γ

P_1 - $(10\bar{1}1)$ ε, (400)$M_{23}C_6$, (201)Co_3Mo, (200)Co_2YSi_2

P_2 – (200)γ, (600)$M_{23}C_6$, (200)NiCrMo

The relatively medium cooling rate also created less favorable conditions for defects that could serve as nucleation sites of isothermal martensite during homogenization treatment. Development of defects (e.g., stacking faults) is known to be favored at high cooling rates [389] and stacking faults might serve as potential ε martensite embryos. However, the amount of athermal martensite is usually lower in fine grained materials and increases with increasing grain size [386]; thereby the lower ε phase amount on yttrium-free samples could arise from its finer microstructure when compared with the yttrium-containing samples.

The above results demonstrated that alloying yttrium did not significantly affect the ratio of the cobalt allotropes.

After deformation, the fraction of ε phase increased to 0.45 in the yttrium-free sample, to 0.51 in 0.5% yttrium-containing sample, and to 0.75 in the 5% yttrium-containing sample, respectively. The $\gamma \rightarrow \varepsilon$ transformation was induced in Stellite 21 by strain, and it appears that yttrium additions promoted the transformation. Such a transformation could improve the performance of the alloy when subjected to mechanical attack due to strain hardening and formation of ε phase with (0001) planes preferably oriented parallel to the worn surface which is easily shared during sliding wear [90,400].

Is should be pointed out that the changes in peak P_0 intensity could be influenced by texture induced by deformation. However, a strong texture may not be possible due to inhomogeneous hammering. Therefore, if the effect of texture existed, it should be minor or negligible.

The hardness of 5% yttrium containing sample increased from 37.4 HRC to 42 HRC caused by the deformation treatment, while that of the yttrium-free sample increased from 39.4 HRC to 41HRC. The trend was similar for the other yttrium-containing samples. It appeared that the yttrium-containing samples had a higher strain-hardening capability.

Although the difference in hardness between the deformed yttrium-free and yttrium-containing samples was small, the higher "strain hardening" capability with yttrium addition would benefit the wear resistance of the alloys.

5.0 EVALUATION OF OXIDE'S SCALE MECHANICAL PROPERTIES

This chapter report results of studies on the mechanical properties of the oxide's scales developed on yttrium-free and yttrium-containing Stellite 21 and 712 alloys after oxidation at elevated temperatures. The goal of the investigation is to collect experimental data for interpreting the influence of yttrium on the wear behavior of cobalt-based alloys. This chapter comprises three sections: (1) the oxide's scale mechanical properties; (2) the interfacial strength of the oxide/matrix interface, and (3) the phases developed in the oxide scale.

5.1 The mechanical behavior of the oxide scale

Stellite 21 and 712 samples with and without yttrium, respectively, were polished with a 0.05 μm alumina slurry and then heated in a furnace and oxidized in air at 600^0C for 20 minutes. The sample's dimensions were 15mm x 8mm x 6 mm. The hardness of oxide scales on yttrium-free and yttrium-containing samples were investigated (using a nano-mechanical probe (Hysitron, Minneapolis, USA) at room temperature after being oxidized at 600^0C. The nano-mechanical probe was a three-sided diamond pyramid (tip angle=90^0). The test was performed under several maximum loads (from 20 to 150μN) and corresponding load-depth curves were recorded. Hardness and elastic behavior of the oxide scales were determined from the curves and each reported value was an average of ten measurements. The smaller the indentation depth under a given maximum load, the harder is the material.

Figure 5.1 and 5.2 show load-depth curves of yttrium-free, 0.5% and 5% yttrium-containing samples of Stellite 21 and 712, respectively. Indentation depth and η values determined from the indentation test are presented in Table 5.1 and 5.2.

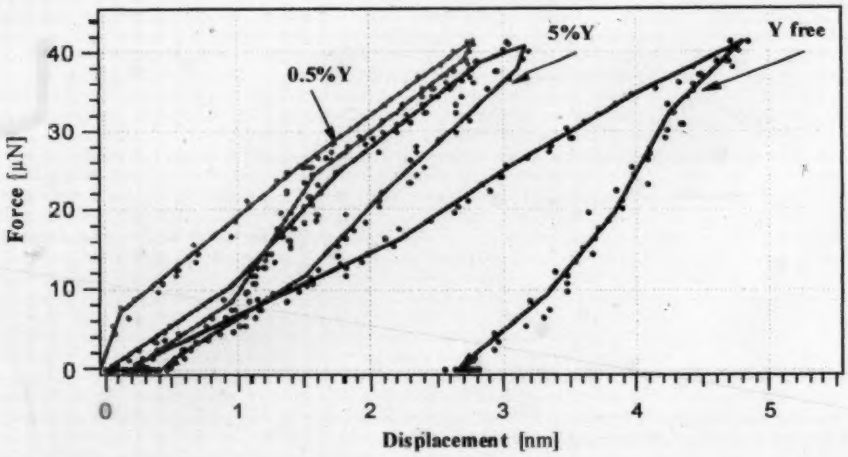

Figure 5.1: Nano-indentation curves of the oxide scales on Yttrium-free and Yttrium-containing samples of Stellite 21.

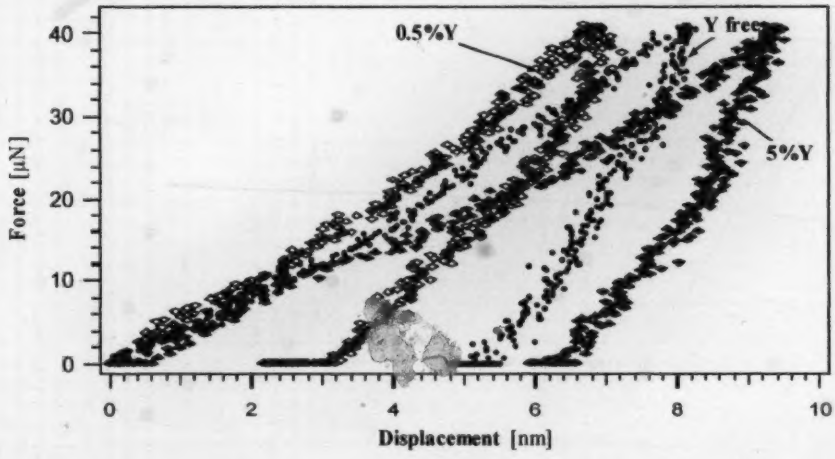

Figure 5.2: Nano-indentation curves of the oxide scales on yttrium-free, 0.5% and 5% yttrium-containing Stellite 712 samples, respectively.

Table 5.1: Mechanical properties of the oxide scale obtained from nano-indentation test (error range depth: ±0.4 nm, η: ±2%)

Material	**Maximum load** [μN]	**Maximum depth of indentation** [nm]	η [%]
Yttrium free Stellite 21	40	4.8	44.8
	80	6.7	46.5
	100	8.6	47.5
	150	11.6	43.7
Stellite 21 – 0.5%Y	40	2.8	66.1
	80	4.9	61.5
	100	6.1	63
	150	8.2	63.6
Stellite 21 – 1%Y	40	3.9	59.5
	80	6.6	58
	100	7.5	58.1
	150	10.2	57.4
Stellite 21 – 2%Y	40	3.2	64
	80	5.7	63
	100	6.7	61.3
	150	9.6	58
Stellite 21 – 5%Y	40	3.2	61
	80	6.3	56.4
	100	8.3	60.8
	150	11	56.5

Table 5.2: Mechanical properties of the oxide scale obtained from nano-indentation test (error range depth: ±0.4 nm; η: ±3%).

Material	**Maximum load** [μN]	**Maximum depth of indentation** [nm]	η [%]
Y-free Stellite 712	20	4.6	33.8
	40	8.4	31.0
	80	13.4	34.0
Stellite712– 0.5%Y	20	4.4	42.3
	40	6.8	40.0
	80	11.3	51.7
Stellite 712 – 1%Y	20	5.1	32.2
	40	7.0	34.2
	80	12.7	35.2
Stellite 712 – 2%Y	20	5.6	27.4
	40	9.5	22.4
	80	13.8	21.0
Stellite 712 – 5%Y	20	5.8	37.0
	40	9.4	32.0
	80	14.7	29.5

The oxide formed on the unmodified Stellite 21 sample was the softest with the largest indentation depth and the smallest η ratio, while the 0.5% yttrium-containing sample showed the best mechanical properties. The nano-indentation tests

demonstrated that the oxide scale developed on yttrium-containing Stellite 21 samples was harder and had higher η values.

Similar to that on Stellite 21, the oxide scale formed on the 0.5% yttrium-containing Stellite 712 was the hardest with the lowest indentation depth and the highest η value. However, high yttrium concentrations did not benefit the oxide scale of Stellite 712 in terms of hardness and η value as Table 5.2 and figure 5.2 illustrate.

5.2 Evaluation of the interfacial strength of the oxide/matrix interface

The interfacial strength at the oxide/matrix interface of the oxide scales developed on yttrium-free and yttrium-containing samples was investigated at room temperature (using a micro-scratch tester (Center for Tribology, Inc., Mountain View, CA, USA) after being oxidized at 600^0C for 20 minutes. The micro-scratch test was performed using a pyramidal tungsten carbide tip under a linear increasing load from 0 to 10 N. The tip was moved at a horizontal velocity of 0.05 mm/s. The electrical contact resistance (ECR) between the tip and the sample was monitored *in situ*. When the tip contacts an oxidized surface, at the beginning of the test, the electrical contact resistance is high because the oxide layer acts as an insulator. As the tip moves horizontally along the surface, under a normal load that is increased continuously, the oxide is broken when the load reaches a certain level. As a result, metallic contact is established between the tip and the substrate, leading to a drop in the electrical contact resistance. The first drop in the electrical contact resistance (ECR) corresponds to failure of an oxide scale. The critical load corresponding to the

ECR drop represents the critical force required to scratch off the surface oxide from the sample and is therefore a measure of the oxide adherence to substrate.

Figure 5.3 and 5.4 show results of micro-scratch test for yttrium-free, 0.5% and 5% yttrium-containing Stellite 21 and 712 samples, respectively. The results presented are the average of at least seven micro-scratch tests. The average error was ± 0.25 N. The yttrium-containing samples showed higher values of critical load than the unmodified sample. Same trend was observed also for 1 and 2% yttrium-containing samples.

The micro-scratch results indicated that the oxide scale developed on yttrium-containing specimens was quite adherent to the substrate compared with that on yttrium-free specimens. It should be pointed out that the scratch test is only a technique for qualitative evaluation of the interfacial strength since the scratch resistance is affected not only by the interfacial strength but also by the mechanical properties of the oxide scale.

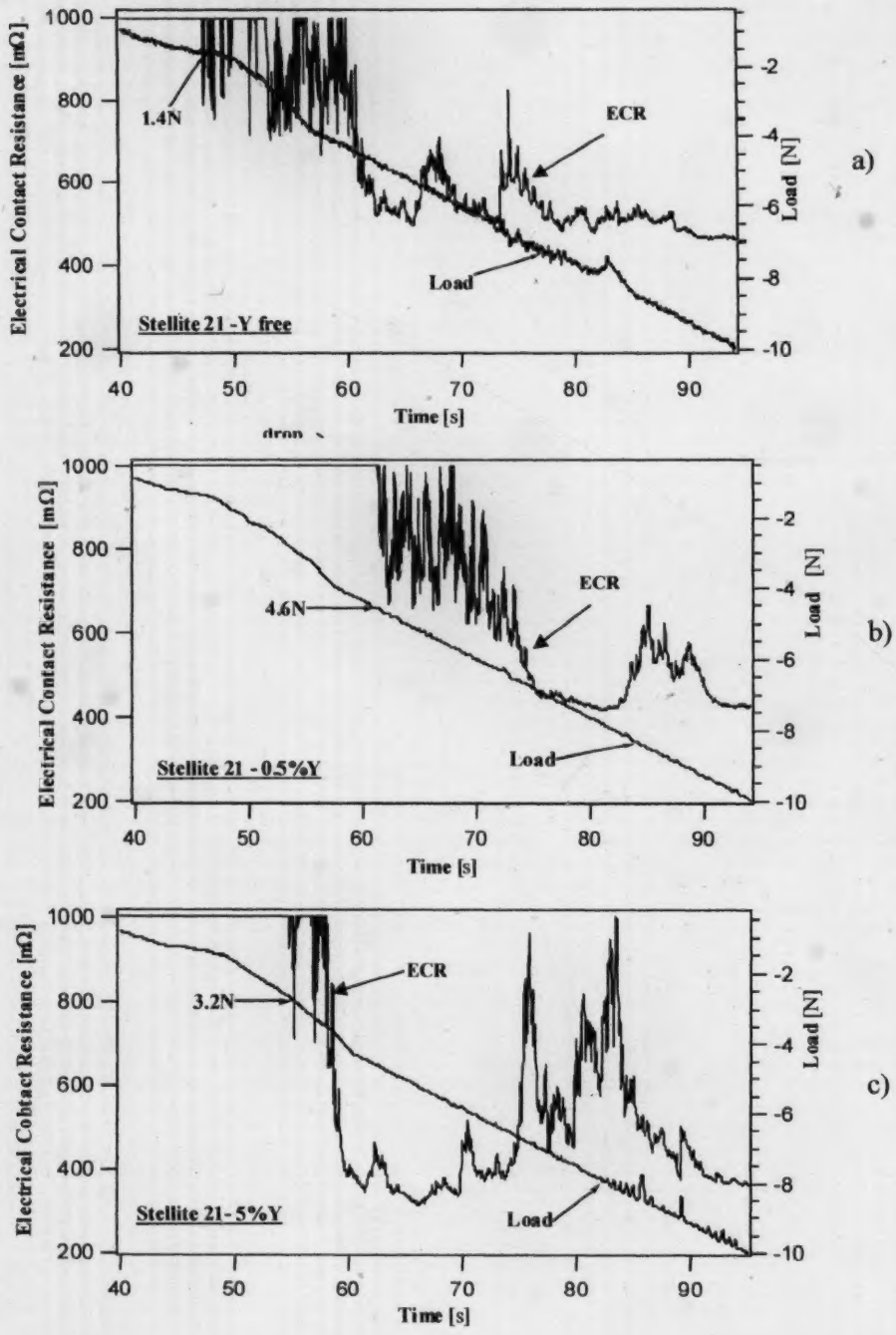

Figure 5.3: Micro-scratch test with *in situ* monitoring changes in electric contact resistance on Stellite 21 specimens: a) Yttrium free; b) 0.5%Y; c) 5%Y.

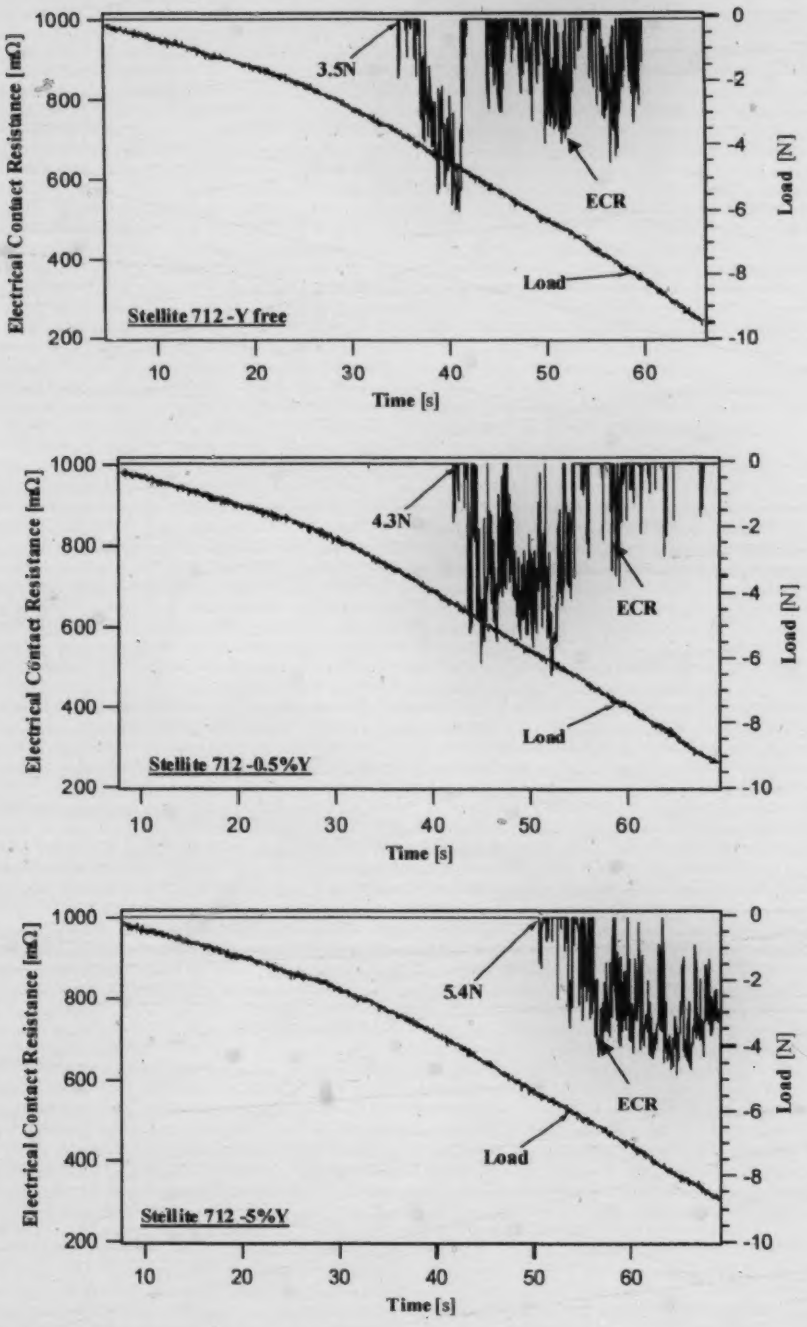

Figure 5.4: Micro-scratch test with *in situ* monitoring changes in electric contact resistance on Stellite 712 specimens: a)Yttrium-free; b) 0.5%Y; c) 5%Y.

5.3 Crystal structure of phases developed in the oxide scale

Structures of the oxide scales formed at 600^0C on different samples were investigated using the low incidence X-ray diffraction technique. The angle between X-ray and the sample surface was 2^o.

Figure 5.5 and 5.6 present low incidence X-ray diffraction patterns of oxide scales developed at 600^0C on yttrium-free, 0.5%, and 5% yttrium-containing Stellite 21 and 712 samples, respectively. The X-ray diffraction patterns for 1 and 2% yttrium-containing samples were similar to that of 0.5% yttrium-containing sample.

The main oxide phase developed on unmodified Stellite 21 was identified as Cr_2O_3. Several minor phases were identified including CoO, NiO, and $Mo_{17}O_{47}$. Other minor phases such as $CoMoO_4$, SiO_2, $CoMn_2O_4$, $CoMoO_3$, and $CoCr_2O_4$ could be present. These phases cannot be positively identified due to peak overlap. However, as shown in chapter 7, at longer oxidation periods, manganese and silicon rich oxides were observed in the oxide scale, as confirmed by SIMS analysis. The oxide scale grown on yttrium-containing samples contained an additional phase: Y_2O_3.

The oxide scale developed on yttrium-free Stellite 712 was formed mainly by Cr_2O_3. Possible minor phases were $Mo_{17}O_{47}$, and $CoMn_2O_4$. The oxide scale grown on the samples containing 0.5 and 1% yttrium did not have the cobalt-manganese oxide but contained a new phase: Y_2O_3. The presence of the yttria phase could be a reason why the oxide scale developed on 0.5 and 1% yttrium containing samples showed higher hardness.

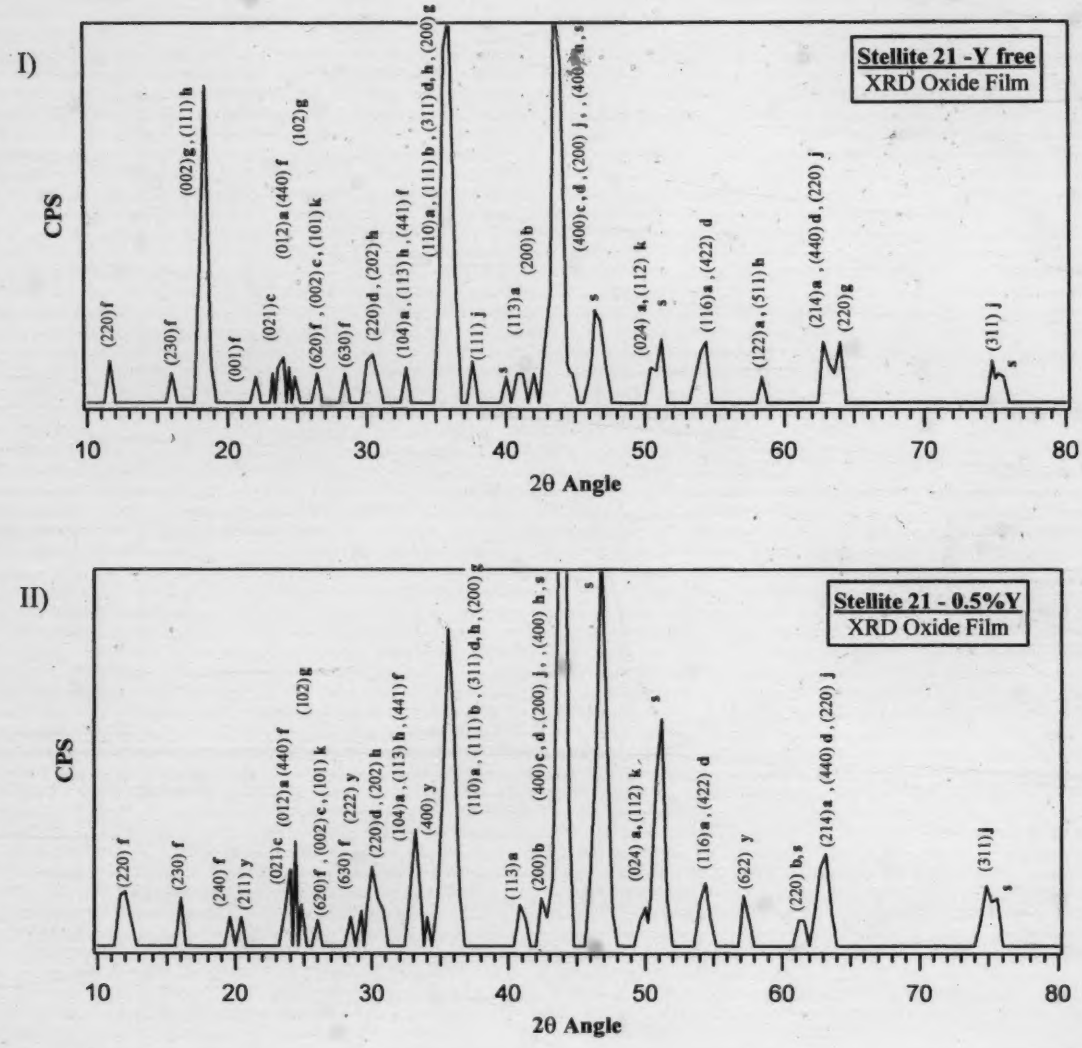

Figure 5.5: Low angle X-ray diffraction patterns of the oxide scales developed on: I) yttrium free; II) 0.5%Y; III) 5% yttrium-containing Stellite 21samples, respectively Where: **a** – Cr_2O_3; **b** – CoO; **c** – $CoMoO_4$; **d** – $CoCr_2O_4$; **f** – $Mo_{17}O_{47}$; **g** – $CoMoO_3$; **h** – $CoMn_2O_4$; **j** – NiO; **k** – SiO_2; **y** – Y_2O_3; **s** – substrate (CPS stands for counts per second).

III)

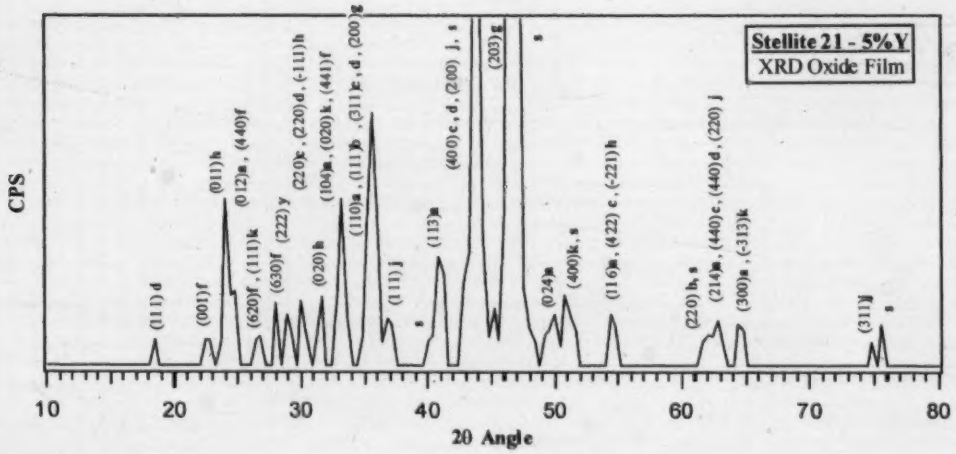

Figure 5.5 (continued):Low angle X-ray diffraction patterns of the oxide scales developed on: I) yttrium free; II) 0.5%Y; III) 5% yttrium-containing Stellite 21 samples, respectively

Where: **a** – Cr_2O_3; **b** – CoO; **c** – $CoMoO_4$; **d** – $CoCr_2O_4$; **f** – $Mo_{17}O_{47}$; **g** – $CoMoO_3$; **h** – $CoMn_2O_4$; **j** – NiO; **k** – SiO_2; **y** – Y_2O_3; **s** – substrate (CPS stands for counts per second).

Besides, the absence of the cobalt-manganese oxide could also be beneficial to the oxide scale. It has been reported that manganese is richer in the outer region of oxide scales on Cr-containing alloys [56,205,235,262,401].

It appears that the diffusion of manganese ions in chromia scales is much faster than chromium ions [402]. Consequently, if the diffusion of Mn is reduced possibly by the existence of large yttrium atoms, the Cr_2O_3 phase may thus take more volume fraction in the oxide scale, resulting in a stronger oxide scale.

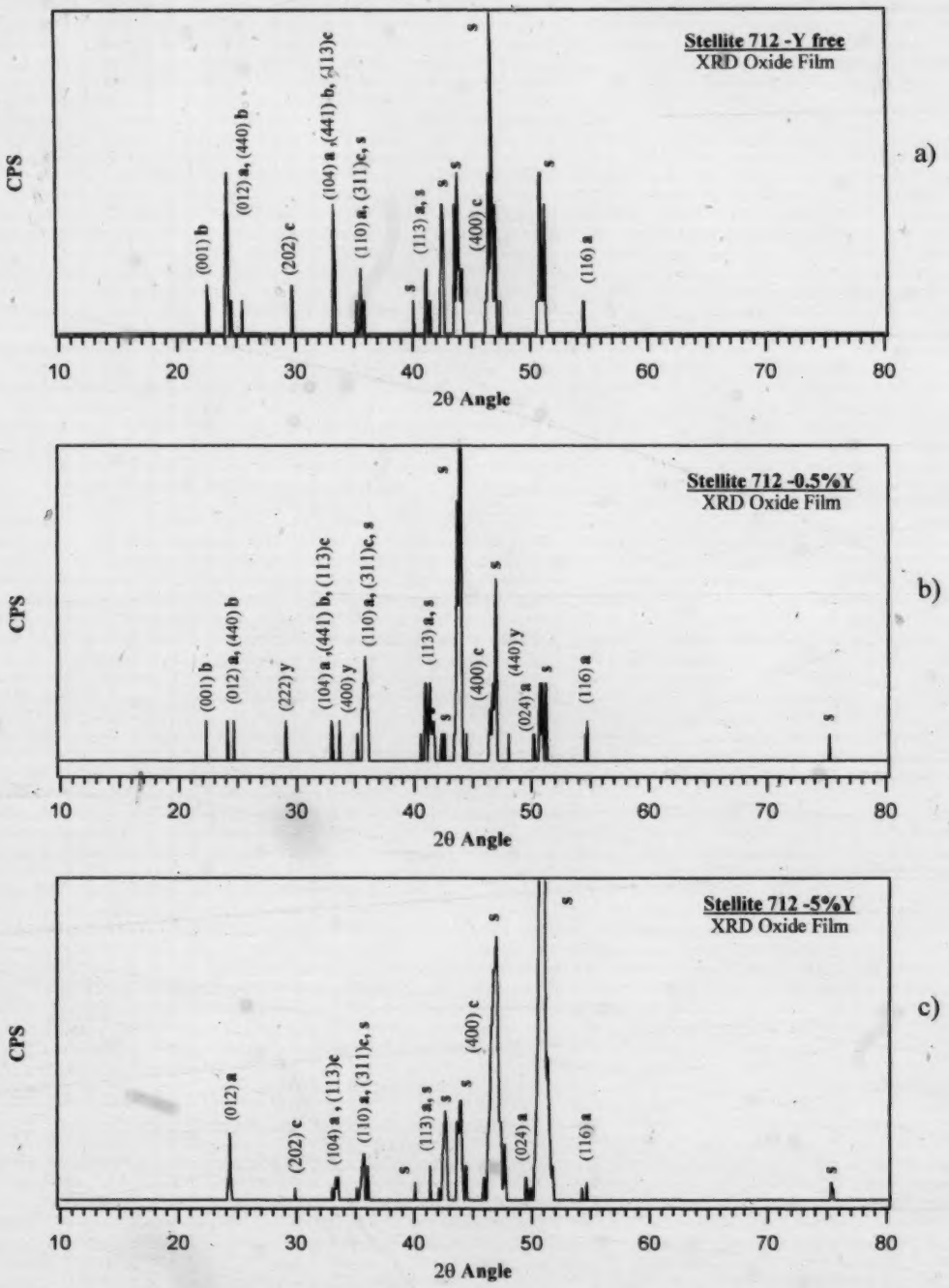

Figure 5.6: Low angle X-ray diffraction patterns of the oxide scales developed on: a) yttrium free; b) 0.5%Y; c) 5% yttrium containing Stellite 712 samples, respectively. a – Cr_2O_3; b – $Mo_{17}O_{47}$; c – $CoMn_2O_4$; y – Y_2O_3; s – substrate (CPS stands for counts per second).

However, Y_2O_3 phase as well as $Mo_{17}O_{47}$ were not detected in the oxide scales developed on 2 and 5% Y-containing specimens. The absence of $Mo_{17}O_{47}$ may be attributed to possible effect of yttrium on the diffusion of Mo into the oxide scale. It is unclear why Y_2O_3 phase was not detected in the oxide scales on specimens with 2 and 5% yttrium. It might be related to the enhanced interaction between Y and Mo, leading to the following two possible effects: 1) the enhanced interaction could also affect the migration of yttrium itself towards the oxide scale when Mo was blocked by yttrium in the surface region, and 2) the amount of Y_2O_3 particles in the oxide scale more likely be too small to be detected using XRD. Further studies are necessary in order to clarify this issue. Anyway, the absence of the yttrium and molybdenum oxide phases in the oxide scales developed on specimens containing 2 and 5% yttrium could explain their lower hardness.

6.0 WEAR BEHAVIOR

This chapter is focused on the evaluation of the wear performance of yttrium-free and yttrium-containing Stellite 21 and 712 alloys, from room temperature up to 600^0C. The purpose of this work is to investigate the effects of yttrium additions on the wear behavior. Chapter six comprises two sections: (1) the wear performance of yttrium-free and yttrium-containing samples from room temperature up to 600^0C; (2) how much an oxide scale contributes to the high-temperature wear resistance.

6.1 Wear performance of yttrium-free and yttrium-containing samples from room temperature up to 600^0C.

6.1.1 Stellite 21

Sliding wear tests were performed with a high-temperature pin-on-disc tribometer (CSEM Instruments, Neuchatel, Switzerland). The disc was the sample under study (15x8x5 mm) and the pin was an alumina ball with its diameter equal to 6 mm. The counterface was chosen to be a ceramic material because at the testing temperatures used for this study its mechanical properties will not be changed. Also, alumina has a high hardness; thereby, it was expected that it would not be significantly worn during the tests. All tests were performed at a sliding speed of 1 cm/s along a circle path of 0.8 mm in radius under a normal load of 2 N. Prior to each wear test the surface of specimens was polished using 6μm-diamond paste.

The volume loss was determined by measuring the profile of wear track using a contact profilometer (Tencor Instruments, USA). Figure 6.1 shows the average wear rate versus temperature under a normal load of 2 N for 4000 laps. All samples reached wear maxima around 200^{0}C followed by a decrease and then an increase in the wear loss as the temperature was continuously raised. The wear loss of the yttrium-free Stellite 21 sample was the greatest at all temperatures. The difference in the wear volume between yttrium-free and yttrium-containing samples became more obvious at higher temperatures.

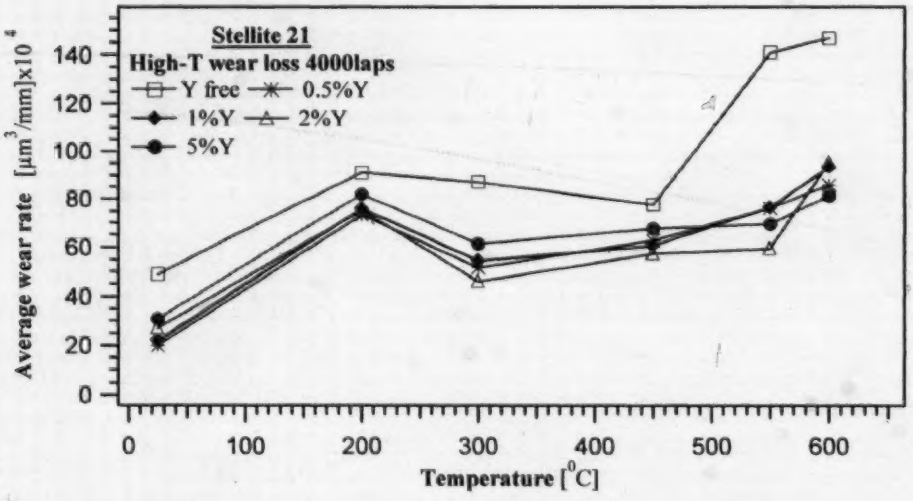

Figure 6.1: Wear loss with respect to temperature of Stellite 21 samples with and without yttrium. Error range:±10[μm^3/mm]x10^4.

Reflected light microscopy and SEM were used to observe morphologies of worn surfaces. EDS was used to determine the local chemical composition of the worn surfaces. Figure 6.2 illustrates optical micrographs of wear tracks on the

samples after sliding wear tests at 600^{0}C for 4000 laps. The yttrium-free Stellite 21 sample showed larger (broader and deeper) wear tracks compared with the yttrium-containing samples as proved also by profilometer measurements.

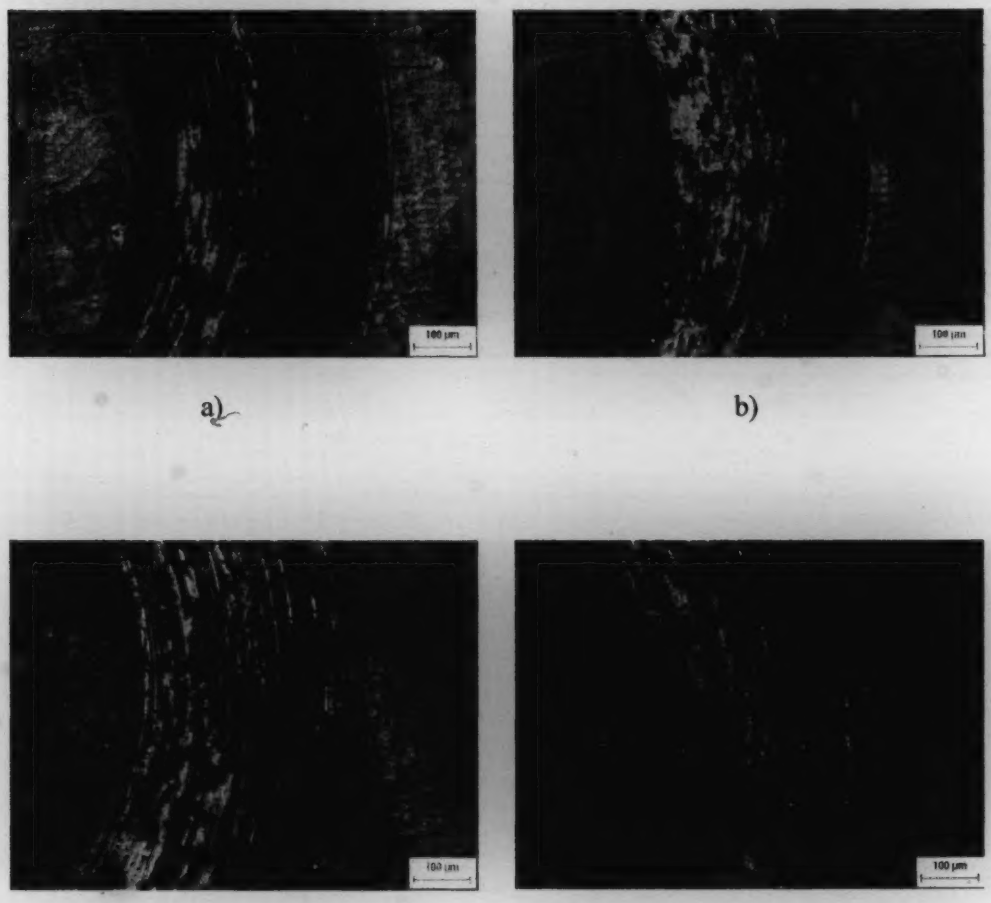

a) b)

c) d)

Figure 6.2: Micrographs of wear tracks at 600^{0}C – 4000 laps: a) Yttrium-free; b) 0.5%Y; c) 1%Y; d) 5%Y – containing Stellite 21 samples.

After sliding at elevated temperatures, glaze layers with a shiny and smooth appearance were observed on the worn surfaces. Such glaze layers formed not necessarily at high temperature; it was observed that the glaze formed even on a surface worn at 150^{0}C. The EDS analysis indicated that the glaze layers formed on the worn surfaces were heavily oxidized. The composition of the glaze layers was similar to that of the alloy but contained oxygen. Distribution of the glaze was not uniform over the wear track; some portions of the wear track did not retain any glaze layer (figure 6.3 a). At 600^{0}C the glaze layer was more compacted and covered more areas (figure 6.3 b). It appeared that the wear debris particles were agglomerated and compacted under the external force to form the glaze layer (figure 6.3 c).

Mechanical properties of glaze formed during wear at elevated temperatures were assessed at room temperature using a micro-mechanical probe (Fisher Technology Ltd., Winsor, CT, USA) under a maximum load of 5 mN. The results demonstrated that yttrium did not influence either the mechanical properties or the coverage of the glaze layer.

The decrease of wear loss in the temperature range from 200 to 450^{0}C could be attributed to the formation of oxide scale and a compacted glaze layer. When the temperature exceeded about 450^{0}C, the wear rate increased again probably due to increased softening of the matrix, which could not effectively support the protective oxide scale and the glaze layer.

It was demonstrated that the presence of yttrium, particularly at the 0.5% level, markedly enhanced the high-temperature wear performance of Stellite 21, especially at temperatures above 500^{0}C. Yttrium did not significantly alter the bulk

mechanical properties of Stellite 21 as well as the mechanical properties or the coverage of the glaze layer; thereby, the wear resistance of Stellite 21 at elevated temperatures was improved only through the positive effect of yttrium on the oxide's mechanical properties and its adherence to the substrate.

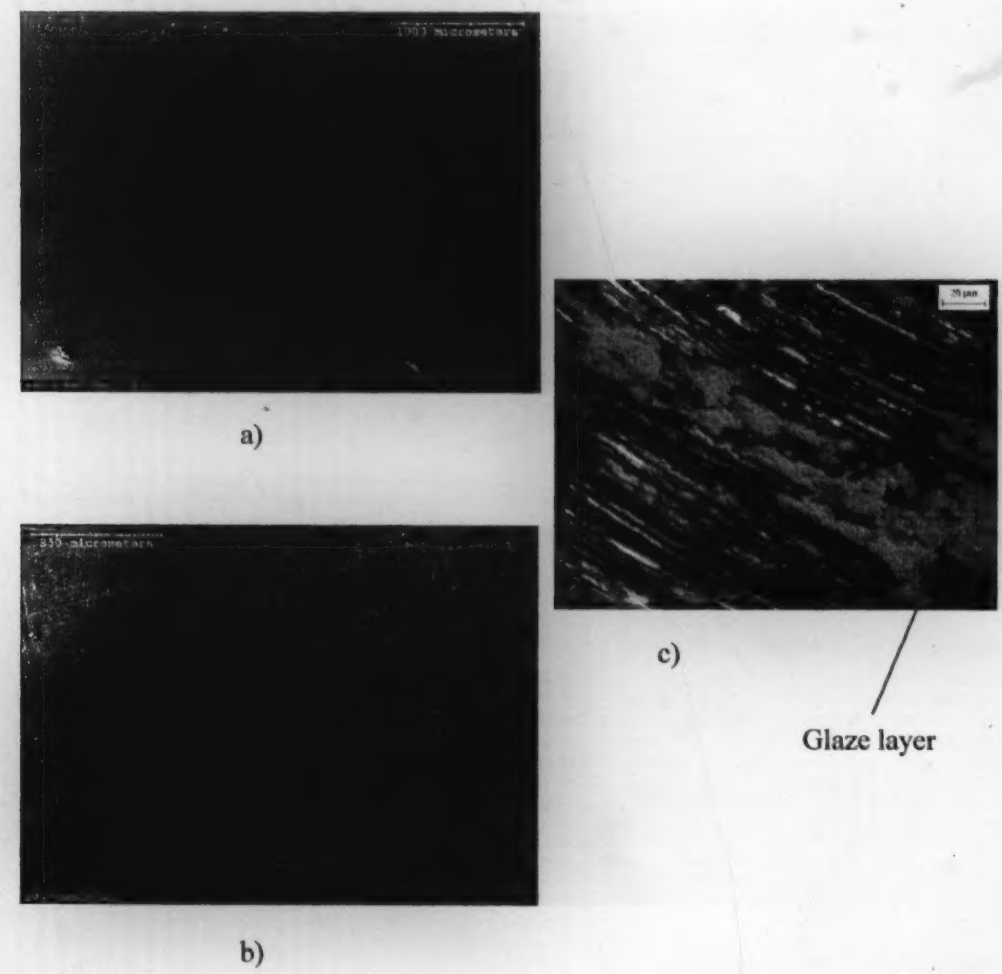

Figure 6.3: Morphology of wear track on sample after sliding for 2000 laps at: a) 150^0C – 0.5%Y; b) 600^0C – 2%Y; c) 600^0C – 2%Y a closer view

At higher temperatures, the diffusion of yttrium to grain boundaries could inhibit the outward diffusion flux of chromium ions and favors inward diffusion of oxygen ions [39, 403]. The inward diffusion of oxygen ions may benefit the oxide's mechanical properties (due to the growth of a fine-grained oxide scale containing the Y_2O_3 phase –see chapter 7) and the oxide adherence to substrate (probably due to the inhibition of vacancy coalescence at the metal-scale interface, and formation of oxide pegs at the interface as will be discussed in chapter 7). Yttrium could also reduce the thickness of oxide scale thus minimizing the interfacial stress and further benefiting interfacial bonding (see chapter 7).

The glaze layer may help enhance the wear resistance of Stellite 21. The composition of the glaze layer was similar to that of the alloy but it contained oxygen. EDS did not detect yttrium in the glaze layer. This implies (besides the unaffected mechanical properties of the glaze) that yttrium did not affect the mechanical behavior of the glaze layer.

It must be pointed out that yttrium had also a small positive influence on the wear behavior at room temperature. This might not be attributed to the positive effects of yttrium on the oxide scale which is too thin to withstand mechanical attack and significantly affect wear rate. Examination of the worn surfaces has shown the presence of a debris film that may cover up to 30% of the worn surface (figure 6.4). EDS analysis revealed that the composition of the debris layer was similar with that of the glaze layer developed at elevated temperature but the oxygen content was much lower. It could be considered that the debris layer consisted of a mixture of metallic and oxidized debris.

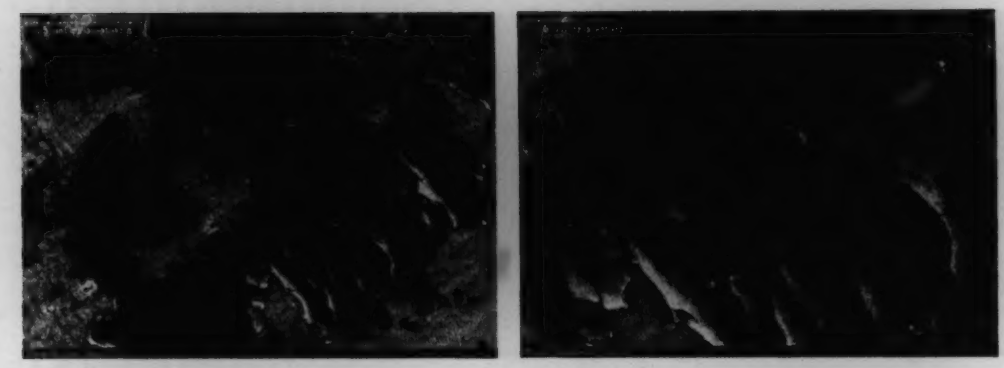

a) b)

Figure 6.4: Morphology of wear track after sliding wear at room temperature: a) 2%Y, b) detailed view showing wide spread cracking of the debris layer.

The presence of oxidized debris at room temperature may arise due to frictional heating as detailed in chapter two. However, large loads and sliding speeds (order of m/s) are usually needed for the above condition to occur [128]. It is unlikely that the surface temperature generated during sliding testing at low loads and sliding speeds is significantly higher than room temperature [404]. As a result, tribochemical reaction should be mainly a consequence of mechanical factors rather than frictional heating. Under sliding wear, chemical reactions could proceed much faster than under static conditions [405,406]. For example, the activation energy of formation of spinel oxide $Fe(Fe_{2-x}Cr_x)O_4$ on a 316 stainless steel markedly decreased when sliding wear was performed [407]. Also, plastic deformation and fragmentation of worn debris induce numerous defects, a larger number of broken chemical bonds and a large surface to volume ratio, which may favor the oxidation process.

However, the coverage of the debris layer over the worn surface was similar for all the samples, with and without yttrium. The debris layer may not account for the observed wear loss difference at room temperature. Micro-indentation tests under a maximum load of 25 mN have shown that the worn surfaces were strain hardened but no discernable difference was observed between yttrium-free and yttrium containing samples as the worn surface properties were heterogeneous.

One possible reason to explain the small difference in the wear volume loss between yttrium-free and yttrium-containing samples is the effect that yttrium might have on promoting the $\gamma \rightarrow \varepsilon$ transformation under mechanical loading as shown in chapter 5. Such a transformation could improve the performance of the alloy when subjected to mechanical attack due to formation of ε phase with (0001) planes preferably oriented parallel to the worn surface which are easily shared during sliding wear [91,400].

6.1.2 Stellite 712

Sliding wear tests of Y-free and Y-containing Stellite 712 samples were performed at room temperature and at 600^0C, respectively. The wear tests showed that the alloyed yttrium did not affect the wear behavior at room temperature, mainly because the microstructure and mechanical properties of the alloy were not modified by the yttrium addition. However, the situation changed at elevated temperatures. Figure 6.5 illustrates average wear rates (from at least two tests) of Y-free and Y-containing specimens at 600^0C.

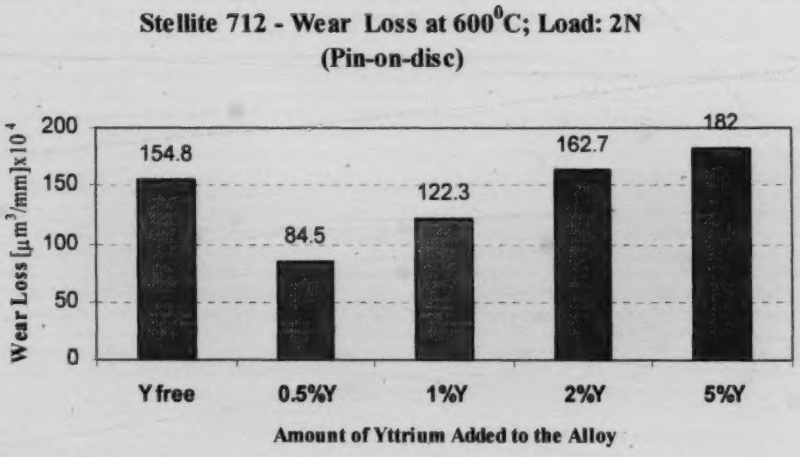

Figure 6.5: Average wear rate of yttrium-free and yttrium-containing Stellite 712 samples at 600^{0}C (error range:± 8[μm^3/mm]x10^4).

As shown, the presence of small amounts of yttrium, particularly at 0.5% level, considerably enhanced the high-temperature wear performance of Stellite 712. The improvement in wear performance could be mainly attributed to improved oxidation behavior. The oxide scales on 0.5% and 1%Y-containing specimens were more protective than that developed on Y-free specimen as the nano-indentation and micro-scratch tests demonstrated. This is consistent with the results on Stellite 21.

However, when a larger amount (e.g., 2 or 5%) of yttrium was added to the alloy, the wear performance was negatively influenced. In this case, the hardness of the oxide scale was reduced as the nano-indentation test demonstrated, although its adherence to substrate was improved. As a result of the decrease in hardness, the oxide scale may not effectively withstand the wearing force, leaving larger bare

metal surface area under oxidation attack. Furthermore, the oxide scale developed on specimens containing more yttrium could be less homogeneous and rougher than oxide scales developed on Y-free specimen and those containing a small amount of yttrium (see chapter 7). A rough and less homogeneous oxide scale with possibly higher residual stress due to lower homogeneity would experience larger stress concentration when in contact with a counterface. As a result, the probability of failure could be higher when the surface is subjected to wear attack.

It should be indicated that the improved high-temperature wear resistance by yttrium is unlikely to be attributed to possibly improved high-temperature strength of bulk material. As demonstrated, yttrium did not affect mechanical properties of the bulk material at room temperature even with the formation of a new second phase (Co_2YSi_2) when the yttrium content was high enough. If the new second phase can help to maintain the material strength to elevated temperatures, one may expect that the sample containing the highest yttrium content (5%) would perform the best. However, such phenomenon was not observed. Therefore, the enhanced oxide scale should play a main role in improving the high-temperature wear performance of Y-containing Stellite 712.

Figure 6.6 illustrates optical micrographs of wear tracks on the Y-free and 0.5% Y-containing samples after sliding wear tests at 600^0C. After sliding at elevated temperatures, no glaze layer was observed on the worn surfaces. As a result, the improvement in the wear behavior of Stellite 712 with a small amount of yttrium mainly results from the positive effects of yttrium on the mechanical behavior of the oxide scale and its adherence to the substrate.

a) b)

c)

Figure 6.6: Micrographs of wear tracks (wear at 600^0C) on Stellite 712 specimens: a) yttrium-free; b) 0.5%Y; c) yttrium-free – a closer view. No glaze layer was observed on both samples.

6.2 The role of oxide scale in resisting wear at elevated temperatures

The emphasis of this study was put on the role of oxide scale in resisting high-temperature wear and the efficiency of alloying yttrium in reducing wear of

Stellite 21 at elevated temperatures. To achieve this goal, wear tests were performed for yttrium-free and yttrium-containing Stellite 21 samples at elevated temperatures in air and in an argon environment with an argon flow (10 liter/min), respectively. Sliding wear tests were performed on a high-temperature pin-on-disc tribometer. The same experimental setup, as presented in chapter 6.1, was used to perform wear tests. All tests were performed at a sliding speed of 1 cm/s along a circular path of 0.8 mm in radius under three normal loads of 2 N, 5 N and 10 N, respectively.

Figure 6.7 shows wear volume losses of the samples at 200^0C under a normal load of 2 N for 2000 laps, in argon and in air, respectively.

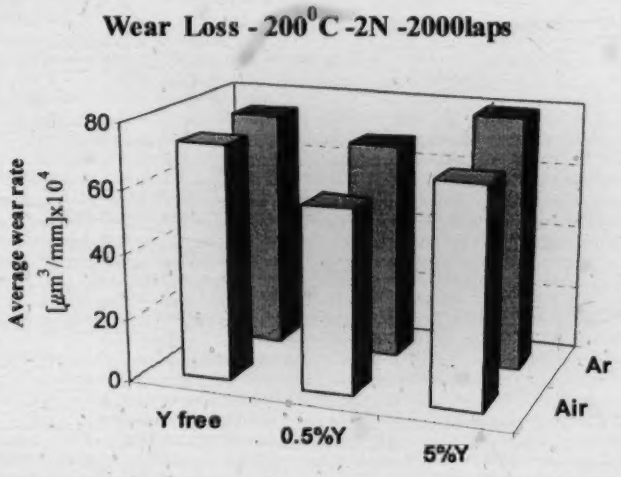

Figure 6.7: Average wear rate at 200^0C under a load of 2N after sliding for 2000 laps in air and in argon, respectively.

The wear losses were determined from the profile of wear tracks using a profilometer. As shown, the yttrium-containing samples showed higher wear loss in the argon environment than in air. Since the oxide scale on yttrium-containing

samples is more protective than that on yttrium-free sample as the nano-indentation and the micro-scratch tests demonstrated, it is understandable why the yttrium-containing samples had less wear loss in air than in argon. In air, the stronger oxide scale on the yttrium-containing samples enhanced the [redacted]ance of the alloy to wear. In the argon environment, the oxide formation was suppressed and this decreased the difference in wear loss between yttrium-free and yttrium-containing samples. This phenomenon is more obvious when the wear tests were performed at higher temperatures, e.g., 600^0C as shown in figure 6.9 and discussed later.

Figure 6.8 illustrates optical and scanning electron micrographs of wear tracks on 0.5% yttrium-containing and yttrium-free samples after sliding wear tests at 200^0C under a normal load of 2 N for 2000 laps. A glaze layer with a shiny appearance was observed on all worn surfaces after sliding at 200^0C in air (e.g. figure 6.8a). Such a glaze layer began to form soon after the test was started. It appeared that the wear debris particles agglomerated and compacted under the external force to form the glaze layer. The EDS analysis indicated that the glaze layer formed on the worn surfaces was heavily oxidized. The glaze layers had a composition similar to that of the alloy but contained oxygen. Distribution of the glaze was not uniform over the wear track (figure 6.8a). Little glaze formed when the test was performed at 200^0C in argon (figure 6.8b). The worn surface was relatively smooth and covered by small islands of contaminant layer that contained partially oxidized fine worn debris (figure 6.8c,d). The above observations indicate that oxidation occurred on the sample surface in air, while in the argon environment oxidation was suppressed to a large degree. As a result, the yttrium-containing

samples, mainly due to their enhanced oxide scales, shown improved wear performance; 0.5% yttrium additions resulted in the most positive effect on wear resistance. However, too much yttrium added to the alloy reduced the benefit because of the formation of a yttrium-containing phase (Co_2YSi_2) which appeared to negatively affect wear resistance [85].

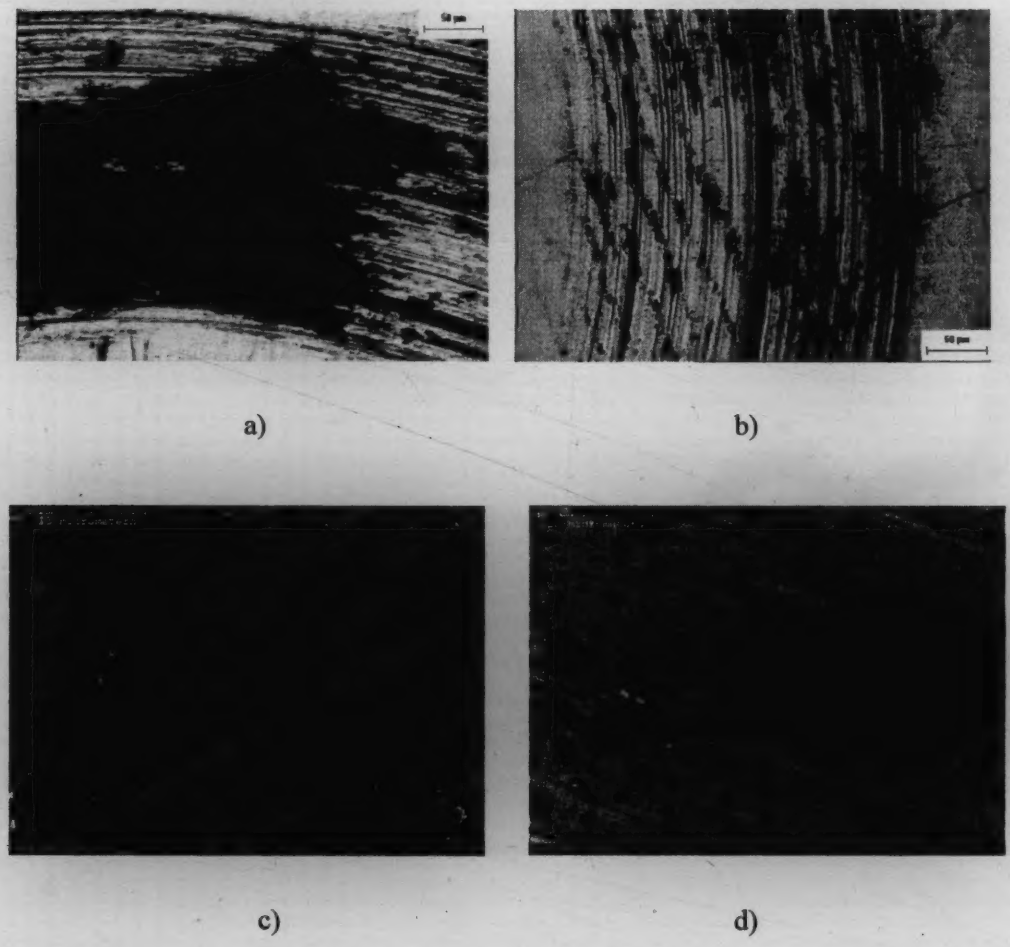

a) b)

c) d)

Figure 6.8: Morphology of wear track on samples after sliding for 2000 laps at 200^0C: a) 0.5%Y in air; b) 0.5%Y in argon; c) Yttrium free in argon (SEM); d) 0.5%Y in argon (SEM).

The glaze layer may also play a role in resisting wear, since it more or less helps to withstand the wearing force as well. Mechanical properties of glaze layers formed on worn samples during wear were assessed using a micro-mechanical probe under a maximum load of 5 mN. No difference in mechanical properties was observed between glaze layers, respectively on yttrium-free and yttrium-containing samples. EDS did not detect yttrium in the glaze layer. This implies that yttrium did not affect the mechanical behavior of the glaze layer but it might influence its adherence to the substrate.

Figure 6.9 shows the wear average wear rates from at least two tests, of yttrium-free, 0.5%, and 5% yttrium-containing samples at 600^0C under a normal load of 2 N for 10000 laps in argon and in air, respectively.

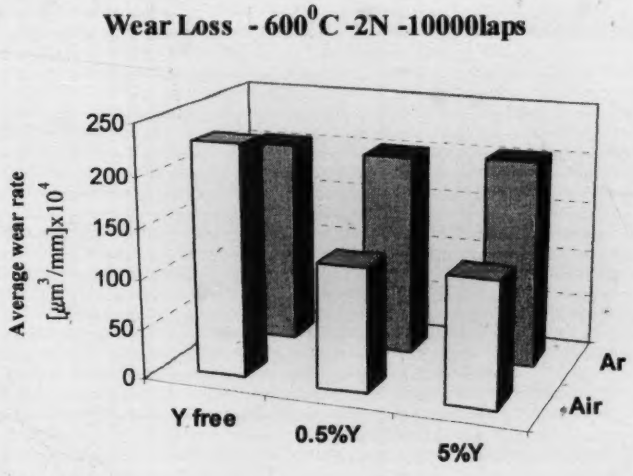

Figure 6.9: Wear loss at 600^0C under a load of 2N after sliding for 10000 laps in air and in argon, respectively.

At the higher temperature, oxidation was promoted. In this case, the wear loss of the yttrium-free Stellite 21 sample was higher in air than in argon while the wear losses of yttrium-containing samples, whose oxide scales were stronger, showed more wear loss in an argon atmosphere than in air. The difference in wear loss between yttrium-free and yttrium-containing samples in air was much larger than that at 200^0C, implying that the benefit of yttrium to the oxide scale and thus to the wear resistance of Stellite 21 were greater at higher temperatures. In addition, the small difference in wear loss between yttrium-free and yttrium-containing samples in argon and the observed larger decrease in wear loss of yttrium-containing samples in air clearly demonstrated the positive role of the strengthened oxide scale by yttrium in resisting wear at elevated temperatures involving oxidation.

However, the oxide scale did not always function. This was demonstrated by wear tests under higher loads. Figure 6.10 shows volume losses of yttrium-free and yttrium-containing samples at 600^0C under a normal load of 5 N for 10000 laps in argon and in air, respectively.

Under the higher load, all samples showed larger wear loss in air than in the argon environment. Similar to the oxide scale, the glaze layer did not function either. Under the higher load, the glaze layer was not able to withstand the wearing force and was removed from the rubbing surfaces leaving fresher metal surface under oxidation attack. The cycle of oxidation – oxide removal - reoxidation accelerated the wear loss. However, in the argon environment less oxidation reduced the synergism of wear and oxidation and thus minimized the wear loss. In addition, the glaze formation was also diminished, which could further decrease the wear loss.

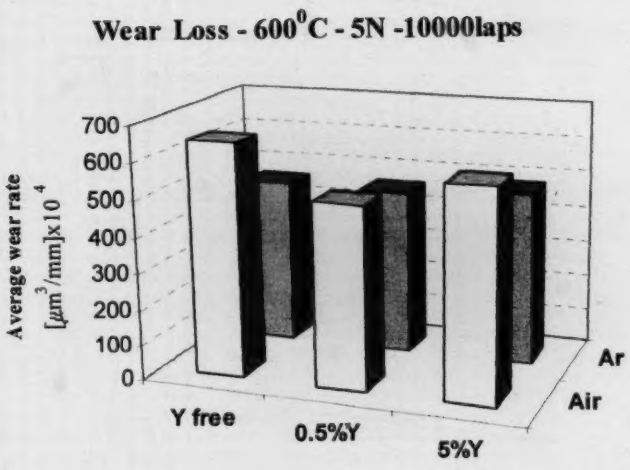

Figure 6.10: Average wear rate at 600^{0}C under a load of 5N after sliding for 10000 laps in air and in argon, respectively.

However, yttrium still benefited the alloy against wear damage in air, since the improved mechanical properties and higher adherence of the oxide scale on the yttrium-containing samples helped to withstand the wearing force, leading to lower wear rates.

When sliding wear was performed in argon, there was little difference in wear losses among yttrium-free and yttrium-containing samples because of less oxidation. This provides another evidence for the positive role of oxide scale in resisting wear.

Figure 6.11 shows volume losses of yttrium-free and yttrium-containing samples at 600^{0}C under a normal load of 10 N for 3000 laps in argon and in air, respectively. At very larger loads (10 N) the effect of oxide scale on high temperature wear is minimal. This is also proved by the larger wear loss in air than in

the argon environment. The wear behavior was similar with that observed at 5 N but at larger loads the beneficial effect of yttrium on oxide scale mechanical properties do not benefit the wear rates as the oxide layer cannot withstand the applied load and is easily removed from the surface. This is proved by the little difference in wear losses among yttrium-free and yttrium-containing samples, both in air and in argon environment.

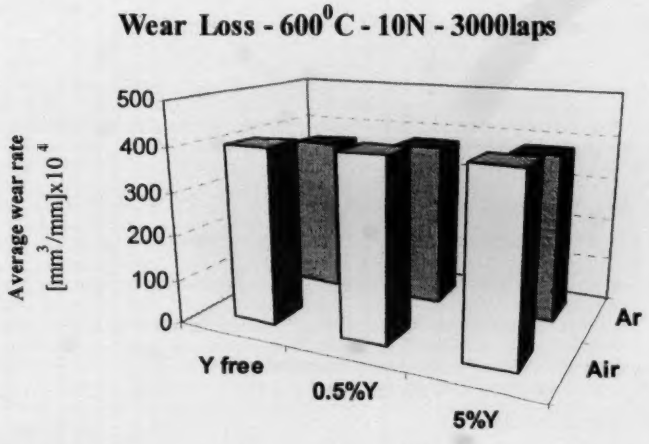

Figure 6.11: Wear loss at 600^{0}C under a load of 10N after sliding for 3000 laps in air and in argon, respectively.

It is clear that there exists a critical load above which the oxide layer has little influence on the wear rates. At lower loads than the critical one, enhancing the properties of the oxide layer will markedly improve the wear behavior.

In order to obtain more general information, the critical contact stress above which the oxide scale had little influence on the average wear rates was estimated.

Before the oxide scale is damaged, the contact between the pin and the target sample could be treated as an elastic contact using Hertz's theory [408]. According to Hertz's theory of contact between a rigid sphere and a flat surface, the radius of the circular contact, a, depends on the applied load, P, the sphere radius, R, and the elastic properties of the materials [408]:

$$a^3 = \frac{3}{4}\frac{PR}{E^*} \qquad \{6.1\}$$

where E^* represents the reduced elastic modulus, which is given by:

$$\frac{1}{E^*} = \frac{\left(1-\nu_0^{\,2}\right)}{E_0} + \frac{\left(1-\nu_1^{\,2}\right)}{E_1} \qquad \{6.2\}$$

In equation {6.2} E_0,ν_0, E_1, and ν_1 represent the elastic modulus and Poisson's ratios of the specimen and the counterface, respectively.

The mean contact stress is given by:

$$\sigma_{mc} = \frac{P}{\pi a^2} \qquad \{6.3\}$$

The mechanical properties of the counterface (i.e., alumina ball) found in literature are: $E_1 = 350-400\,GPa$ [409,410] and $\nu = 0.23-0.27$ [409,410], while those of the specimen the oxide layer (composed mainly of chromia as demonstrated in chapter 3.4) are $E_0 = 202-327\,GPa$ and $\nu = 0.29$ [409]. For estimation, the value of the mechanical properties was chosen as follows: $E_1 = 375\,GPa$, $E_0 = 260\,GPa$, $\nu_0 = 0.25$, and $\nu_1 = 0.29$.

The calculation shows that the critical contact stress corresponding to a load of 5 N, above which the the oxide scale had little influence on the average wear

rates, is 960 MPa. However, this value must be treated with caution as the oxide scale is composed of chromia and other possible oxides that have lower Young's modulus such as CoO (131 GPa), NiO (192 GPa), SiO_2 (87 GPa) or Y_2O_3 (123 GPa). In addition, Young's modulus usually decreases with increasing temperature, by up to 20% at 600^0C [409].

7.0 OXIDATION BEHAVIOR OF YTTRIUM-FREE AND YTTRIUM-CONTAINING STELLITE 21 AND 712

This chapter presents results of the study on the effect of yttrium addition on the oxidation behavior of Stellite 21 and 712 alloys at elevated temperatures for relatively longer time. The purpose of this research is to obtain a better understanding of yttrium effects on high-temperature oxidation behavior and corresponding improvement of the performance of the alloys. This chapter comprises two sections, which present the studies on the oxidation behavior of yttrium-free and yttrium-containing Stellite 21 at 600^0C and 1000^0C, respectively.

7.1 The oxidation behavior of yttrium-free and yttrium-containing Stellite 21 and 712 samples at 600^0C.

Yttrium-free and yttrium-containing Stellite 21 samples (15x10x5 mm) were oxidized at 600^0C in air. Prior to the oxidation treatment, the samples were ground with abrasive papers and finally polished with a 0.05 μm alumina slurry, followed by ultrasonically cleaning with alcohol and acetone.

Various experimental techniques were used to examine the produced oxide scales, including AFM (Atomic Force Microscopy), SIMS (Secondary Ion Mass Spectroscopy), and micro- and nano-mechanical probes.

The hardness of oxide scales on yttrium-free and yttrium-containing samples, resulting from oxidation at 600^0C for 1 min, was investigated at room temperature

using a nano-mechanical probe (Hysitron, Minneapolis, USA) with a three-sided diamond pyramid tip (tip angle=90^0). The test was performed under a maximum load of 25 μN and the corresponding force-depth curves were recorded. Hardness and elastic behavior of the oxide scales were determined from the indentation curves and each reported value was an average of fifty measurements. Indentation depth and η values determined from the indentation test are presented in figure 7.1.

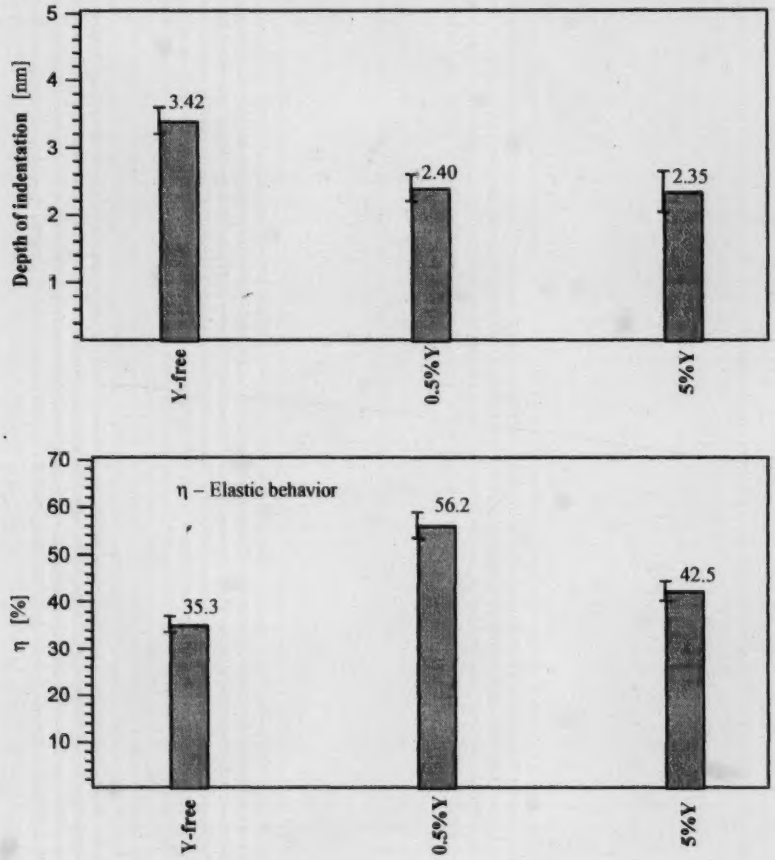

Figure 7.1: Mechanical properties of the oxide scales resulting from oxidation at 600^0C for 1 min: a) Depth of indentation, b) Elastic behavior - η value.

As shown, the oxide formed on the unmodified Stellite 21 sample was the softest with the largest indentation depth and the least elastic behavior characterized by the smallest η ratio, while 0.5% yttrium-containing sample showed the best combination of the mechanical properties. The benefit of the yttrium addition could arrive from the presence of hard yttria phase in the oxide scale and resultant modification to the properties of the oxide (see chapter 5).

In order to understand the effect of yttrium on the oxidation behavior of Stellite 21 alloy, the morphology of the oxide film developed after isothermal oxidation at 600^0C for 1 min was examined.

SEM investigation of the oxide scale developed on yttrium-free and yttrium-containing samples revealed that no spallation occurred when cooling down in air from 600^0C. However, the SEM images recorded were not able to reveal the grain morphology due to very small features present on the surface. In addition, EDS results were influenced by the substrate due to the relatively thin scales developed. Attempts to examine sections of the scales, transverse to the oxide/matrix interface by SEM-EDS also were unsuccessful due to the small thickness of the oxide scale, which made it difficult to show the presence of oxide pegs (figure 7.2).

Atomic force microscopy technique was used to study the morphology of the oxide film developed after isothermal oxidation at 600^0C. AFM is a very sensitive technique, which provides improved vertical resolution compared with SEM [411]. Secondary electrons used to modulate the image in SEM are derived both from the surface and various depths below the surface. AFM is based on the measurement of intermolecular forces between a sharp tip and the sample's surface [412].

Figure 7.2: SEM image of the polished cross-section of the scale formed on yttrium-free sample.

As a result, the surface imaged using AFM are much rougher than those imaged using SEM [411]. The sharp pyramidal tip used by AFM is mounted on the underside of a cantilever. When the tip is brought close to the surface, the intermolecular forces (predominantly inter-atomic repulsive forces but also other "long-range" forces could act, such as Coulomb forces or capillarity forces due to an absorbed film on the surface), to cause the cantilever to bend. A laser beam is reflected form the top surface of the cantilever onto a four-quadrant photo-detector as the sample is scanned [411,412]. The variation in relative light intensities produces a varying potential signal, which is used to construct the AFM image [411]. As a matter of fact, the tip is actually touching the surface (100 nN contact force for contact AFM mode); as the contact surface is very small, the contact stress could be high and could disrupt the sample's surface [411]. Under the present experimental conditions, the contact stress does not affect the oxide film due to its high hardness.

It was noticed that after collecting about 50 images, the AFM tip was changed as the high hardness of the oxide film caused wear of the AFM tip and affected its resolution.

An atomic force microscope (Digital Instruments, Santa Barbara, CA, USA) was used to determine the three-dimensional topography of the sample surfaces within a scan area of 2μm x 2μm with a scan rate of 1 Hz. The mean surface roughness (R_a) was determined from the AFM images using the NanoScope SPM image analysis software (Version 4.42). Each reported roughness value is an average of fifty measurements.

It is well known that an AFM profile shows positive or negative background slopes due to the tilt of the sample holder [413]. Prior to the surface roughness calculation, the tilt was removed by digital leveling. However, the extent of leveling might affect roughness values [413]. For this investigation, only first level leveling was used as it is sufficient to remove the effect of sample tilt [413].

Figure 7.3 illustrates AFM three-dimensional topographic images (2x2μm) of the oxide scales developed on yttrium-free and Y-containing Stellite 21 samples, respectively. The oxide scale on the yttrium-free sample showed the largest roughness (figure 7.4) while that on the 0.5% yttrium-containing samples, which appeared to be the most homogeneous scale, showed the least roughness.

Roughness of the oxide scale could influence the wear behavior; each contact point had high stress concentration that might lead to premature failure of the oxide scale, thus exposing fresh metal surface for further oxidation.

Top views of the oxide scales formed during oxidation for 1min were obtained from the recorded AFM images using the NanoScope SPM software (version 4.42).

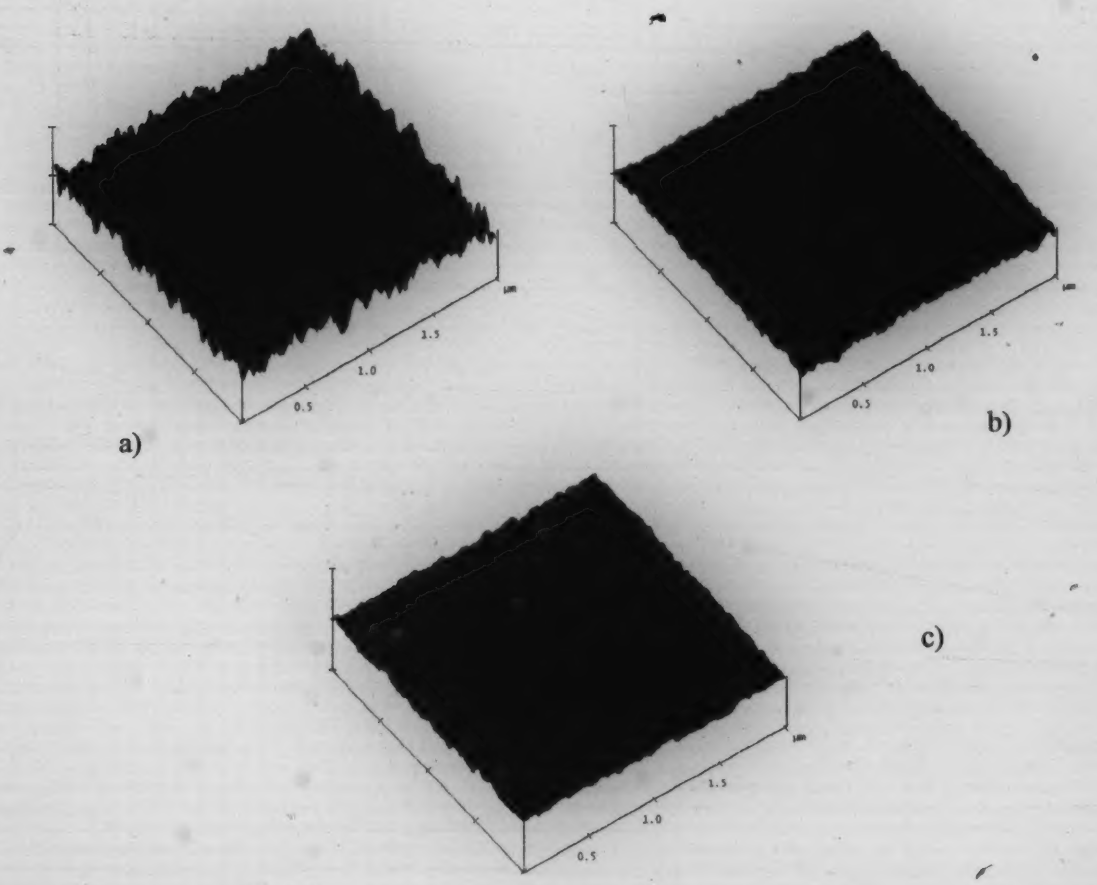

Figure 7.3: AFM three-dimensional topographic profiles (2 x 2μm) of the oxide scales developed on samples of Stellite 21 after oxidation at 600^0C for 1 min: a) Yttrium-free; b) 0.5%Y; and c) 5%Y. Vertical scale: 50 nm.

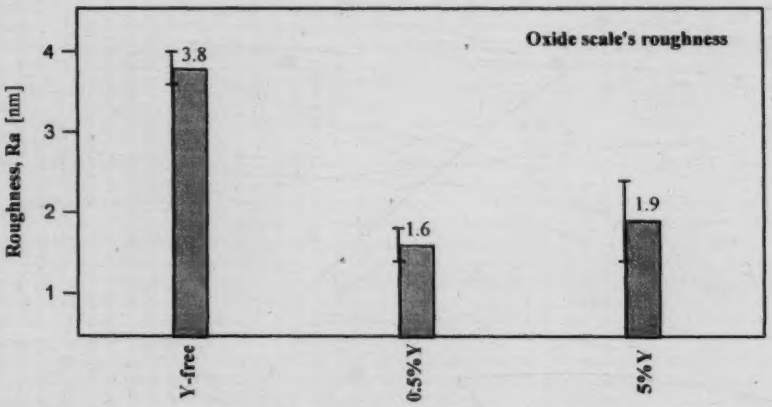

Figure 7.4: Roughness of the oxide scales formed at 600^0C for 1 min on Stellite 21 with and without yttrium.

Figure 7.5 presents representative images, from which the mean grain size of the oxide scale was determined along randomly selected directions. The mean size diameter was calculated using the random line intercept method [414]. Three concentric circles were drawn on the microstructures having a radius of 10, 20, and 30 mm; then the total length of the circles was corrected for the magnification. The number of grain boundary intersections with the lines per unit length (n_L) was counted (one entry for each intersection, 1.5 for each triple point intersection, and 0.5 when a grain boundary was tangent to a line). The mean size diameter is given by the following relation: $d = C\frac{1}{n_L}$, where C represents a constant equal to 1.78 for typical microstructures.

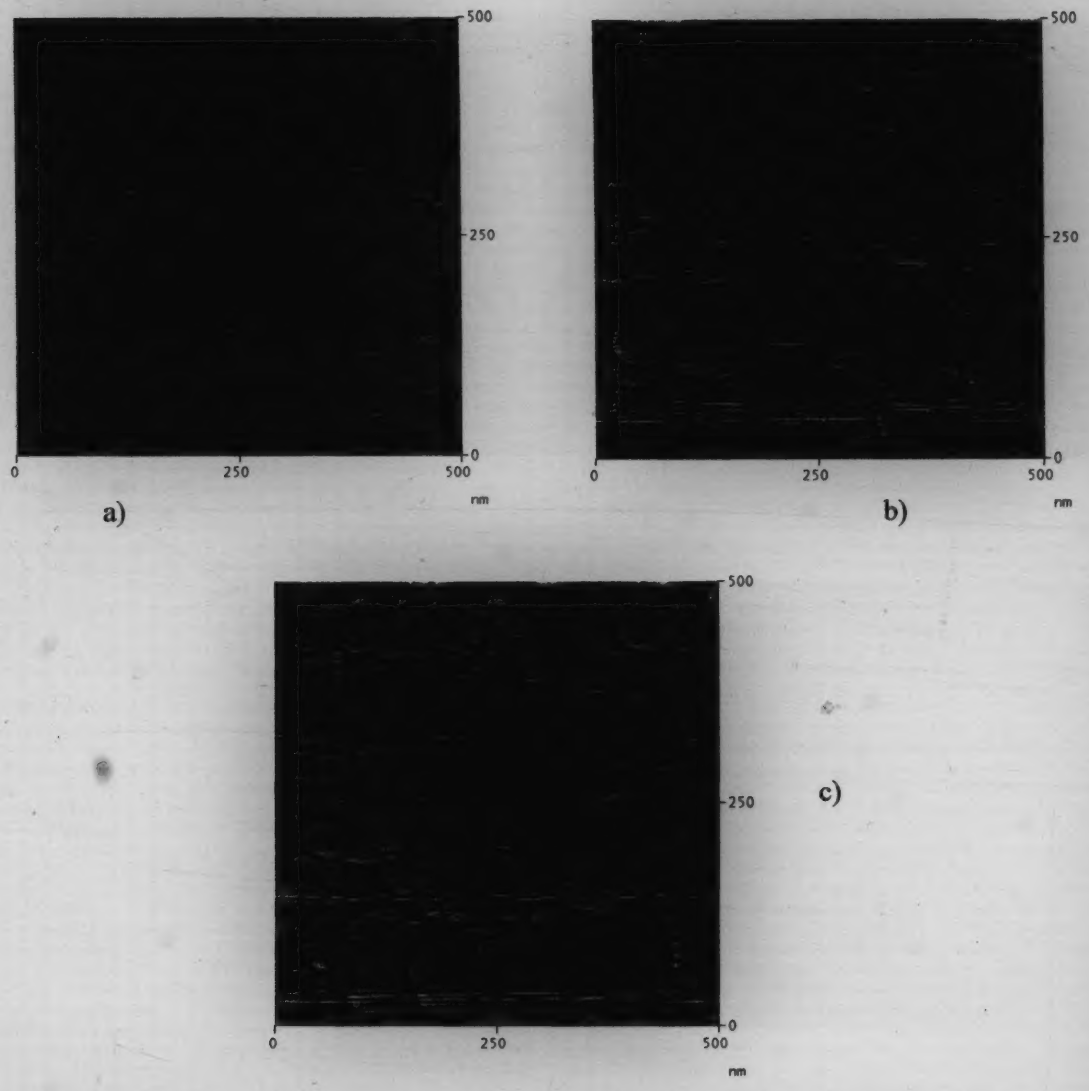

Figure 7.5: AFM images of the oxide scales developed after oxidation of Stellite 21 samples at 600^0C for 1 min a) Yttrium-free; b) 0.5%Y; c) 5%Y.

Figure 7.6 illustrates the mean grain sizes of the oxides formed on different samples. As shown, the oxide's mean grain size (diameter) is smaller for the yttrium-containing samples. It is known that yttrium has high affinity for oxygen and could

act as active nucleation sites for chromia, which may decrease the distance between adjacent chromia nuclei and thus reduce the space for them to grow laterally, leading to a decrease in the grain size. In addition, yttria phase could segregate at the oxide grain boundaries [258] and hinder oxide grain growth when exposed to elevated temperatures for a long period of time.

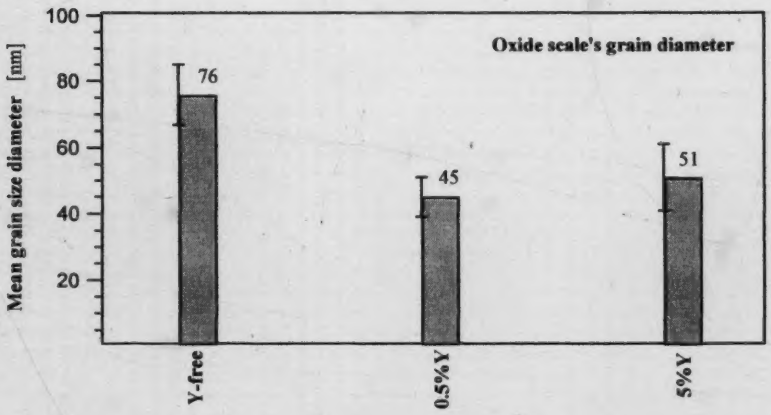

Figure 7.6: Mean grain sizes (diameter) of oxide scales developed on Stellite 21 samples with and without yttrium after 1min-exposure in air at 600^0C.

SIMS experiments were performed on yttrium-free and yttrium-containing Stellite 21 samples that were oxidized at 600^0C for 125 hours in order to investigate the influence of yttrium on the distribution of elements in the oxide scales and their thickness values.

The target surface was bombarded by an energetic beam of focused ions (e.g., Ar^+, Ga^+, Cs^+, O^-) in a high vacuum environment during SIMS experiments

[412,415-419]. The primary ions that hit the surface transfer their energy (momentum) to the target atoms and initiate the emission of sputtered particles. The sputtered particles may be mono-atomic or molecular clusters [418]. A small fraction (less than 1%) of these sputtered particles became charged (positively or negatively) depending on the electronic properties of the matrix (called the matrix effect). Sputtering of the surface by electropositive species such as Cs^+ leads to an enhanced production of negative secondary ions that makes the elemental analysis less sensitive to matrix effects and /or to residual elements such as hydrogen, and oxygen present in the vacuum environment during analysis [418,420]. The secondary ions are analyzed using a mass spectrometer [416-418]. One or more of the secondary ion signals are registered as a function of sputtering time (or depth) for depth profiling analysis. The quantitative analysis of a SIMS pattern is relatively complicated, due to the variation in detection sensitivity from element to element [419]. The spectra generated during the first minutes of sputtering (around 10 nm) are not useful due to gradual build up of the concentration of the implanted primary ions in the surface; therefore, ion yields and sputtering rates vary until equilibrium is established [419].

The element distribution as a function of distance from the surface was determined layer by layer, achieved by sputtering a surface area of 200 x 200μm using a Cs^+ primary beam with its energy equal to 1 keV and current of 2 nA, respectively. An area of 50 x 50μm in the center of the scanned area was analyzed for all samples in order to avoid any crater side-wall effects. Positive ions were analyzed for all samples. The sputtering rate was determined by dividing the final crater depth (measured using a contact profilometer, Tencor Instruments, USA) by

the sputtering time with the assumption that the depth of the sputtered region was a linear function of the sputtering time.

Figures 7.7 to 7.9 show SIMS composition profiles of oxide scales on yttrium-free, 0.5%Y-, and 5%Y-containing Stellite 21 samples. The interface between the oxide scale and the substrate can be determined based on the change in secondary ion yield between the oxide scale and the alloy substrate. The distributions of elements in the surface layer were similar for the samples with and without yttrium. Cr^+ Y^+ and Mn^+ ion signals are used to represent their oxides (figures 7.7 to 7.9) rather than using signals of CrO^+, YO^+ and $MnOH^+$ since intensities of the later species are relatively weak. All oxidized samples show peaks of Co^+ and Si^+ signals at approximately 2/3 of the scale thickness (away from the oxide/substrate interface). The Cr^+ peak appears on the top of the Co^+ and Si^+ peaks, closer to the oxide surface.

Previous glancing incidence XRD examination (see Chapter 5) and the presently determined Cr^+ distribution through the oxide scale indicate that the oxide scale is mainly composed of chromium oxide. However, the oxidation process is complex due to the presence of minor alloying elements, leading to the formation of a layered oxide scale. The amount of Mn oxides is higher in the outer part of the scale, implying a higher diffusion rate of Mn ions through chromia than the other alloying elements [402].

As shown, yttrium is relatively rich at the oxide/substrate interface. Yttrium has a low diffusion rate and could block the diffusion of other elements [421].

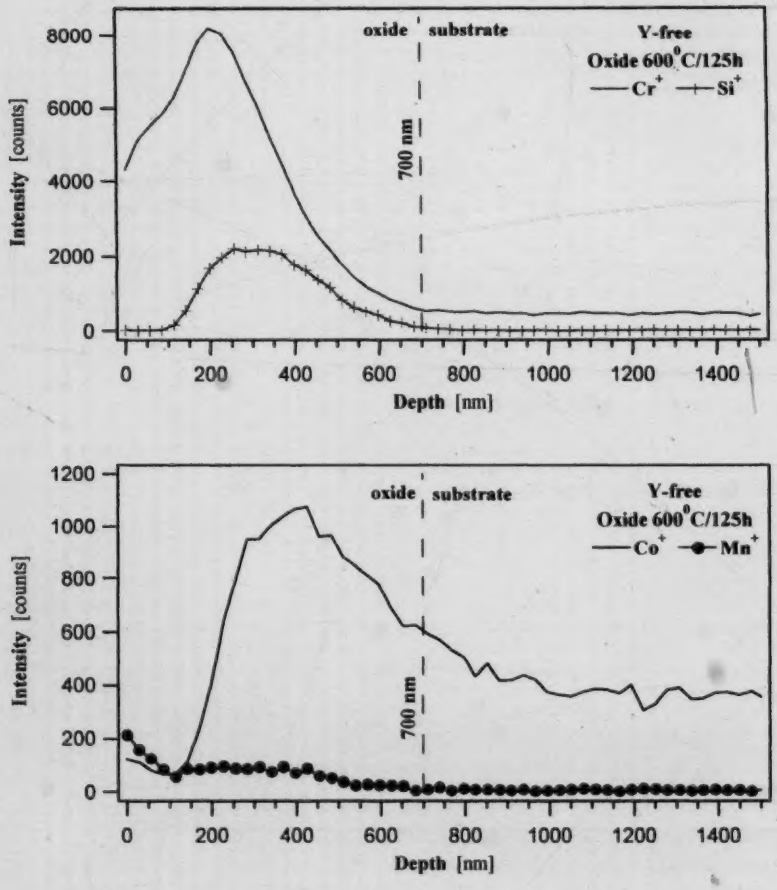

Figure 7.7: SIMS composition-depth profiles of the oxide developed on Y-free Stellite 21 sample after oxidation at 600^0C for 125 hours.

As illustrated in figures 7.7-7.9, the oxide scale thickness was decreased with increasing the yttrium amount.

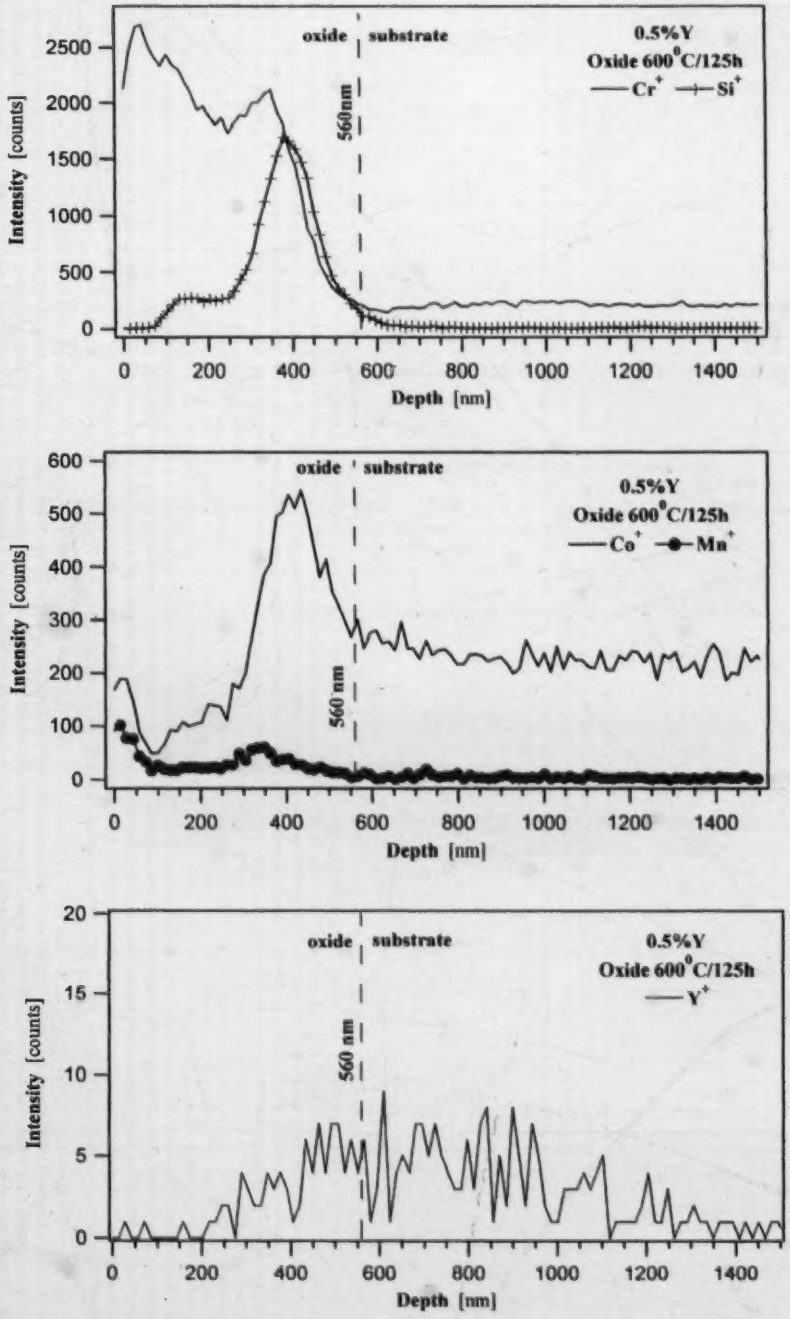

Figure 7.8: SIMS composition-depth profiles of the oxide developed on 0.5% Y-containing Stellite 21 sample after oxidation at 600^0C for 125 hours.

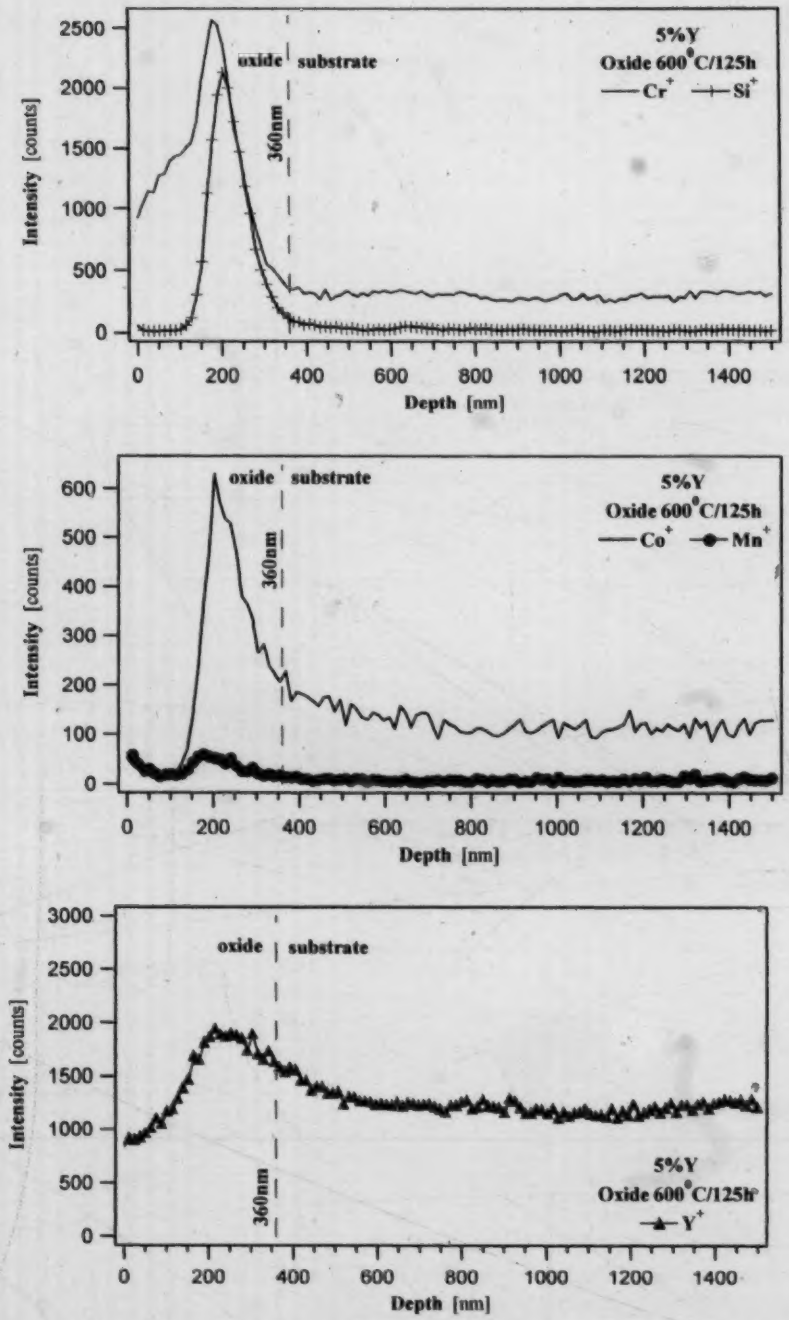

Figure 7.9: SIMS composition-depth profiles of the oxide developed on 5% Y-containing Stellite 21 sample after oxidation at 600^0C for 125 hours.

The oxidation mechanisms of Stellite 21 with and without yttrium were investigated using the $^{18}O/^{16}O$ SIMS technique. Samples were oxidized at 600^0C first in $^{16}O_2$ for 8 hours then in $^{18}O_2$ for 24 hours without cooling when the $^{16}O_2$ environment was changed to the $^{18}O_2$ one. Figure 7.10 illustrates $Cr_2{}^{16}O_3$ and $Cr_2{}^{18}O_3$ SIMS profiles of the oxide scales obtained after the dual gas oxidation. For the yttrium-free sample, there is a separate $Cr_2{}^{18}O_3$ layer on the top of $Cr_2{}^{16}O_3$ layer, indicating that oxidation took place predominantly by an outward diffusion of Cr cations while the SIMS profiles of the yttrium-containing samples indicate that inward ^{18}O diffusion through the ^{16}O layer occurred during oxidation in $^{18}O_2$, which was a result of the change in the oxidation mechanism from predominant outward cation diffusion to predominant inward anion diffusion.

The improved adherence of oxide scales on the yttrium-containing samples (see Chapter 5) could largely benefit from the predominant inward oxygen diffusion because this suppresses vacancy condensation at the oxide/matrix interface which is usually caused by the outward diffusion of metallic elements.

Furthermore, the inward oxygen diffusion may enhance the effect of oxide keying into the grain boundaries of the substrate, thus further increasing the oxide adherence to the substrate. It is known that yttrium may congregate at the oxide grain boundaries in the form of Y_2O_3 or perovskite compounds such as $YCrO_3$ and inhibit outward diffusion of chromium ions; this helps achieve the change from the outward diffusion of metallic elements to the inward diffusion of oxygen ions [280].

Krishnamurthy & all [422] suggest that the oxide film has relatively homogeneous compressive stress distributed within it ,

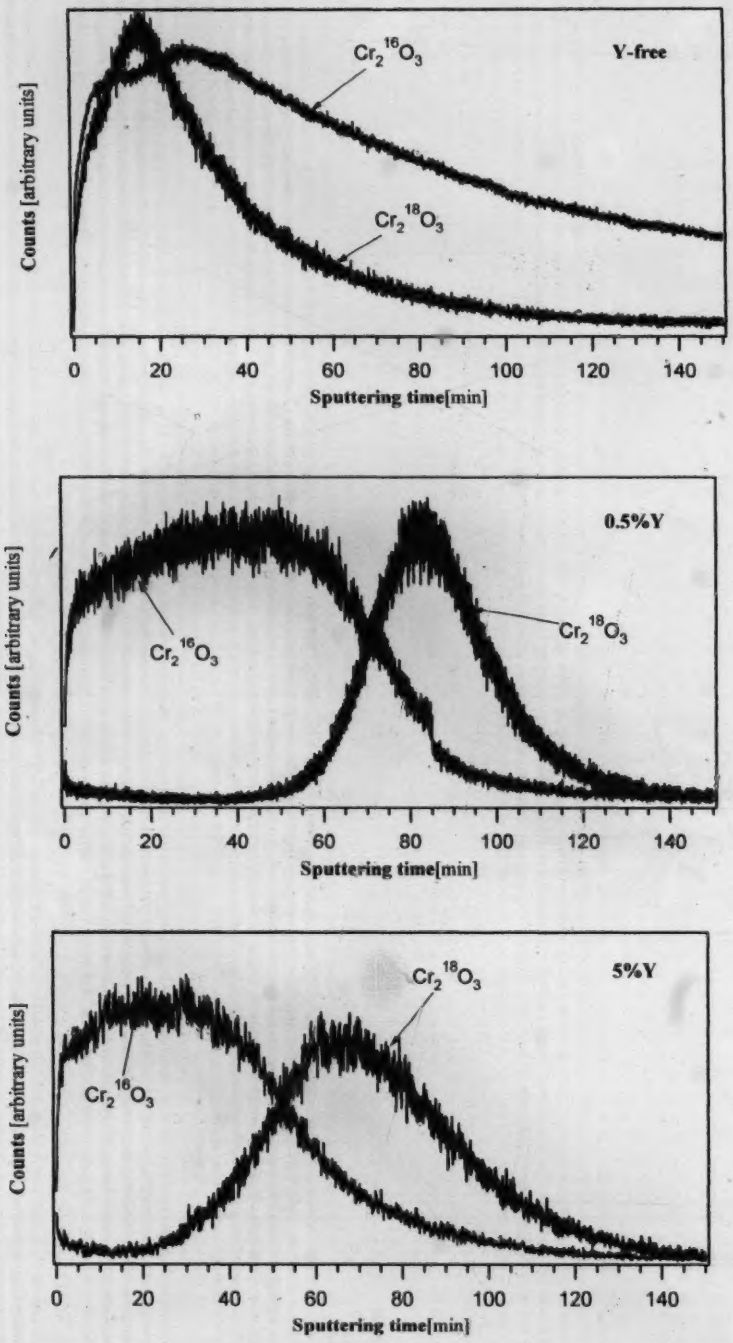

Figure 7.10: Negative SIMS profiles of oxide scales formed at 600^{0}C in $^{16}O_2$ for 8 hours followed by 24-hours oxidation in $^{18}O_2$ on a) yttrium-free, b) 0.5% yttrium-containing, and c) 5% yttrium-containing Stellite 21 samples.

except in the regions near the oxide grain boundaries where the stress changes from compressive near the oxide/matrix interface to tensile near the oxide surface. As the ratio of cation diffusivity to that of anion decreases, both the tensile stress near the oxide surface and the stress gradient through the oxide scale decrease [422]. This may also help to minimize wear attack, bearing in mind that the residual tensile stress is detrimental.

The change in surface morphology should be related to changes in the oxidation rate: a slower growing oxide scale may result in a smaller surface roughness since oxide crystals grow slowly in the direction perpendicular to the surface, which may help lateral growth to diminish the height difference between adjacent crystals.

It should be mentioned that the reduction of the oxide grain size by yttrium may also play a positive role in improving the mechanical properties of the oxide scale such as hardness, elastic behavior, and resistance to scratching. A nano-structured oxide should have not only its hardness enhanced but also its toughness [423]. The formation of a stronger and tougher oxide film would certainly help to minimize wear attack at elevated temperatures.

During longer exposure at elevated temperatures, the properties of the oxide scale could change, which may affect the wear behavior of the material at elevated temperatures. Oxidation experiments with an exposure time from 1 min to 125 hours were performed at 600^0C in order to investigate the evolution of oxide scale properties. Figure 7.11 illustrates changes in roughness, surface grain size, and hardness of the oxide scales (50 μm maximum indentation load) formed on samples

with and without yttrium, respectively. As shown, the grain size, roughness and indentation depth increased with the oxidation time following a parabolic behavior. The increases in grain size and roughness were more pronounced for the yttrium-free oxide scale which may be related to its growth mechanism: the relatively faster outward diffusion of metallic ions and lower nucleation rate due to fewer active nucleation sites compared to that with the active yttrium addition. As well, the presence of yttrium in its oxide form could block grain growth by pinning the movement of grain boundaries in the oxide scale.

The decrease in hardness of the oxide scale with the oxidation time could be related to the change in oxidation mechanism as well as the faster diffusion rate of Mn.

After exposure at 600^0C, the top surface of the oxide surface layer was rich in manganese oxides (figs. 7.7-7.9), which may imply that Mn atoms could diffuse more readily than others in the present system. For a long exposure period, the ratio of manganese oxide to the chromia oxide could increase at the outer surface when oxidation took place by the predominant inward diffusion mode (i.e. yttrium was present).

Mn oxide could be weaker than the Cr oxide. In order to confirm this, nano-indentation tests were performed on oxide scales developed on pure Cr and Mn samples after oxidation at 600^0C for 8 hours. Figure 7.12 illustrates obtained force-depth curves, which demonstrate that the Mn oxide is much softer than the Cr oxide. This explains why the measured hardness of oxide scales on Stellite 21 with and without yttrium addition decreased with the oxidation time.

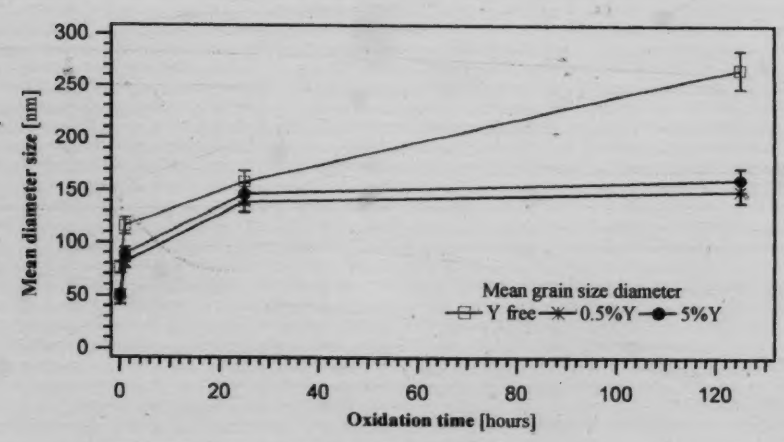

a)

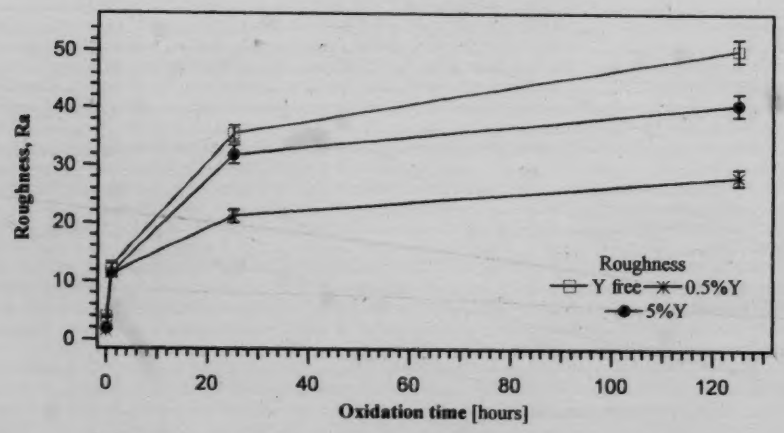

b)

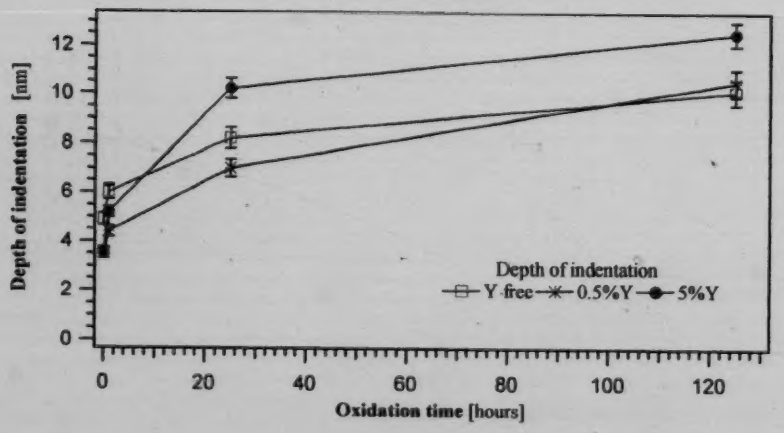

c)

Figure 7.11: Changes in grain size, roughness, and hardness or indentation depth (50 μm maximum indentation load) of oxides formed on different samples with respect to the oxidation time: a) grain size, b) roughness, c) depth of indentation.

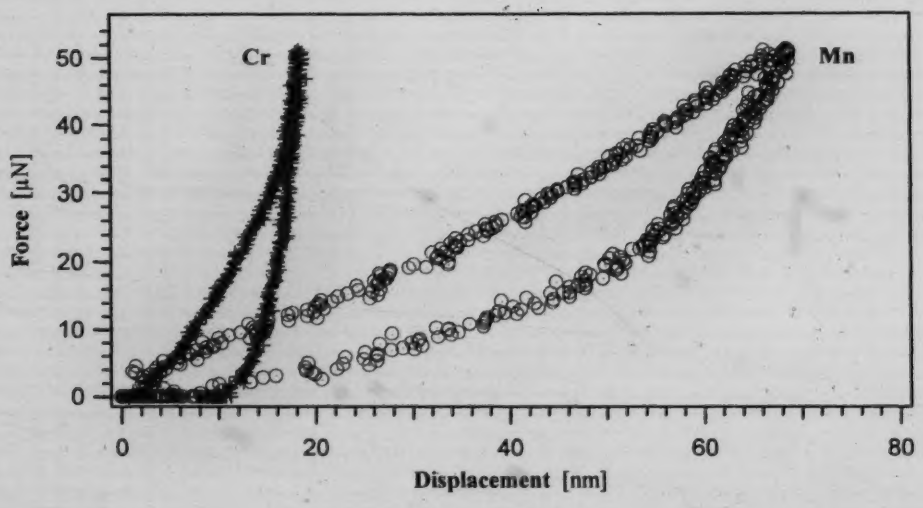

Figure 7.12: Nano-indentation curves of oxide scales developed on pure Cr and Mn samples after oxidation at 600^0C for 8 hours.

It is worth indicating that the mechanical properties of the oxide scale formed after long exposure times are not homogeneous. The decrease in hardness of yttrium-containing oxide scale does not mean that yttrium negatively affected the oxide's mechanical properties, since the degradation in mechanical properties only occurred at the top surface. Instead, the beneficial effect of yttrium on the oxide adherence and mechanical behavior (not at the top surface of a thick oxide) considerably increase the resistance of Stellite 21 to wear at elevated temperatures as demonstrated in previous chapters of this thesis.

The oxidation process could be described as follows: in the initial stage of oxidation all the component elements of the alloy will diffuse along grain boundaries through the substrate/gas interface. Diffusion through the grains is relatively slow at

this temperature; thereby, the diffusion process is taking place mainly along grain boundaries of the alloy. Nucleation of oxide takes place preferentially at grain boundaries, impurities, and dislocations. Yttrium could create additional sites for oxide nucleation, decreasing the inter-nuclei spacing and, consequently, the time required for the nuclei to grow laterally to form a continuous oxide layer. As a result, the grain size of the scale is decreased.

The growth rates of NiO and CoO are relatively higher than that of Cr_2O_3. As a result, CoO nuclei will overgrow and undercut the transient nuclei forming a rich Co oxide layer on the top of the nuclei. The Co-rich oxide layer is not an effective barrier to cation/anion diffusion; thereby, Cr and Si will react with oxygen to form a continuous protective layer. According to the SIMS profile, it seems that the Si diffusion rate is lower than that of Cr, leading to a rich Cr oxide layer on top of the rich Si oxide layer. A silica rich layer could also influence the incorporation of cations into the scale.

After the formation of the dense protective Cr rich oxide layer, further oxidation will be controlled by the transport of anions and cations through this layer. In addition, yttrium will affect the boundary transport of cations, especially Cr, and its supply through the oxide layer. As a result, the oxidation kinetics is reduced, leading to thinner oxide scales. Meanwhile, the inward diffusion of anions may dominate the oxidation process. The scale growth would be controlled by the proportion of boundaries affected by yttrium segregation which is a function of the amount of yttrium supplied at the interface. This explains why the oxide scales developed on alloys having larger amounts of yttrium are thinner. Manganese

diffuses faster through the grain boundaries than the other elements and thus enriches the top surface of the oxide layer.

Regarding Stellite 712, based on previous results (see chapter 5), one may see that yttrium addition has similar effects on the oxidation behavior as that for Stellite 21. However, the surface roughness of the oxide was affected by yttrium addition differently and seems to have a relatively larger influence on the wear behavior of this alloy. To clarify this, the AFM technique was used to study the morphology of oxide films developed after isothermal oxidation at 600^0C for 25 hours on Y-free and Y-containing Stellite 712 samples. An atomic force microscope (Digital Instruments, Santa Barbara, CA, USA) was used to analyze the three-dimensional topography of a sample surface with a scan size of 10 x 10μm and a scan rate of 1 Hz. The cantilever probe was a silicon nitride tip. Mean surface roughness (R_a) and 10-point mean roughness (R_z) were determined from recorded AFM images using the NanoScope SPM software, version 4.42. Each value of R_a and R_z reported is an average of fifty measurements. AFM three-dimensional topographic pictures (10x10μm) and roughness profiles of the oxide surface layer developed on Y-free, 0.5%Y, and 5%Y-containing Stellite 712 specimens after oxidation at 600^0C for 25 hours are presented in figure 7.13. Table 7.1 presents the corresponding R_a and R_z values. The Y-free Stellite 712 specimen showed the lowest roughness and the most homogeneous outer surface of the oxide layer.

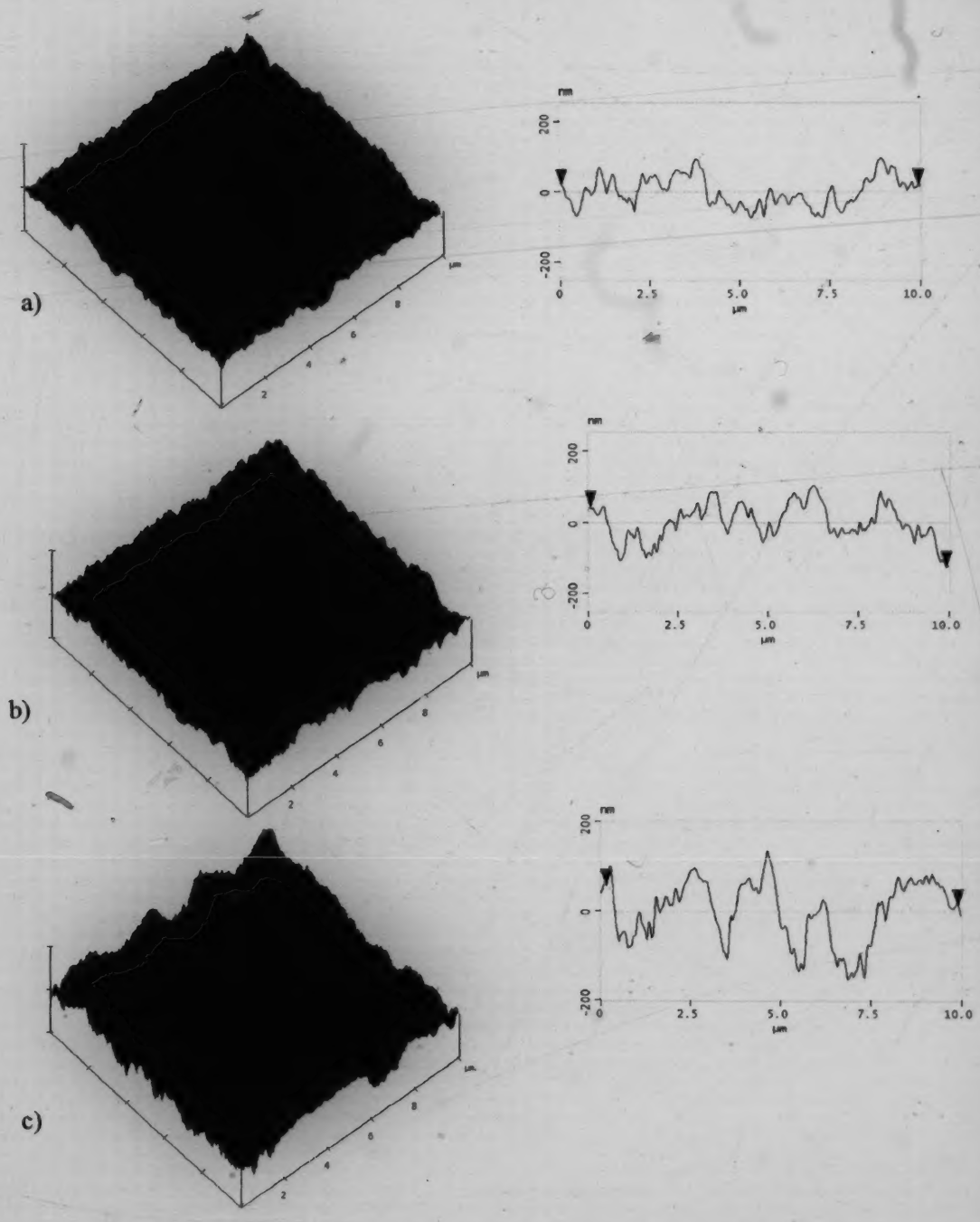

Figure 7.13: AFM three-dimensional topographic pictures (10x10µm) and roughness profiles of the oxide scales developed at 600^0C for 25 hours on a) Yttrium-free; b) 0.5%Y; c) 5%Y – containing Stellite 712 samples.

Table 7.1: Surface roughness of oxide scales developed on yttrium-free and yttrium-containing Stellite712 samples after oxidation at 600^0C for 25 hours. Error range: R_a: ±5%, R_z: ±4%.

Material	Mean roughness, R_a	10 Pt. Mean roughness, R_z
Y-free Stellite 712	40.7	137.5
Stellite 712 – 0.5%Y	42.7	147.5
Stellite 712 – 1%Y	49.2	167.5
Stellite 712 – 2%Y	49	167.1
Stellite 712 – 5%Y	59	184

From the figures, one may also see that the oxide developed on the Y-free specimen was smooth (Fig.7.14 (a)), compared to those on Y-containing specimens (Figs. 7.14(b) and (c)). Yttrium is an oxygen-active element, which may affect the oxide growth in addition to its properties. Therefore, the growth of oxide on a specific area should be influenced by the local yttrium concentration. Since yttrium concentration was not very homogeneous as fig.3.7 illustrates, a relatively rough oxide scale could thus be generated, compared to that developed on a Y-free specimen.

A rough and less homogeneous oxide scale with possibly higher residual stress due to lower homogeneity would experience a larger stress concentration when in contact with a counterface.

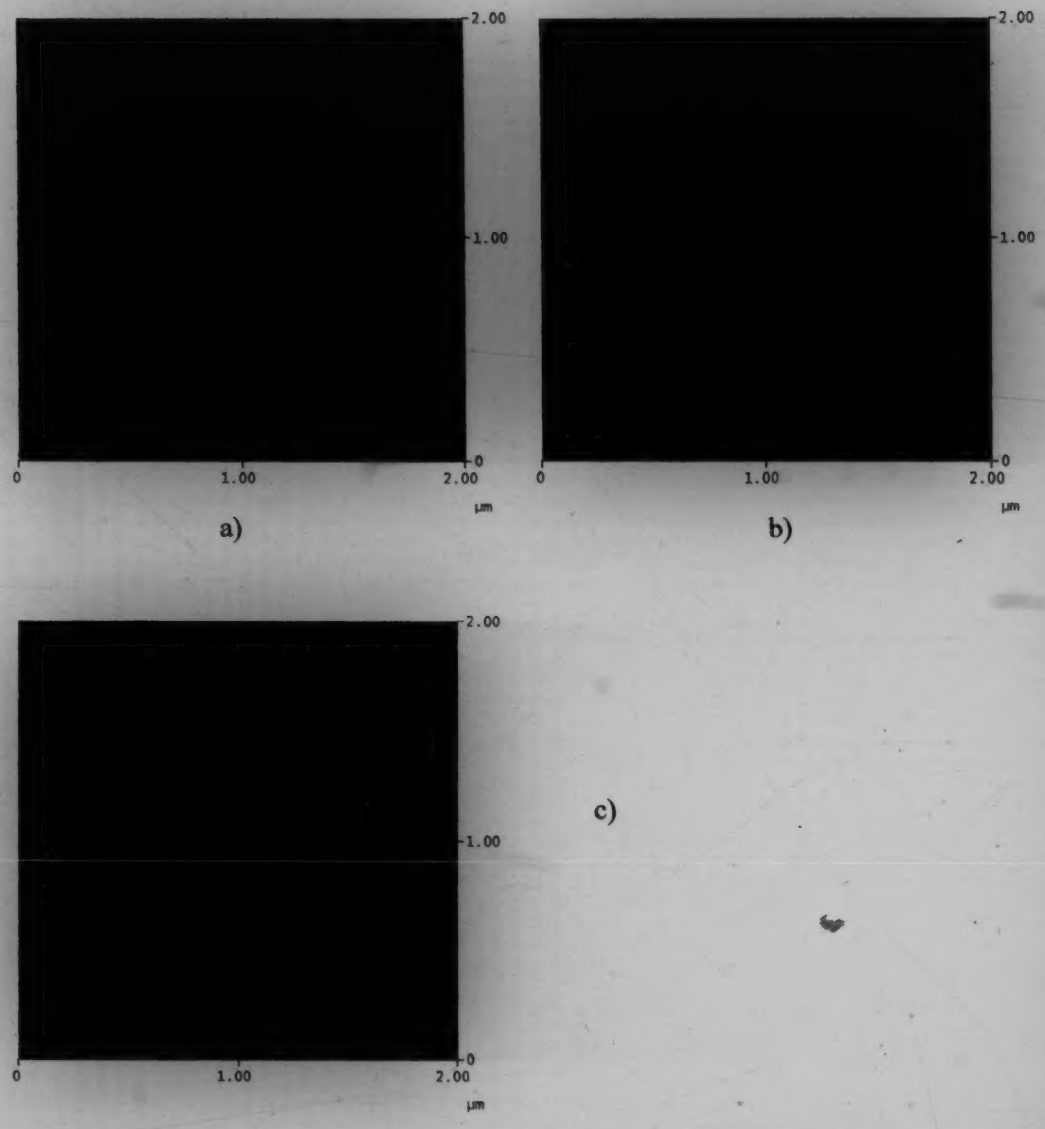

Figure 7.14: AFM images of oxide scales developed at 600^0C for 25 hours on different Stellite 712 samples: a) Yttrium-free; b) 0.5%Y; c) 5%Y.

As a result, the probability of failure would be higher when the surface is subjected to wear attack. This could explain why only a small amount of yttrium addition to Stellite 712 positively affected its wear resistance.

It is clear that in addition to hardness, grain size, thickness, elastic behavior of the oxide layer and its adherence to the substrate, roughness and surface homogeneity play also important roles in resisting high-temperature wear.

7.2 Oxidation of yttrium-free and yttrium-containing Stellite 21 samples at 1000^0C.

The effectiveness of the reactive elements seems to reach a maximum in a temperature range from 0.4 to 0.6 of the absolute melting temperature of the oxide scale (e.g. >750^0C for chromia scales) and then decreases with a continuous decrease in temperature [203,291]. Yttrium-free and yttrium containing Stellite 21 samples were oxidized at 1000^0C and atmospheric pressure of air in order to evaluate the maximum benefits of yttrium to the oxidation behavior. Prior to the oxidizing step the samples (15x10x5 mm) were polished with 0.05 μm alumina slurry in the final polishing step, then ultrasonically cleaned with alcohol and acetone. The samples were heated to the oxidizing temperature at a rate of 20^0C/min, maintained at 1000^0C for 125 hours, then cooled with the furnace open for 10 min and then were removed from the furnace and left to cool down to room temperature. The above cooling procedure was chosen because at higher cooling rates large areas of oxide scale were

lost by spallation. A wide range of experimental techniques including SEM/EDS, micro- and nano-mechanical probe, were used to examine the resulting oxide scales.

SEM images of the oxide surface morphology of yttrium-free and yttrium-containing samples after oxidation at 1000^0C are presented in figure 7.15.

Large spalled areas were identified on the surface of the yttrium-free sample, as indicated by arrows in image 7.15 a. Less spalled areas were present on the surface of the 0.5% yttrium-containing sample while almost no spallation occurred on the surface of the 5% yttrium-containing sample. Lower spallation is an indicator of better oxide scale adhesion; thereby, the results demonstrated that the oxide scale adherence to the substrate was increased with increasing yttrium amount when cooling down from 1000^0C.

At higher magnifications it was shown that the surface morphology of the oxide developed on yttrium-free sample was composed of large facetted grains (columnar grains) of around 3 to 5μm diameter (figure 7.16 a). This morphology is typical for chromia scales [310,424]. The oxide external surface of 5% yttrium-containing sample shows a fine and equiaxed grain structure (figure 7.16 c). The oxide grains developed on 0.5% yttrium-containing sample are much finer than those observed on the unmodified alloy with some large columnar grains still present (figure 7.16 b).

It was shown in literature that one possible effect of adding reactive elements to alloys is to reduce the oxide grain size [5,205,207,209,217,218,231,234-239,243,244,247-249].

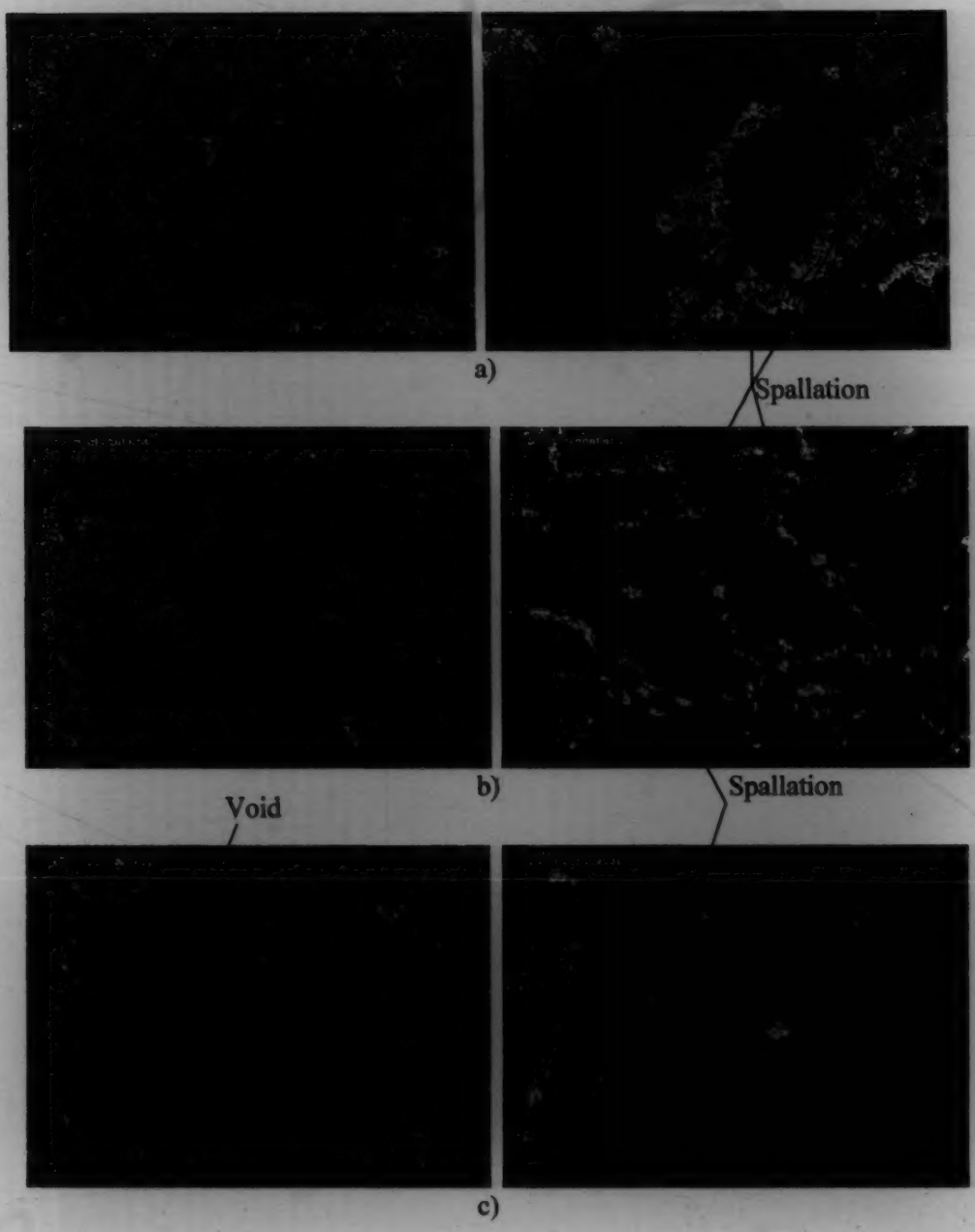

Figure 7.15: SEM images of the oxide surface morphology: a) Y-free, b) 0.5%Y, c) 5%Y.

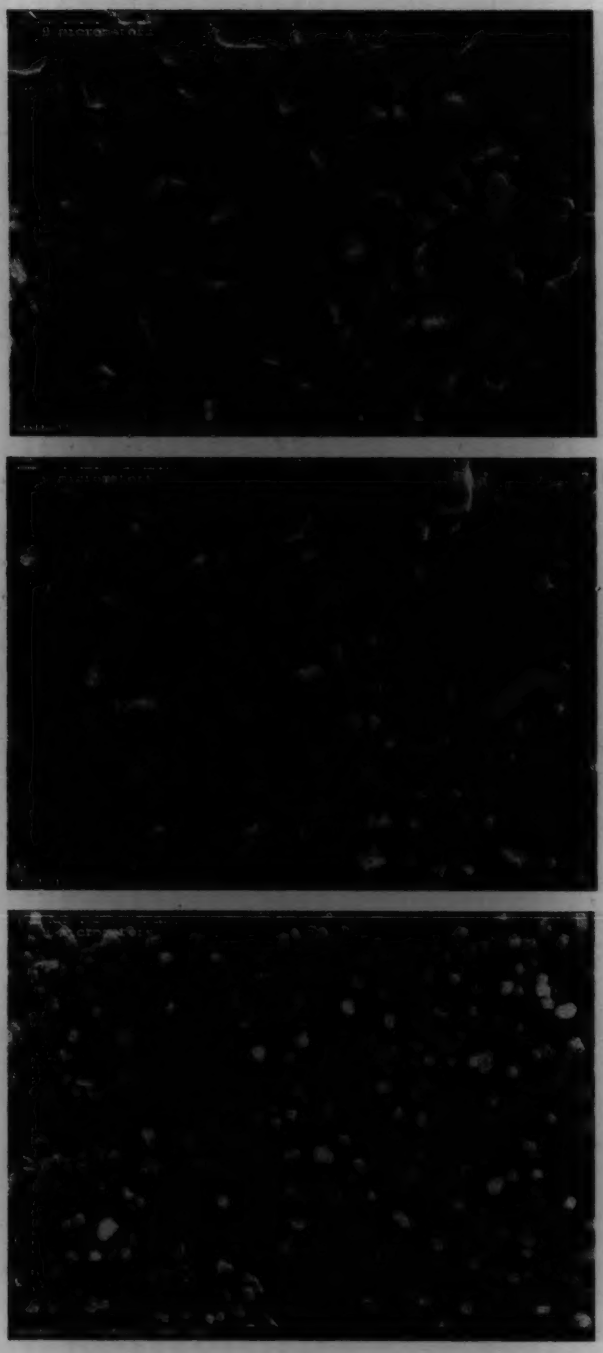

Figure 7.16: Detailed view of the oxide surface morphology: a) Y-free, b) 0.5%Y, c) 5%Y.

However, it is not very clear if the reactive element additions promote the finer grain size of the oxide throughout the scale thickness or just at the scale/gas interface [217]. In other instances, the reactive elements did not promote a finer oxide grain size [311,332]. The oxide developed on a Co-45%Cr alloy with and without yttrium after oxidation at 1000^0C for 25 hours showed a similar grain size near the oxide/matrix interface but increased toward the oxide/gas interface [261].

Oxide scale failure depends on the fracture toughness of the oxide and the distribution of defects present in the scale [250]. Most of the spallation originated at defects (voids) present in the scale (see figure 7.15). Figure 7.17 shows a detail of a zone where spallation of oxide occurred due to the presence of a void. It is believed that reactive elements reduce the amount of defects at the oxide/substrate interface following the sulfur getter mechanism or the dynamic segregation model as mentioned in Chapter 2.

Spallation may involve scale fracture following two routes: (1) nucleation of a shear crack within the oxide scale, usually at a pre-existing defect, followed by propagation toward the oxide/substrate interface and detachment of wedged-shaped sections of the scale which happens when the strength of the oxide/substrate interface is higher than the compressive fracture strength of the oxide, and (2) decohesion at the oxide/substrate interface that results in progressive buckling and rumpling of the oxide scale leading to failure [425].

It seems that failure of the oxide scale following the first route was the primary mechanism by which the oxide scale failed. Failure did not take place on larger areas at the oxide/substrate interface for the yttrium-containing samples.

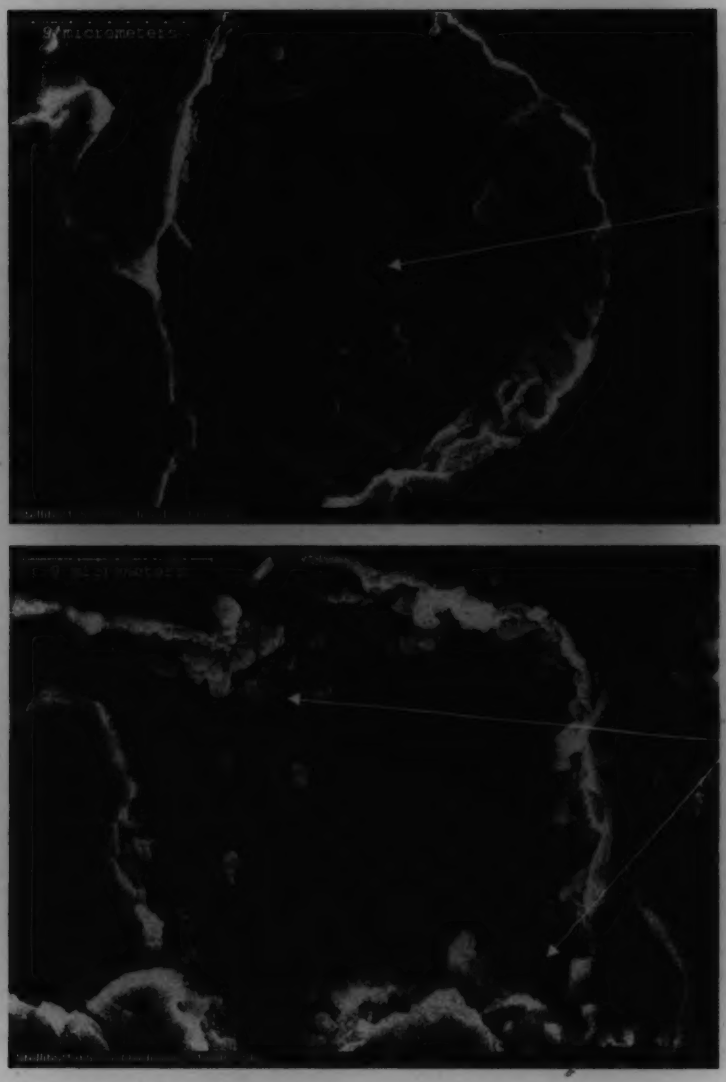

Figure 7.17: Details of an area where spallation occurred; a) 5%Y, b) 0.5%Y.

This is beneficial for prolonging the alloy lifetime through reducing the surface area of fresh metal exposed to the environment thereby reducing the metal loss by oxidation. Also, in figure 7.17 b, one may see that the nucleation of new

oxide grains took place homogeneously to a certain degree on the spalled surface, implying that bulk diffusion could be predominant at this temperature.

SEM investigations of the oxide surface revealed that the oxide scale was formed mainly by chromium oxide (most probable Cr_2O_3 -see composition at point 1 and 2 – table 7.2 and figure 7.18) but the oxide scale also had a fairly large manganese oxide concentration on the top surface (point 1).

Figure 7.18: SEM image of the oxide scale developed on 5% yttrium-containing sample showing the locations of the EDS point analysis.

In addition, the white-like areas showed a chemical composition close to that of the substrate; thereby, it could be assumed that these represent failure of the scale near the oxide/substrate interface. The presence of the large amount of manganese oxide near oxide/gas interface is consistent with that reported in literature for other alloys systems (chromia formers) where manganese was a residual element

[56,235,244,262,401]. The amount of manganese in the alloy is low; thereby, its large amount in the outer part of the oxide scale could be explained by the fast diffusion of manganese ions in chromia scales (two order of magnitude faster than chromium ions) [402].

Table 7.2: Chemical composition of the scale developed on 5% yttrium-containing sample as revealed by EDS analysis.

Element → / Position ↓	O [%]	Mo [%]	Cr [%]	Fe [%]	Co [%]	Ni [%]	Mn [%]
1	3.97	-	64.72	0.41	11.5	0.47	18.3
2	5.25	-	93.45	-	0.98	0.32	-
3	0.41	4.24	17.06	0.87	74.79	3.04	-

It seems that yttrium enhanced the manganese ion diffusion to the external surface of the oxide scale as proven by the overall EDS analysis on the oxide scale (see table 7.3). However, yttrium was not detected in the scale, probably because yttrium may be mainly located at the oxide/substrate interface [235,292,426,427].

The oxide scale's hardness was evaluated using a nano-mechanical probe (Hysitron, Minneapolis, USA). The same experimental setup as presented in Chapter 4 was used to perform the measurements. The test was performed under a 200 μm maximum load and corresponding load-depth curves were recorded. Hardness and elastic behavior of the oxide scales were determined from the curves and each value reported was an average of sixty measurements. The results are presented in figures

7.19 and 7.20. The oxide scale formed on 5% yttrium-containing sample showed the lowest hardness of the oxide scale while the yttrium-free and 0.5% yttrium containing samples showed similar hardness.

Table 7.3: The overall chemical composition of the top surface of the oxide scales.

Sample	O [%]	Mo [%]	Si [%]	Cr [%]	Fe [%]	Co [%]	Ni [%]	Mn [%]
5%Y	3.35	0.34	0.96	62.99	0.32	20.75	1.15	10.14
Y-free	3.42	0.86	1.27	51.22	0.55	37.45	1.22	4.01

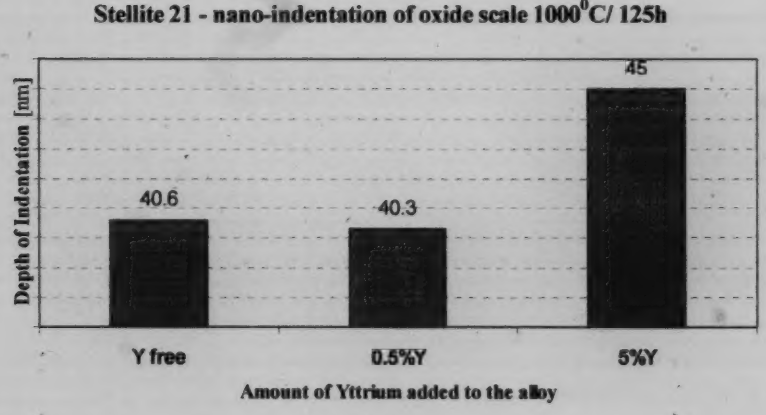

Figure 7.19: Hardness of the oxide scale developed at 1000^{0}C for 125 hours. Error range: ±3%.

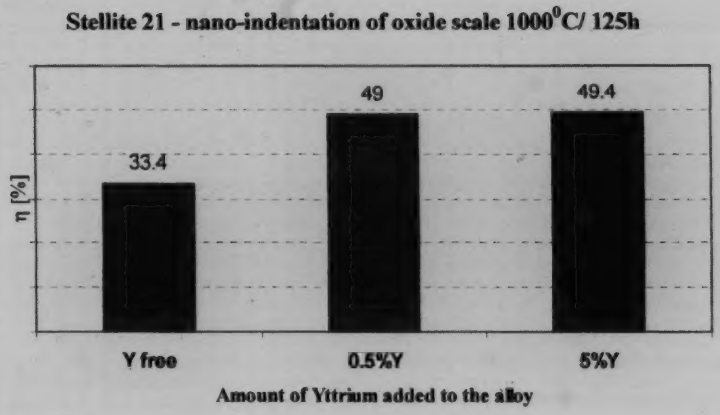

Figure 7.20: η ratio of the oxide scale developed at 1000^0C for 125 hours. Error range: ±3%.

However, the yttrium-containing samples possess larger η ratios, which are an indication that these scales behave more elastically under applied stress. The presence of larger amounts of manganese oxide on the top layer of the oxide scale developed on the 5% yttrium-containing sample could be the reason why its hardness was lower than that of yttrium-free sample. The larger η ratio calculated for the yttrium-containing samples could arise also from the smaller grain size of their oxide scales.

Cross-sections of the oxide scales were examined by SEM-EDS. Prior to the SEM investigation, the samples were mounted in Bakelite, ground and polished with 0.05 μm alumina slurry for the last step and then cleaned with acetone. Figure 7.21 and 7.22 shows SEM images of the oxide scale's cross sections.

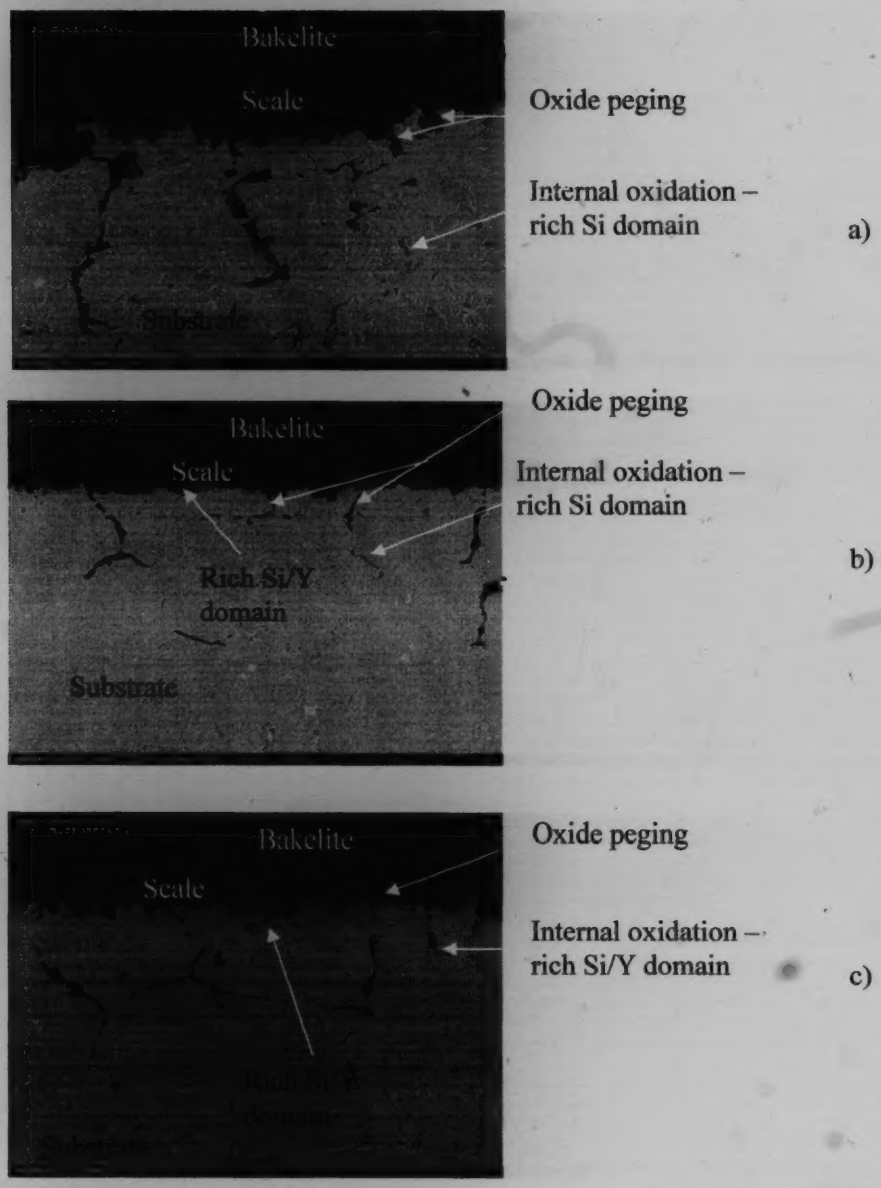

Figure 7.21: SEM images of the cross-section of the scale formed on a) yttrium- free, b) 0.5%Y, and c) 1%Y-containing Stellite 21 samples.

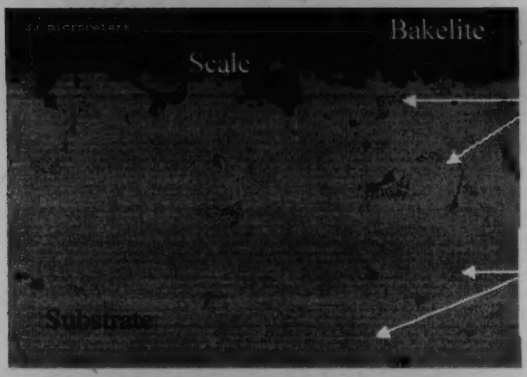

a)

b)

Figure 7.22: SEM images of the cross-section of the oxide scale formed on a) 5%Y, and b) the substrate in cross-section after exposure at 1000^0C for 125 hours.

The images showed the difference in scale thickness between the samples with and without yttrium after oxidation for 125 hours at 1000^0C. It is clear that the oxide scales on the yttrium-containing samples were significantly thinner (e.g. 6 μm for 5% yttrium-containing sample) than that on the unmodified alloy (around 15 μm). Clearly, yttrium led to a decrease in the oxidation growth rate.

In addition, thicker oxide scales could fail at lower levels of applied stress than thin scales. However, a wavy interface between the oxide and the substrate is preferred because of the larger interfacial area as well as the periodic array of tensile and compressive zones that reduce the probability of a crack extending into a region of compressive stress [428].

At the oxide/metal interface protrusions or pegs were observed. It was shown in literature that small additions of silicon to chromia former alloys could lead to the formation of silica rich pegs along grain boundaries or to a continuous layer of silicon oxides at the oxide/substrate interface [218,235,237,239,244,306,338,429-432]. As shown in figures 7.21 and 7.22, a silicon enriched internal oxidation zone has been formed. Apparently, yttrium promoted the formation of silicon oxide at the oxide/substrate interface for the samples containing up to 2% yttrium. This observation is in agreement with the literature [239,306,339]. For the 5% yttrium-containing sample, the yttrium rich phases intersecting the oxide/substrate interface could be also regarded as pegs. The rich silicon oxide at the oxide/substrate interface could act as a barrier to outward cation diffusion. However, a continuous layer of silicon oxide at the oxide/substrate interface could be detrimental to overall spallation behavior because silica has inferior fracture toughness than the chromia or the substrate; thereby, the detachment of the oxide scale could be favored [433].

The oxide pegs could improve the scale adherence to the substrate due to their potential to arrest crack propagation at the oxide/substrate interface; therefore, they may limit spallation of the oxide scale [339]. The pegs promote the mechanical stability of the scale through keying, by intrusion into the substrate.

It seems that large additions of reactive element (5%) lead to an increase of the internal oxidation depth. The size of the internal oxidation depth on the yttrium-free sample and those containing up to 2% yttrium was relatively similar (40 μm). Due to its high affinity for oxygen, the reactive element will easily oxidize internally. It is known that rare earth oxides show unusual diffusion properties [283]. Diffusion of metal atoms through rare earth oxides is not significant when temperature is below one-half of the melting temperatures (~1200^{0}C – known as Tammann temperature) but oxygen becomes mobile even at temperatures lower than 300^{0}C. Despite the high oxygen mobility, the rare earths are thermally stable compounds [283]. Furthermore, very low solubility of yttrium favors the internal oxidation process. The yttrium-rich phases formed in the 5% yttrium-containing sample could act as short diffusion paths for oxygen, enhancing its penetration inside the substrate which, however, could result in a non-homogeneous distribution of yttrium in the oxide scale.

Cross-sectional EDS analysis of the oxide showed that the amount of yttrium oxide in the rich silicon oxide domains was higher near the oxide/substrate interface. This could happen as a consequence of yttrium segregation at the oxide/substrate interface.

In order to obtain more information on the oxide pegging, the oxide scale was removed by polishing with 0.05 μm alumina slurry to reveal the oxide/substrate interface. Figure 7.23 presents SEM images of the oxide/matrix interface. Based on these images it is clear that the oxide layer was keyed to the substrate by pegs composed of rich silicon and yttrium oxides. The internal oxide domains can be seen

along grain boundaries and also within the grains. Within the grains, the pegs likely formed at stacking faults or dislocations.

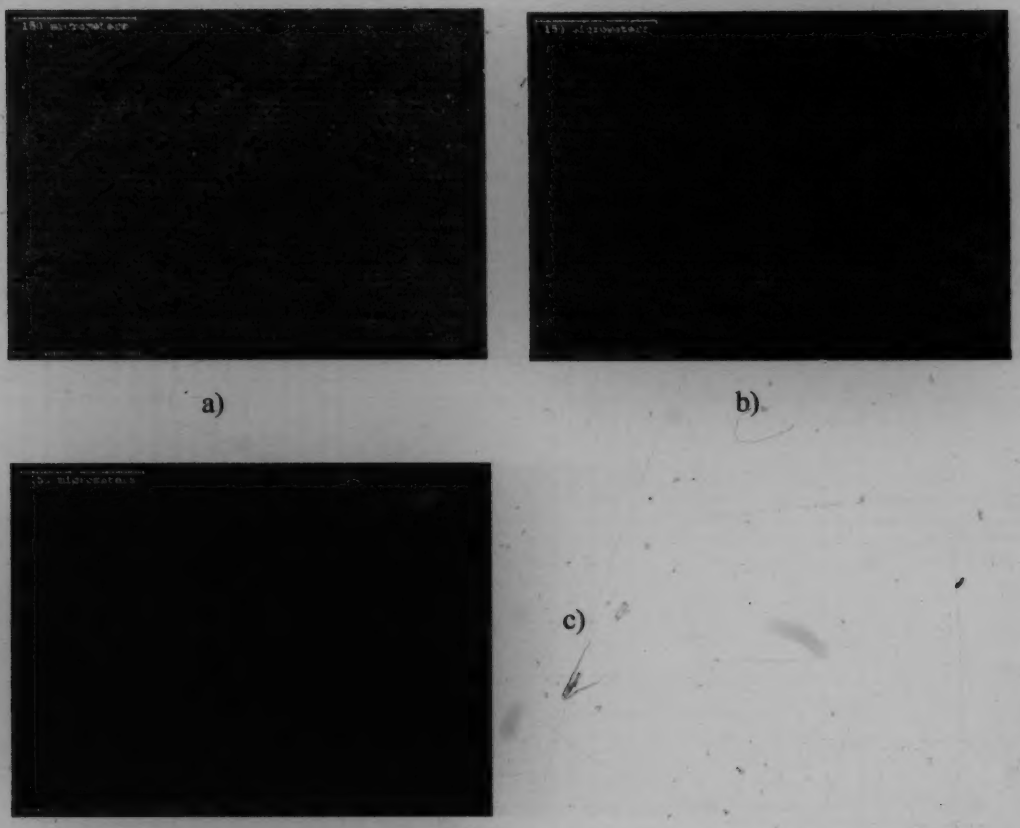

a) b)

c)

Figure 7.23: SEM images of the oxide/substrate interface; a) yttrium-free; b) 0.5%Y; c) 5%Y-containing Stellite 21 samples. The dark colored domains are cross sections of oxide pegs after the oxide scale was removed.

Yttrium additions promoted a finer and more homogeneous distribution of the pegs, which could explain the improved spallation behavior with increasing yttrium content.

The mechanical properties of the pegs could largely affect the spallation behavior. Local mechanical properties of pegs and substrate were determined using a micro-mechanical probe (Fisher Technology Ltd., Windsor, CT, USA) under a maximum load of 100 mN and corresponding load-depth curves were recorded. Each reported value is an average of twenty measurements. Hardness and elastic behavior of the oxide scales were determined from the curves. The results are presented in figure 7.24. The oxide pegs formed on yttrium-free Stellite 21 sample showed the lowest hardness with the largest indentation depth while those developed on yttrium-containing sample showed higher hardness; 5% yttrium-containing sample had the hardest pegs. This is related to the beneficial presence of a yttrium-oxide phase inside the silicon-rich pegs. The η value, which is a measure of elasticity, was not significantly modified by the yttrium addition. It is worthy to observe that the hardness of the pegs is lower than that of the substrate, especially for the yttrium-free sample. In addition, the peg-like structure was coarser and relatively uneven on yttrium-free samples. Lower inter-peg distances and even distribution could favorable affect the spallation behavior of the oxide scale. It seems that the effectiveness of pegs to reduce spallation depend to a larger degree on metallurgical factors rather than interaction with the oxide scale.

The local mechanical properties of the alloy substrate near the oxide/substrate interface were determined using a micro-mechanical probe under a maximum load of 25 mN as described previously. For each sample, 50 measurements were performed at different distances from the oxide/substrate interface at random locations.

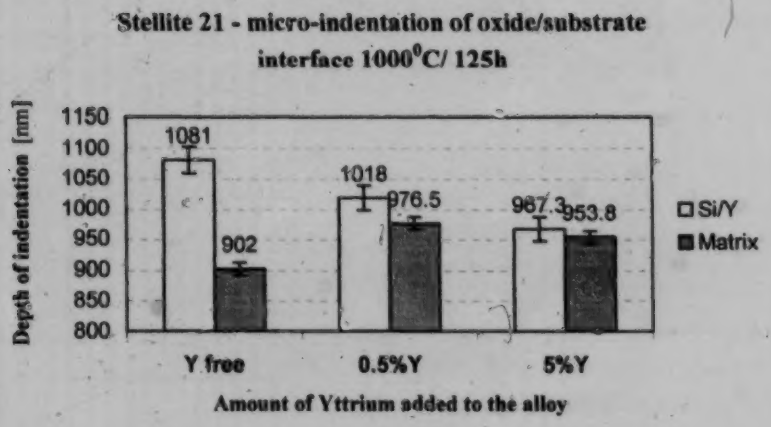

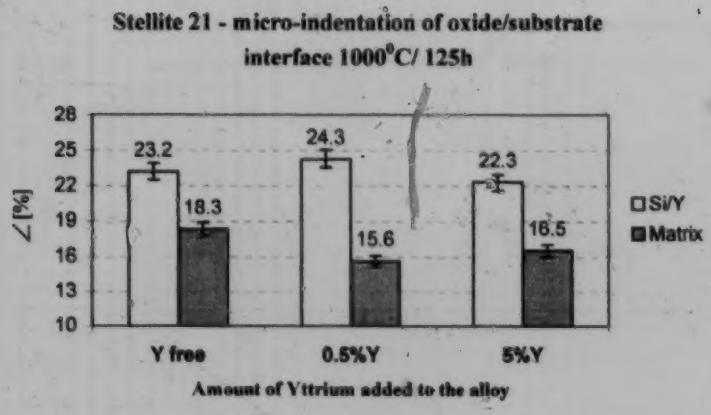

Figure 7.24: Depth of indentation and η ratio of the substrate and peg-like structure near the oxide/matrix interface.

Position of each measurement was recorded and then identified using a light microscope (Olympus PME3-ADL, Japan). The distance from the interface was determined using the image acquisition computer software (Image-Pro Plus). The indentation depth versus distance from the interface is presented in figure 7.25.

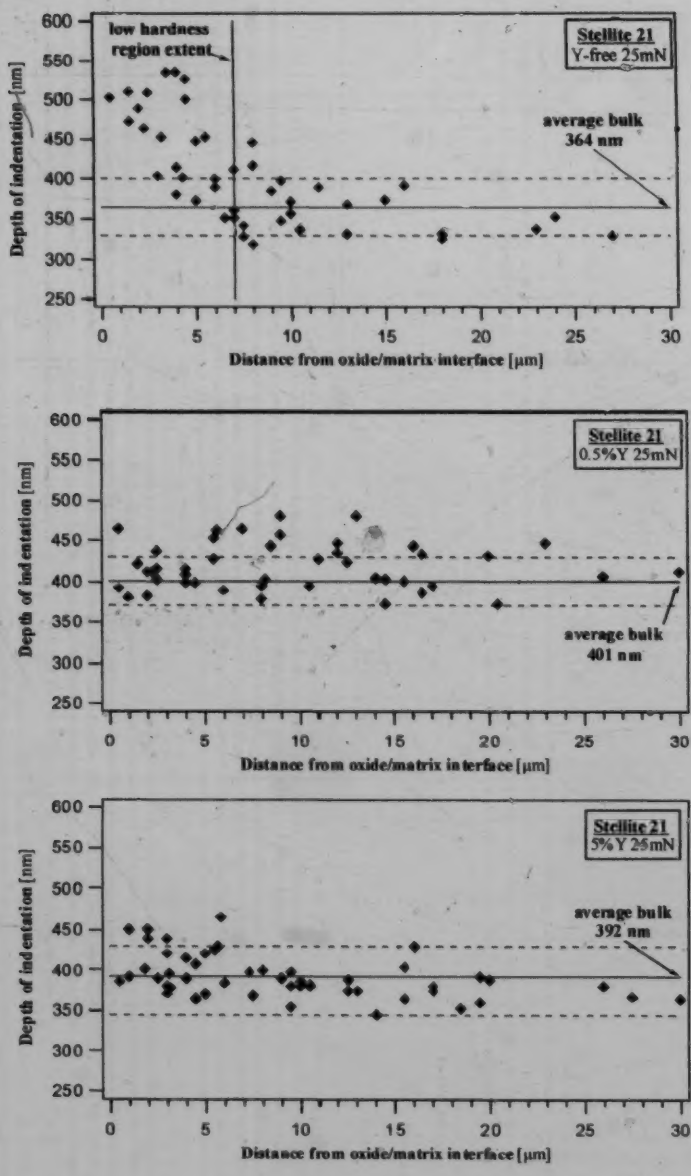

Figure 7.25: Depth of indentation versus distance from oxide/substrate interface a) Y-free; b) 0.5%Y; c) 5%Y - containing Stellite 21.

The dotted lines represent the lower and upper limit of the depth of indentation values recorded from the bulk regions of the samples. The higher is the indentation depth the lower is the hardness. It was observed that for the yttrium-free sample there exists a region (6-7μm) just below the oxide/substrate interface that showed a considerably lower hardness than the substrate. The substrate of the yttrium-containing samples did not show any regions with lower hardness.

EDS line scan analysis was performed in order to determine the concentration profile of the main alloying elements near the oxide/substrate interface. No variation in elemental concentration was detected in the substrate just below the oxide/substrate interface, except for chromium. Figure 7.26 presents the chromium profiles across the oxide/substrate interface. It was demonstrated that the chromium profile had a steeper decrease across the region just below the oxide/substrate interface for the yttrium-free sample. The depression of chromium was less significant for the yttrium-containing samples. The above observation explains the hardness drop just below the oxide/substrate interface of the yttrium-free specimen. Reducing the amount of chromium depletion in the alloy, just beneath the growing oxide scale was also reported in literature for alloys containing yttrium and cerium additions [434]. This is an indirect proof that yttrium reduces the amount of chromium required to form a protective chromia scale.

It is clear that the reactive element addition proved to be effective in a similar manner, both at higher (1000^0C) and lower (600^0C) temperatures.

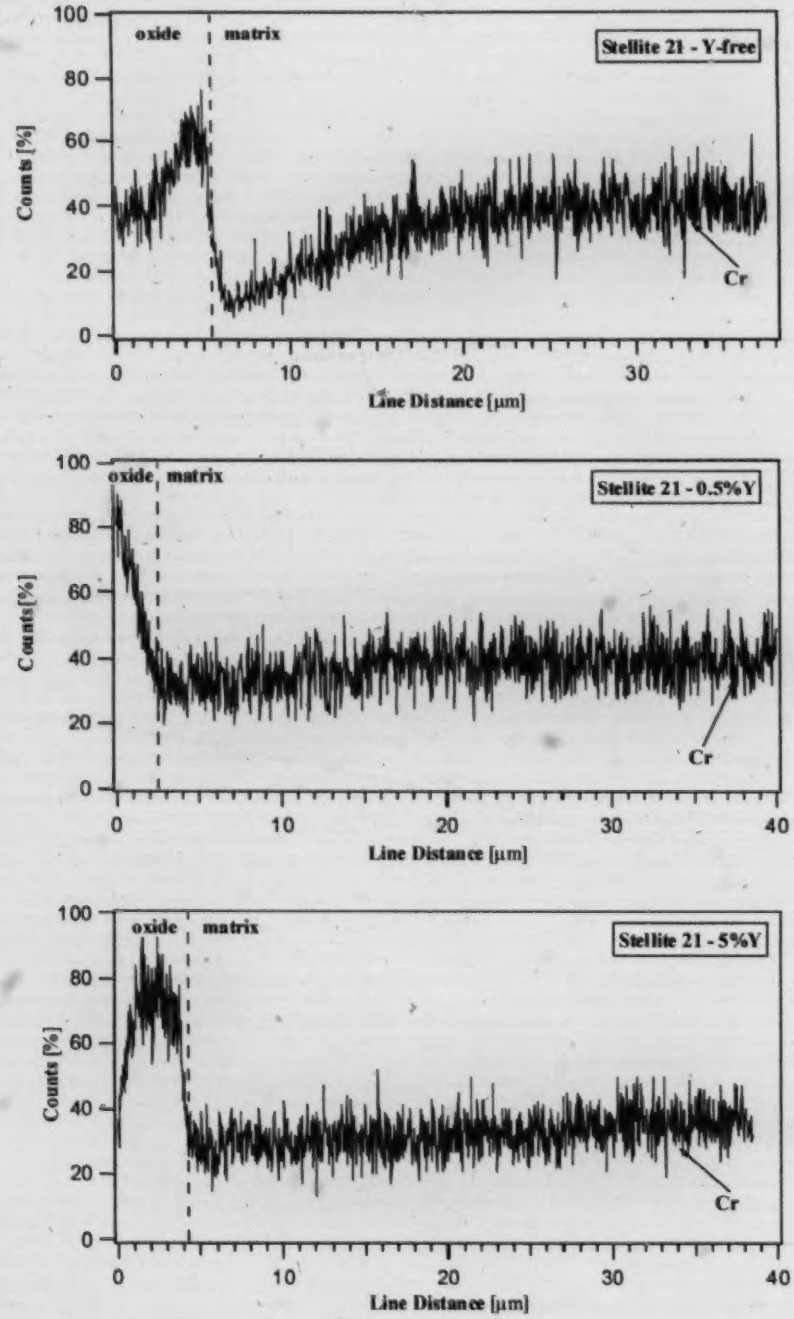

Figure 7.26: Chromium EDS profiles across the oxide/substrate interface: a) Y-free; b) 0.5%Y; c) 5%Y – containing Stellite 21.

8.0 CONCLUSIONS AND POSSIBLE FURTHER RESEARCH TOPICS

This Chapter summarizes the effects of yttrium additions on Stellite 21 and 712 microstructure, mechanical properties of the alloy and its oxide scale, thermal stability, oxidation behavior, and high temperature wear performance. Possible further research topics are suggested.

8.1 Conclusions

1. Stellite 21 consists mainly of Co_3Mo, ε, and γ cobalt phases. Some minor phases such as $M_{23}C_6$ and NiCrCoMo are possibly present. Small additions of yttrium did not result in the formation of new phases in the alloy but coarsened its microstructure. However, a new phase (Co_2YSi_2) was formed at higher yttrium contents, e.g., at 5%. Identified phases in Stellite 712 were similar to those found in Stellite 21 but contained one additional minor phase: Fe_2Mo_3. Similar to Stellite 21, Stellite 712 formed a new phase (Co_2YSi_2) when a relatively large amount of yttrium was added.

2. The bulk hardness of Stellite 21 and 712 was not significantly affected by the yttrium addition.

3. Strain-induced γ→ε transformation (SIT) may play an important role in the wear behavior of Stellite 21 alloy. It was shown that yttrium promotes the SIT.

4. Alloying with yttrium markedly enhanced the mechanical properties of the oxide scale, as well as its adherence to the substrate. The oxide scale developed on yttrium-containing samples contained a new phase, Y_2O_3. However, at larger yttrium addition to Stellite 712, the hardness and roughness of the oxide scale were negatively influenced.

5. The presence of yttrium particularly at a 0.5% level markedly enhanced the high-temperature wear performance of Stellite 21 and 712. Such an improvement may largely result from the superior mechanical properties of the oxide scale containing the Y_2O_3 phase. The formation of a glaze layer also benefited the high-temperature wear resistance of Stellite 21 to some degree. However, the yttrium addition did not noticeably influence the mechanical behavior of the glaze layer.

6. The benefit of an oxide scale to the wear resistance of Stellite 21 was demonstrated by its lower wear in air than in argon. However, the oxide scale became less protective as the normal force was increased. Under high loads (5 N) the oxide film was easier to destroy and the cycle of oxidation- oxide removal - reoxidation could accelerate wear or result in more wear in air than in argon. However, yttrium still benefited the wear resistance at elevated temperatures in air under a larger wearing force. When the load was increased to 10 N the oxide

scale's mechanical properties played a minimal role in resisting high temperature wear.

7. The 0.5% yttrium-containing sample showed the best performance under all conditions at elevated temperatures especially due to its strongest oxide scale with the highest adherence to the substrate. Larger amounts of yttrium negatively affected the high temperature wear performance.

8. It was demonstrated that addition of yttrium to Stellite 21 and 712 had a marked impact on their oxidation behavior. Yttrium led to a significantly improved oxide scale having enhanced adherence to the substrate, higher hardness, smaller grain size, and smaller thickness. It is believed that reactive element additions are more effective at temperatures above 900^0C. The reactive element addition proved to be effective in a similar manner, both at higher and lower temperatures. It was also shown that the oxide scales developed on Stellite 21, with and without yttrium are very complex, consisting of different layers. It was demonstrated that yttrium additions lead to a change in the oxidation mechanism from predominantly outward cation diffusion to predominantly inward anion diffusion.

9. Yttrium has been found to be present near the oxide/substrate interface and at grain boundaries which help reduce the diffusion of both anions and cations across the interface. The decrease of grain boundary diffusion could arise from yttrium segregation at grain boundaries and at the interface (demonstrated in

literature), as its solubility in chromia is low. The 0.5% yttrium-containing sample showed the best performance and the most homogeneous oxide at lower temperatures.

10. At higher temperatures, the oxide layer is keyed to the substrate by pegs composed of rich silicon and yttrium oxides. Yttrium additions led to a finer and more homogeneous distribution of the pegs, which could explain the improved spallation behavior with increasing yttrium content. Also, yttrium modified the morphology of the scale formed: the oxide grain size was reduced after transient oxidation, having the lowest roughness and the most homogeneous outer surface. Exposure to 1000^0C produced internal oxidation of yttrium and silicon. The penetration of oxygen in the alloy is faster along grain boundaries and yttrium-rich phases. Chromium was depleted from the region just below the oxide/matrix interface for the unmodified sample, while less depletion occurred for yttrium-containing samples. The absence of yttrium depletion in the alloy and the similarities of the oxidized zone and the microstructure of the original matrix could be attributed to the low solubility of yttrium and/or the presence of an intermetallic compound (Co_2YSi_2).

11. At longer exposure times at elevated temperature the properties of the oxide scale could be negatively influenced. It was demonstrated that roughness and grain size increased with exposure time following a parabolic behavior. The

increase was more pronounced for yttrium-free scales, which was related to their growth mechanism.

8.2 Suggested further research topics

1. One promising strategy to improve oxidation behavior is the addition of two reactive elements [339,435]. The reason of co-doping is to reduce the amount of the reactive element needed to maintain a good scale adhesion, and a slow growth rate of the oxide scale. Relatively few studies have been performed on the effects of co-doping on oxidation behavior. Most of these studies have focused on nickel and iron based alumina-forming scales alloys. The main effects of co-doping on high temperature oxidation compared to single reactive element additions were to reduce further the oxidation rate, the amount of internal oxidation, and the amount of reactive element oxides incorporated into the oxide scale.

   Investigating the effects of co-doping reactive elements in Stellite alloys on their wear and oxidation behavior may be worthy being studied. As a suggestion, the reactive elements that should be considered for co-doping in addition to yttrium are Hf, Ce and La.

2. It was shown in Chapter 1 that different processing techniques could have a large influence on the wear behavior of the alloys, since each technique could result in specific microstructural features. As a result, it would be of interest to determine

the effect of processing techniques (such as HIP, hardfacing) on the wear performance of Stellite alloys as well as the influence of yttrium in each case.

3. It was shown in Chapter 3 that yttrium had a deleterious effect on arc stability of GTAW and GMAW welding processes; thereby, further research is needed to find the proper welding process that could be used to deposit materials having a large amount of reactive element. Plasma or laser welding might be the right choice. In this case it seems that yttrium will not be used as a metallic addition but rather as an oxide addition to the welding powder due to its high oxygen reactivity and the lower cost of the reactive element oxide. However, the effect of welding parameters on the microstructure and mechanical properties of the welded layer as well the wear resistance must also be assessed.

   In addition, reactive element oxides such as ceria and lantana are used to improve the thermionic emission of tungsten electrodes used by the GTAW process. It will be desirable to use negative polarity on the electrode wire of a GMAW process to increase deposition rates and, thus productivity. This may be achieved by using filler metals having a coating containing reactive elements. However, previous attempts at using emissive coatings such as $CaSO_4$ or $NaCO_3$ under negative polarity were not of practical use. Small amounts of yttrium (Y-SiFe compound) could be used to a flux-cored wire coupling with an "acidic" SMAW electrode (E4303) to improve the mechanical properties of the weld metal [226]. This represents a promising strategy that could avoid the arc instabilities provoked by yttrium presence.

4. As was presented in Chapter 3, the temperature at which $\gamma \rightarrow \varepsilon$ transformation occurs in alloyed cobalt depends on the alloying elements. The transformation temperature for Stellite 21 alloy has not been determined; thereby, DSC experiments are recommended. The influence of yttrium on the transformation temperature could be investigated. The potential answer to the above subjects would lead to a better understanding of the high-temperature behavior of alloys with and without yttrium. In addition, finding the means to control the transformation allows controlling the fraction of γ and ε phases that in turn could control the wear behavior.

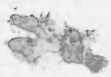

5. Yttrium improved the strain hardening capability of the Stellite 21 alloy (see Chapter 4.2). Further research is needed to determine on the atomic level the mechanism by which yttrium affects the strain induced transformation. The effects of aging temperature and duration on the fractions of γ and ε phases as well as the effect of yttrium on athermal martensite formation need further study.

6. It has been demonstrated that the properties of the oxide layer play a major role in the high-temperature wear behavior under relatively low loads. In practice, the high-temperature alloy scales are based on different types of oxide such as chromia, alumina, or titania. However, there is no knowledge as to which of these oxide scales is more suitable for applications where high temperature wear is a concern. Ranking the wear resistances of different oxide scale combinations

developed on different alloys might be proven useful in designing new alloys and methods to resist high temperature wear.

9.0 BIBLIOGRAPHY

1. E. Rabinowicz, Friction and wear of materials Wiley, New York, 1995, 315.

2. Associate Community on Tribology, NRC Canada, report no. 26556, 1986.

3. M.E. Sikorski, The adhesion of metals and factors that influence it, Wear 7 (1964) 144-162.

4. K.-H. Zum Gahr, Microstructure and wear of materials Elsevier, New York, 1987.

5. E. Pflunger, A. Schroer, P. Voumard, L. Donohue, W.D. Munz, Influence of incorporation of Cr and Y on the wear performance of TiAlN coatings at elevated temperatures, Surface & Coatings Technology, 115 (1999) 17-23.

6. J.L. Sullivan, N.W. Granville, Reciprocating sliding wear of 9% Cr steel in carbon-dioxide at elevated temperatures, Tribology International, 17 (1984) 63-71.

7. S. Atamert, H.K.D.H. Bhadeshia, Comparison of the microstructure and abrasive wear properties of Stellite hardfacing alloys deposited by arc welding and laser cladding, Metals Technology, 20 (1989) 1037-1054.

8. J.N. Aoh, Y.R. Jeng, E.L. Chu, L.T. Wu, On the behavior of surface clad layers under high temperature, Wear, 225-229 (1999) 1114-1122.

9. J.N. Aoh, J.C. Chen, On the wear characteristics of cobalt-based hardfacing layer after thermal fatigue and oxidation, Wear, 250 (2001) 611-620.

10. J. Takadoum, Tribological behavior of alumina sliding on several kinds of materials, Wear, 170 (1993) 285-290.

11. A. Frenk, W. Kurz, Microstructural effects on the sliding wear resistance of a cobalt-based alloy, Wear, 174 (1994) 157-164.

12. L. Wang, D.Y. Li, Effects of yttrium on microstructure, mechanical properties and high-temperature wear behavior of cast Stellite 6 alloy, Wear, 255 (2003) 535-544.

13. A. Halstead, R.D. Rawlings, The effect of iron additions on the microstructure and properties of the Tribaloy Co-Mo-Cr-Si wear resistant alloys, Journal of Materials Science, 20 (1985) 1693-1704.

14. T. C. Sims, N. S. Stoloff, W. C. Hagel, eds. Superalloys II, John Wiley & Sons, New York, 1987.

15. M. Hawkins, Why we need cobalt?, Transactions of the Institution of Mining and Metallurgy B, 110 (2001) B66-B70.

16. J.S. Garcia, M.A. Medrano, A.S. Rodriguez, Formation of hcp martensite during the isothermal aging of an fcc Co-27Cr-5Mo-0.05C implant alloy, Metallurgical and Materials Transactions A, 30 (1999) 1177-1184.

17. C. Montero-Ocampo, M. Talavera, H. Lopez, Effect of alloy preheating on the mechanical properties of as-cast Co-Cr-Mo-C alloys, Metallurgical and Materials Transactions A, 30 (1999) 611-620.

18. L. M. Torres, A.S. Rodriguez, Plastic deformation behavior of low carbon Co-Cr-Mo alloys, Processing and Fabrication of Advanced Materials, 5 (1996) 691-702.

19. M.S. Aguilar, H.F. Lopez, A.S. Rodriguez, The effect of carbon on the mechanical strength of heat treated cast Co27Cr5Mo alloys, Processing and Fabrication of Advanced Materials, 5 (1996) 69-79.

20. L.Z. Zhuang, E.W. Langer, Effects of alloy additions on the microstructures and tensile properties of cast Co-Cr-Mo alloy used for surgical implants, Journal of Materials Science, 24 (1989) 4324-4330.

21. L.Q. Shi, D.O. Northwood, Z.W. Cao, The properties of a wrought biomedical cobalt-chromium alloy, Journal of Materials Science, 29 (1994) 1233-1238.

22. A.J. Saldivar, A.M. Medrano, A.S. Rodriguez, Effect of solution treatment on the fcc/hcp isothermal transformation in Co27Cr5Mo0.05C aged at 800^{0}C, Scripta Materialia, 40 (1999) 712-722.

23. H. L. Du, P.K. Datta, I. Inman, R. Geurts, C. Kubel, Microscopy of wear affected surface produced during sliding of Nimonic 80A against Stellite 6 at 20^{0}C, Materials Science and Engineering A, 357 (2003) 412-422.

24. P. Crook, Cobalt and Cobalt Alloys, ASM Metal Handbook, vol. 2. Materials Park, Ohio, (1993) 446-456.

25. E. Lemaire, M. Le Calvar, Evidence of tribocorrosion wear in pressurized water reactors, Wear, 249 (2001) 338-344.

26. ASM International, Nickel, cobalt and their alloys, Materials Park, Ohio, (2000).

27. K.C. Antony, Wear resistant cobalt base alloys, Journal of Metals, 35 (1983) 52-60.

28. A.J. Persson, S. Jacobson, S. Hogmark, Effect of temperature on friction and galling of laser processed Norem 02 and Stellite 21, Wear, 255 (2003) 498-503.

29. J.R. Nicholls, Coatings and hardfacing alloys for corrosion and wear resistance in diesel engines, Materials Science and Technology, 10 (1994) 1002-1012.

30. J.R. Nicholls, Corrosion and wear resistance of some novel and current diesel exhaust valve materials, Materials at High Temperatures, 12 (1994) 35-46.

31. G.N. Beddoes, Valve materials and design, Powder Metallurgy, 35 (1992) 260-266.

32. J. Vikstrom, Galling resistance of hardfacing alloys replacing Stellite, Wear, 143 (1994) 143-146.

33. H.J. Kim, B.H. Yoon, C.H. Lee, Sliding wear performance in molten Zn-Al bath of cobalt-based over-layers produced by plasma transferred arc weld-surfacing, Wear, 254 (2003) 408-414.

34. S.C. Agarwal, H. Ocken, The microstructure and galling wear of a laser-melted cobalt-base hardfacing alloy, Wear, 140 (1990) 223-233.

35. E.S. Hannan, New valve materials for diesel engines, in: High temperature materials for power engineering, Liege, Belgium, (1990) 817-842.

36. I. Kvernes, P. Kofstad, M. Seiersten, High temperature corrosion and protection of diesel engine exhaust valves, in: Proceedings of the 14th International congress on combustion engines, Diesel engines, CIMAC, Helsinki, (1981).

37. T. Yamada, H. Sekiguchi, M. Mizushina, Development of ceramic exhaust valves, in: CIMAC, Proceedings of the 16th international congress on combustion engines, Diesel engines, Vol. II, Oslo, (1985).

38. T. Yamada, H. Sekiguchi, M. Mizushina, K. Takahashi, N. Yoshida, Ceramic coating exhaust valve, in: CIMAC, Proceedings of the 17th international congress on combustion engines, Vol. 2D, Warsaw, (1987).

39. H. Ocken, Reducing the cobalt inventory in light water reactors, Nuclear Technology, 68 (1984) 18-28.

40. H. Ocken, Activation of Co released by in-core and ex-core sources Health Physics, 58 (1990) 259-261.

41. M. Corchia, P. Delogu, F. Nenci, A. Belmondo, S. Corcoruto, W. Stabielli, Microstructural aspects of wear-resistant Stellite and Colmonoy coatings by laser processing, Wear, 119 (1987). 137-152.

42. H.J. Kim, Y.J. Kim, Wear and corrosion resistance of PTA weld surfaced Ni and Co based alloy layers, Surface Engineering, 15 (1999) 495-501.

43. K. Lee, S. Lee, Y. Kim, H.S. Hong, Y. Oh, S. Kim, The effects of additive elements on the sliding wear behavior of Fe-base hardfacing alloys, Wear, 255 (2003) 481-488.

44. H. Ocken, The galling wear resistance of new iron-base hardfacing alloys: a comparison with established fcobalt- and nickel-base alloys, Surface & Coatings Technology, 76-77 (1995) 456-461.

45. C.B. Bahn, B.C. Han, J.S. Bum, I.S. Hwang, C.B. Lee, Wear performance and activity reduction effect of Co-free valves in PWR environment, Nuclear Engineering & Design 231 (2004) 51-65.

46. G.L. Goswami, S. Kumar, R. Galun, B.L. Mordike, Laser cladding of Ni-Mo alloys for hardfacing applications, Lasers in Engineering, 13 (2003) 1-12.

47. S.H. Kang, T. Shinoda, Y. Kato, H.S. and Jeong, Thermal fatigue characteristics of PTA hardfaced steels, Surface Engineering, 17 (2001) 498-504.

48. A. Osma, E.S. Kayali, M.L. Ovecoglu, The effect of elevated temperature and silicon addition on a cobalt-based wear resistant superlloy, Journal of Materials Science, 31 (1996) 4603-4608.

49. V. Kuzuku, M. Ceylan, H. Celik, I. Aksoy, Microstructure and phase analyses of Stellite 6 plus 6 wt% Mo alloy Journal of Materials Processing & Technology, 69 (1997) 257-263.

50. V. Kuzuku, M. Ceylan, H. Celik, I. Aksoy, Phase investigation of a cobalt base alloy containing Cr, Ni, W and C Journal of Materials Processing & Technology, 74 (1998) 137-141.

51. V. Kuzuku, M. Ceylan, H. Celik, I. Aksoy, An investigation of Stellite 6 containing 5 wt% silicon, Journal of Materials Processing & Technology, 79 (1998) 47-51.

52. J.D. Gates, G.J. Gore, Wear of metals: Philosophies and practicalities, Materials Forum, 19 (1995) 53-89.

53. H. Czichos, Tribology: a systems approach to the science and technology of friction, lubrication, and wear, Elsevier Scientific Pub. Co., New York, (1978) 14-23.

54. M. Scherge, D. Shakhvorostov, K. and Pohlmann, Fundamental wear mechanism of metals, Wear, 255 (2003) 395-400.

55. K. Kato, Micro-mechanisms of Wear – Wear modes, Wear, 153 (1992) 277-295.

56. S. Chevalier, G. Bonnet, P. Fielitz, G. Strehl, S. Weber, G. Borchardt, J.C. Colson, J.P. Larpin, Effects of a reactive element on isothermal and cyclioc oxidation of chromia-forming alloys: SEM/EDS, TEM, and SIMS investigations, Materials at High Temperatures, 17 (2000) 247-256.

57. M. Boas, A. Rosen, Effect of load on adhesive wear of steels, Wear 44 (1977) 213-222.

58. J.A. Greenwoo, J.B. Williams, Contact of nominally flat surfaces, Proceedings of the Royal Society of London A, 295 (1966) 300-319.

59. J.S. Robinson, J. McCracken, Combating industrial wear by hardfacing, Materials Forum 22 (1998) 97-121.

60. A. Iwabuchi, H. Kuboshawa, K. Hori, The dependence of the transition from severe to mild wear on load and surface roughness when the oxide particles are supplied before sliding, Wear 139 (1990) 319-333.

61. F.P. Bowden, J.E. Young, Friction of clean metals and the influence of adsorbed films, Proceedings of the Royal Society of London A, 208 (1951) 311-325.

62. D.P. Smith, Tribology of the belt-driven data tape cartridge, Tribology International 31 (1998) 465-477.

63. M Jasty, D. D. Goetz, C. R. Bragdon, K. R. Lee, A. E. Hanson, J. R. Elder, W.H. Harris, Wear of polyethylene acetabular components in total hip arthroplasty. An analysis of one hundred and twenty-eight components retrieved at autopsy or revision operations, Journal of Bone and Joint Surgery American 79 (1997) 348-358.

64. I.M. Hutchings, Tribology: friction and wear of engineering materials, CRC Press, Boca Raton, (1992).

65. K. Hokkirigawa, K. Kato, An experimental and theoretical investigation of plowing, cutting and wedge formation during abrasive wear, Tribology Internationa, 21 (1988) 51-57.

66. K.M. Mashloosh, T.S. Eyre, Abrasive wear and its application to digger teeth, Tribology International 18 (1985) 259-266.

67. D.J. Stein, D. Hetherington, T. Guilinger, J.L. Cecchi, In situ electrochemical investigation of tungsten electrochemical behavior during chemical mechanical polishing, Journal of the Electrochemical Society 145 (1998) 3190-3196.

68. J.M. Steigerwald, S.P. Murarka, R.J. Gutmann, Chemical mechanical planarization of microelectronic materials, John Wiley & Sons, Inc., (1997).

69. M.R. Olivier, Chemical-mechanical planarization of semiconductor materials, Vol. 69, Springer, Berlin, (2004).

70. K.G. Budinski, Surface engineering for wear resistance, Prentice Hall, Englewood Cliffs, N.J., (1988).

71. E. Rabinowicz, Friction seizure and galling seizure, Wear 25 (1973) 357-363.

72. A. Ekberg, Wear - Some Notes, in: Contact mechanics and wear, Department of Solid Mechanics, Chalmers University of Technology, (1997).

73. G.W. Stachowiak, Tribology of wear resistant surfaces, Materials Forum, 22 (1998) 63-77.

74. J.F. Archard, Contact and rubbing of flat surfaces, Journal of Applied Physics, 24 (1953) 981-988.

75. M.J. Murray, P.J. Mutton, J.D. Watson, Abrasive wear mechanisms in steels, Journal of Lubrication Technology, 104 (1982) 9-16.

76. K. Hokkirigawa, K. Kato, Z.Z. Li, The effect of hardness on the transition of the abrasive wear mechanism of steels, Wear, 123 (1988) 241-251.

77. M.O.A. Mokhtar, The effect of hardness on the frictional behavior of metals, Wear, 78 (1982) 297-304.

78. N.P. Suh, Delamination Theory of Wear, Wear, 25 (1973) 111-124.

79. D.Y. Li, X. Ma, Variations in wear resistance of a novel triboalloy - Pseudoelastic TiNi alloy - with respect to its pseudoelasticity and hardness, Journal of Materials Science & Technology, 17 (2001) 45-46.

80. R. Liu, D.Y. Li, Modification of Archard's equation by taking account of elastic/pseudoelastic properties of materials, Wear, 250 (2001) 956-964.

81. N.C. Welsh, Dry wear of steels .I. General pattern of behaviour, Philosophical Transactions of the Royal Society of London Series A, 257 (1965) 31-71.

82. C. Subramanian, Wear of Al-12.3 wt-percent Si alloy sliding against various counterface materials, Scripta Metallurgica & Materialia, 25 (1991) 1369-1374.

83. E. Rabinowicz. Influence of compatibility on different tribological phenomena, ASLE Transactions, 14 (1971) 206-213.

84. E. Rabinowicz, Determination of compatibility of metals through static friction tests, ASLE Transactions, 14 (1971) 198-205.

85. D.H. Buckley, R.L. Johnson, Friction and wear of hexagonal metals and alloys as related to crystal structure and lattice parameters in vacuum, ASLE Transaction, 9 (1966) 121-135.

86. F.P. Bowden, T.H.C. Childs, Friction and deformation of clean metals at very low temperatures, Proceedings of the Royal Society of London A, 312 (1969) 451-466.

87. D.H. Buckley, R.L. Johnson, Influence of crystal structure and some properties of hexagonal metals on friction and adhesion, Wear, 11 (1968) 405-419.

88. K.J. Bhansali, Adhesive wear of Ni and Co-base alloys, Wear, 60 (1980) 95-110.

89. H. Mishina, Chemisorption of Ddiatomic gas molecules and atmospheric characteristics in adhesive wear and friction of metals, Wear, 180 (1995) 1-7.

90. D.H.E. Persson, S. Jacobson, S. Hogmark, The influence of phase transformations and oxidation on the galling resistance and low friction behavior of a laser processed Co—based alloy, Wear, 254 (2003) 1134-1140.

91. G.I. Finch, R.T. Spurr, Surface changes due to sliding - Discussion, Proceedings of the Royal Society of London A, 212 (1952) 462-464.

92. Z.Y. Yang, M.G.S. Naylor, D.A. Rigney, Sliding wear of 304 and 310 stainless-steels, Wear, 105 (1985) 73-86.

93. S.H. Bian, S. Maj, D.W. Borland, The unlubricated sliding wear of steels - the role of the hardness of the friction pair, Wea, 166 (1993) 1-5.

94. D.A. Rigney, The roles of hardness in the sliding behavior of materials, Wear, 175 (1994) 63-69.

95. H.H. Uhlig, R.W. Revie, Corrosion and corrosion control: an introduction to corrosion science and engineering,Wiley, New York, (1985).

96. G. Wranglén, An introduction to corrosion and protection of metals, Chapman & Hall, London, (1985).

97. B.D. Craig, Fundamental aspects of corrosion films in corrosion science, Plenum Press, New York, (1991).

98. S. Jahanmir, N.P. Suh, E.P. Abrahamson, Microscopic observations of wear sheet formation by delamination, Wear 28 (1974) 235-249.

99. S. Jahanmir, N.P. Suh, Mechanics of subsurface void nucleation in delamination Wear, Wear 44 (1977) 17-38.

100. N.P. Suh, Overview of delamination theory of wear, Wear 44 (1977) 1-16.

101. J.R. Fleming, N.P. Suh, Mechanics of crack-propagation in delamination Wear, Wear 44 (1977) 39-56.

102. N. Saka, A.M. Eleiche, N.P. Suh, Wear of metals at high sliding speeds, Wear, 44 (1977) 109-125.

103. D.A. Rigney, W.A. Glaeser, Significance of near-surface microstructure in wear process, Wear, 46 (1978) 241-250.

104. D.A. Rigney, J.P. Hirth, Plastic deformation and sliding friction of metals, Wear, 53 (1979) 345-370.

105. J.P. Hirth, D.A. Rigney, Crystal plasticity and delamination theory of wear, Wea,r 39 (1976) 133-141.

106. A.A.W. Thompson, Yielding in nickel as a function of grain or cell-size, Acta Metallurgica, 23 (1975) 1337-1342.

107. I.I. Garbar, Formation and separation of the fragmented surface of low-carbon steel and copper under friction, Wear, 198 (1996) 86-92.

108. I.I. Garbar, J.V. Skorinin, Metal-Surface layer structure formation under sliding friction, Wear, 51 (1978) 327-336.

109. D.A. Hughes, Microstructure and flow-stress of deformed polycrystalline metals, Scripta Metallurgica & Materialia, 27 (1992) 969-974.

110. I.I. Garbar, Gradation of oxidational wear of metals, Tribology International, 35 (2002) 749-755.

111. H. Mishina, Atmospheric characteristics in friction and wear of metals, Wear, 152 (1992) 99-110.

112. H. Mishina, Chemisorption of diatomic gas molecules and atmospheric characteristics in adhesive wear and friction of metals, Wear 180 (1995) 1-7.

113. T.S. Eyre, D. Maynard, Surface aspects of unlubricated metal-to-metal wear, Wear, 18 (1971) 301-310.

114. A. Iwabuchi, H. Kuboshawa, K. Hori, The dependence of the transition from severe to mild wear on load and surface roughness when the oxide particles are supplied before sliding, Wear 139 (1990) 319-333.

115. J.F. Archard, W. Hirst, The wear of metals under unlubricated conditions, Proceedings of the Royal Society of London A, 236 (1956) 397-410.

116. C. Subramanian, Effects of sliding speed on the unlubricated wear behavior of Al-12.3wt-Percent Si alloy, Wear, 151 (1991) 97-110.

117. R.M. Farrell, T.S. Eyre, Relationship between load and sliding distance in initiation of mild wear in steels, Wear, 15 (1970) 359-372.

118. N.C. Welsh, Frictional heating and its influence on the wear of steel, Journal of Applied Physics, 28 (1957) 960-968.

119. S.C. Lim, M.F. Ashby, J.H. Brunton, Wear-rate transitions and their relationship to wear mechanisms, Acta Metallurgica, 35 (1987) 1343-1348.

120. T.F.J. Quinn, Oxidational wear modelling Part III. The effects of speed and elevated temperatures, Wear, 216 (1998) 262-275.

121. T.F.J. Quinn, Review of oxidational wear. 1. The origins of oxidational wear, Tribology International, 16 (1983) 257-271.

122. J.L. Sullivan, T.F.J. Quinn, D.M. Rowson, Developments in the oxidational theory of mild wear, Tribology International, 13 (1980) 153-158.

123. H. So, The mechanism of oxidational wear, Wear 184 (1995) 161-167.

124. T.F.J. Quinn, Oxidational wear modeling. 2. The general-theory of oxidational wear, Wear, 175 (1994) 199-208.

125. T.F.J. Quinn, Computational methods applied to oxidational wear, Wear, 199 (1996) 169-180.

126. T.F.J. Quinn, The oxidational wear of low alloy steels, Tribology International, 35 (2002) 691-715.

127. T.F.J. Quinn, Review of oxidational wear. 2. Recent developments and future-trends in oxidational wear research, Tribology International, 16 (1983) 305-315.

128. T.F.J. Quinn, Oxidational wear, Wear, 18 (1971) 413-419.

129. T.F.J. Quinn, Oxidational wear modeling- Part1, Wear, 153 (1992) 179-200.

130. S.C. Lim, M.F. Ashby, Wear mechanism maps, Acta Metallurgica, 35 (1987) 1-24.

131. J. Molgaard, Discussion of oxidation, oxide thickness and oxide transfer in wear, Wear, 40 (1976) 277-291.

132. J. Molgaard, V.K. Srivastava, Activation-energy of oxidation in wear, Wear, 41 (1977) 263-270.

133. W.M. Rainforth, A.J. Leonard, C. Perrin, A. Bedolla-Jacuinde, Y. Wang, H. Jones, Q. Luo, High resolution observations of friction-induced oxide and its interaction with the worn surface, Tribology International, 35 (2002) 731-748.

134. H.S. Hong, The role of atmospheres and lubricants in the oxidational wear of metals, Tribology International, 35 (2002) 725-729.

135. T.F.J. Quinn, D.M. Rowson, J.L. Sullivan, Application of the oxidational theory of mild wear to the sliding wear of low-alloy steel, Wear, 65 (1980) 1-20.

136. T.F.J. Quinn, J.L. Sullivan, D.M. Rowson, Origins and development of oxidational wear at low ambient-temperatures, Wear, 94 (1984) 175-191.

137. D.J. Barnes, J.E. Wilson, F.H. Stott, G.C. Wood, Influence of oxide-films on friction and wear of Fe-5% Cr alloy in controlled environments, Wear, 45 (1977) 161-176.

138. P.D. Wood, P.K. Datta, J.S. Burnell-Gray, N. Wood, Investigation into the high temperature properties of alloys contacting against different counterfaces, Materials Science Forum, 251-254 (1992) 467-474.

139. F.H. Stott, High-temperature sliding wear of metals, Tribology International, 35 (2002) 489-495.

140. P. Kofstad, High-temperature oxidation of metals, Wiley, New York, (1966).

141. A.P. Semenov, Tribology at high temperatures, Tribology International, 28 (1995) 45-50.

142. F.H. Stott, The role of oxidation in the wear of alloys, Tribology International, 31 (1998) 61-71.

143. F. Murray, S.J. Calabrese, Low speed sliding behavior of metallic couples at temperatures up to 800^0C, Lubrication Engineering, 49 (1993) 387-397.

144. F.H. Stott, G.C. Wood, The influence of oxides on the friction and wear of alloys, Tribology International, 11 (1978) 211-218.

145. J.E. Wilson, F.H. Stott, G.C. Wood, The development of wear protective oxides and their influence on sliding friction, Proceedings of the Royal Society of London A, 369 (1980) 557-574.

146. J.L. Sullivan, S.S. Athwal, Mild wear of a low alloy steel at temperature up to 500^0C, Tribology International, 16 (1983) 123-131.

147. J.K. Lancaster, Formation of surface films at transition between mild and severe metallic wear, Proceedings of the Royal Society of London A, 273 (1963) 466-483.

148. F.H. Stott, D.S. Lin, G.C. Wood, Structure and mechanism of formation of glaze oxide layers produced on nickel-based alloys during wear at high-temperatures, Corrosion Science, 13 (1973) 449-469.

149. F.H. Stott, J. Glascott, G.C. Wood, The sliding wear of commercial Fe-12% Cr alloys at high-temperature, Wear, 101 (1985) 311-324.

150. F.H. Stott, D.S. Lin, G.C. Wood, C.W. Stevenson, Tribological behavior of nickel and nickel-chromium alloys at temperatures from 20^0C to 800^0C, Wear, 36 (1976) 147-174.

151. P.T. Newman, J. Skinner, The high-temperature sliding wear of stainless-steel in a CO_2 atmosphere - The effect of adding low concentrations of O_2, Wear, 112 (1986) 291-325.

152. S.W.E. Earles, N. Tenwick, Friction and wear properties of Nimonic 75 at ambient temperatures up to 810^0C, Wear, 19 (1972) 287-299.

153. D.Y. Wang, D.L. Shu, X.C. Guo, Effect of microstructure and properties on the high-temperature wear characteristics of 3Cr2W8V (H21) steel, Wear, 119 (1987) 101-117.

154. A.F. Smith, The unlubricated reciprocating sliding wear of 316 stainless-steel in CO_2 at 20^0C and at 600^0C, Tribology International, 19 (1986) 65-71.

155. J.L. Sullivan, N.W. Granville, Reciprocating sliding wear of 9% Cr steel in carbon-dioxide at elevated temperatures, Tribology International, 17 (1984) 63-71.

156. P.M. Dunckley, T.F.J. Quinn, J. Salter, D.H. Buckley, Studies of unlubricated wear of a commercial cobalt-base alloy at temperatures up to about 400^0C, ASLE Transactions, 19 (1976) 221-231.

157. D.S. Lin, G.C. Wood, M.B. Peterson, T.F.J. Quinn, Effects of elevated ambient-temperatures on friction and wear behavior of some commercial nickel-base alloys, ASLE Transactions, 17 (1974) 251-262.

158. J.P. Tu, X.H. Jie, Z.Y. Mao, M. Matsumura, The effect of temperatures on the unlubricated sliding wear of 5CrNiMo steel against 40 MnB steeel in the range 400-600^0C, Tribology International, 31 (1998) 347-353.

159. P.J. Blau, Friction microprobe investigation of particle layer effects on sliding friction, Wear, 162-164 (1993)102-109.

160. F.H. Stott, G.C. Wood, The influence of oxides in high-temperature wear". High Temperature Corrosion, NACE, Huston, (1983), 406-412.

161. Y.S. Wang, S. Narasimhan, J.M. Larson, J.E. Larson, G.C.Barber, The effect of operating conditions on heavy duty engine valve seat wear, Wear, 201 (1996) 15-25.

162. D.J. Barnes, J.E. Wilson, F.H. Stott, G.C. Wood, Influence of specimen geometry and sliding mode on friction and wear of iron-chromium alloys in controlled environments, Wear, 45 (1977) 97-111.

163. F.H. Stott, C.W. Stevenson, G.C. Wood, Friction and wear properties of Stellite 31 at temperatures from 293 to 1073 K, Metals Technology, 4 (1977) 66-74.

164. D.J. Barnes, F.H. Stott, G.C. Wood, Frictional behavior of iron and iron-chromium alloys at elevated temperatures, Wear, 45 (1977) 199-209.

165. J. Jiang, F.H. Stott, M.M. Stack, The effect of partial pressure of oxygen on the tribological behavior of a nickel-based alloy at elevated temperatures, Wear, 203-204 (1997) 615-625.

166. D.J. Barnes, A.E. Lee, D. Tabor, Effect of temperature and environment on friction of some well characterized refractory surfaces, Wear, 31 (1975) 63-76.

167. J. Jiang, F.H. Stott, M.M. Stack, The role of triboparticulates in dry sliding wear, Tribology International, 31 (1998) 245-256.

168. J. Glascott, G.C. Wood, F.H. Stott, The influence of experimental variables on the development and maintenance of wear protective oxides during sliding of high-temperature iron-base alloys, Proceedings of the Institution of Mechanical Engineers C 199 (1985) 35-41.

169. P.J. Blau, Mechanisms for transitional friction and wear behavior of sliding metals, Wear, 72 (1981) 55-66.

170. F.H. Stott, J.Glascott, G.C. Wood, Models for the generation of oxides during sliding wear, Proceedings of the Royal Society of London A, 402 (1985) 167-186.

171. F.H. Stott, D.S. Lin, G.C. Wood, C.W. Stevenson, The mechanism of oxide film formation during the wear of Ni- and Co-base alloys in air at elevated temperatures, in: Proceedings of the sixth International Congress on Metallic Corrosion, Vol. 1, Sydney (1975) 1010-1026.

172. E.R. Leheup, R.E. Pendlebury, Unlubricated reciprocating wear of stainless-steel with an interfacial air-flow, Wear, 142 (1991) 351-372.

173. A. Iwabuchi, K. Hori, H. Kubosawa, The effect of oxide particles supplied at the interface before sliding on the severe mild wear transition, Wear, 128 (1988) 123-137.

174. J. Jiang, F.H. Stott, M.M. Stack, A generic model for dry sliding wear of metals at elevated temperatures, Wear, 256 (2004) 973-985.

175. J. Jiang, F.H. Stott, M.M. Stack, A mathematical model for sliding wear of metals at elevated temperatures, Wear, 181 (1995) 20-31.

176. H.Y. Lee, I.S. Kim, S.S. Kang, H.D. Chung, A study on wear coefficients and mechanisms of steam generator tube materials, Wear, 250 (2001) 718-725.

177. I.W. Lyo, H.S. Ahn, D.S. Lim, Microstructure and tribological properties of plasma-sprayed chromium oxide-molybdenum oxide composite coatings, Surface & Coatings Technology, 163-164 (2003) 413-421.

178. I.A. Inman, S.R. Rose, P.K. Datta, Studies of high temperature sliding wear of metallic dissimilar interfaces II: Incoloy MA956 versus Stellite 6, Tribology International 39 (2006) 1361-1375.

179. H. Kashani, A. Amadeh, H.M. Ghasemi, Room and high temperature wear behaviors of nickel and cobalt base weld overlay coatings on hot forging dies, Wear 262 (2007) 800-806.

180. H.L. Du, S. Datta, S. Inman, J.S. Burnell-Gray, Q. Luo, Microscopy of glazed layers formed during high temperature sliding wear at 750^0C, Wear 254 (2003) 461-467.

181. H.L. Du, P.K. Datta, I.A. Inman, E. Kuzman, K. Suvegh, T. Marek, A. Vertes, Investigations of microstructure and defect structures in wear affected region created on Nimonic 80A during high temperature wear, Tribology Letters, 18 (2005) 395-404.

182. J. Jiang, F.H. Stott, M.M. Stack, Characterization of wear scar surfaces using combined three-dimensional topographic analysis and contact resistance measurements, Tribology International, 30 (1997) 517-526.

183. F.H. Stott, M.P. Jordan, The effects of load and substrate hardness on the development and maintenance of wear-protective layers during sliding at elevated temperatures, Wear, 250 (2001) 391-400.

184. A. Fischer, Mechanisms of high temperature sliding abrasion of metallic materials, Wear, 152 (1992) 151-159.

185. H. Berns, A. Fischer, Tribological stability of metallic materials at elevated-temperatures, Wear, 162 (1993) 441-449.

186. E. Pfluger, A. Schroer, P. Voumard, L. Donohue, W.D. Munz, Influence of incorporation of Cr and Y on the wear performance of TiAlN coatings at elevated temperatures, Surface & Coatings Technology, 115 (1999) 17-23.

187. T. Polcar, N.M.G. Parreira, R. Novak, Friction and wear behavior of CrN coating at temperatures up to 500^0C, Surface & Coatings Technology, 201 (2007) 5228-5235.

188. C. Muratore, J.J. Hu, A.A. Voevodin, Adaptive nanocomposite coatings with a titanium nitride diffusion barrier mask for high-temperature tribological applications, Thin Solid Films, 515 (2007) 3638-3643.

189. M. Labaiz, I. Guillot, G. Beranger, High temperature friction and wear of the pair of steels 28NCDV10 and Z20C13. Influence of preoxidation. Comparison with Al_2O_3, and Al_2O_3-TiO_2 ceramics, Revue De Metallurgie, 92 (1995) 1331-1340.

190. C.R. Das, S.K. Albert, A.K. Bhaduri, G. Kempulraj, A novel procedure for fabrication of wear-resistant bushes for high-temperature application, Journal of Materials Processing Technology, 141 (2003) 60-66.

191. C.K. Kim, S. Lee, J.Y. Jung, S. Ahn, Effects of complex carbide fraction on high-temperature wear properties of hardfacing alloys reinforced with complex carbides, Materials Science and Engineering A, 349 (2003) 1-11.

192. X.B. Liu, H.M. Wang, Microstructure and tribological properties of laser clad gamma/Cr7C3/TiC composite coatings on gamma-TiA1 intermetallic alloy, Wear, 262 (2007) 514-521.

193. P. Hancock, J.R. Nicholls, failure of oxides scales, Materials at High Temperatures, 12 (1994) 209-217.

194. J.H. Arps, R.A. Page, G. Dearnaley, Reduction of wear in critical engine components using ion-beam-assisted deposition and ion implantation, Surface & Coatings Technology, 84 (1996) 579-583.

195. H. Koiprasert, S. Dumrongrattana, P. Niranatlumpong, Thermally sprayed coatings for protection of fretting wear in land-based gas-turbine engine, Wear, 257 (2004) 1-7.

196. Y. Chen, H.M. Wang, High-temperature wear resistance of a laser clad TiC reinforced FeAl in situ composite coating, Surface & Coatings Technology, 179 (2004) 252-256.

197. Y. Chen, H.M. Wang, Microstructure and high-temperature wear resistance of a laser surface alloyed gamma-TiAl with carbon, Applied Surface Science, 220 (2003) 186-192.

198. A. Ramalho, J.P. Celis, High temperature fretting behavior of plasma vapor deposition TiN coatings, Surface & Coatings Technology, 155 (2002) 169-175.

199. W.C. Wang, Application of a high temperature self-lubricating composite coating on steam turbine components, Surface & Coatings Technology, 177 (2004) 12-17.

200. G.H. Liu, F. Robbevalloire, R. Gras, J. Blouet, Improvement in tribological properties of chromium-oxide coating at high-temperature by solid lubricants, Wear 160 (1993) 181-189.

201. H. Berns, Comparison of wear resistant MMC and white cast iron, Wear, 254 (2003) 47-54.

202. H. Celik, M. Kaplan, Effects of silicon on the wear behavior of cobalt-based alloys at elevated temperature, Wear, 257 (2004) 606-611.

203. J. Castaing, Effects of impurities on the mechanical properties of oxides, in: The Role of Reactive Elements in Oxidation at High Temperatures, E Lang eds. Ohio, OH: Prentice Hall (1989) 67-77.

204. H.M. Jin, T.F. Li, M.S. Li, J.I. Shen, L. Xin, and J.Y. Huang, Influence of yttrium implantation on oxidation behavior of Co-40Cr alloy at 900^0C, Journal of Rare Earths, 17 (1999) 34-37.

205. F.J. Perez, M.J. Cristobal, M.P. Hierro, G. Arnau, J. Botella, Corrosion protection of low-nickel austenitic stainless steel by yttrium and erbium-ion implantation against isothermal oxidation, Oxidation of Metals, 54 (2000) 87-101.

206. D.P. Whittle, J. Stringer, Improvements in high-temperature oxidation resistance by additions of reactive elements or oxide dispersions, Philosophical Transactions of the Royal Society of London Series A, 295 (1980) 309-329.

207. S. Chevalier, C. Valot, G. Bonnet, J.C. Colson, J.P. Larpin, The reactive element effect on thermally grown chromia scale residual stress, Materials Science and Engineering A, 343 (2003) 257-264.

208. F.J. Perez, M.J. Cristobal, M.P. Hierro, F. Pedraza, G. Arnau, P. Merino, Effect of yttrium and erbium ion implantation on the oxidation behaviour of the AISI 304 austenitic steel, Surface & Coatings Technology, 126 (2000) 116-122.

209. P.Y. Hou, J. Stringer, The effect of reactive element additions on the selective oxidation, growth and adhesion of chromia scales, Materials Science and Engineering A, 202 (1995) 1-10.

210. J. Deakin, V. Prunier, G.C. Wood, F.H. Stott, High temperature oxidation of Fe-Cr-Al alloys containing reactive elements, Materials Science Forum, 251-254 (1997) 41-48.

211. F.H. Stott, Principles of growth and adhesion of oxide scales, in: The Role of Reactive Elements in Oxidation at High Temperatures, E Lang eds. Ohio, OH: Prentice Hall (1989) 3-21.

212. Y.P. Jacob, H. Buscail, E. Caudron, R. Cueff, M.F. Stroosnijder, Various X-ray diffraction investigations to study the oxidation mechanism of yttrium implanted chromium at elevate temperatures, Journal De Physique IV, 12 (2002) 207-214.

213. J. Stringer, The Reactive Element Effect in High-Temperature Corrosion, Materials Science and Engineering A, 120 (1989) 129-137.

214. K.L. Luthra, C.L. Briant, The role of surface segregation and stresses in scale adherence, Materials Science Forum, 43 (1989) 299-326.

215. F.H. Stott, G.C. Wood, J. Stringer, The influence of alloying elements on the development and maintenance of protective scales, Oxidation of Metals, 44 (1995) 113-145.

216. P. Berthod, S. Michon, J. Di Martino, S. Mathieu, S. Noel, R. Podor, C. Rapin, Thermodynamic calculations for studying high temperature oxidation of superalloys, Computer Coupling of Phase Diagrams and Thermochemistry, 27 (2003) 279-288.

217. K. Przybylski, G.J. Yurek, The influence of implanted yttrium on the mechanism of growth of chromia scales, Materials Science Forum, 43 (1989) 1-74.

218. S. Chevalier, G. Bonnet, K. Przybylski, J.C. Colson, J.P. Larpin, Segregation of neodymium in chromia grain-boundaries during high-temperature oxidation of neodymium oxide-coated chromia-forming alloys, Oxidation of Metals 54 (2000) 527-547.

219. H.J. Grabke, Surface and interface segregation in the oxidation of metals, Surface and Interface Analysis 30 (2000) 112-119.

220. H.J. Grabke, The role of the interface oxide/metal in the high temperature corrosion resistance of alloys, Materials Science Forum, 294-296 (1999) 135-138.

221. A. Tomkings, Scaling the problems of protective oxides, Materials World, 6 (1998) 344-345.

222. J. Barbehon, A. Rahmel, M. Schutze, Behavior of the scale on a 9.5Cr steel under cyclical deformation of the base metal, Oxidation of Metals, 30 (1988) 85-94.

223. M. Schmitz-Niederau, M. Schutze, Cracking and healing of oxide scales on Ti-Al alloys at 900 degrees C, Oxidation of Metals, 52 (1999) 241-276.

224. M. Schutze, The healing behavior of protective oxide scales on heat-resistant steels after cracking under tensile strain, Oxidation of Metals, 25 (1986) 409-421.

225. M. Schutze, Deformation and cracking behavior of protective oxide scales on heat-resistant steels under tensile strain, Oxidation of Metals, 24 (1985) 199-232.

226. W.T. Griffith, L.B. Pfeil, UK Patent No. 459848, 1937.

227. Z.Y. Liu, W. Gao, Y.D. He, Modeling of oxidation kinetics of Y-doped Fe-Cr-Al alloys, Oxidation of Metals, 53 (2000) 341-350.

228. D.P. Moon, Role of reactive elements in alloy protection, Materials Science and Technology, 5 (1989) 754-764.

229. A. Kumar, Nasralla.M, D.L. Douglass, Effect of Yttrium and Thorium on Oxidation Behavior of Ni-Cr-Al Alloys, Oxidation of Metals, 8 (1974) 227-263.

230. G. Beranger, F. Armanet, M. Lambertin, Active elements in oxidation and their properties, in: The Role of Reactive Elements in Oxidation at High Temperature, E Lang eds. Ohio, OH: Prentice Hall (1989) 33-51.

231. J. Jedlinscki, The influence of active elements on the stress-relaxation in the scale and substrate of alumina-forming alloys, The Role of Reactive Elements in Oxidation at High Temperatures, E Lang eds. Ohio, OH: Prentice Hall (1989) 131-151.

232. F. Riffard, H. Buscail, E. Caudron, R. Cueff, F. Rabaste, C. Issartel, In situ and glancing angle X-ray diffraction of the structure change during and after the high temperature oxidation at 1000^0C in air of an yttrium-implanted 304 steel, Journal De Physique IV, 12 (2002) 265-272.

233. E. Caudron, H. Buscail, R. Cueff, C. Issartel, S. Perrier, F. Riffard, GAXRD and in situ X-ray diffraction characterizations of the yttrium implantation effect on pure iron oxidation at high temperature, Journal De Physique IV, 12 (2002) 417-426.

234. E. Caudron, H. Buscail, Initial stages of oxidation of yttrium-implanted pure iron and various steels at 700^0C under low oxygen partial pressure, Corrosion Science, 43 (2001) 1477-1495.

235. F. Riffard, H. Buscail, E. Caudron, R. Cueff, C. Issartel, S. Perrier, Yttrium implantation effect on 304L stainless steel high temperature oxidation at 1000^0C, Journal of Materials Science, 37 (2002) 3925-3933.

236. K. Przybylski, The influence of implanted yttrium on the oxidation properties of a Co-25Cr-1Al alloy, Materials Science and Engineering A, 120 (1989) 509-517.

237. D.P. Moon, M.J. Bennett, The effects of reactive element oxide coatings on the oxidation behavior of metals and alloys at high temperatures, Materials Science Forum, 43 (1989) 269-298.

238. B. Pieraggi, R.A. Rapp, Interfacial Scaling Reactions and the Reactive Element Effect, Materials at High Temperatures, 12 (1994) 229-235.

239. F. Riffard, H. Buscail, E. Caudron, R. Cueff, C. Issartel, S. Perrier, In-situ characterization of the oxide scale formed on yttrium-coated 304 stainless steel at 1000^0C, Materials Characterization, 49 (2002) 55-65.

240. M.J. Bennett, A.T. Tuson, Improved high-temperature oxidation behavior of alloys by ion-implantation, Materials Science and Engineering A, 116 (1989) 79-87.

241. H. Huntz, Effect of reactive elements on oxidation, Materials Science Forum, 43 (1989) 154-174.

242. E. Caudron, F. Riffard, H. Buscail, R. Cueff, C. Issartel, A. Perrier, Yttrium implantation and addition element effects on high temperature oxidation behavior of reference steels, European Physical Journal, 17 (2002) 87-97.

243. M.F. Stroosnijder, J.D. Sunderkotter, M.J. Cristobal, H. Jenett, K. Isenbugel, M.A. Baker, The influence of yttrium ion implantation on the oxidation behavior of powder metallurgically produced chromium, Surface & Coatings Technology, 83 (1996) 205-211.

244. H. Fujikawa, T. Morimoto, Y. Nishiyama, S.B. Newcomb, The effects of small additions of yttrium on the high-temperature oxidation resistance of a Si-containing austenitic stainless steel, Oxidation of Metals, 59 (2003) 23-40.

245. J. Quadakkers, L. Singheiser, Practical aspects of the reactive element effect, Materials Science Forum, 369-372 (2001) 77-92.

246. H. Buscail, C. Courty, M.F. Stroosnijder, Y.P. Jacob, J.P. Larpin, The influence of yttrium implantation on the oxidation of impure iron containing C and Mn at 700^0C, Oxidation of Metals, 49 (1998) 561-581.

247. B.A. Pint, Experimental observations in support of the dynamic-segregation theory to explain the reactive-element effect, Oxidation of Metals 45 (1996) 1-37.

248. S. Mrowec, J. Jedlinski, A. Gil, The influence of certain reactive elements on the oxidation behavior of chromia-forming and alumina-forming alloys, Materials Science and Engineering A,120 (1989) 169-173.

249. H. Fujikawa, T. Morimoto, Y. Nishiyama, Direct observation and analysis of the oxide scale formed on Y-treated austenitic stainless steels at high temperature, Materials at High Temperatures, 17 (2000) 293-298.

250. J.R. Nicholls, P. Hancock, An alternative view of the effect of active elements on the mechanical properties of scales, The Role of Reactive Elements in Oxidation at High Temperatures, E Lang eds. Ohio, OH: Prentice Hall (1989) 195-219.

251. S. Weinbruch, A. Anastassiadis, H.M. Ortner, H.P. Martinz, P. Wilhartitz, On the mechanism of high-temperature oxidation of ODS superalloys: Significance of yttrium depletion within the oxide scales, Oxidation of Metals, 51 (1999) 111-128.

252. B.A. Pint, K.L. More, P.F. Tortorelli, W.D. Porter, I.G. Wright, Optimizing the imperfect oxidation performance of iron aluminides, High Temperature Corrosion and Protection of Materials 5, Pts 1 and 2, 369-3 (2001) 411-418.

253. B.A. Pint, M. Treska, L.W. Hobbs, The effect of various oxide dispersions on the phase composition and morphology of Al_2O_3 scales grown on beta-NiAl, Oxidation of Metals, 47 (1997) 1-20.

254. T.N. Rhysjones, H.J. Grabke, H. Kudielka, The effects of various amounts of alloyed cerium and cerium oxide on the high-temperature oxidation of Fe-10Cr and Fe-20Cr alloys, Corrosion Science, 27 (1987) 49-73.

255. A.M. Huntz, S.C. Tsai, J. Balmain, K. Messaoudi, B. Lessage, C. Dolin, Atomic transport in Cr_2O_3 and Al_2O_3 scales: growth mechanism and effect of yttrium, Materials Science Forum, 251-254 (1997) 313-324.

256. M.J. Cristobal, P.N. Gibson, M.F. Stroosnijder, Study of the initial stages of oxidation of yttrium-implanted chromium using X-ray diffraction and absorption spectroscopy, Corrosion Science, 38 (1996) 805-822.

257. J.E. Antill, M.J. Bennett, R.F.A. Carney, G. Dearnaley, F.H. Fern, P.D. Goode, B.L. Myatt, J.F. Turner, J.B. Warburton, Effect of surface implantation of yttrium and cerium upon oxidation behavior of stainless steels and aluminized coatings at high-temperatures, Corrosion Science, 16 (1976) 729-745.

258. P.Y. Hou, J. Stringer, The influence of ion implanted yttrium on the selective oxidation of chromium in Co-25%Cr, Oxidation of Metals, 29 (1988) 45-73.

259. A. Gil, S. Mrowec, J. Jedlinski, G. Borchardt, The effect of implanted lanthanum on chemical diffusion in Cr_2O_3 scales on Co-40%Cr alloy, Solid State Ionics, 58 (1992) 13-21.

260. C.M. Cotell, G.J. Yurek, R.J. Hussey, D.F. Mitchell, M.J. Graham, The influence of implanted yttrium on the mechanism of growth of Cr_2O_3 on Cr, Journal of the Electrochemical Society, 134 (1987) 1871-1872.

261. K. Przybylski, G.J. Yurek, The influence of implanted yttrium on the microstructures of chromia scales formed on a Co-45 weight percent Cr alloy, Journal of the Electrochemical Society, 135 (1988) 517-523.

262. S. Chevalier, G. Bonnet, J.P. Larpin, J.C. Colson, The combined effect of refractory coatings containing reactive elements on high temperature oxidation behavior of chromia-forming alloys, Corrosion Science, 45 (2003) 1661-1673.

263. S. Chevalier, J.P. Larpin, Influence of reactive element oxide coatings on the high temperature cyclic oxidation of chromia-forming steels, Materials Science and Engineering A, 363 (2003) 116-125.

264. G. Bonnet, G. Aguilar, J.C. Colson, J.P. Larpin, The effect of rare-earths deposited on steel surfaces, by different processes on high-temperature corrosion behavior, Corrosion Science, 35 (1993) 893-899.

265. G. Bonnet, J.P. Larpin, J.C. Colson, MOCVD of neodymium oxide film effect on AISI 304 steel high-temperature corrosion behavior, Solid State Ionics, 51 (1992) 11-13.

266. S. Chevalier, G. Bonnet, J.P. Larpin, J.C. Colson, Effects of chromia coatings on the high-temperature behavior of F17Ti stainless steel in air. Effect of rare-earth-element oxides, Oxidation of Metals, 47 (1997) 53-67.

267. S. Chevalier, G. Bonnet, J.P. Larpin, Metal-organic chemical vapor deposition of Cr_2O_3 and Nd_2O_3 coatings. Oxide growth kinetics and characterization, Applied Surface Science, 167 (2000) 125-133.

268. K.M. Hubbard, B.F. Espinoza, Corrosion-resistant erbium oxide coatings by organometallic chemical vapor deposition, Thin Solid Films, 366 (2000) 175-180.

269. S.K. Mitra, S.K. Roy, S.K. Bose, Influence of superficial coating of CeO_2 on the oxidation behavior of AISI-304 stainless steel, Oxidation of Metals, 39 (1993) 221-229.

270. S. Roure, F. Czerwinski, A. Petric, Influence of CeO_2 coating on the high-temperature oxidation of chromium, Oxidation of Metals, 42 (1994) 75-102.

271. R. Cueff, H. Buscail, E. Caudron, F. Riffard, The effect of yttrium on the oxidation of a commercial Fe-Cr-Al alloy at 1173 K, High Temperature Corrosion and Protection of Materials 5, Pts 1 and 2, 369-3 (2001) 311-318.

272. R. Cueff, H. Buscail, E. Caudron, C. Issartel, F. Riffard, Influence of yttrium-alloying addition on the oxidation of alumina formers at 1173 K, Oxidation of Metals, 58 (2002) 439-455.

273. H. Yedong, F.H. Stott, The selective oxidation of Ni-15%Cr and Ni-10%Cr alloys promoted by surface-applied thin oxide films, Corrosion Science, 36 (1994) 1869-1884.

274. P.Y. Hou, J. Stringer, Effect of surface applied reactive element oxide on the oxidation of binary alloys containing Cr, Journal of the Electrochemical Society, 134 (1987) 1836-1849.

275. M.F. Stroosnijder, J.D. Sunderkotter, M.J. Cristobal, H. Jenett, K. Isenbugel, M.A. Baker, The influence of yttrium ion implantation on the oxidation behavior of powder metallurgically produced chromium, Surface & Coatings Technology, 83 (1996) 205-211.

276. G.M. Ecer, R.B. Singh, G.H. Meier, The influence of superficially applied oxide powders on the high-temperature oxidation behavior of Cr_2O_3-forming alloys, Oxidation of Metals, 18 (1982) 55-81.

277. J. Jedlinski, General aspects of the reactive element effect, Corrosion Science, 35 (1993) 863-869.

278. J. Jedlinski, The influence of reactive elements on the high temperature oxidation behavior of alumina-forming materials, Solid State Phenomena, 21-22 (1992) 335-390.

279. S. Chevalier, G. Strehl, H. Buscail, G. Borchardt, J.P. Larpin, Influence of the mode of introduction of a reactive element on the high temperature oxidation behavior of an alumina-forming alloy - Part 1: Isothermal oxidation tests, Materials and Corrosion, 55 (2004) 352-357.

280. R.J. Hussey, M.J. Graham, The influence of reactive-element coatings on the high-temperature oxidation of pure-Cr and high-Cr-content alloys, Oxidation of Metals, 45 (1996) 349-374.

281. L.V. Ramanathan, Role of rare-earth elements on high-temperature oxidation behavior of Fe-Cr, Ni-Cr and Ni-Cr-Al alloys, Corrosion Science, 35 (1993) 871-878.

282. S. Chevalier, G. Bonnet, G. Borchardt, J.C. Colson, J.P. Larpin, Mechanisms involved by reactive elements upon high temperature chromia scale growth, High Temperature Corrosion and Protection of Materials 5, Pts 1 and 2, 369-3 (2001) 327-336.

283. G. Adachi, N. Imanaka, The binary rare earth oxides, Chemical Reviews, 98 (1998) 1479-1514.

284. G. Bonnet, M. Lachkar, J.P. Larpin, J.C. Colson, Organometallic chemical-vapor-deposition of rare-earth oxide thin films - Application for steel protection against high-temperature oxidation, Solid State Ionics, 72 (1994) 344-348.

285. S. Chevalier, J.P. Larpin, Formation of perovskite type phases during the high temperature oxidation of stainless steels coated with reactive element oxides, Acta Materialia, 50 (2002) 3105-3114.

286. P. Paul, J.A. Odriozola, Development of a modified CVD coating process for the enhancement of the high temperature oxidation resistance of Cr_2O_3 and Al_2O_3 forming alloys, Materials Science and Engineering A, 300 (2001) 22-33.

287. K. Przybylski, A.J. Garrattreed, B.A. Pint, E.P. Katz, G.J. Yurek, Segregation of Y to grain boundaries in the Al_2O_3 scale formed on an ODS Alloy, Journal of the Electrochemical Society, 134 (1987) 3207-3208.

288. B.A. Pint, K.B. Alexander, Grain boundary segregation of cation dopants in alpha-Al_2O_3 scales, Journal of the Electrochemical Society, 145 (1998) 1819-1829.

289. D.A. Downham, S.B. Shendye, Observations of chromium oxide films containing cerium and yttrium using transmission electron microscopy, Oxidation of Metals, 43 (1995) 411-433.

290. S.B. Shendye, D.A. Downham, Characterization of Ni-25%Cr alloys containing reactive elements and the oxide scales grown on them at high temperatures using transmission electron microscopy, Oxidation of Metals, 43 (1995) 435-457.

291. K. Przybylski, A.J. Garrattreed, G.J. Yurek, Grain-Boundary Segregation of Yttrium in Chromia Scales, Journal of the Electrochemical Society, 135 (1988) 509-517.

292. C.L. Zeng, F.C. Rizzo, M.J. Monteiro, W.T. Wu, The oxidation of Fe-2 and 5%Y alloys at 600-800^{0}C in air, Oxidation of Metals, 51 (1999) 495-506.

293. W. Yi, C.Q. Zheng, P. Fan, S.H. Cheng, W. Li, G.F. Ying, Effect of rare earth on oxidation resistance of iron base fluxing alloy spray welding coating, Journal of Alloys and Compounds, 311 (2000) 65-68.

294. J.D. Kuenzly, D.L. Douglass, Oxidation Mechanism of Ni_3Al Containing Yttrium, Oxidation of Metals 8 (1974) 139-178.

295. Y. Niu, Y.S. Li, F. Gesmundo, F. Viani, The oxidation of a Co-15% yttrium alloy in 1 atm O_2 at 600-800^{0}C, Intermetallics, 8 (2000) 293-298.

296. A.M. Huntz, Influence of active elements on the oxidation mechanism of M-Cr-Al alloys, Materials Science and Engineering, 87 (1987) 251-260.

297. F.A. Golightly, F.H. Stott, G.C. Wood, Relationship between oxide grain morphology and growth mechanisms for Fe-Cr-Al and Fe-Cr-Al-Y alloys, Journal of the Electrochemical Society, 126 (1979) 1035-1042.

298. E.A. Polman, T. Fransen, P.J. Gellings, High-temperature corrosion and mechanical properties of protective scales on Incoloy 800H - The influence of preoxidation and ioniImplantation, Oxidation of Metals, 33 (1990) 135-155.

299. D. Delaunay, A.M. Huntz, P. Lacombe, Mechanical stresses developed in high-temperature resistant alloys during isothermal and cyclic oxidation treatments - The influence of yttrium additions on oxide scale adherence, Corrosion Science, 20 (1980) 1109-1117.

300. M.F. Stroosnijder, V. Guttmann, T. Fransen, J.H.W. Dewit, Corrosion of lloy 800H and the effect of surface-applied CeO_2 in a sulfidizing oxidizing carburizing environment at 700^{0}C, Oxidation of Metals, 33 (1990) 371-397.

301. J. Stringer, B.A. Wilcox, R.I. Jaffee, High-temperature oxidation of nickel-20% chromium-alloys containing dispersed oxide phases, Oxidation of Metals, 5 (1972) 11-47.

302. J. Stringer, I.G. Wright, High-temperature oxidation of cobalt-21% chromium-3 % Y_2O_3 alloys, Oxidation of Metals, 5 (1972) 59-84.

303. J.M. Hampikian, D.I. Potter, The effects of yttrium ion implantation on the oxidation of nickel chromium alloys 2. Oxidation of yttrium implanted Ni-20Cr, Oxidation of Metals, 38 (1992) 139-161.

304. J. Stringer, G.R. Wallwork, B.A. Wilcox, A.Z. Hed, Effect of a thoria dispersion on high-temperature oxidation of chromium, Corrosion Science, 12 (1972) 625-636.

305. C. Mennicke, E. Schumann, M. Ruhle, R.J. Hussey, G.I. Sproule, M.J. Graham, The effect of yttrium on the growth process and microstructure of alpha-Al2O3 on FeCrAl, Oxidation of Metals, 49 (1998) 455-466.

306. H. Fujikawa, T. Morimoto, Y. Nishiyama, S.B. Newcomb, The effects of small additions of yttrium on the high-temperature oxidation resistance of a Si-containing austenitic stainless steel, Oxidation of Metals, 59 (2003) 23-40.

307. F.A. Golightly, F.H. Stott, G.C. Wood, Influence of Yttrium Additions on Oxide-Scale Adhesion to an Iron-Chromium-Aluminum Alloy, Oxidation of Metals, 10 (1976) 163-187.

308. K. Koshelev, A.P. Paulikas, S. Uran, M.B. Beno, G. Jennings, J. Linton, B.W. Veal, Influence of a reactive element on the growth of a thermally grown chromia scale: A grazing emission X-ray fluorescence study, Oxidation of Metals, 59 (2003) 469-481.

309. G.J. Yurek, K. Przybylski, A.J. Garrattreed, Segregation of Y to grain-boundaries in Cr_2O_3 and NiO scales formed on an ODS alloy, Journal of the Electrochemical Society, 134 (1987) 2643-2644.

310. C.M. Cotell, G.J. Yurek, R.J. Hussey, D.F. Mitchell, M.J. Graham, The influence of grain boundary segregation of Y in Cr_2O_3 on the oxidation of Cr Metal, Oxidation of Metals, 34 (1990) 173-200.

311. B.A. Pint, J.R. Martin, L.W. Hobbs, O-18/SIMS Characterization of the growth mechanism of doped and undoped alpha-Al_2O_3, Oxidation of Metals, 39 (1993) 167-195.

312. P. Papaiacovou, R.J. Hussey, D.F. Mitchell, M.J. Graham, The effect of CeO_2 coatings on the oxidation behavior of Fe-20Cr alloys in O_2 at 1173K, Corrosion Science, 30 (1990) 451-460.

313. F.A. Golightly, F.H. Stott, G.C. Wood, Influence of yttrium additions on oxide-scale adhesion to an iron-chromium-aluminum alloy, Oxidation of Metals, 10 (1976) 163-187.

314. H. Hindam, D.P. Whittle, Peg formation by short circuit diffusion in Al_2O_3 scales containing oxide dispersions, Journal of the Electrochemical Society, 129 (1982) 1147-1149.

315. C. Mennicke, M.Y. He, D.R. Clarke, J.S. Smith, The role of secondary oxide inclusions ("pegs") on the spalling resistance of oxide films, Acta Materialia, 48 (2000) 2941-2949.

316. I.M. Allam, D.P. Whittle, J. Stringer, Oxidation behavior of CoCrAl systems containing active element additions, Oxidation of Metals, 12 (1978) 35-66.

317. C.S. Giggins, B.H. Kear, F.S. Pettit, J.K. Tien, Factors affecting adhesion of oxide scales on alloys, Metallurgical Transactions, 5 (1974) 1685-1688.

318. H. Hindam, D.P. Whittle, Microstructure, adhesion and growth kinetics of protective scales on metals and alloys, Oxidation of Metals, 18 (1982) 245-284.

319. J.K. Tien, F.S. Pettit, Mechanism of oxide adherence on Fe-25Cr-4Al (Y or Sc) alloys, Metallurgical Transactions, 3 (1972) 1587-1589.

320. A.B. Anderson, S.P. Mehandru, J.L. Smialek, Dopant effect of yttrium and the growth and adherence of alumina on nickel-aluminum alloys, Journal of the Electrochemical Society, 132 (1985) 1695-1701.

321. A. Ul-Hamid, TEM study of scale microstructures formed on Ni-10Cr and Ni-10Cr-5Al alloys with and without Y addition, Oxidation of Metals, 58 (2002) 41-56.

322. T. Amano, H. Isobe, N. Sakai, T. Shishido, The effects of yttrium addition on high-temperature oxidation of heat-resistant alloy with sulfur, Journal of Alloys and Compounds 344 (2002) 394-400.

323. A.W. Funkenbusch, J.G. Smeggil, N.S. Bornstein, Reactive element sulfur interaction and oxide scale adherence, Metallurgical Transactions A, 16 (1985) 1164-1166.

324. J.G. Smeggil, A.W. Funkenbusch, N.S. Bornstein, A Relationship between indigenous impurity elements and protective oxide scale adherence characteristics, Metallurgical Transactions A, 17 (1986) 923-932.

325. J.L. Smialek, Effect of sulfur removal on Al_2O_3 scale adhesion, Metallurgical Transactions A, 22 (1991) 739-752.

326. J.G. Smeggil, G.G. Peterson, Nature of indigenous sulfur segregated to the free metal surface and to the scale metal interface, Oxidation of Metals, 29 (1988) 103-119.

327. D.G. Lees, On the reasons for the effects of dispersions of stable oxides and additions of reactive elements on the adhesion and growth mechanisms of chromia and alumina scales - The sulfur effect, Oxidation of Metals, 27 (1987) 75-81.

328. B. Pieraggi, R.A. Rapp, Chromia scale growth in alloy oxidation and the reactive element effect, Journal of the Electrochemical Society, 140 (1993) 2844-2850.

329. H.E. Evans, Cracking and spalling of protective oxide layers, Materials Science and Engineering A, 120 (1989) 139-146.

330. D. Zhu, J.H. Stout, D.A. Shores, Determination of stress gradients in a thermally grown oxide layer using x-ray diffraction, Materials Science Forum, 251-254 (1997) 333-340.

331. A.G. vans, R.M. Cannon, Stresses in oxide films and relationships with cracking and spalling, Materials Science Forum, 43 (1989) 243-268.

332. M. Skeldon, J.M. Calvert, D.G. Lees, An investigation of the growth mechanism of Cr_2O_3 on pure chromium in 1 Atm oxygen at 950^0C, Oxidation of Metals, 28 (1987) 109-125.

333. H.E. Evans, R.C. Lobb, Conditions for the initiation of oxide scale cracking and spallation, Corrosion Science, 24 (1984) 209-222.

334. S.C. Tsai, A.M. Huntz, C. Dolin, Growth mechanism of Cr2O3 scales: Oxygen and chromium diffusion, oxidation kinetics and effect of yttrium, Materials Science and Engineering A, 212 (1996) 6-13.

335. M.J. Graham, R.J. Hussey, Characterization and growth of oxide films, Corrosion Science 44 (2002) 319-330.

336. S. Chevalier, G. Strehl, J. Favergeon, F. Desserrey, S. Weber, O. Heintz, G. Borchardt, J.P. Larpin, Use of oxygen isotope to study the transport mechanism during high temperature oxide scale growth, Materials at High Temperatures, 20 (2003) 253-259.

337. B.A. Pint, K.B. Alexander, Foreign ion segregation on Al_2O_3 scale grain boundaries, Microscopy of Oxidation 3, S.B. Newcomb, J.A. Little, eds. The Institute of Materials, 16-18 September (1996) 153-165.

338. Y. Saito, T. Maruyama, T. Amano, Adherence of oxide scale formed on Ni-20Cr-1Si alloys with small additions of rare earth elements, Materials Science and Engineering, 87 (1987) 275-280.

339. B.A. Pint, Optimization of reactive element addition to improve oxidation performance of alumina forming alloys, Alumina, 86 (2003) 686-695.

340. T.A. Ramanarayanan, M. Raghavan, R. Petkovicluton, The characteristics of alumina scales formed on Fe-based yttria dispersed alloys, Journal of the Electrochemical Society, 131 (1984) 923-931.

341. T.A. Ramanarayanan, R. Ayer, R. Petkovicluton, D.P. Leta, The influence of yttrium on oxide scale growth and adherence, Oxidation of Metals, 29 (1988) 445-472.

342. O.T. Goncel, J. Stringer, D.P. Whittle, Effect of internal stable nitride and oxide dispersion on high-temperature oxidation of Fe-Cr alloys, Corrosion Science, 18 (1978) 701-719.

343. J. Quadakkers, K.G. Briefs, H. Holzbrecher, H. Beske, The effect of yttria dispersion on the growth mechanism and morphology of chromia and alumina scales, in: The Role of Reactive Elements in Oxidation at High Temperatures, E Lang eds. Ohio, OH: Prentice Hall (1989) 155-173.

344. A. Rahmel, M. Schutze, Mechanical aspects of the rare earth effect, Oxidation of Metals, 38 (1992) 255-266.

345. P.Y. Hou, J. Stringer, Oxide scale adhesion and impurity segregation at the scale metal interface, Oxidation of Metals, 38 (1992) 323-345.

346. H.J. Grabke, D. Wiemer, H. Viefhaus, Segregation of sulfur during growth of oxide scales, Applied Surface Science, 47 (1991) 243-250.

347. C. Mennicke, E. Schumann, J. Le Coze, J.L. Smialek, G.H. Meier, M. Ruhle, SEM and TEM Studies of the oxidation of FeCrAl, in: Microscopy of Oxidation 3, Newcomb, S.B. and Little, J.A. eds. The Institute of Materials, 16-18 September (1996) 93-104.

348. Amano, H. Isobe, K. Yamada, T. Shishido, The morphology of alumina scales formed on Fe-20Cr-4Al-S alloys with reactive element (Y, Hf) additions at 1273 K, Materials at High Temperatures, 20 (2003) 387-393.

349. M.J. Graham, J.I. Eldrige, D.F. Mitchell, R.J. Hussey, Anion transport in growing Cr_2O_3 and Al_2O_3 scales, Materials Science Forum, 43 (1989) 207-242.

350. B. Pieraggi, R.A. Rapp, Stress generation and vacancy annihilation during Scale growth limited by cation vacancy diffusion, Acta Metallurgica, 36 (1988) 1281-1289.

351. J.P. Hirth, B. Pieraggi, R.A. Rapp, The role of interface dislocations and ledges as sources sinks for point defects in scaling reactions, Acta Metallurgica & Materialia ,43 (1995) 1065-1073.

352. B. Pieraggi, R.A. Rapp, J.P. Hirth, Role of interface structure and interfacial defects in oxide scale growth, Oxidation of Metals, 44 (1995) 63-79.

353. R. Liu, D.Y. Li, Protective effect of yttrium additive in lubricants on corrosive wear, Wear, 229 (1999) 968-974.

354. L.G. Yu, Y.F. Lian, Q.J. Xue, The tribological behaviors of some rare earth complexes as lubricating additives - Part 1. An investigation of the friction-reducing behaviors and an XPS study of the tribochemical characteristics, Wear, 214 (1998) 47-53.

355. L.G. Yu, Y.F. Lian, Q.J. Xue, The tribological behaviors of some rare earth complexes as lubricating additives Part 2 - The antiwear and extreme pressure properties in lithium grease, Wear, 214 (1998) 151-155.

356. L.G. Yu, M.D. Nie, Y.F. Lian, The tribological behaviour and application of rare earth lubricants, Wear, 197 (1996) 206-210.

357. T.C. Zhang, D.Y. Li, Improvement in the resistance of aluminum with yttria particles to sliding wear in air and in a corrosive medium, Wear, 250 (2001) 1250-1256.

358. X.Y. Wang, D.Y. Li, Beneficial effects of yttrium on the mechanical failure and chemical stability of the passive film of 304 stainless steel, Materials Science and Engineering A, 315 (2001) 158-165.

359. T.C. Zhang, D.Y. Li, Effects of yttrium on sliding wear of 304 stainless steel in dilute sulphuric acid and air, Materials Science and Technology, 15 (1999) 1441-1446.

360. T.C. Zhang, Y.C. Luo, D.Y. Li, Erosion behavior of aluminide coating modified with yttrium addition under different erosion conditions, Surface & Coatings Technology, 126 (2000) 102-109.

361. T.C. Zhang, D.Y. Li, Beneficial effect of oxygen-active elements on the resistance of aluminide coatings to corrosive erosion and dry erosion, Surface & Coatings Technology, 130 (2000) 57-63.

362. X.Y. Wang, D.Y. Li, Effects of yttrium on mechanical properties and chemical stability of passive film of aluminide coating on 1045 steel, Surface & Coatings Technology, 160 (2002) 20-28.

363. H. Ahmadi, D.Y. Li, Mechanical and tribological properties of aluminide coating modified with yttrium, Surface & Coatings Technology, 161 (2002) 210-217.

364. H. Ahmadi, D.Y. Li, Beneficial effects of yttrium on mechanical properties and high-temperature wear behavior of surface aluminized 1045 steel, Wear, 255 (2003) 933-942.

365. T.C. Zhang, D.Y. Li, Effects of yttrium on corrosive erosion and dry sand erosion of FeAlCr(Y) diffusion coatings on 1030 steel, Materials Science and Engineering A, 277 (2000) 18-24.

366. X.H. Cheng, C.Y. Xie, Effect of rare earth elements on the erosion resistance of nitrided 40Cr steel, Wear 254 (2003) 415-420.

367. Q.Q. Shangguan, X.H. Cheng, Effect of rare earth elements on erosion resistance of nitrocarburized layers of 38CrMoAl steel, Journal of Rare Earths, 22 (2004) 406-409.

368. T.C. Zhang, D.Y. Li, Improvement in the corrosion-erosion resistance of 304 stainless steel with alloyed yttrium, Journal of Materials Science, 36 (2001) 3479-3486.

369. T.C. Zhang, D.Y. Li, Effect of alloying yttrium on corrosion-erosion behavior of 27Cr cast white iron in different corrosive slurries, Materials Science and Engineering A, 325 (2002) 87-97.

370. T.H. Zhang, J.D. Xie, C.Z. Ji, J. Chen, H. Xu, J. Li, G.R. Sun, H.X. Zhang, Influence of the structure of implanted steel with Y, Y+C and Y+Cr on the behaviors of wear, oxidation and corrosion resistance, Surface & Coatings Technology, 72 (1995) 93-98.

371. J.L.D. vanOtterloo, J.T.M. DeHosson, Microstructural features and mechanical properties of a cobalt-based laser coating, Acta Materialia, 45 (1997) 1225-1236.

372. J.C. Jin, H. Jin, M. Sakai, C.L. Wu, Improving the surface behaviors of bearing by adding rare-earth Er implantation, Wear, 205 (1997) 214-219.

373. Y.F. Lian, Q.J. Xue, H.Q. Wang, The Tribological Behavior of GCr15 Bearing Steel Implanted with Cerium, Surface & Coatings Technology, 73 (1995) 98-104.

374. K.L. Wang, Q.B. Zhang, M.L. Sun, Y.M. Zhu, Effect of laser surface cladding of ceria on the wear and corrosion of nickel-based alloys, Surface & Coatings Technology, 96 (1997) 267-271.

375. Y.F. Lian, L.G. Yu, Q.J. Xue, The effect of cerium dioxide on the friction and wear properties of flame spraying nickel-based alloy coating, Wear, 181 (1995) 436-441.

376. K.L. Wang, Q.B. Zhang, M.L. Sun, X.G. Wei, Y.M. Zhu, Rare earth elements modification of laser-clad nickel-based alloy coatings, Applied Surface Science, 174 (2001) 191-200.

377. X.H. Wang, M. Zhang, Z.D. Zou, S.Y. Qu, Microstructure and properties of laser clad TiC+NiCrBSi plus rare earth composite coatings, Surface & Coatings Technology, 161 (2002) 195-199.

378. M. Harun, I.A. Talib, A.R. Daud, Effect of element additions on wear property of eutectic aluminium-silicon alloys, Wear, 194 (1996) 54-59.

379. Y.F. Lian, L.G. Yu, Q.J. Xue, The improved friction and wear properties of cast Fe-Mo-S wear-resistant alloy by cerium dioxide doping, Wear, 199 (1996) 181-186.

380. L. Remy, A. Pineau, Twinning and strain-induced Fcc-Hcp transformation on mechanical properties of Co-Ni-Cr-Mo alloys, Materials Science and Engineering, 26 (1976) 123-132.

381. A. Halstead, R.D. Rawlings, Structure and hardness of Co-Mo-Cr-Si wear resistant Alloys (Tribaloys), Metal Science, 18 (1984) 491-500.

382. C. Montero-Ocampo, R. Juarez, A.S. Rodriguez, Effect of fcc-hcp phase transformation produced by isothermal aging on the corrosion resistance of a Co-

27Cr-5Mo-0.05C alloy, Metallurgical and Materials Transactions A, 33 (2002) 2229-2235.

383. G. Bouquet, B. Dubois, Influence of the fcc phase retained at room temperature on the mechanical properties of cobalt, Scripta Metallurgica, 12 (1978) 1079-1081.

384. P. Huang, H.F. Lopez, Strain induced epsilon-martensite in a Co-Cr-Mo alloy: grain size effect, Materials Letters, 39 (1999) 244-248.

385. A.J. Salinas, G.L. Rodriguez-Galicia, Deformation behavior of low-carbon Co-Cr-Mo alloys for low friction implant applications, Journal of Biomedical Materials Research, 31 (1996) 409-419.

386. P. Huang, H.F. Lopez, Athermal epsilon-martensite in a Co-Cr-Mo alloy: grain size effects, Materials Letters, 39 (1999) 249-253.

387. A.J. Saldivar, H.F. Lopez, Role of aging on the martensitic transformation in a cast cobalt alloy, Scripta Materialia, 45 (2001) 427-433.

388. G.D. Pigrova, A.I. Rybnikov, Kinetics of polymorphic transformations in the Co-Cr-Al-Y coatings, Physics of Metals and Metallography, 89 (2000) 622-626.

389. P. Huang, H.F. Lopez, Effects of grain size on development of athermal and strain induced epsilon martensite in Co-Cr-Mo implant alloy, Materials Science and Technology 15 (1999) 157-164.

390. P. Crook, P. C.C. Li, The elevated temperature metal to metal wear behavior of selected hardfacing alloys, Wear of Materials IV, (1983) 272-279.

391. S. Atamert, J. Stekly, Microstructure, wear resistance, and stability of cobalt based hardfacing alloys, Surface Engineering, 9 (1993) 231-241.

392. K.J. Bhansali, A.E. Miller, The role of stacking fault energy on galling and wear behavior, Wear, 75 (1982) 241-252.

393. T.C. Tisone, Concentration and temperature dependence of stacking fault energy in fcc Co-Fe alloys, Acta Metallurgica, 21 (1973) 229-236.

394. H.B. Michaelson, Work function of elements and its periodicity, Journal of Applied Physics, 48 (1977) 4729-4733.

395. J.C. Yang, Z.R. Nie, Y.M. Wang, Microstructure and emission ability of rare earth oxides doped molybdenum cathodes, Applied Surface Science, 215 (2003) 87-95.

396. M. Ushio, A.A. Sadek, F. Matsuda, Comparison of temperature and work function measurements obtained with different GTA electrodes, Plasma Chemistry and Plasma Processing, 11 (1991) 81-101.

397. H. Berns, Microstructural properties of wear-resistant alloys, Wear, 181 (1995) 271-279.

398. R. Liu, D.Y. Li, Y.S. Xie, R. Llewellyn, H.M. Hawthorne, Indentation behavior of pseudoelastic TiNi alloy, Scripta Materialia, 41 (1999) 691-696.

399. M. Sage, Methode d'analyse quantitative des varietes allotropiques du cobalt par les rayons X, Revue de Metallurgie, 47 (1950) 139-145.

400. H. Kashani, A. Amadeh, A. Ohadizadeh, Effect of temperature on the strain induced γ to ε phase transformation in Stellite 21 during wear test, Materials Science and Engineering A, 435 (2006) 474-477.

401. H.P. Soo, Y.L. Yun, D.L. Yong, Y.K. Kwang, Effect of Si addition on the scale adhesion of 19Cr-Ti ferritic stainless steel, in: Microscopy of Oxidation 3, S.B. Newcomb, J.A. Little, eds. The Institute of Materials, 16-18 September 1996 551-559.

402. R.E. Lobnig, H.P. Schmidt, K. Hennesen, H.J. Grabke, Diffusion of cations in chromia layers grown on iron-base alloys, Oxidation of Metals, 37 (1992) 81-93.

403. M.J. Bennet, D.P. Moon, Effect of active elements on the oxidation behavior of Cr_2O_3 formers, in: The Role of Reactive Elements in Oxidation at High Temperatures, E Lang eds. Ohio, OH: Prentice Hall (1989) 111-127.

404. M. Kalin, Influence of flash temperatures on the tribological behavior in low-speed sliding: a review, Materials Science and Engineering A, 374 (2004) 390-397.

405. V. Aronov, Formation and destruction kinetics of transformed structures of metals in frictional contact, Wear, 38 (1976) 305-310.

406. V. Aronov, Kinetic characteristics of transformation and failure of surface layers of metals under dry friction, Wear, 41 (1977) 205-212.

407. H. Hong, R.F. Hochman, T.F.J. Quinn, A new approach to the oxidational theory of mild wear, Tribology Transactions, 31 (1988) 71-75.

408. A.C. Fischer-Cripps, Introduction to contact mechanics, Springer Science, New York, (2007) 101-107.

409. J.R. Nicholls, D.J. Hall, P.F. Tortorelli, Hardness and modulus measurements on oxide scales, Materials at High Temperatures, 12 (2007) 141-150.

410. R. Riedel, Handbook of ceramic hard materials, Willey-VCN, Weinheim, (2000).

411. J.R. Smith, S. Breakspear, S.A. Campbell, A[illegible]n surface finishing: Part I. An introduction, Transactions of the Institute of Metal F[illegible]hing, 81 (2003) B26-B29.

412. H. Bubert, H. Jenett (Eds.), Surface and thin film analysis - Principles, instrumentation, applications, Wiley, New York (2002).

413. J.R. Smith, S. Breakspear, S.A. Campbell, AFM in surface finishing: Part II. Surface roughness, Transactions of the Institute of Metal Finishing, 81 (2003) B55-B58.

414. ASTM E 112 - Standard test methods for determining average grain size, (2006).

415. J.C. Vickerman, SIMS, time-of-flight, and surface analysis, Encyclopedia of Materials: Science and Technology, Elsevier Science Ltd. (2001) 8624-8629.

416. L. Van Vaeck, A. Adriaens, R. Gijbels, Static secondary ion mass spectrometry: (S-SIMS) Part 1. Methodology and structural interpretation, Mass Spectrometry Reviews, 18 (1999) 1-47.

417. A. Adriaens, L. Van Vaeck, F. Adams, Static secondary ion mass spectrometry (S-SIMS) Part 2: Material science applications, Mass Spectrometry Reviews, 18 (1999) 48-81.

418. Pantano, Secondary ion mass spectroscopy, in: ASM Handbook, Vol. 10 (New York, (2002) 272-279.

419. H.E. Bishop, Applications of dynamic SIMS to the study of oxidation, in: M.J. Bennet, S.B. Newcomb (Eds.), Proceedings of the Second International Conference on Microscopy of Oxidation, The University Press Cambridge, Selwyn College, University of Cambridge, (1993) 14-22.

420. P. Willich, C. Steinberg, SIMS depth profile analysis of wear resistant coatings on cutting tools and technical components, Applied Surface Science, 179 (2001) 264-269.

421. A.M. Huntz, J. Balmain, S.C. Tsai, K. Messaoudi, B. Loudjani, B. Lesage, J. Li, Diffusion studies in oxides scales grown on alumina- and chromia-forming alloys, Scripta Materialia 37 (1997) 651-660.

422. R. Krishnamurthy, D.J. Srolovitz, Stress distribution in growing polycristalline oxide films, Acta Materialia 52 (2004) 3761-3780.

423. C.C. Koch, D.G. Morris, K. Lu, A. Inoue, Ductility of nanostructured materials, Mrs Bulletin 24 (1999) 54-58.

424. S. Chevalier, G. Bonnet, J.C. Colson, J.P. Larpin, Influence of a reactive element oxide coating on the high temperature oxidation of chromia-former alloys, Journal De Chimie Physique Et De Physico-Chimie Biologique, 95 (1998) 2083-2101.

425. H.E. Evans, R.C. Lobb, Conditions for the initiation of oxide scale cracking and spallation, Corrosion Science, 24 (1984) 209-222.

426. W.J. Quadakkers, J.F. Norton, J. Penkalla, U. Breuer, A. Gil, T. Rieck, M. Hansel, SNMS and TEM studies on the oxidation behavior of Cr-based ODS alloys, in: Microscopy of Oxidation 3. S.B. Newcomb, J.A. Little, eds. The Institute of Materials, 16-18 September (1996) 221-230.

427. C.H. Yang, G.E. Welsch, T.E. Mitchell, Analytical electron microscopy investigation of the oxide scale on an yttrium-implanted Ni-20wt%t Cr alloy, Materials Science and Engineering, 69 (1985) 351-357.

428. A.G. Evans, G.B. Crumley, R.E. Demaray, On the mechanical behavior of brittle coatings and layers, Oxidation of Metals, 20 (1983) 193-216.

429. V. Lanteri, D. Huin, P. Drillet, D. Bouleau, P. Henry,H. Gaye, Internal oxidation of Fe-Si alloys in the presence of external scale, in: Microscopy of Oxidation 3. S.B. Newcomb, J.A. Little, eds. The Institute of Materials, 16-18 September (1996) 535-549.

430. F. Delaunay, C. Berthier, D. Galy, J.M. Lameille, M. Lenglet, Scanning electron microscopy contribution to the study of high temperature oxidation mechanism of the alloy Incoloy 800 in: Microscopy of Oxidation 3. S.B. Newcomb, J.A. Little, eds. The Institute of Materials, 16-18 September (1996). 587-595.

431. M. Landkof, A.V. Levy, D.H. Boone, R. Gray, E. Yaniv, The effect of surface additives on the oxidation of chromia-forming alloys, Corrosion, 41 (1985) 344-357.

432. A.S. Nagelberg, R.W. Bradshaw, Chemical characterization of complex oxide products on titanium-enriched 310 stainless steel, Journal of the Electrochemical Society, 128 (1981) 2655-2659.

433. F.H. Stott, Methods of improving adherence, Materials Science and Technology 4 (1988) 431-438.

434. A. Green, B. Bastow, The effect of RE additions upon alloy depletion profiles resulting from the preferential removal of the less noble element during alloy oxidation, in: M.J. Bennet, S.B. Newcomb (Eds.), Microscopy of Oxidation 2 (The University Press Cambridge, Selwyn College, University of Cambridge, (1993) 137-149.

435. B.A. Pint, K.L. More, I.G. Wright, The use of two reactive elements to optimize oxidation performance of alumina-forming alloys, Materials at High Temperatures, 20 (2003) 375-386.